SKB

Modelling bentonite resaturation in the Bentonite Rock Interaction Experiment (BRIE)

Task 8C of SKB Task Forces EBS and GWFTS

Steven Baxter

David Holton

Andrew Hoch

Modelling bentonite resaturation in the Bentonite Rock Interaction Experiment (BRIE)

Task 8C of SKB Task Forces EBS and GWFTS

Steven Baxter, David Holton, Andrew Hoch

Amec Foster Wheeler

Abstract

The Nuclear Decommissioning Authority (NDA) Radioactive Waste Management Directorate (RWMD) are studying and considering the safe disposal of high level wastes and spent fuel within the UK Geological Disposal Facility (GDF). A range of potential concepts are being considered, and include the possible use of bentonite as a buffer material as part of an engineered barrier system (EBS) to surround certain containers being considered for disposal. Participation in the SKB EBS Task Force offers NDA RWMD the unique opportunity to further the UK's capabilities by assisting the development of modelling of coupled thermal, hydraulic, mechanical and chemical processes relevant to bentonite. One of modelling projects within the Task Force consists of modelling the Bentonite Rock Interaction Experiment (BRIE) at the Äspö Hard Rock Laboratory (HRL) and is the focus of this report.

Sammanfattning

Radioactive Waste Management Directorate (RWMD) utgör en gren av den brittiska myndigheten för hantering av radioaktivt avfall (NDA). RWMD studerar och överväger säker deponering av högaktivt avfall och använt kärnbränsle inom det brittiska konceptet Geological Disposal Facility (GDF). En rad potentiella koncept beaktas och inkluderar möjlig användning av bentonit som buffertmaterial som en del av ett konstruerat barriärsystem (EBS) för att omge behållare avsedda för deponering. Deltagandet i SKB EBS Task Force erbjuder NDA RWMD den unika möjligheten att vidareutveckla Storbritanniens kapacitet genom att bistå med utvecklingen av modellering av de kopplade termiska, hydrauliska, mekaniska och kemiska processer som är relevanta för bentonit. I fokus för denna rapport är ett av modelleringsprojekten inom arbetsgruppen (EBS TF) som består av att modellera Bentonite Rock Interaction Experiment (BRIE) som utfördes i Äspö Hard Rock Laboratory (HRL).

Executive summary

The Nuclear Decommissioning Authority (NDA) Radioactive Waste Management Directorate (RWMD) are studying and considering the safe disposal of high level wastes and spent fuel within the UK Geological Disposal Facility (GDF). A range of potential concepts are being considered, and include the use of bentonite as a buffer material as part of an engineered barrier system (EBS) to surround the disposal canisters.

Required safety functions to be performed by the bentonite buffer include:

- Protecting the disposal containers from detrimental thermal, hydraulic, mechanical and chemical processes.

- Retarding radionuclide release from any failed waste container.

Participation in the Äspö Engineered Barrier System Task Force, offers NDA RWMD the unique opportunity to further the UK's capabilities by assisting the development of modelling of coupled thermal, hydraulic, mechanical and chemical processes relevant to bentonite. Within the Task Force, these research fields are currently subdivided into two research areas, one considering thermal, hydraulic and mechanical processes, the other thermal, hydraulic and chemical processes. Within these research areas, modelling tasks are identified to develop the understanding of these coupled processes.

One of these tasks consists of modelling the Bentonite Rock Interaction Experiment (BRIE) at the Äspö Hard Rock Laboratory (HRL), and is the focus of this report. It has allowed the UK to develop modelling approaches as part of a collaborative international project, and has provided NDA RWMD the opportunity to

- compare and verify techniques and processes developed for modelling the bedrock/bentonite interface with other teams participating in the Task Force,

- identify the important data used to parameterise the rock, to provide a basis for modelling resaturation,

- explore important parameter uncertainty and evaluate the consequences (e.g. rock matrix permeability),

- derive a methodology to integrate the approach taken to both the rock and bentonite,

- build confidence in the ability to model resaturation processes once data becomes available to compare to predictions, and

- develop methodologies to represent the interaction between the groundwater flow from the rock, and the resaturation of the bentonite material.

Modelling the BRIE at the Äspö HRL has demonstrated the feasibility of using a physically realistic approach to simulate the interface between bentonite and fractured host rock. The developed approach has identified:

- Accurate representation of the surrounding fractured bedrock is critical to understanding the hydration of emplaced bentonite. The saturation of bentonite is highly heterogeneous, revealing significant differences to the homogeneous assumptions commonly made to estimate bentonite resaturation.

- The significant potential of the combination of CONNECTFLOW and TOUGH2 software to simulate the heterogeneous hydration of the bentonite.

- Saturation rates of bentonite by a fractured host rock are significantly affected by:
  - the locations of groundwater ingress to the deposition hole, and
  - the total inflows observed under open deposition hole conditions.

- The permeability of the rock matrix is important in the prediction of the resaturation times of the emplaced bentonite.

Finally, although models to date have been developed that are specific to the BRIE at the Äspö HRL, the tools, techniques and methodologies developed are generic, and are directly applicable to any future work carried out on UK specific issues for the simulation of bentonite hydration in a fractured host rock.

List of acronyms and abbreviations

BRIE	Bentonite Rock Interaction Experiment
CCDF	Complementary Cumulative Density Function
CONNECTFLOW	A software package, developed by AMEC, for modelling groundwater flow and transport on a variety of scales
CPM	Continuous Porous Medium
DFN	Discrete Fracture Network
EBS	Engineered Barrier System
ECPM	Equivalent Continuous Porous Medium
EOS	Equation-Of-State
GDF	Geological Disposal Facility
GID	Pre and post processing software for numerical simulations, http://gid.cimne.upc.edu/
GOCAD	Subsurface modelling software, http://www.pdgm.com/products/gocad.aspx
GWFT	Groundwater Flow and Transport of solutes
HRL	Hard Rock Laboratory
NDA	Nuclear Decommissioning Authority
RWMD	Radioactive Waste Management Directorate
SDM	Site Descriptive Modelling
TOUGH2	A software package, developed by Lawrence Berkeley National Laboratory, for simulating nonisothermal, multiphase fluid flows in both porous and fractured media

Contents

1 Introduction and objectives

The Nuclear Decommissioning Authority (NDA) has established the Radioactive Waste Management Directorate (RWMD) to manage the delivery of geological disposal for higher-activity radioactive wastes. The safe disposal of these wastes utilises a multiple barrier concept to isolate the wastes from the biosphere. Although the UK does not currently have a defined concept for its Geological Disposal Facility (GDF), for all Spent Fuel disposal concepts excepting disposal in salt, the generic designs for a UK GDF (NDA 2010) utilise a bentonite buffer material as part of an engineered barrier system (EBS). This bentonite buffer is used to surround the disposal container, and in combination with crushed rock spoil, could also form the mass backfill used within deposition tunnels of the GDF. A bentonite buffer material is also proposed in the GDF concepts of a number of other countries, for example SKB and Posiva's KBS-3 concept (SKB 2006). The required safety functions to be performed by the bentonite buffer are detailed in Holton et al. (2012), and include:

- Protecting the disposal containers from detrimental processes, including thermal, hydraulic, mechanical and chemical effects.

- Retarding the release of radionuclides from any failed waste container.

Consequently the understanding of bentonite behaviour is relevant to the current generic UK disposal concept, and as part of their research programme, NDA RWMD, reviewed UK specific factors influencing the performance of the bentonite barrier (Wilson et al. 2010). In 2011, NDA RWMD decided to provide support for a UK modelling team to participate in this collaborative international project. Through participation in the EBS Task Force, NDA RWMD intends to build on, and strengthen the UK's capabilities by assisting the development of modelling of processes relevant to bentonite, applicable either to the current generic disposal concepts or to future site-specific stages of the UK disposal programme.

The SKB EBS Task Force programme considers coupled Thermal (T), Hydraulic (H), Mechanical (M) and Chemical (C) processes of a bentonite buffer material. Currently, two research areas of coupled modelling exist, one considering THM processes, and the other THC processes. Projects within the Task Force considering coupled THM processes include the investigation of hydraulic interactions between bedrock and the bentonite interface, Task 8 and the Bentonite Rock Interaction Experiment (BRIE); the homogenisation of bentonite as it hydrates; a sensitivity analysis; and the modelling of the "prototype repository". Research into THC processes includes the investigation of diffusion through bentonite, as well as in situ transport experiments.

This report describes the modelling of Task 8 of the EBS Task Force, considers the interaction between engineered and natural barriers, and provides an assessment of a fractured bedrock description in the wetting processes of bentonite at deposition tunnel scale (Vidstrand et al. 2017). Task 8 is split into a number of subtasks. Specifically, modelling results of Task 8C are presented in this report. This task is concerned with predicting the resaturation of the central deposition holes of the BRIE. Through participation in this collaborative, international project the following objectives are identified:

- Compare and verify techniques and processes developed for modelling the bedrock/bentonite interface with other teams participating in the Task Force.

- Identify the important data used to parameterise the rock, to provide a basis for modelling resaturation.

- Explore important parameter uncertainty and evaluate the consequences (e.g. rock matrix permeability).

- Derive a methodology to integrate the approach taken to both the rock and bentonite.

- Build confidence in the ability to model resaturation processes once data becomes available to compare to predictions.

- Develop methodologies to represent the interaction between the groundwater flow from the rock, and the resaturation of the bentonite material.

It is noted that although the models developed in this study are specific to the BRIE at the Äspö Hard Rock Laboratory, the tools, techniques and methodologies developed are generic, and are directly applicable to any future work carried out on UK specific issues for the simulation of the hydration of emplaced bentonite by a surrounding fractured rock.

1.1 Background of Task 8

Task 8 is a collaborative research project between the Äspö Task Forces on Groundwater Flow and Transport of Solutes (GWFT), and Engineered Barrier Systems (EBS). The intention of Task 8 (Vidstrand et al. 2017) is to improve:

- the scientific understanding of the exchange of water between the sparsely fractured rock and the bentonite,

- the predictions of the wetting of the bentonite buffer,

- the characterisation methods of canister deposition boreholes, and

- the methods used for establishing deposition hole criteria.

The basis of this task is the BRIE, conducted at the Äspö Hard Rock Laboratory (HRL), and running concurrently. The BRIE (Vidstrand et al. 2017) involves

- selection of a site at Äspö to host the experiment using existing understanding of hydrogeological conditions at the Äspö HRL and a limited number of exploratory boreholes,

- the drilling of central boreholes and subsequent characterisation of the site using borehole logging and hydraulic tests, and

- the characterisation of two central boreholes for the installation of a bentonite buffer.

The participating collaborative modelling groups in Task 8 have been asked to consider many aspects of the BRIE. These form a number of subtasks (8A–8D, and 8F), summarised below:

- **Task 8A:** Scoping of methodologies to accurately represent the bentonite – bedrock interface, and characterise the importance of hydraulically active fractures on bentonite wetting.

- **Task 8B:** Scoping calculations of the TASO tunnel, host of the BRIE, and includes developing methodologies to represent both the rock matrix and fracture contribution to groundwater flow.

- **Task 8C:** Prediction of inflows and subsequent resaturation profiles of emplaced bentonite for central deposition holes of the BRIE. Calculations are based on statistical representation of the fracture network, with only a limited characterisation of the deposition holes available. This task is the focus of this report.

- **Task 8D:** Follows on from Task 8C, updating models to predict inflows and resaturation of emplaced bentonite for deposition holes KO0017G01 and KO0018G01 using detailed characterisation data.

- **Task 8F:** A final update of the models using all experimental data collected from the BRIE to further refine inflow and resaturation predictions.

1.2 Scope of Task 8C: Predictions for central depositon holes

Task 8 aims to improve the knowledge and modelling of the bedrock/bentonite interface, important for the inflow into the boreholes and resaturation of emplaced bentonite. In particular, Task 8C considers predictions of inflow to central boreholes planned for the TASO tunnel of the BRIE. The modelling of Task 8C is subdivided into two parts, namely Task 8C1 and Task 8C2, with the objectives for each of these subtasks detailed below.

1.2.1 Task 8C1

For Task 8C1, the deposition holes drilled in the TASO tunnel are open to flow, allowing groundwater into the boreholes. The aim of this task is to predict inflow to these central boreholes using the selected modelling tools and the limited data available.

The main objectives for Task 8C1 (Vidstrand et al. 2017) are to

- develop models of the TASO tunnel and surrounding bedrock,

- examine the boundary conditions provided as part of the task description [5], with relation to three site-specific deformation zones, and

- predict the distribution of inflows to the boreholes.

1.2.2 Task 8C2

Task 8C2 considers the wetting of bentonite emplaced within the deposition holes considered as part of Task 8C1, with results from 8C1 feeding directly into these simulations (e.g. flow fields).

The main objectives for Task 8C2 (Vidstrand et al. 2017) are to

- evaluate the effects of the location of fractures intersecting the deposition hole on the resulting wetting of the bentonite,

- to provide a base case for comparison with future simulations using a more elaborated hydrogeological model.

1.3 Report structure

This report presents the modelling results for Task 8C of the joint GWFT and EBS Task Force. This involves making predictions for the central deposition holes of the BRIE at the Äspö HRL. The report structure is as follows:

- Chapter 2 provides details of the specification of Task 8C as described in the task description (Vidstrand et al. 2017), and adapted for the implementations considered in this report.

- Chapter 3 provides an overview of the concepts and methodologies used for modelling Task 8C, and a description of the numerical models developed.

- Chapter 4 and Chapter 5 present results for both modelling Tasks 8C1 and 8C2 respectively. The former considers open boreholes within the BRIE, with the later simulating the subsequent saturation of emplaced bentonite.

- Chapter 6 provides a discussion of results, outlining the main conclusions drawn from the predictive modelling of the BRIE.

2 Task 8C specification

Task 8C considers the development of methodologies for integrating the modelling approach taken to the bentonite and fractured host rock. Using the techniques developed, predictions of the BRIE experiment are made for

- the distribution of inflows to the boreholes (Task 8C1), and
- resaturation profiles and times of emplaced bentonite (Task 8C2).

Data for Task 8 were delivered as part of task description (Vidstrand et al. 2017) with the details presented in the following subsections are based on the associated Task 8C case specification. In general, figures and data presented within Chapter 2 are directly reproduced from (Vidstrand et al. 2017).

2.1 Geometrical set-up

The coordinate system used in Task 8 is the Swedish RT90 system. The chosen model domain occupies a volume of approximately $40 \times 40 \times 40$ m³, bounded by the set of coordinates in Table 2-1.

The BRIE uses the TASO tunnel as its primary investigation area, and consequently specifications used are based on the sub-local scale of the TASO tunnel area at the Äspö Hard Rock Laboratory (HRL). The suggested model domain relative to the Äspö HRL is shown in Figure 2-1. In addition, as the BRIE progresses, more detailed information will emerge that can subsequently be incorporated into the model development phase of Task 8C.

The geometrical framework of the Äspö HRL is provided as part of the task description (Vidstrand et al. 2017) via the CAD file TASO_V0.1_TG.dxf. This file also provides location data for the five probing boreholes so far established in the BRIE. In addition, three hydrogeological structures are identified that fully intersect the proposed model domain, referred to as wfracture_01, wfracture_02 and NNW4. The framework for these geological structures is provided via the CAD file TASO_V0.1_DET.dxf.

A complete set of geometrical information, including principal stress orientations, covering the proposed model domain, is detailed in TASO_V1.1_ALL.dxf. Figure 2-2 illustrates the key features from this file, including the positions of main tunnels, hydrogeological structures, and the proposed model domain.

Table 2-1. Bounding coordinates for the proposed model domain, with coordinates specified in the Swedish RT90 system. This table is reproduced from the task description (Vidstrand et al. 2017).

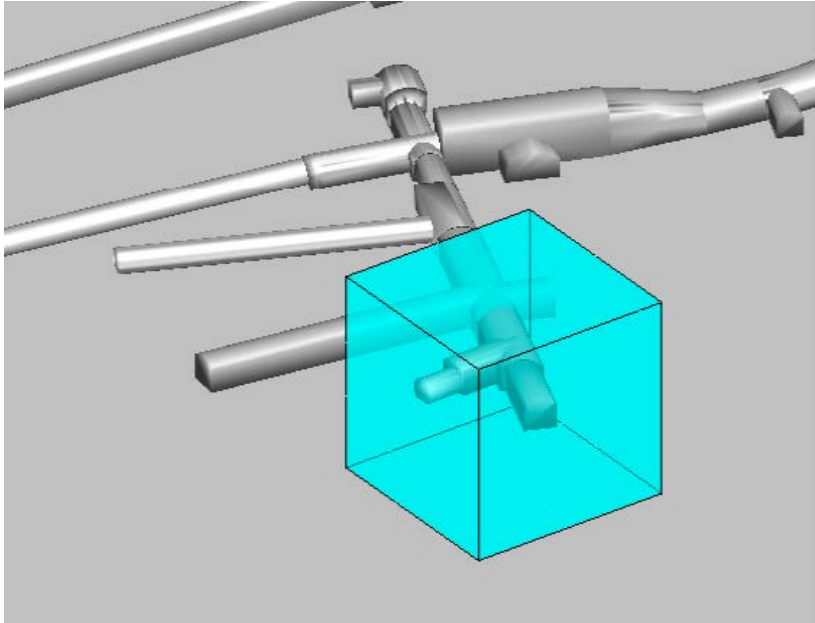| x	y	z
1551603	6367769	−396
1551629	6367799	−396
1551600	6367826	−396
1551573	6367796	−396
1551603	6367769	−436
1551629	6367799	−436
1551600	6367826	−436
1551573	6367796	−436

Figure 2-1. *Illustration of the suggested model domain in the vicinity of the assembly hall at the Äspö HRL. The model domain includes the TASO tunnel and is approximately (40)³ m³. This figure is reproduced from the task description (Vidstrand et al. 2017).*
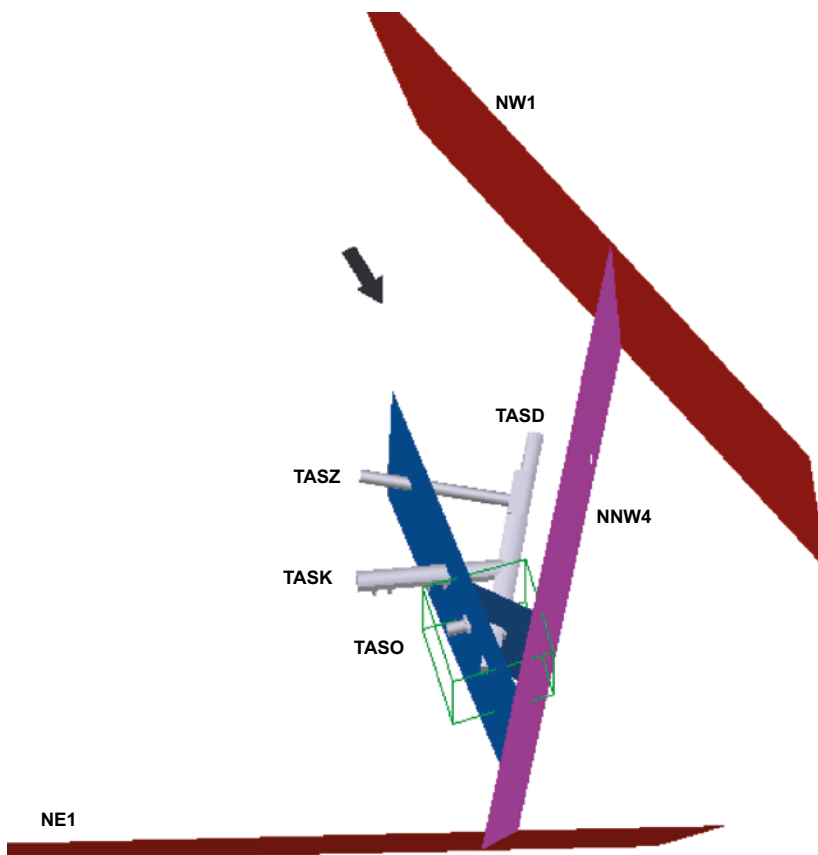

Figure 2-2. *Illustration of the CAD data along with the suggested model domain. The large structures are named according to the Äspö HRL model, with tunnel names given for orientation. The thick black arrow indicates the principal stress orientation. This figure is reproduced from the task description (Vidstrand et al. 2017).*
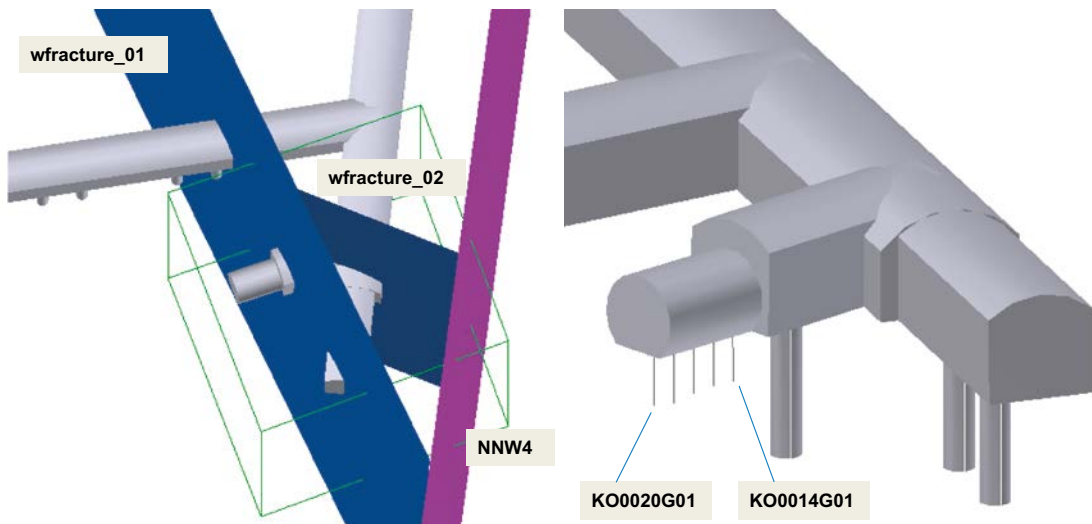
Figure 2-3. *Illustration of CAD data provided local to the TASO tunnel, naming the three deterministic hydrogeological structures that are contained within the suggested model domain. The five probing boreholes are illustrated on the right. The figure includes an indication of the naming of the boreholes by giving the outer borehole names. See Figure 2-5 for the naming of boreholes in between. This figure is reproduced from the task description (Vidstrand et al. 2017).*
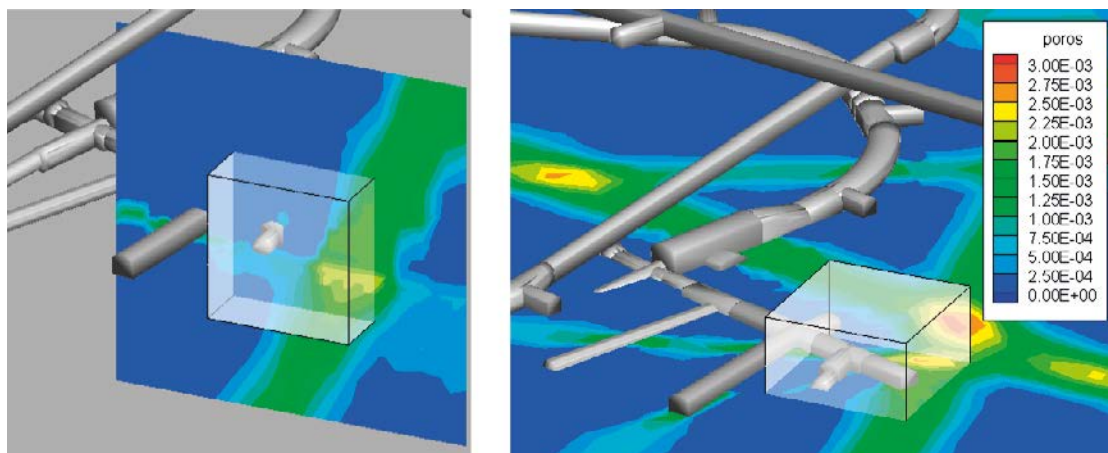

Figure 2-4. *Illustration of the proposed model domain, set within a larger scale DarcyTools set-up. Observe how one of the bounding sides is following a large structure, NE1 as identified in Figure 2-2. This figure is reproduced from the task description (Vidstrand et al. 2017).*

Figure 2-5. *Illustration of probe borehole spacing and naming. The dotted lines indicate proposed overcoring of the selected probe boreholes. This figure is reproduced from the task description (Vidstrand et al. 2017).*

2.2 Fracture statistics used to describe the 'background' discrete fracture network model of the rock

Groundwater flow in the granitic bedrock at the Äspö Hard Rock Laboratory (HRL) occurs through a series of interconnected fractures, with characterisation of this highly heterogeneous flow system required for models to accurately reflect the hydraulic nature of the site. A Continuous Porous Medium (CPM) modelling approach, using bulk hydraulic properties, is insufficient to represent details of the local flow and transport pathways within the fractured bedrock. In turn, this will significantly limit the accuracy to which inflows and resaturation profiles can be predicted as part of the BRIE. In contrast, a Discrete Fracture Network (DFN) model explicitly represents the flow conducting fractures, providing an explicit representation of the flow and transport at a local level. The DFN concept requires characterisation of several properties within its definition, including fracture orientations; fracture size and shape; fracture openings and hydraulics; and the spatial distribution of fractures. Although geological mappings can be used to define statistical distributions for properties such as orientation and intensity; others, such as fracture size and shape are more uncertain. In addition, the fracture data used to infer the statistical distributions of the DFN model are often constrained by censoring effects due to limitations in the mapping procedures adopted in boreholes and tunnels. However, assuming sufficient characterisation data is available to adequately define the DFN, the calculation of groundwater flow through the connected fracture network will represent the inherent heterogeneity of the fractured rock; accurately predicting both inflows to deposition holes, and resaturation profiles of emplaced bentonite.

This section discusses the development of a hydrogeological DFN model of the fractured bedrock local to the TASO tunnel and the BRIE. It provides an overview of the processes conducted to establish the statistical parameters used to generate the fracture models, as summarised in Table 2-2.

2.2.1 Development of DFN Model

As part of the modelling in Task 8C, there are limitations in the quality[1] of the data used for developing a DFN model, and thus a level of uncertainty when evaluating the data. This reflects typical constraints initially found on a local scale, with fracture data mainly limited to tunnel mappings. Following the current analysis, Task 8D will be launched, with additional hydraulic fracture data provided; typical of the additional data available during repository construction in support of siting decisions for deposition holes. This will allow the fracture models local to the BRIE developed as part of Task 8C to be refined. With the DFN models developed as part of Task 8C severely limited by the lack of quality data, minimal refinement is possible. In addition, "expert judgement" has been used to supplement this lack of high quality data where possible. The subsections below provide a short description of data used and how it has been interpreted.

2.2.2 Input data

The locations of fracture data are shown in Figure 2-2. After analysis, a number of limitations of the input data were identified:

- Fracture orientations from the individual deposition holes are highly uncertain (as Task 8C details do not provide this information).

- The BRIE is located in TASO tunnel, where there is a small fracture data sample.

- The TASK tunnel is furthest away from the BRIE, and situated in a different rock type.

- The TASD tunnel in conjunction with TASO provide a relatively large amount of data.

These constraints allow the available primary fracture data to be ranked according to quality, with data from the TASO tunnel, when existing, ranked highest, and followed by data from the TASD tunnel. Data from the TASK tunnel and two further deposition holes are interpreted in a more cautious way.

---

[1] Additional data will be provided as part of Task 8D.

2.2.3 Orientation distribution

A stereonet of the orientation data is shown in Figure 2-6, obtained from the compilation of

- trace data from two deposition holes, DD0086G01 and DD0092G01,
- trace data from three tunnels, TASD, TASK and TASO, and
- a desktop study of two virtual scanlines in the floor of the tunnels TASD and TASK.

The interpretation shown in Figure 2-6 does not provide an obvious means for division into sets. This is partly because multiple poles are plotted on top of each other, at even 5° locations, but also because of large uncertainties in the underlying orientation data, especially for the two deposition holes. This first issue is addressed by adding a small, uniformly distributed random value, ±2°, to both strike and dip, as shown in the stereonet Figure 2-7. Two sets are now visually apparent, with mean fracture pole trend/plunge approximately around 280°/20° and 20°/10°.

Figure 2-8 shows stereonets of the division of data into the three tunnels: TASD, TASK and TASO. Results indicate a gently dipping set with a mean pole trend of around 120°, and plunge of approximately 50°.
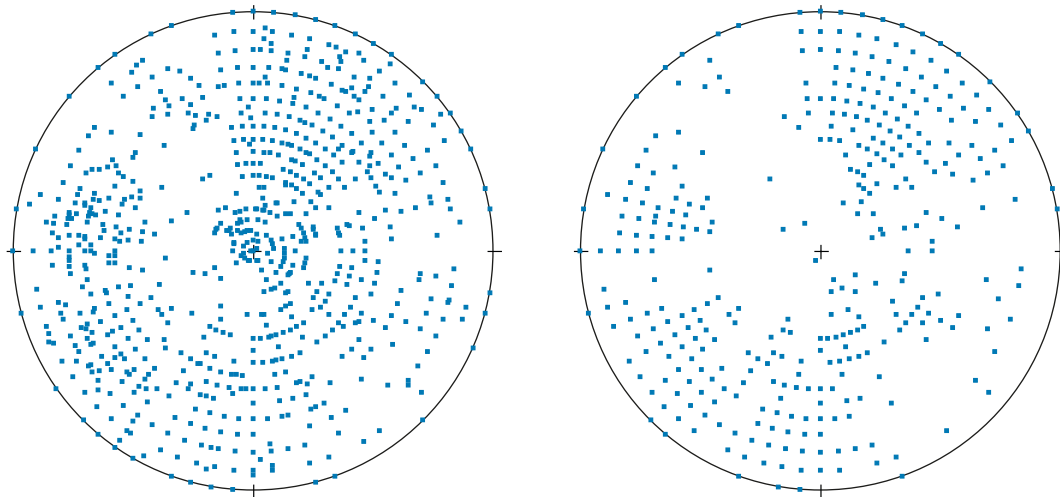

Figure 2-6. Fracture poles. Left: Orientation of all, 1 772, fractures from the two deposition holes and the three tunnels. Right: Orientation of the 762 fractures mapped at the floor in the TASD and TASK. This figure is reproduced from the task description (Vidstrand et al. 2017).
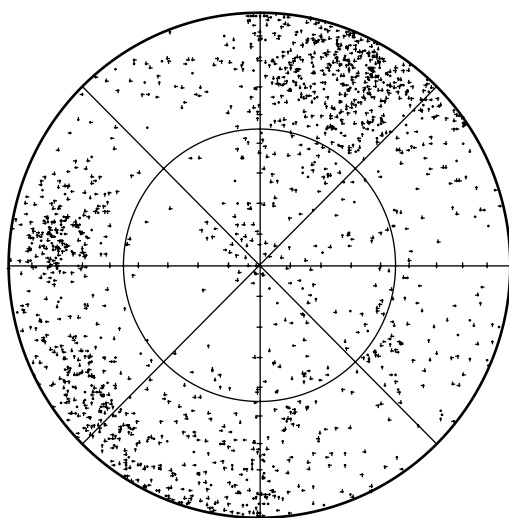

Figure 2-7. Fracture poles when a uniformly random value is added. This figure is reproduced from the task description (Vidstrand et al. 2017).
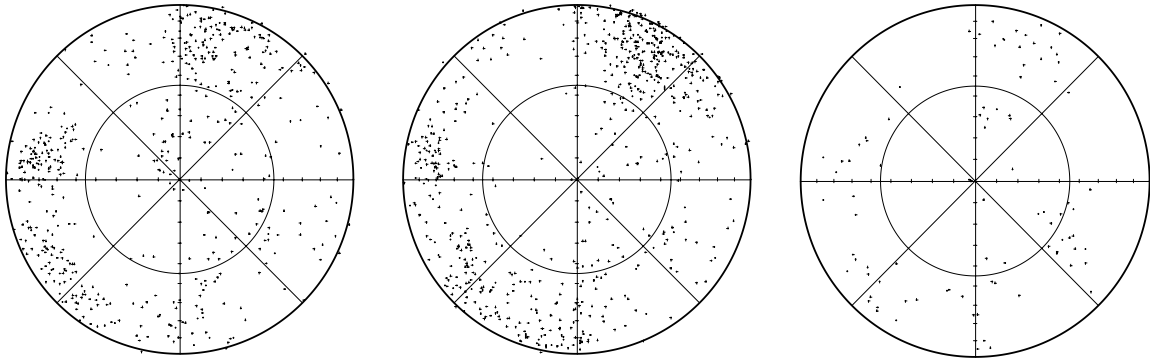
Figure 2-8. *Fracture poles from left: TASD, middle: TASK and right: TASO. This figure is reproduced from the task description (Vidstrand et al. 2017).*

Visual inspection is used to identify three sets for the orientation data, with a Fisher distribution proposed for each set. Fisher concentrations, κ, are estimated to be 10, 15 and 10 respectively for each of the three sets. The assignment of the fracture poles to each of these sets is shown in Figure 2-9, with relative intensity between each set 0.29/0.52/0.20.

2.2.4 Spatial distribution

Fracture centres are distributed in space using a Poisson point process.

2.2.5 Size distribution

A power-law fracture size distribution,

$$f(r) = \frac{k_r r_0^{k_r}}{r^{k_r+1}},$$
(2-1)

is chosen, where the power law exponent is k_r, the fracture radius is r, and the location parameter is r_0, and to be determined.
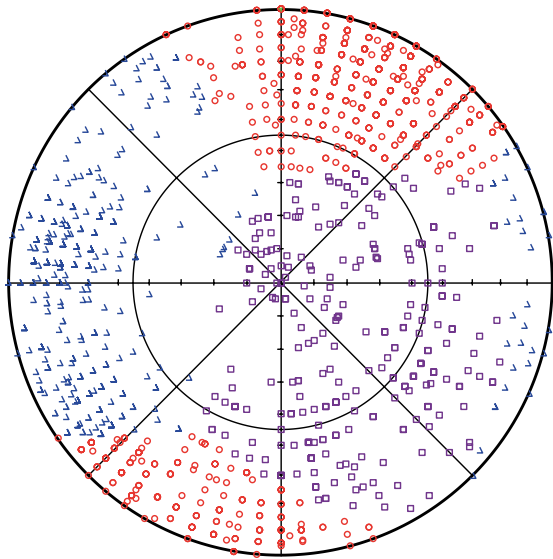

Figure 2-9. *Fracture poles assigned to the three sets. Set 1: Blue triangles, set 2: red circles and set 3: purple squares. This figure is reproduced from the task description (Vidstrand et al. 2017).*

The slope of the size distribution is calculated from the fracture traces mapped on the tunnel walls, roofs and floors, together with the traces in the two deposition holes. Unfortunately the cut-off value, as well as the censoring, is different for the different tunnels and holes. In DD0086G01 it is 0.3 m, in DD0092G01 0.2 m, TASK and TASD 0.4 m and TASO 1.0 m. However, truncation (lower bound) or censoring (upper bound) will only affect the data interval and location of the CCDF (Complementary Cumulative Density Function). The slope of the curve is not affected. The distributions of trace lengths are shown in Figure 2-10. The slope of the distribution is, by visual inspection, estimated to be −1.6, which corresponds to a Power law exponent, k_r, equal to 2.6 of the parent fracture size distribution. This slope provides a reasonable fit to measurement data at all 5 locations, although it is noted that the CCDF curve of the TASK tunnel does not have any straight segment where the slope can be evaluated.

From Äspö HRL geologists, the shortest trace of the scanlines in tunnels TASD and TASK is 0.5 m, yielding a location parameter (i.e. the smallest regarded fracture), of 0.25 m. However, the location parameter, r_0, cannot be evaluated solely by use of the trace length distributions, since it is closely related to the intensity of the Power law function. The location parameter is further discussed in the following subsection.

2.2.6   Intensity

The fracture areal intensity, P_{32}, is estimated from the fracture intersections with scanlines. The orientation of the scanlines are corrected for orientation sampling bias by applying a Terzaghi weighting factor. However, the intensity of fractures is independent of the fracture-size distribution and consequently some modelling is required to estimate the size-intensity relationship. A scanline on the TASD tunnel floor is considered to relate the P_{32} to this underlying fracture-size distribution. Unfortunately the TASD scanline is short, only 16.5 m with 23 intersections which makes the intensity estimation highly uncertain.

The task description (Vidstrand et al. 2017) considers the relation between P_{32} and r_0 by evaluating three scanlines, 16.5 m long, within ten realisations of the fracture model, yielding 30 scanlines in total for analysis. The results from these realisations are shown in Figure 2-11. With the underlying orientation model defined, together with the assumed relative intensities between different fracture sets (see Section 2.2.3), it is impossible to replicate the data measured in the TASD tunnel.
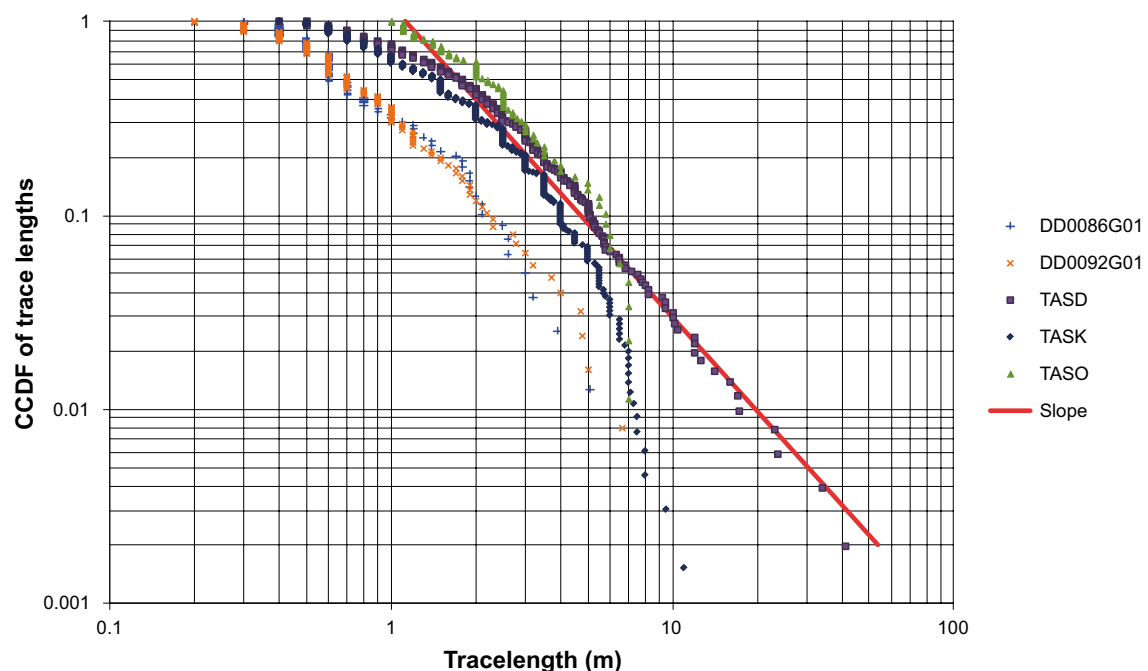

Figure 2-10. The distribution of trace lengths at the different mapped locations. This figure is reproduced from the task description (Vidstrand et al. 2017).
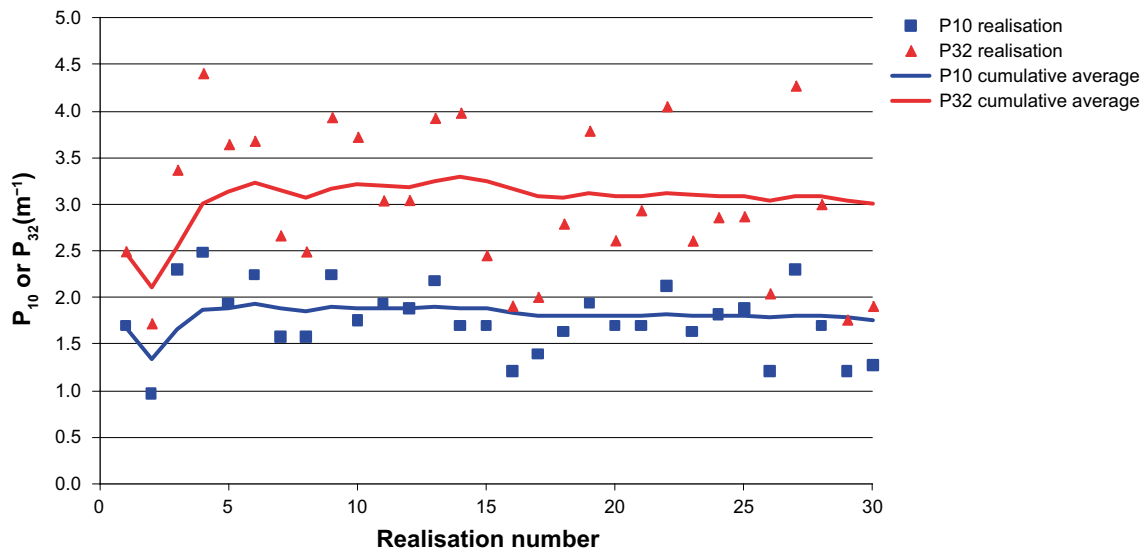
Figure 2-11. *Results from the 30 modelled scanlines. This figure is reproduced from the task description (Vidstrand et al. 2017).*

The model proposed in Vidstrand et al. (2017) is a compromise between underestimating the given intensity P_{32} by approximately 10 %, and overestimating the linear intensity P_{10} by approximately 25 %. The intensities for the three different sets, $P_{32,\,r>0.25}$ are 1.1, 2.0 and 0.75 m²/m³ respectively. Uncertainties in the estimated fracture intensity will be considered as part Task 8D, a follow up task that will consider additional hydraulic fracture data local to the BRIE.

2.2.7 Uncertainty

The statistical parameters used to generate DFN models local to the TASO tunnel and BRIE are derived from the analysis of the limited data provided. Specifically, the use of lower quality data yields potentially large uncertainties in the defined model. Uncertainties are estimated by Vidstrand et al. (2017) for the following parameters:

- Mean pole 15° (dihedral angle).
- Power law exponent, kr ± 0.15.
- Fracture areal intensity, $P_{32} \pm 25$ %.

2.2.8 Fracture statistics

Statistics for the three fracture sets identified local to the TASO tunnel are presented in Table 2-2. However, as a consequence of the small data sample available, two aspects which may contradict the proposed interpretation are identified:

- Fractures smaller than 1 m seem to follow slightly different statistics.
- Of the analysed data, only the inner part of TASD and the entire TASO tunnel share the same rock type.

Table 2-2. Fracture statistics to be used for the TASO tunnel, supplied as part of the task description (Vidstrand et al. 2017).

Set	Orientation			Size		Spatial Distribution	Intensity P32 (r_0,∞)
	Trend	Plunge	Fisher Concentration	r_0	k_r		
1	280	20	10	0.25	2.6	Poissonian	1.1
2	20	10	15	0.25	2.6	Poissonian	2
3	120	50	10	0.25	2.6	Poissonian	0.75

SKB P-17-14

2.3 Boundary conditions

Boundary conditions are extracted from the current official hydro-model of the Äspö HRL, based on the SDM-Site Laxemar Deformation Zone Model. As reported in the task description (Vidstrand et al. 2017) issues regarding model scale have resulted in known location errors within this model.

Using a DarcyTools v3.3 sub-grid, values for pressure, salinity (from groundwater constituents), and velocities along the x, y, and z coordinates are exported from the full regional Äspö HRL model (Äspömodel05). This data is provided by Vidstrand et al. (2017) over a volume approximately $(100 \text{ m})^3$, incorporating the suggested model domain. Figure 2-12 illustrates the residual pressure field, P^R from this model, on a slice through the TASO and TASD tunnels. The total pressure P^T is calculated from the residual pressure by

$$P^T = P^R - \rho_0 g \, (z - z_0). \tag{2-2}$$

where $z_0 = 0$ metres above see level, a reference altitude at the present day shore line, and ρ_0 is the fresh water density. Data are provided via the spreadsheet *TASO_pressure_salinity_velocities_rev20101123.xls*, as part of the task description (Vidstrand et al. 2017).

The spatially variable salinity mass fraction, S, is specified as part of these boundary conditions, with the salinity-density dependence defined as:

$$\rho = 1\,000(1 + 0.0078 \cdot S) \tag{2-3}$$

In addition, atmospheric boundary conditions are prescribed for all of the tunnels.

Uncertainties associated with the prescribed boundary conditions could be considered through a series of sensitivity cases.
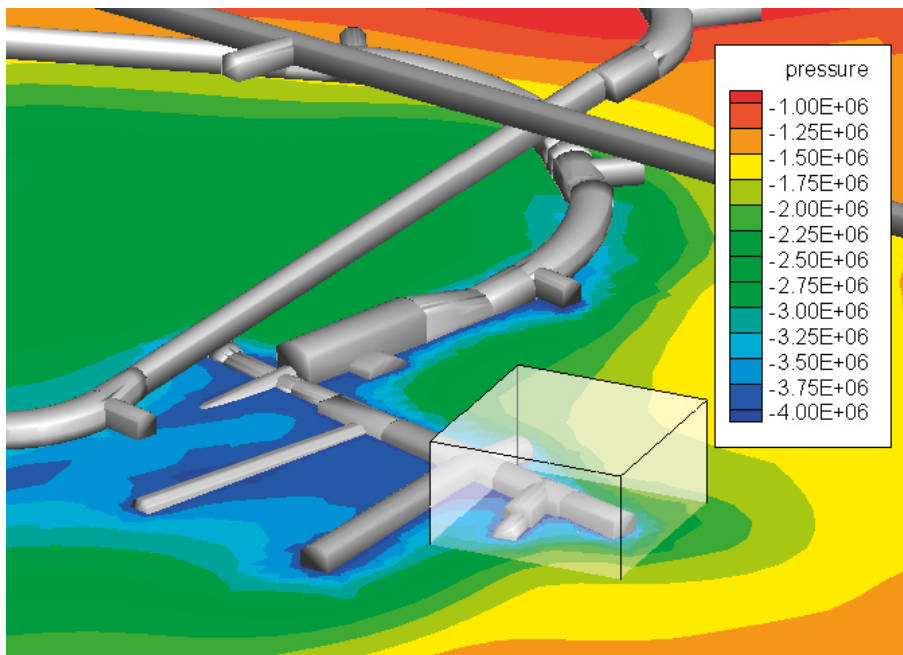

Figure 2-12. *Illustration of the pressure field (Pa), with reference elevation at the present day shore line (0 altitude). This figure is reproduced from the task description (Vidstrand et al. 2017).*

2.4 Initial conditions

For Task 8C1, both pressure build up in, and inflows to, the five probe boreholes are considered. Far field boundary conditions for the model are determined from the large scale Äspö model (Vidstrand et al. 2017; see Section 2.3), with tunnels held at atmospheric pressure. For pressure build up measurements, each of the boreholes are packed-off using a 1 m upper seal, with each opened to the tunnel in turn to calculate inflows. An equivalent prescription of the initial conditions is made when considering the overcored boreholes KO0017G01 and KO0018G01.

For Task 8C2, initial conditions for the resaturation of the emplaced bentonite are taken from the modelling results of Task 8C1. In addition, local to the deposition holes

- the emplaced bentonite is initially assumed to be at atmospheric pressure, and

- the initial degree of bentonite saturation is 0.36, corresponding to a suction value of 100 MPa when using the retention curve in Figure 3-9.

2.5 Material specifications

Material specifications, as detailed within the task description (Vidstrand et al. 2017) are adopted, with values based on expert judgment and/or theory. The intact rock matrix (fracture free) is detailed in Table 2-3, with properties for geological structure models of fractures wfracture_01, wfracture_02 and NNW4 presented in Table 2-4, Table 2-5 and Table 2-6 respectively. These three features are based solely on expert judgement, with no site-specific information available at present. Table 2-7 details the bentonite specification.

Table 2-3. Properties for intact rock (fracture free, matrix), supplied as part of the task description (Vidstrand et al. 2017).

Property	Value
Hydraulic conductivity	1×10^{-14} m/s
Kinematic porosity	1×10^{-5}
Specific storage	1×10^{-11} m^{-1}

Table 2-4. Properties for wfracture_01, supplied as part of the task description (Vidstrand et al. 2017).

Property	Value
Geological width	1.0 m
Transmissivity	2×10^{-8} m^2/s
Porosity for porous media descriptions	1×10^{-3}
Transport aperture for DFN descriptions	1×10^{-5} m
Storativity	1×10^{-8}

Table 2-5. Properties for wfracture_02, supplied as part of the task description (Vidstrand et al. 2017).

Property	Value
Single plan, geological width	0.001 m
Transmissivity	2×10^{-9} m^2/s
Porosity for porous media descriptions	1×10^{-3}
Transport aperture for DFN descriptions	1×10^{-5} m

Table 2-6. Properties for NNW4, supplied as part of the task description (Vidstrand et al. 2017).

Property	Value
Geological width	10.0 m
Transmissivity	6.5×10^{-7} m^2/s
Porosity for porous media descriptions	1×10^{-3}
Transport aperture for DFN descriptions	1×10^{-5} m
Storativity	1×10^{-7}

Table 2-7. Properties for Bentonite, supplied as part of the task description (Vidstrand et al. 2017).

Property	Value
Hydraulic conductivity	6.4×10^{-14} m/s
Porosity	0.44
Specific Storage	1×10^{-6} m^{-1}

2.6 Calibration targets

Calibration targets for Task 8C1 take the form of measured inflows to the probing boreholes and pressure build up tests. All boreholes were initially packed-off, with a packer sealing the upper 1 m of the borehole. Subsequently, the built-up pressure P, was measured in each of the five probe boreholes. Where no pressure is given in Table 2-8, no inflow large enough to fill the borehole occurred by the measurement time. The pressure development in the five probe boreholes is illustrated in Figure 2-13 and Figure 2-14. Thereafter, one borehole at a time was opened and the outflow was measured, i.e. yielding the inflow for atmospheric pressure at the top of the boreholes.

Flow and pressure data during injection tests in probe boreholes KO0014G01 and KO0017G01 are also available, as well as some early geological data, although this information has not been used in calibrating the developed models.

Table 2-8. Initial pressures built-up in closed (packed-off) boreholes and outflow measurements conducted in one borehole at a time thereafter. The second row indicates flow during the injection test. No flow results in KO0018G01 and KO0015G01 are recorded for the first test. This may be due to measurement limitations and/or "leakage" in the upper parts of the boreholes. This table is reproduced from the task description (Vidstrand et al. 2017).

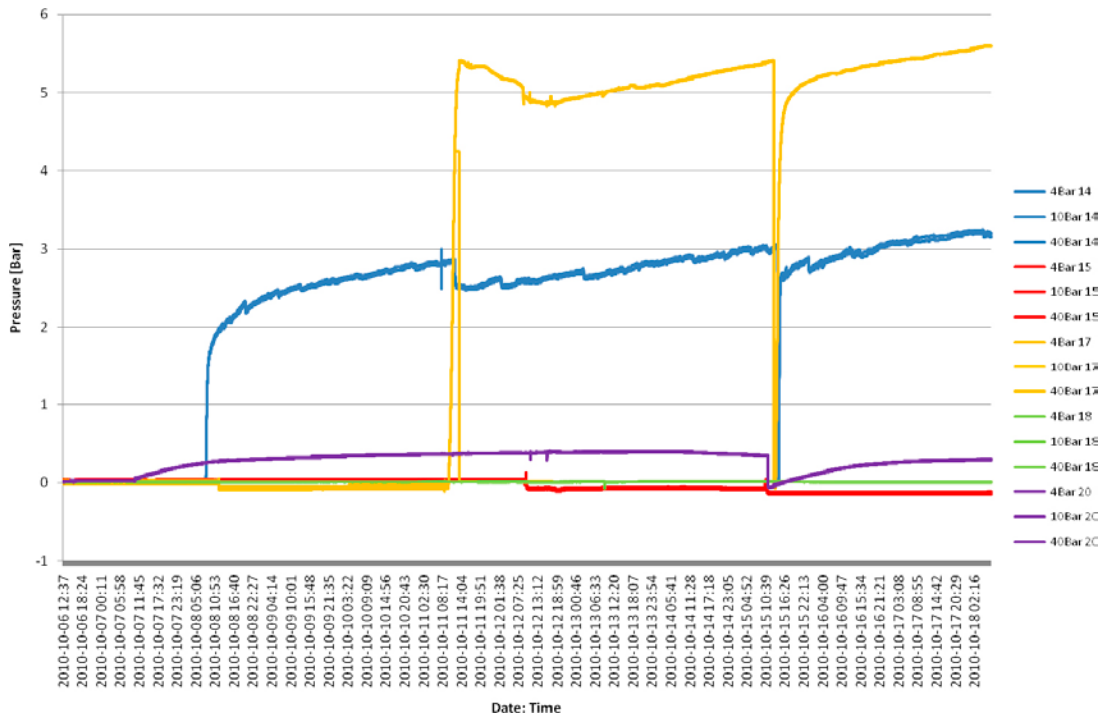|	KO0020G01	KO0018G01	KO0017G01	KO0015G01	KO0014G01
Inflow	Inflows not sufficient to fill the borehole during the measurement	No inflows recorded: Measurement limitations	Q ≈ 0.5 ml/min p ≈ 6 bar ≈ 2–3 m	No inflows recorded: Measurement limitations	Q ≈ 1 ml/min p ≈ 3 bar ≈ 0.5–1 m
Injection	Inflows not sufficient to fill the borehole during the measurement	**Above 1 m:** Inflows not sufficient to fill the borehole during the measurement **Below 1 m:** No inflows recorded: Measurement limitations	Inflows not sufficient to fill the borehole during the measurement	Inflows not sufficient to fill the borehole during the measurement	Inflows not sufficient to fill the borehole during the measurement

Figure 2-13. *Pressure development in borehole KO0014G01–KO0020G01 at the early times, just after drilling. This figure is reproduced from the task description (Vidstrand et al. 2017).*
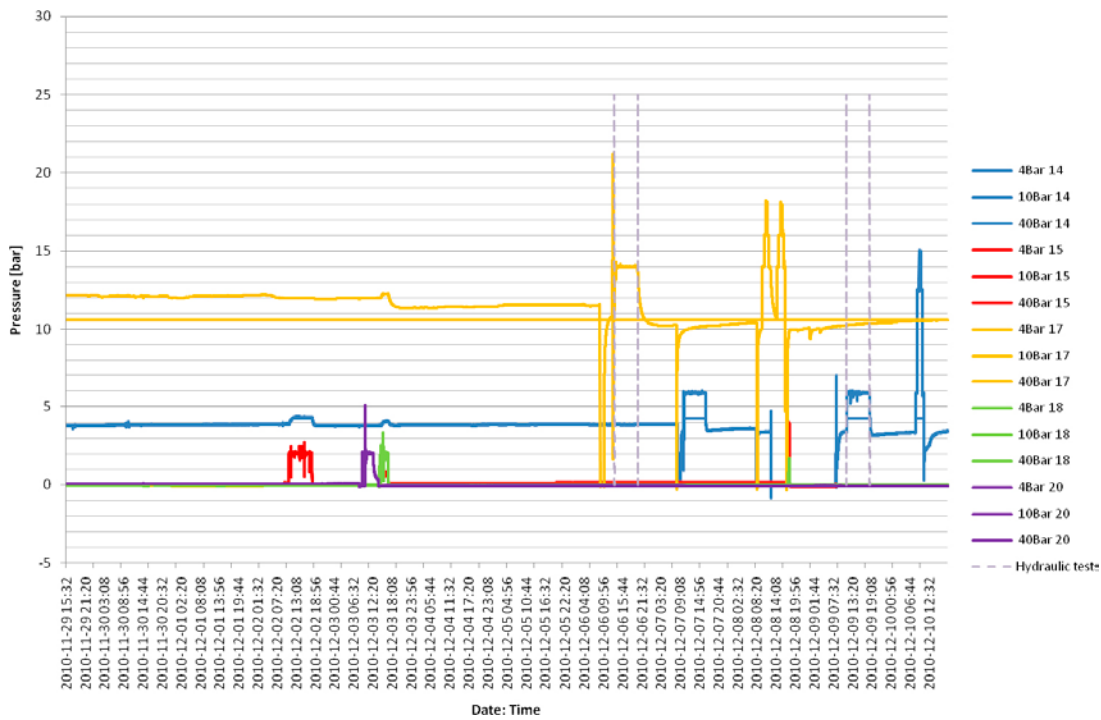

Figure 2-14. *Pressure development in borehole KO0014G01–KO0020G01 after steady conditions have started to prevail. At the second half of the diagram dashed lines indicate time periods for hydraulic tests. This figure is reproduced from the task description (Vidstrand et al. 2017).*

2.7   Bentonite emplacement method

The resaturation of a bentonite buffer material emplaced directly within the five deposition holes of the BRIE is considered in Task 8C2. The models developed consider buffer – rock interactions on all surfaces of the deposition hole, allowing wetting of the bentonite from all directions. However, in reality the emplacement of the buffer is more complex, using a metal construction that contains a steel plate, hydraulically isolating the bentonite from the fractured rock at the bottom of the deposition hole, as shown in Figure 2-15. The influence of this impermeable plate on the resaturation of the bentonite buffer is not considered in the current study. This is not expected to be significant because:

1. Contributions to bentonite wetting from the rock matrix are constrained by the size of the bentonite – rock matrix interface, and the surface area of the bottom of the hole (0.07 m^2) is small compared to the sides of the deposition hole (2.83 m^2).

2. For groundwater supplied to the deposition hole through the fracture system, it is expected that large-scale fractures will be dominant. The size of these more transmissive fractures is such that the likelihood they solely intersect the bottom of the deposition hole is low, with intersection with the side wall of the deposition hole more likely.
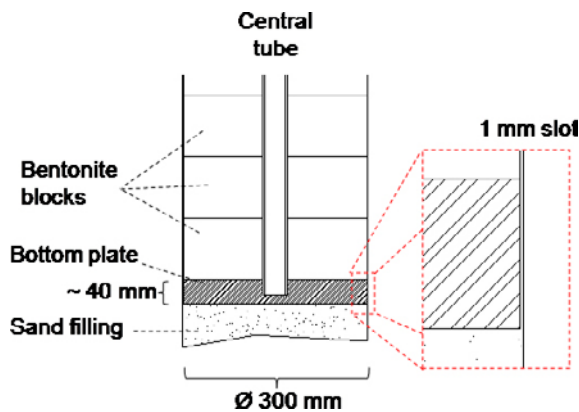

Figure 2-15. *Preliminary outline of the bottom part of the BRIE installations. This figure is reproduced from the task description (Vidstrand et al. 2017).*

3 Modelling Task 8C

The techniques adopted for modelling Task 8C of the BRIE are discussed in this section, with details of the modelling concepts implemented, including a review of the software packages selected, presented in Section 3.1. Subsequently, a description of specific models developed for Task 8C, identifying any assumptions and simplifications necessary, is provided in Section 3.2.

3.1 Concepts and methodology

Task 8C focuses on the hydraulic interaction between the bentonite buffer and the surrounding fractured host rock. As such, modelling tools capable of representing both the groundwater flow through a discrete fracture network, as well as the multiphase flow occurring during resaturation of the buffer, are required. The two software packages used in this study are respectively

- CONNECTFLOW, and
- TOUGH2.

More details on both of these computer codes are presented in Sections 3.1.1 and 3.1.2 below.

3.1.1 CONNECTFLOW

CONNECTFLOW is a suite of software, developed by AMEC, for modelling groundwater flow and ransport on a variety of scales. It consists of a discrete fracture network (DFN) module, and a continuum porous media (CPM) module, referred to as NAPSAC and NAMMU respectively. A detailed overview of the mathematical formulation adopted by CONNECTFLOW is presented in AMEC (2012a,b,c) with a high-level description in Joyce et al. (2010) summarised below for the aspects of the software package directly applicable to modelling Task 8C.

Groundwater flow through the bedrock at Äspö HRL primarily occurs through a series of interconnected flow-conducting fractures, and the discrete fracture network concept provides the ability to explicitly represent the groundwater moving from one fracture to another at the intersections between them. Five properties characterising the fracture network are

- spatial distribution of the fractures (e.g. Poisson, clustered),
- fracture intensity, usually expressed as a P32 (fracture area per unit volume),
- fracture orientation (usually classified by sets),
- fracture size (e.g. log-normal, power-law distributions), and
- fracture transmissivity (can be correlated to the fracture size).

Fracture network models are generated using a stochastic approach, with fractures (represented as 2D planes) sampled from probability distribution functions (PDFs) specified for each fracture set. The statistical parameters for each fracture set are usually determined through field experiments such as borehole logging and hydraulic tests. The DFN concept is a powerful methodology; it inherently reflects the individual flow conduits in fractured rock, and the available field data.

With regards to the emplaced bentonite, the representation of individual fractures intersecting a deposition hole, and subsequent heterogeneous wetting of the buffer material, is an important concept to consider. To successfully capture the resaturation processes, an alternative numerical code, TOUGH2 was used. TOUGH2 (described in Section 3.1.2) is based on a continuum concept, and it is therefore necessary to convert the properties of the network of discrete fractures into equivalent continuous porous medium (ECPM) block properties. This process is known as upscaling, and can be performed by CONNECTFLOW to calculate an effective, directional permeability tensor and fracture kinematic porosity for grid blocks overlaying the fracture network. This upscaling process uses a method that requires flow simulations to be performed through the DFN model on the scale of individual grid cells to produce an equivalent continuum model. A schematic of these flow calculations for a given grid block and 2D DFN model is shown in Figure 3-1, reproduced from Joyce et al. (2010). The effective permeability is calculated by simulating flux through the fracture network for a linear head gradient in each of the axial directions.
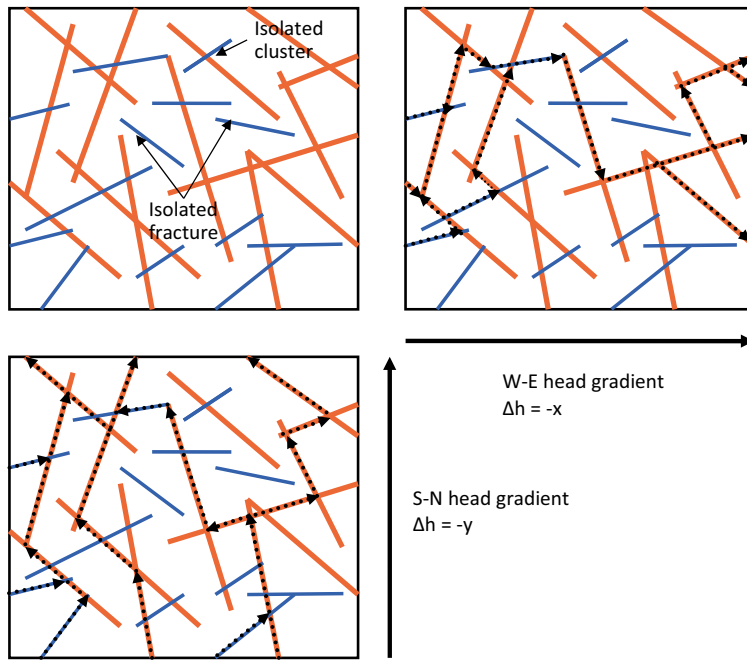
Figure 3-1. *A 2D illustration of flow through a network of fractures, reproduced from Joyce et al. (2010). Top left: illustrates a random network of fractures, with variable length and transmissivity (red fractures are highly transmissive, with blue fractures indicating low transmissivity). Top right: illustration of flow paths through the fracture network for a linear head-gradient decreasing along the x-axis. Bottom left: illustration of flow paths through the fracture network for a linear head-gradient decreasing along the y-axis.*

Several groundwater flow-paths are possible within DFN models due to the number and variety of connections observed across the network. Consequently, cross-flows can form, a common characteristic of DFN models, occurring non-parallel to the head gradient. Cross-flows are accounted for in the upscaling processes by an anisotropic permeability and, for a 3D analysis, CONNECTFLOW uses six directional components to characterise a symmetric permeability tensor. For each head gradient direction, the DFN models are used to calculate the fluxes through each face of the block. The permeability tensor is then derived by a least-squares fit to these flux responses for the fixed head gradients (Jackson et al. 2000).

The kinematic porosity, ϕ, of each grid block is calculated by

$$\phi = \frac{\sum\limits_{f} e_t a_f}{V},$$ (3-1)

where V is the volume of the grid block, a_f is the area of each fracture in the block and e_t is the transport aperture of the fracture. The transport aperture is related to the hydraulic aperture, e_h by,

$$e_t = 10e_h,$$ (3-2)

as used in Hartley et al. 2012), with similar relationships interpreted from tracer test programs, e.g. Hjerne et al. (2010). The hydraulic aperture is related to the transmissivity, T, by the cubic-law for connected fractures

$$e_h = (12\mu T/\rho g)^{1/3},$$ (3-3)

where μ is the fluid viscosity, ρ is the fluid density, and g is gravitational acceleration. Although this upscaling processes reflects flow through the underlying DFN model, the methodology can yield over-prediction of hydraulic conductivity for individual grid blocks, a consequence of flows through fractures cutting the corner of the block that are unrepresentative of flows through the in-situ fracture network (Figure 3-2). These over-predictions are most significant in sparse heterogeneous fracture networks, where the flux through the network of interconnected fractures is affected by 'bottlenecks'
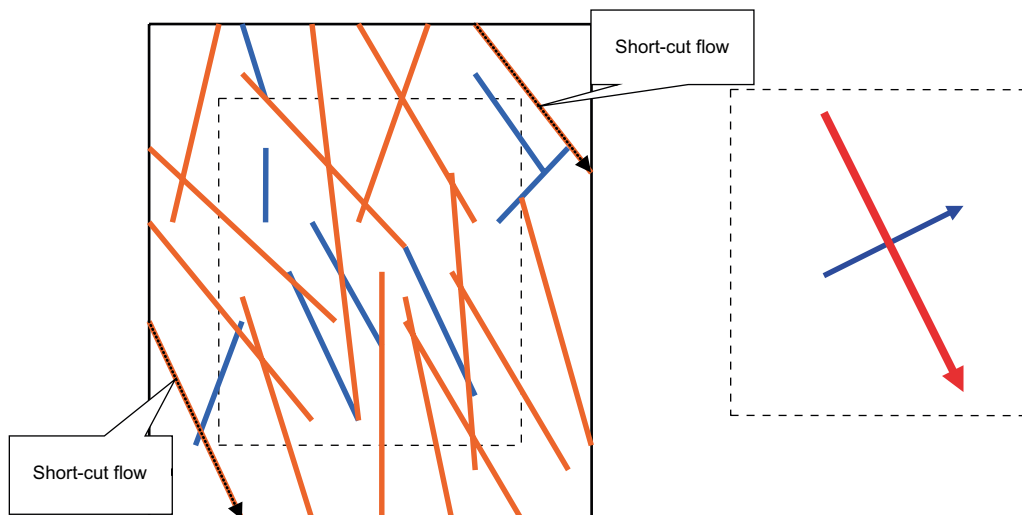
Figure 3-2. 2D illustration of how block-scale hydraulic conductivity can be overestimated, reproduced from Joyce et al. (2010).

through untransmissive fractures, which is quite different to the flux through single fractures. This discrepancy can be reduced by refining the upscaling methodology to simulate flow through a slightly larger domain than the block size required for the ECPM properties, but then calculating the flux responses through the correct block size. The additional area around the block is referred to as a "*guard zone*", and is further discussed in Rhén et al. (2009).

3.1.2 TOUGH 2

TOUGH2 is an extensively used modelling package for simulating nonisothermal, multiphase fluid flows in both porous and fractured media. It was developed by Lawrence Berkeley National Laboratory (Pruess et al. 1999) and is available to download from the Energy Science and Technology Software Centre of the U.S. Department of Energy. TOUGH2 provides a tool for in-depth numerical analysis of the bentonite resaturation process, modelling the flow of the gaseous and aqueous phases by mass conversation and a modified form of Darcy's Law (including the multiphase nature of the flow via a relative permeability function). Numerically, TOUGH2 is formulated with an integrated finite-volume spatial discretisation, with upstream weighting, and a fully implicit first-order backward difference for discretisation in time. Time-stepping is optimised using an automatic algorithm based on the convergence of the model. Non-linearities within the formulation are handled using a series of Newton-Raphson iterations, and for each of these iterations a preconditioned conjugate gradient algorithm is used to solve the remaining system of linear equations.

TOUGH2 incorporates Equation-Of-State (EOS) modules which include fluid properties required for assembling the governing equations (Pruess et al. 1999). The EOS7R[2] module (Oldenburg and Pruess 1995) is used in this study for modelling the resaturation of bentonite, and includes mass components water, brine and air. A mass fraction of brine is used to determine the salinity of the aqueous phase, with both viscosity and density interpolated from the water and brine specification. In addition, Henry's law is used to model the solubility of the gas phase (*i.e.* the solubility is proportional to the partial pressure of the gas). The relative permeabilities and capillary pressure functions utilised in the resaturation models developed are discussed in Section 3.2.5.

In application to modelling the BRIE, the fractured bedrock at the Äspö HRL provides a highly hetero-geneous medium for groundwater flow to ingress the deposition holes and resaturate the bentonite. As described previously, CONNECTFLOW can be used to efficiently calculate permeabilities on all

---

[2] The EOS7R module has been enhanced by Amec Foster Wheeler to include additional checks to stop any variables entering unphysical regions of phase space as well as including a modification which more accurately implements mass conservation during changes in phase (e.g. upon full saturation of the bentonite).

elements of the grid, and AMEC have previously modified TOUGH2 to allow this spatially varying permeability tensor to be imported (Hawkins and Swift 2009). A summary of the methodology adopted is presented below.

The permeabilities and porosities calculated using CONNECTFLOW for a GID formatted mesh are exported in GOCAD format, which retains the same element ordering as the GID mesh file. Using a Perl script, the GID mesh, permeability, porosities and TOUGH2 mesh are analysed, and for each cell centre of the TOUGH2 mesh, the corresponding element within the GID mesh is located, obtaining the permeabilities and porosities calculated for that element. These data are then associated with the given element in the TOUGH2 mesh and the permeabilities are subsequently written to file providing a new TOUGH2 input data block denoted 'PERMA'. Modifications are made to the TOUGH2 source code to calculate the permeability for each connection by projecting the tensor permeability for a given element in the 'PERMA' block according to the connection direction that is being discretised.

It is noted that the algorithm for finding the cell centre of each element of the TOUGH2 mesh within the GID mesh involves $O(n^2)$ operations, where n is the number of elements. This can result in prohibitive analysis times for large meshes, and consequently the following refined algorithm has been adopted:

1. A box is defined which bounds the GID mesh.

2. This box is recursively subdivided, until containing less than 100 elements.

3. When searching for a TOUGH2 cell centre, the bounding box tree is traversed from the top through to the lowest level box.

4. Once the lowest level bounding box is identified, a bounding box test is conducted for each of the 100 elements.

5. If the TOUGH2 cell centre lies within an elements' bounding box, that element is subdivided into 12 tetrahedra using the centroid of the element. A test is performed for each tetrahedron to determine whether the point is within the element.

The use of this algorithm allows TOUGH2 meshes with differing cell resolution to the original upscaling to be considered.

3.2 Model description

The following sections overview the Task 8C model description as used within this report.

3.2.1 Geometrical description

The primary investigation area for the BRIE is in the vicinity of the TASO tunnel of the Äspö HRL. For Task 8C1, the model domain is selected based on the case specification Table 2-1, forming a $(40 \text{ m})^3$ block as shown in Figure 3-3. The base of the TASO tunnel is located at an elevation of -417.0 m, with five boreholes extending a further 3 m deep. The dimensions for both the TASO and TASD tunnels are extracted from CAD files supplied with the task description (Vidstrand et al. 2017).

For hydration models developed as part of Task 8C2, numerical requirements are significantly greater, with extensive refinement necessary local to the resaturation front. Consequently, the model domain is reduced so that computations remain tractable. This smaller region is defined local to the five boreholes, as shown in Figure 3-4.

3.2.2 Processes considered

Hydraulic processes are considered for both Task 8C1 and 8C2, with brief details provided below:

- Task 8C1 uses CONNECTFLOW to calculate single-phase fresh-water flow through the fractured bedrock explicitly. Simulations aim to predict the ingress of groundwater to the five probe boreholes.

- Task 8C2 uses TOUGH2 to simulate two-phase saline groundwater flow through an upscaled representation of the 8C1 bedrock. Calculations predict the profile of resaturation within the emplaced bentonite.
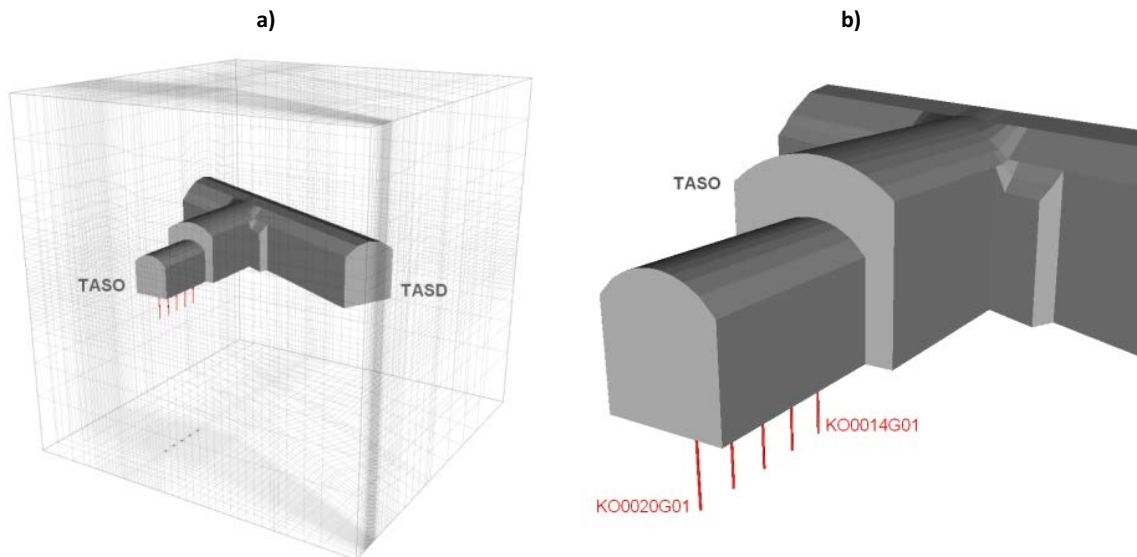
Figure 3-3. (a) Location of BRIE with the TASO and TASD tunnel at the Äspö Hard Rock Laboratory in Sweden. (b) The five boreholes for investigation as part of Task 8C are shown in red.
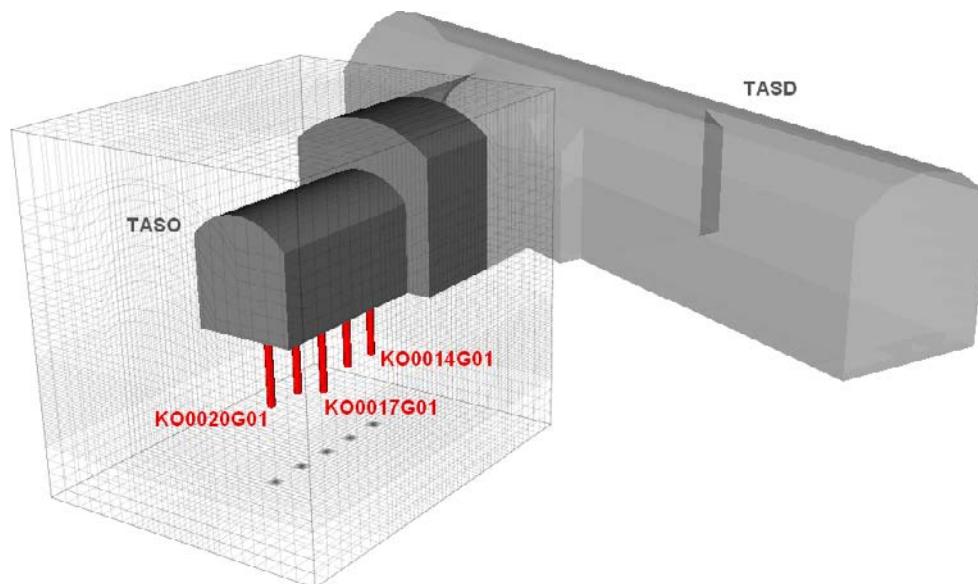

Figure 3-4. Local region to the boreholes, selected for mesh refinement necessary for hydration calculations.

3.2.3   Boundary and initial conditions

Pressure and salinity boundary/initial conditions are provided as part of the task description (Vidstrand et al. 2017), obtained from a full regional simulation of the Äspö HRL. The TASO and TASD tunnels within the model are held at atmospheric pressure throughout. TOUGH2 interpolates the groundwater density between end-members ρ_{water} = 997.16 kg/m^3 and ρ_{brine} = 1 185.1 kg/m^3 at reference conditions, using the equation

$$\frac{1}{\rho} = \frac{1-x}{\rho_{water}} + \frac{x}{\rho_{brine}} \tag{3-4}$$

for a mass fraction of brine, x. This mass fraction is calculated from the prescribed salinity density dependence of the task description, ensuring density is consistent with the full regional simulation of the Äspö HRL. The interpolated pressure and groundwater salinity for the (40 m)^3 model domain are shown in Figure 3-5.
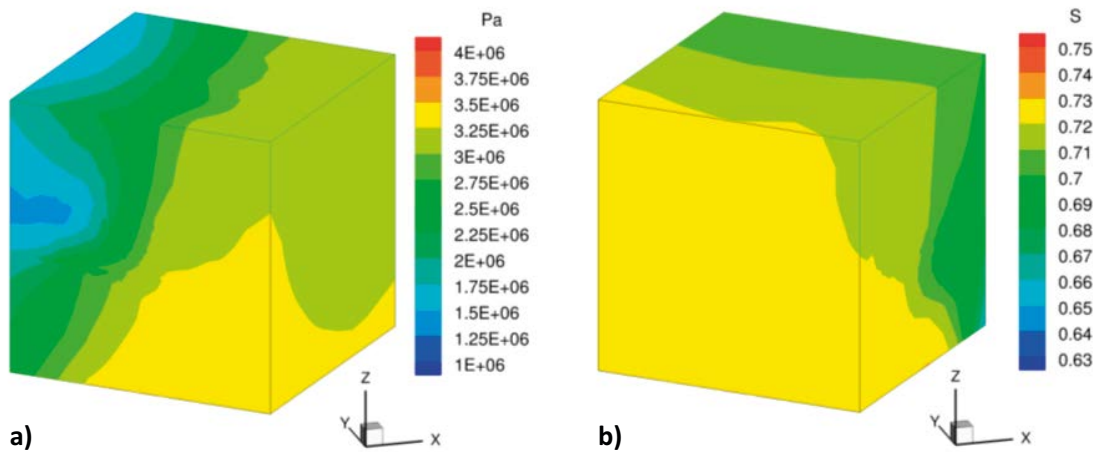
Figure 3-5. *(a) Pressure (Pa) and (b) groundwater salinity (-) prescribed for the model domain from the specified initial conditions. Values are interpolated from the task description (Vidstrand et al. 2017).*

Variation in groundwater density across the model domain is very limited, with maximum and minimum values of 1005.7 kg/m^3 and 1005.1 kg/m^3 respectively. Consequently the potential for buoyancy effects to significantly affect the groundwater pathways through the fractured bedrock is severely limited, especially compared to uncertainties in DFN parameters and hydraulic properties of the fracture network. Therefore inflow and pressure build up calculations for Task 8C1 will ignore the effects of salinity, performing freshwater simulations instead. However, when considering the resaturation of the Bentonite as part of Task 8C2, groundwater salinity will be included. This is because the presence of saline groundwater is an important aspect for the performance of the bentonite as a buffer material, and its ability to fulfil required safety functions such as attain suitable swelling pressures. Buoyancy effects from considering groundwater salinity in Task 8C2 are expected to be negligible.

For each of the tasks, different treatment of the five boreholes is applied:

* For Task 8C1, inflows to the five probe boreholes are calculated for open borehole conditions (i.e. held at atmospheric pressure).

* For Task 8C2, the bentonite within the deposition holes is initially held at atmospheric pressure, and allowed to evolve with time. The bentonite is initially saturated to 36 %, corresponding to a suction value of ~ 100 MPa.

3.2.4 Parameters

Parameters necessary for modelling both Task 8C1 and 8C2 are detailed below.

Deterministic Features

Three significant geological features were determined local to the TASO tunnel, and data were provided as part of the task description (Vidstrand et al. 2017), as shown in Figure 2-2 and Figure 2-3. These deterministically specified features, named wfracture_01, wfracture_02 and NNW4, are represented as flowing fractures within the DFN representation of Task 8C1, and were upscaled to equivalent rock permeabilities as part of Task 8C2. The parameterisations of these features are provided in Table 2-4 through Table 2-6, and are represented within the DFN models developed as shown in Figure 3-6.

Stochastic fracture statistics

Background fracture statistics were provided as part of the task description (Vidstrand et al. 2017), and specified in Section 2.2, including

* fracture orientation,

* fracture intensity,

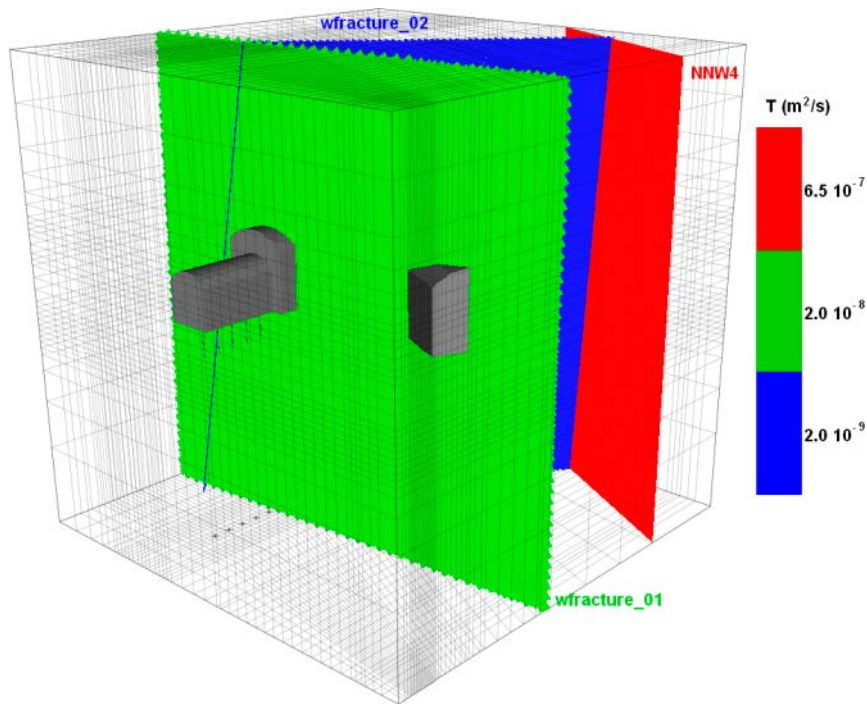* fracture distribution, and

* fracture size relationships.

Figure 3-6. Three deterministic features, coloured by transmissivity, local to the TASO tunnel and within the model region defined in the task description (Vidstrand et al. 2017).

The parameterisation of the bedrock provided in Section 2.2 was implemented in the CONNECTFLOW software package.

The task description (Vidstrand et al. 2017) noted during data collection that no fractures were identified that cut the entire tunnel periphery (other than the deterministic geological features). To avoid the generation of many large fractures which could contradict this physical understanding, a maximum side length of 10 m is assumed for the background fractures. In addition, for calculations to remain computationally tractable, a minimum fracture side length of 0.5 m is specified. The removal of these very small fractures is unlikely to affect the overall hydraulic nature of the bedrock, with flows primarily occurring through larger, more transmissive fractures. Consequently, the assessed length interval of fractures is restricted to those with a side length between 0.5 m and 10 m.

For the power-law fracture size distribution implemented, it is possible to rescale the intensity for this truncated range of fracture sizes according to the following equation:

$$P_{32, r_a - r_b} = P_{32, r_1 - r_2} \cdot \frac{r_a^{2-k_r} - r_b^{2-k_r}}{r_1^{2-k_r} - r_2^{2-k_r}}, \qquad (3-5)$$

where the power law exponent, k_r is 2.6 and the range of fracture sizes r_a up to r_b (and corresponding intensity $P_{32, ra-rb}$) are a subset of the fracture sizes r_1 up to r_2 (and corresponding intensity $P_{32, r1-r2}$). Applying Equation (3-5), with $r_a = 0.28$ m, the equivalent radius to a side length of 0.5 m; $r_b = 5.64$ m, corresponding to a side length of 10 m; $r_1 = r_0 = 0.25$ m; and $r_2 = \infty$, the reduced intensities are calculated and detailed in Table 3-1 by set.

Table 3-1. Fracture intensities by set, used for Task 8C fracture generation.

Set	Intensity $P_{32}(r_0, \infty)$	Intensity $P_{32}(0.28, 5.64)$
1	1.1	0.85
2	2	1.55
3	0.75	0.58

Characterisation of the site identified three fracture sets (orientations) in the vicinity of the TASO tunnel as recorded in Table 2-2. These consist of a set of fractures sub-horizontal, dipping gently to the south-east, and two further steeply dipping (sub-vertical) sets aligned approximately N-S and E-W. Fracture orientations were calculated using a Fisher distribution for each set. Figure 3-7 illustrates the fracture orientations observed in the five probe boreholes for 100 realisations of the stochastic fracture network. These simulated fracture poles can be compared with those determined during data collection, as shown in Figure 2-9.

The stochastically generated background fractures also require their transmissivity to be specified. Transmissivities (T) for individual fractures within the network were determined directly from the fracture size, following the power-law relation:

$$T = 7 \cdot 10^{-11} L^{1.7} \tag{3-6}$$

where L is the fracture length. This empirical relationship is consistent with estimates derived from a variety of fracture scales at the Äspö site. The correlation (3-6) is shown in Figure 3-8, along with measured data.

Diffusion coefficients

Groundwater flow in the fractured bedrock at Äspö is dominated by flow through a series of interconnected fractures. Simulation of flow through these discrete fractures is sufficient for representing the inflows and pressure build up for each of the probe boreholes as part of Task 8C1. However, when modelling the resaturation of low permeability buffer material such as bentonite, the diffusive fluxes of the groundwater components can become significant. For the two-phase TOUGH2 simulations performed for Task 8C2, diffusion coefficients within both the aqueous and gaseous phases are required, and specified in Table 3-2. Diffusion coefficients in the gaseous phase are provided by Marrero and Mason (1972). For the liquid phase, the diffusion of brine is taken from Hoch and James (2011), with the diffusion for air calculated from Cussler (1984) and Han and Bartels (1996).
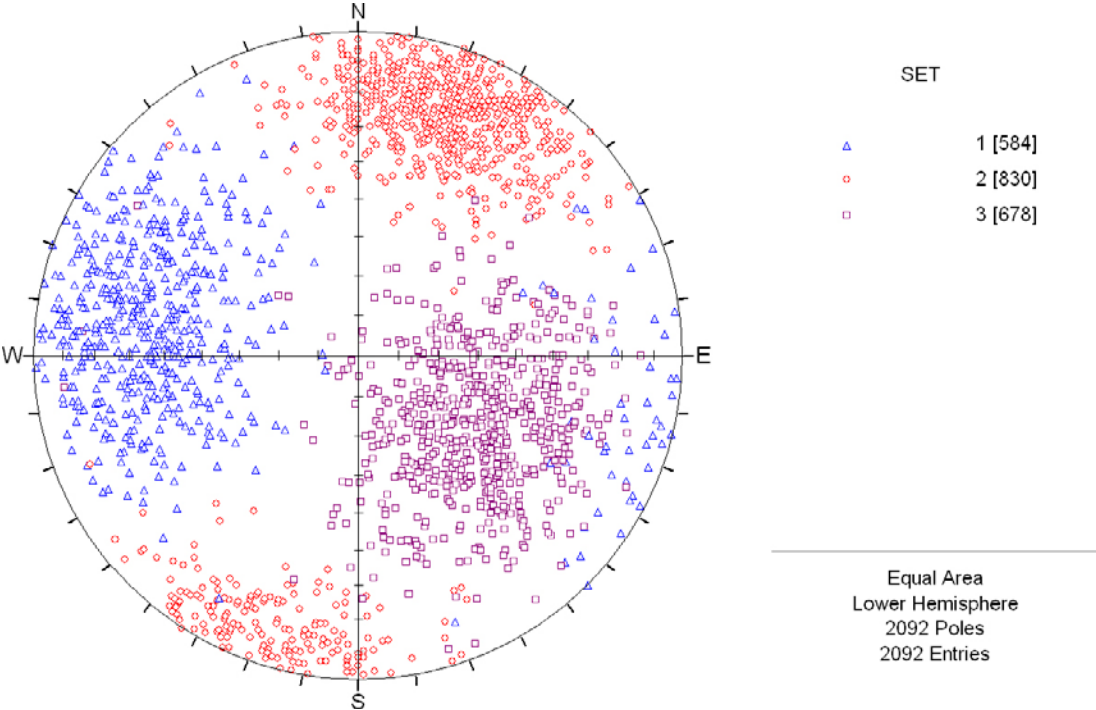
Figure 3-7. Stereonet illustrating the orientation of fractures intersecting the probe holes for 100 realisations of the stochastic fracture network.
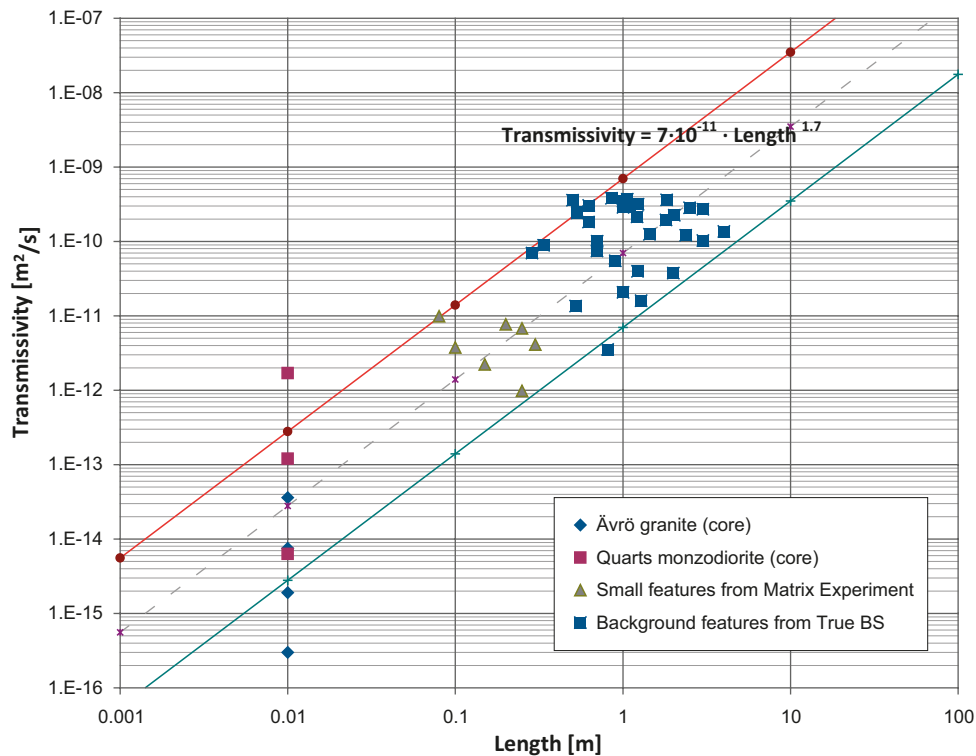
Figure 3-8. *Transmissivity correlation applied to stochastic fractures within the BRIE. The central dashed line corresponds to Equation (3-6), with the red and blue lines indicating plus and minus one order of magnitude from this power-law relation.*

Table 3-2. Diffusion coefficients for water, brine and air within both gas and liquid phases.

Component	Gas Phase	Liquid Phase
Water	2.09×10^{-5} m^{2}s^{-1}	–
Brine	–	1.0×10^{-9} m^{2}s^{-1}
Air [1]	1.79×10^{-5} m^{2}s^{-1}	1.9×10^{-9} m^{2}s^{-1}

[1] Air is assumed to be composed of 80 % nitrogen, 20 % oxygen, with diffusion coefficients interpolated from nitrogen and oxygen endmembers.

Porosities

Upon upscaling the fracture network, the porosity of each grid block within the model will be calculated. In addition, the porosity of the rock matrix is taken as 0.5 %, consistent with measurements from laboratory samples provided during the course of Task 8C modelling and forming part of the Task 8D task description (Vidstrand et al. 2017). Recall from Section 2.5 for intact rock (fracture free matrix) the porosity was estimated at 10^{-5} and the increased porosity of the laboratory samples is assumed to take into account unmapped microfractures which do not form part of the DFN description.

3.2.5 Proposed relationships

Task 8 relationships for the rock matrix, fractured rock and bentonite are proposed as a reference case as part of the Task Description (Vidstrand et al. 2017), and form the basis for the constitutive relationships implemented within TOUGH2. It is also noted that TOUGH2 calculations constrain the maximum capillary pressure of the bentonite to 95 MPa. Gas trapping mechanisms are not considered in any of the simulations performed.

Constitutive relations for bentonite

The **capillary pressure** (P_{cap}) of the bentonite uses a model suggested by van Genuchten, and implemented in TOUGH2 (Pruess et al. 1999) as,

$$P_{cap} = -P_0 \left(\widetilde{S}^{-1/\lambda} - 1 \right)^{1-\lambda},$$
(3-7)

where

$$\widetilde{S} = \frac{S_a - S_{ar}}{1 - S_{ar}},$$
(3-8)

and S_a is the saturation of the aqueous phase; S_{ar} is the residual saturation of the aqueous phase; and parameters λ and P_0 are empirical constants. Therefore the capillary pressure Function (3-7) is implemented with:

$\lambda = 0.3$,

$S_{ar} = 0$,

$P_0 = 9.23$ MPa

as defined from the task description (Vidstrand et al. 2017).

Within the bentonite, the Fatt and Klikoff cubic-law representation of the **relative permeabilities** for the aqueous (k_{ra}) and gaseous (k_{rg}) phases are considered, implemented in TOUGH2 (Pruess et al. 1999) as

$$k_{ra} = \widetilde{S}^3,$$
$$k_{rg} = \left(1 - \widetilde{S}\right)^3,$$
(3-9)

where $\widetilde{S}$ is defined as Equation (3-8), and

$S_{ar} = 0.01$

Constitutive relations for the rock matrix

The **capillary pressure** of the rock matrix is modelled identically to the bentonite (3-7), but with parameters

$\lambda = 0.6$,

$S_{ar} = 0$,

$P_0 = 1.74$ MPa

as defined from the task description (Vidstrand et al. 2017).

For the rock matrix, **relative permeabilities** for the aqueous and gas phases also use a van Genuchten function, implemented in TOUGH2 (Pruess et al. 1999), as:

$$k_{ra} = \sqrt{\widetilde{S}} \left(1 - \left[1 - \widetilde{S}^{1/\lambda} \right]^{\lambda} \right)^2,$$
$$k_{rg} = \sqrt{1 - \widetilde{S}} \left(1 - \widetilde{S}^{1/\lambda} \right)^{2\lambda},$$
(3-10)

where $\widetilde{S}$ is defined as Equation (3-8) and λ is the van Genuchten parameter determined above. Consequently, the relative permeability Function (3-10) is evaluated with

$S_{ar} = 0.01$,

$\lambda = 0.6$

Constitutive relations for fractured rock

The **capillary pressure** of the fractured rock is modelled identically to the bentonite (3-7). The parameters λ and P_0 for fractured rock are inferred from Figure 3-9, provided as part of the task description (Vidstrand et al. 2017). Here

$$\lambda = 1 - \frac{1}{n},$$
$$P_o = \frac{\rho g}{\delta},$$

(3-11)

and the mean hydraulic aperture for the fractures is approximately 3.8×10^{-3} mm, calculated from the transmissivity correlation (3-6) and cubic law (3-3) for fully saturated conditions. With ln $(3.8 \times 10^{-3}) = -5.6$, inspection of Figure 3-9 identifies values for n and δ of 2.25 and 2.0 respectively. Consequently, the capillary pressure Function (3-7) is evaluated with

$S_{ar} = 0,$

$\lambda = 0.56,$

$P_0 = 4\,905$ Pa.

For fractured bedrock, **relative permeabilities** for the aqueous and gaseous phases are modelled identically to the rock matrix (3-10), with λ as determined above. Consequently, the relative permeability Function (3-10) is evaluated with

$S_{ar} = 0.01,$

$\lambda = 0.56.$

3.2.6 Numerical model

The numerical models developed for Tasks 8C1 and 8C2 are conceptually quite different. In Task 8C1 the fractures are represented explicitly, and created stochastically by parameters outlined in Chapter 2. It is assumed that the measured pressures and inflows for each of the five probe boreholes have stabilised, and consequently a steady-state flow solution is appropriate. Ten realisations of the stochastic fracture network were calculated using CONNECTFLOW, with models containing approximately 206,000 individual fractures of which around 157,000 are connected and flowing.

Task 8C2 primarily focuses on the use of TOUGH2 to model the transient resaturation of bentonite emplaced within the deposition holes. TOUGH2 is based on a continuum approach, and the mesh must be refined sufficiently to capture the saturation front within the bentonite. The deposition holes are 3 m deep, with the exception of borehole KO0017G01, which is extended to 3.5 m length on excavation. In addition, the deposition holes have a diameter of 0.3 m. The bentonite emplaced within the TOUGH2 mesh is discretised 8 times azimuthally, 10 times radially, with elements ~0.125 m long (vertically). In addition, although the DFN conceptual model from Task 8C1 and the continuum model used in Task 8C2 are equivalent by the use of upscaling (see Section 3.1.1) at the scale of individual grid blocks within the mesh, the upscaling approach will result in some "homogenisation" of the fracture properties. Therefore it is necessary to also include sufficient refinement of the host rock within the grid to suitably discretise the fractures intersecting the deposition holes. These refined grids provide challenging whilst maintaining computationally tractable simulations. Finally it is noted that if the mesh considered in the TOUGH2 continuum model was sufficiently refined, predicted inflows to open deposition holes using TOUGH2 should equate to the predictions made by CONNECTFLOW in Task 8C1, within the limits of the different underlying assumptions between the two conceptual models.

3.2.7 Model conditioning and calibration

To date, no direct calibration or conditioning of the fracture network has taken place. However, Task 8D, following on from Task 8C, will provide additional hydraulic fracture data for calibration of the DFN models. In particular the following aspects of the model could be considered:

- Current fracture networks are based on statistics derived for all fractures, rather than those hydraulically active. Therefore all fractures within the DFN are capable of flow depending on their connectivity to the wider network. However, this forms an upper limit on connectivity and flow, and one calibration approach could consider only a proportion of the total fracture area open to flow (with the remaining fracture area sealed). This calibration approach may be particularly pertinent if the current models are found to over-predict the total flow and the intensity of flowing features observed in the boreholes and overcored deposition holes. Additional fracture intersection data would allow the suitability of the background fracture statistics used for Task 8C to be assessed.

- On the scale of deposition holes, additional data providing individual fracture intersections, including their hydraulic properties, allows stochastic fracture networks to be modified to reflect each of these hydraulic connections. Model parameters could be further calibrated based on the inflow measurements.
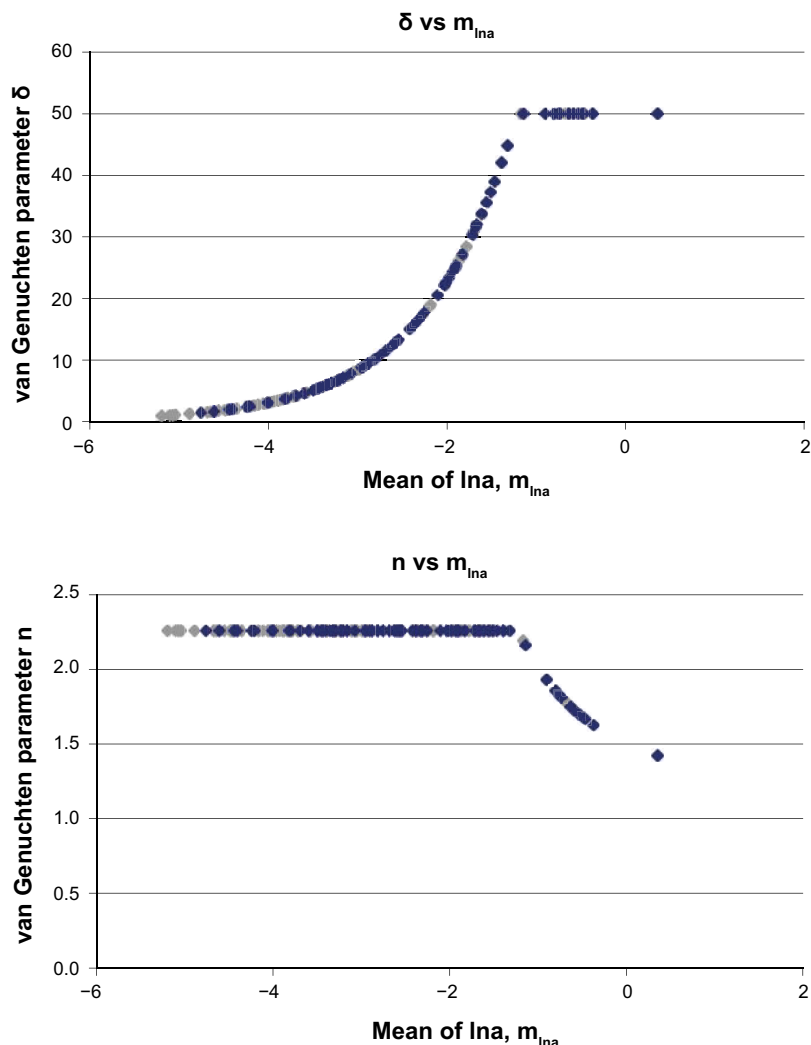
Figure 3-9. *Retention curves for van Genuchten capillary pressure (3-7) and relative permeability (3-10) functions for the fractured rock. The van Genuchten parameters δ and n are plotted for a range of mean hydraulic apertures (measured in mm) of the fracture network. Equation (3-11) relates the plotted parameters δ and n to the constitutive relations presented in Section 3.2.5. Graphs are reproduced from the task description (Vidstrand et al. 2017).*

4 Results for Task 8C1

Task 8C1 considers the water ingress and pressure build up for five probe boreholes of the TASO tunnel. Simulations were performed using CONNECTFLOW, considering 10 realisations of the stochastic fracture network, with results presented in Section 4.1. Subsequently, boreholes KO0017G01 and KO0018G01 were overcored to deposition holes 0.3 m in diameter, with inflow calculations reassessed to investigate changes.

4.1 Probing boreholes

The task description (Vidstrand et al. 2017) provides a series of calibration targets for the five probe boreholes. These include inflow tests to open borehole conditions as well as pressure build up from packed-off boreholes. The calibration targets are presented in Table 2-8. Subsequent to analysing the models against these measured values, predictive modelling for the inflows to overcored boreholes KO0017G01 and KO0018G01 were made.

4.1.1 Inflow estimates

Initial estimates for the inflow to each of the five open boreholes located along the centreline of the TASO tunnel are illustrated in Figure 4-1a. For each of these realisations the observed inflows are relatively consistent, and within the range statistically expected. Groundwater ingress is seen to vary from below the detection limit of 0.1 ml/min to over 10 ml/min between boreholes and realisations. Aggregated inflows for the 10 realisations are summarised in Table 4-1, and compared to measured values.

Average inflows calculated for each of the five probe boreholes over predict measurements by approximately a factor of 8, with the second realisation of the stochastic fracture network providing the most consistent results with the observed inflow magnitudes. With a statistical DFN model, each realisation provides one possible fracture model that adheres to the bulk statistics of the fractured rock, but not in practice the specific geological mappings used to infer the underlying statistics. Therefore, there is no statistical basis for calibrating the DFN models such that the average inflow corresponds directly to observations, rather it is sufficient that the ensemble of realisations considered are within an appropriate confidence interval of the measured inflows; indicating a consistency of the fracture statistics with the flow measurements. There is no quantitative measure for defining an appropriate confidence interval, rather it is left to the modeller to assess; however for a limited set of realisations, the following criteria should highlight any obvious inconsistencies between the DFN model predictions and flow measurements:

- The mean of the model predictions should be within an order of magnitude of the inflow measurements.

- For boreholes with non-zero inflow measurements, model predictions should span the measurement value.

- For boreholes with no recorded inflow, some realisations of the DFN model should predict inflows below the detection limit of the flow measurement tool.

For the ten realisations considered, it is noted that although the aggregated inflows from simulations are larger than those measured, for all boreholes except KO0018G01 the above criteria are met, and therefore the DFN description is considered consistent with this set of flow measurements. Details of the inflows simulated to each of the probe boreholes are recorded in Table 4-1.

Table 4-1. Table of inflows to each borehole, aggregated over 10 realisations.

Borehole	Average Inflow (ml/min)	Realisation 2 Inflow (ml/min)	Measured Inflow (ml/min)
KO0020	4.6	0.0	–
KO0018	7.1	0.7	–
KO0017	4.8	1.0	0.5
KO0015	6.6	0.7	–
KO0014	6.4	3.1	1
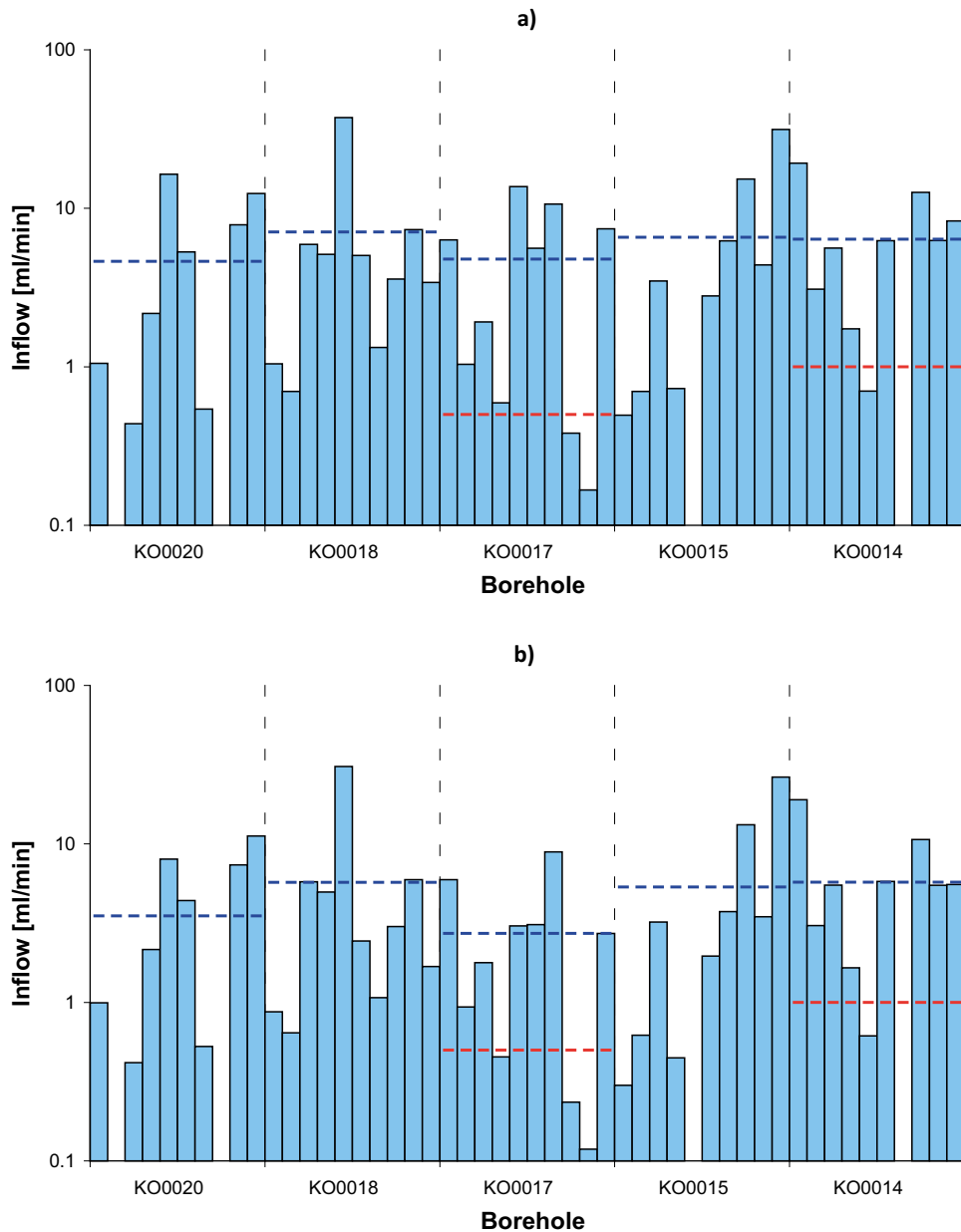
Figure 4-1. *Inflows to each borehole for each of the 10 flow simulations where (a) each borehole is opened in turn, and (b) where all boreholes are opened together. The average inflow is shown in dark blue, and observed groundwater ingress shown in red.*

For the second realisation of the fracture network, the transmissivity of fractures clustered around the probe holes, as well as the location of the inflows within specific boreholes are illustrated in Figure 4-2. In general, groundwater ingress is greatest in locations corresponding to the more transmissive inter-sections with the borehole, with a number of the fracture intersections providing inflows to the borehole less than the detection limit of 0.1 ml/min.

A variant scenario, where all probe boreholes are opened to inflow simultaneously has also been considered, with inflows illustrated in Figure 4-1b. Groundwater ingress is generally decreased when compared to individual opening of the probe holes, with trends across the realisations largely unchanged. Table 4-2 summarises the average inflows to each borehole for this variant, along with the percentage change in inflows. As expected, the central borehole, KO0017G01, experiences the greatest reduction in inflow (~43 %) when its surrounding boreholes are also opened.

a)

b)
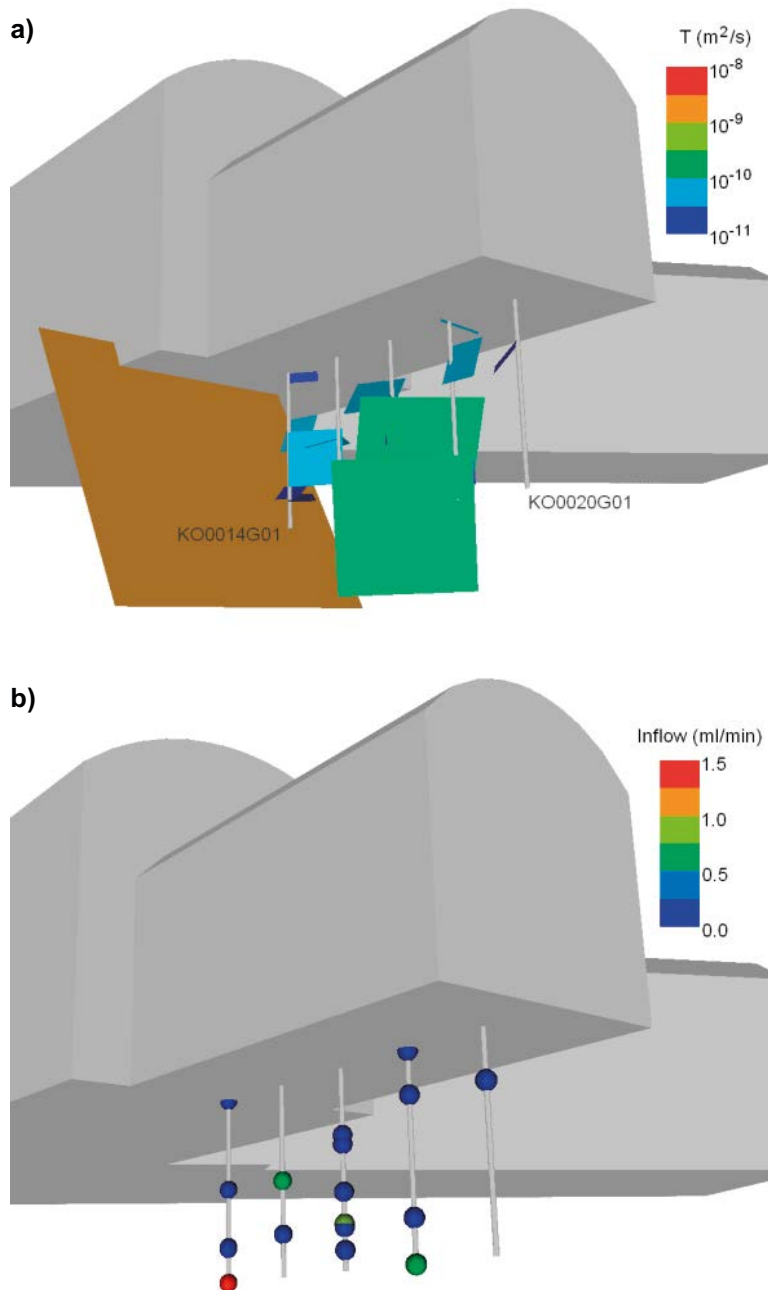
Figure 4-2. Realisation 2 of the stochastic fracture network illustrating (a) the local fracture tessellates coloured by transmissivity, and (b) inflows to boreholes KO0020G01 through KO0014G01.

Table 4-2. Average inflows to the five probe boreholes, comparing individual and collective opening of the boreholes to atmospheric conditions. Inflows to each borehole are aggregated over 10 realisations of the fracture network.

Borehole	Average Inflow (ml/min)		% Change of Inflows
	Individual Borehole Opening	Collective Borehole Opening	
KO0020	4.6	3.5	−24.0 %
KO0018	7.1	5.7	−19.2 %
KO0017	4.8	2.7	−43.0 %
KO0015	6.6	5.3	−18.6 %
KO0014	6.4	5.7	−10.2 %

4.1.2   Pressure build up

Pressure tests have been performed as part of the BRIE (Vidstrand et al. 2017) for each of the 5 bore-holes in turn, including packing of the top 1 m, and recording the build up of pressure. Figure 4-3 illustrates the calculated pressures within each of the five probe boreholes for 10 realisations of the stochastic fracture network. As for the inflow estimates, the pressures observed for each of these realisations are relatively consistent, and within the range statistically expected. It is also noted that measurable pressures can be obtained for intervals where the corresponding inflow is small (lower than the detection limit). Aggregated results for the multiple realisations are compared with observed values in Table 4-3.

The ensemble of realisations considered simulated pressure build up within 50 probe boreholes (5 boreholes, 10 realisations). Of these, only 3 do not exhibit any response to being closed, i.e. they are disconnected from the wider fracture network within the packer interval. This is in contrast to observation, where only 2 of the 5 probe boreholes record a pressure when packed-off to 1 m below the tunnel floor. This difference could be due to:

1. **Measurement limitations:** For a pressure to be recorded within each of the closed boreholes, it is required that inflows are sufficient to fill the borehole within the duration of the measurement.

2. **Fracture network connectivity:** Data provided as part of Task 8C does not allow differentiation between hydraulically active fractures, and those closed to flow. Consequently the hydrogeological models developed as part of Task 8C are based on statistics derived for all fractures, with a propensity to over predict the intensity of potentially flowing fractures.

Table 4-3. Table of pressure build up in each borehole when packed-off. Values are aggregated over 10 realisations.

Borehole	Average Pressure (bar)	Realisation 2 Pressure (bar)	Measured Pressure (bar)
KO0020	7.0	0.0	–
KO0018	5.2	8.1	–
KO0017	5.1	5.6	6
KO0015	4.3	2.6	–
KO0014	4.3	4.0	3
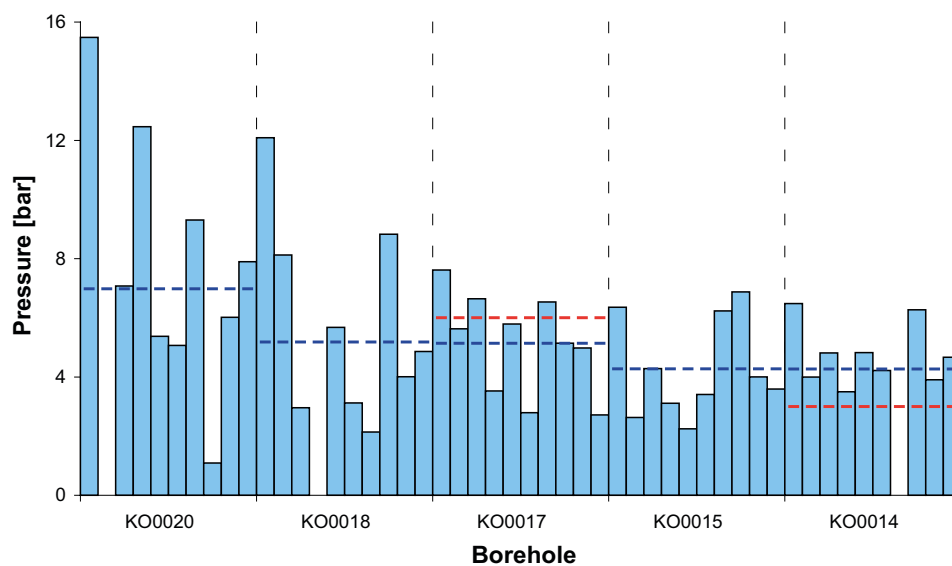
Figure 4-3. *Pressure within each packed-off borehole for each of the 10 simulations performed. The average pressure is shown in dark blue, with the measured values shown in red.*

Inflow estimates identified realisation 2 of the stochastic fracture network as the closest match to measured values. Figure 4-4 illustrates the intersections with the five packed-off probe boreholes. The sole intersection with borehole KO0020G01, as observed for the inflows calculations (see Figure 4-2b) occurs above the location of the 1 m packer, and consequently no pressure build up is simulated in this borehole. The pressures calculated in boreholes KO0017G01 and KO0014G01 are consistent with those observed, with differences of −0.4 bar, and +1.0 bar respectively. However, pressures also rise in probe boreholes KO0015G01 and KO0018G01 due to their intersection with the wider stochastic fracture network, although no build-up in pressure was measured in these boreholes.

4.1.3   Realisation 2

Through analysis of inflows, as well as pressure build up in packed-off boreholes, realisation 2 of the stochastic fracture model is identified as the most representative of the observed network. It is noted that the selection of this realisation is based solely on its correlation to the limited measurements available and if additional realisations of the stochastic fracture network were considered, an alternative realisation may be selected as optimal. No specific calibration of this fracture network has occurred.

Figure 4-5 illustrates two slices through the second model realisation, one vertical cross-section incorporating all five probing boreholes, and one horizontal cross-section cutting through at the depth of −418 m. In both cases fracture slices depict transmissivities in the deposition near-field. The correlated transmissivity model is clearly seen, with larger fractures more transmissive and lower transmissivities assigned to smaller fractures. The highly transmissive (red) fracture trace found at the bottom right-hand corner of Figure 4-5b is deterministic fracture NNW, with a transmissivity of $6.5 \ 10^{-7}$ m^2/s. The large orange fracture trace, crossing vertically in both Figure 4-5a and Figure 4-5b is deterministic fracture wfracture_01, and has a transmissivity $2.0 \ 10^{-8}$ m^2/s. Equivalent illustrations for stochastic fracture realisations 1, and 3 through 10 are shown in Appendix 1, Figure A1-1 through Figure A1-9 respectively.

Figure 4-6 illustrates equivalent fracture slices to those shown in Figure 4-5 for the second realisation of the fracture network, depicting the solution pressures. Simulation results correspond to the scenario of shut-in pressures at the five boreholes packed-off at 1 m. The drawdown caused by the TASO/TASD tunnels, as well as deposition boreholes, held at atmospheric conditions is clearly seen. Equivalent illustrations for stochastic fracture realisations 1, and 3 through 10 are shown in Appendix 1, Figure A1-10 through Figure A1-18 respectively.
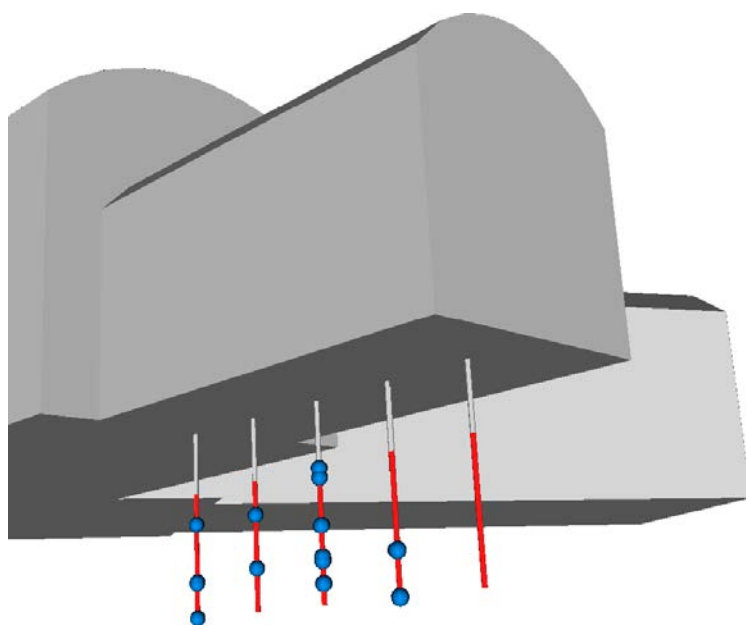
Figure 4-4. Five probe boreholes, packed-off at −418 m, are shown in red, with the location of intersections contributing to pressure build up in the boreholes shown for realisation 2 of the fracture network.
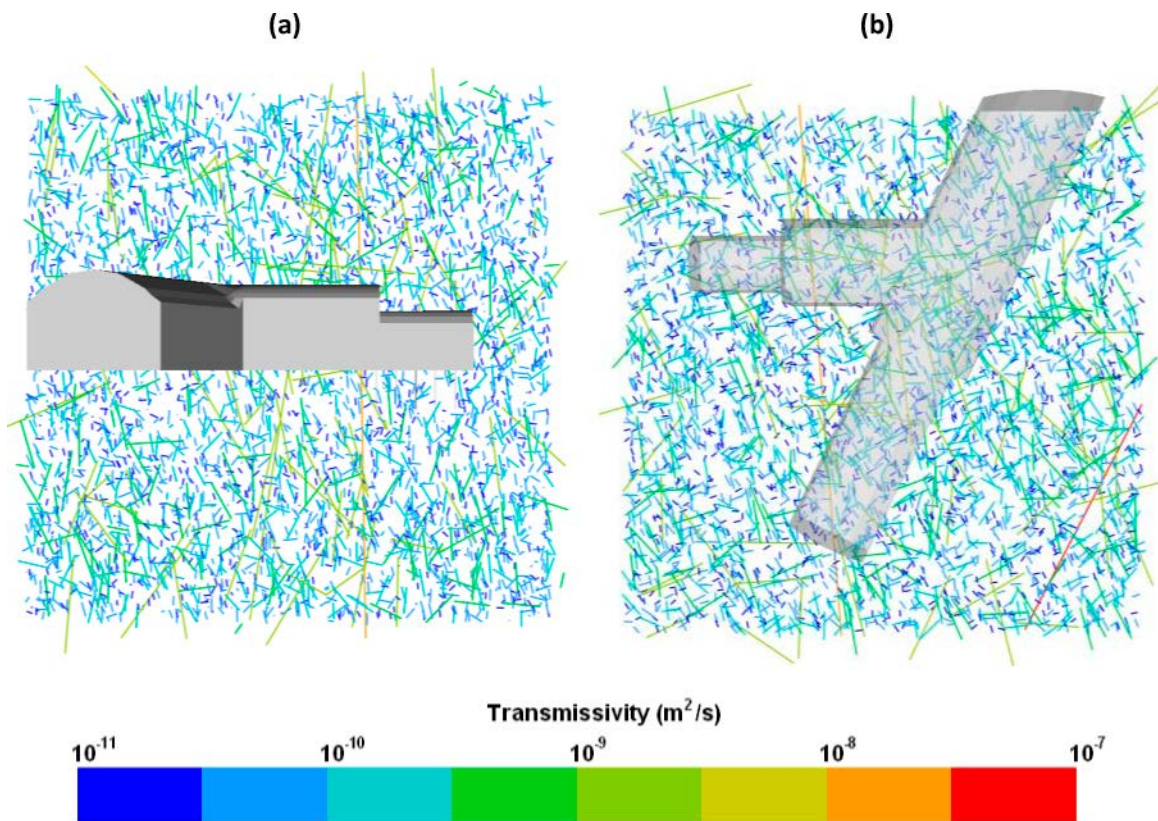
Figure 4-5. Transmissivity (m²/s) in the borehole near-field for (a) a vertical slice through all five probe boreholes; and (b) a horizontal slice at an elevation of −418 m. Results are shown for the second realisation of the stochastic fracture network.
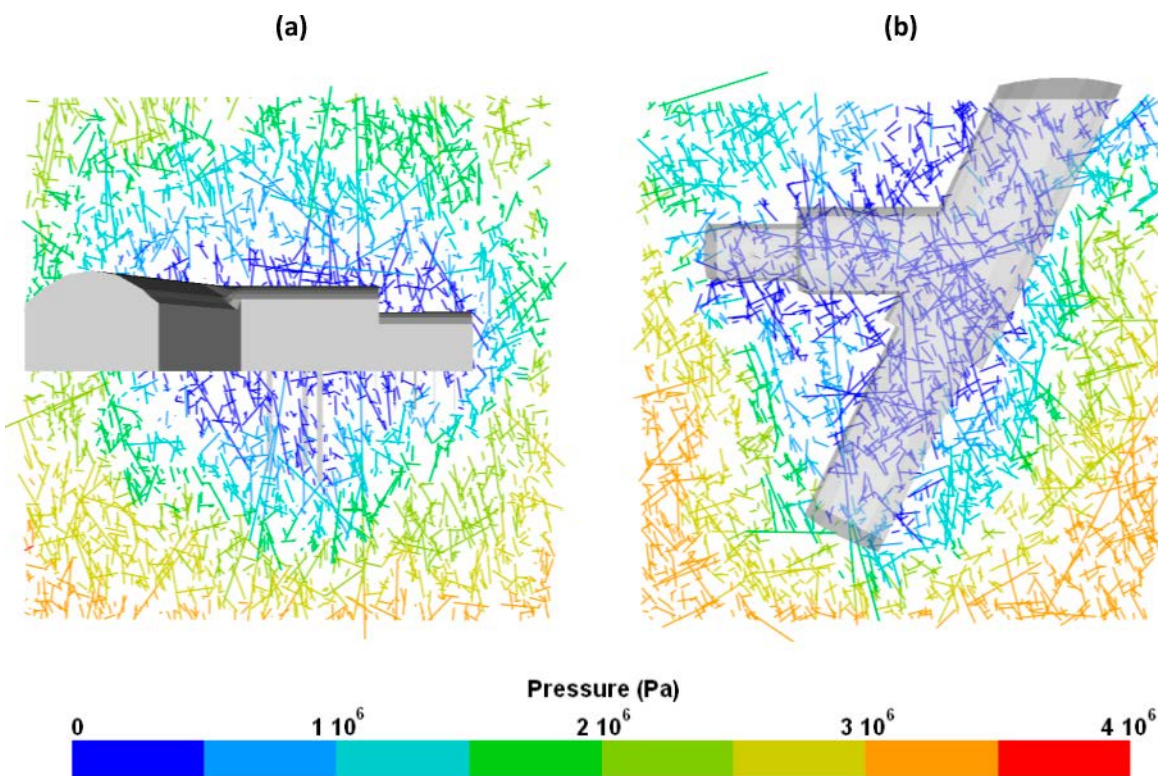
Figure 4-6. Pressure (Pa) in the deposition hole near-field for (a) a vertical slice through all five probe boreholes; and (b) a horizontal slice at an elevation of −418 m. Results are shown for the second realisation of the stochastic fracture network.

4.2 Deposition boreholes KO0017G01 and KO0018G01

As part of the BRIE, probe boreholes KO0017G01 and KO0018G01 were identified for overcoring into deposition holes of diameter 0.3 m. The excavation process of KO0017G01 resulted in its length extending by 0.5 m to a depth of −420.5 m. The length of deposition hole KO0018G01 is unchanged. Before the emplacement of bentonite and subsequent resaturation process are considered, inflows to these overcored boreholes were predicted using the models developed for the 5 probe holes. This initial predictive modelling exercise is an opportunity to test and to build confidence in the methodologies developed to date.

Figure 4-7 illustrates the number of inflows greater than the detection limit of 0.1 ml/min to each of the deposition boreholes KO0018G01 and KO0017G01. The average number of detectable inflows, aggregated over the 10 realisations, is similar in both cases, with an average of 3.8 found in deposition hole KO0017G01, and 3.4 in deposition hole KO0018G01. For both deposition holes, the maximum number of detectable inflows found over the 10 realisations is 8, with the least identified number of inflows of 1.

Figure 4-8 compares total inflows to probe boreholes KO0017G01 and KO0018G01 with results for the deposition hole models. Changes to the average groundwater ingress, aggregated over the 10 realisations of the fracture network, are also presented in Table 4-4. In general, results show an average increase in inflows to both deposition holes. Likely causes of this increase are:

• Increasing the borehole radius will increase groundwater ingress for a given drawdown (e.g. Thiem solution).

• As the boreholes are overcored (and in the case of KO0017G01, lengthened), the borehole will intersect additional fractures, increasing the potential for groundwater ingress to the deposition hole. Figure 4-9 illustrates the additional intersections observed in the two overcored boreholes for realisation 2 of the stochastic fracture network.

However, although the majority of realisations result in an increase to the total inflows to the deposition holes when compared to the previous probe borehole models, a small number of model realisations exhibit the reverse of this trend. In these cases lower total inflows are found to the deposition holes when compared to the same stochastic fracture network, including probe boreholes. For example, in Figure 4-8b realisation 1, the inflow is seen to increase on overcoring the probe boreholes, whereas in realisation 7 a small decrease is observed. It is noted that whilst the probe boreholes have been opened individually to record inflows to each borehole in turn, deposition holes KO0017G01 and KO0018G01 were opened together. Overall this will limit the total inflow to these deposition holes, as their small separation (1.2 m apart) will limit the extent to which the drawdown for each deposition hole is experienced within the wider fracture network. For a few realisations of the fracture network this results in a reduction in total inflow when overcoring the probe boreholes.

Once boreholes KO0017G01 and KO0018G01 have been overcored, inflow rates will be measured as part of the BRIE, and compared to these predictive simulations.
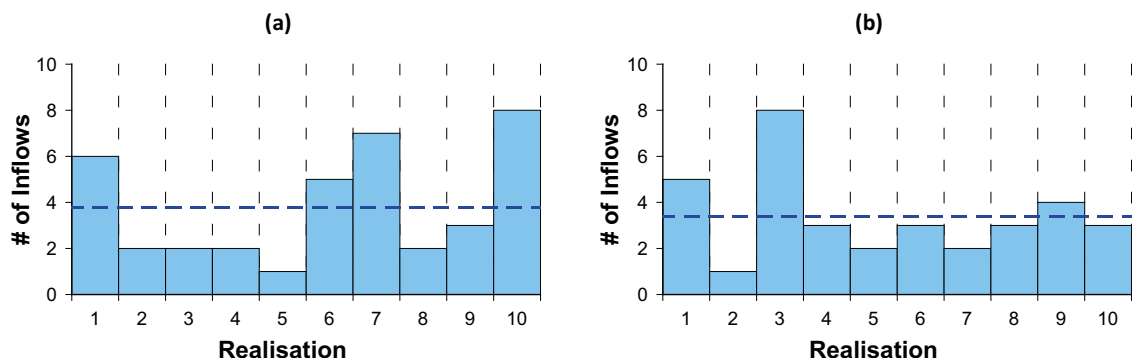
Figure 4-7. *Number of inflows greater than the detection limit of 0.1 ml/min to deposition borehole (a) KO0017G01; and (b) KO0018G01. Results are shown for 10 realisations of the stochastic fracture network, with an average count shown in black.*

Table 4-4. Inflows to each borehole after overcoring of probe holes KO0017G01 and KO0018G01 to deposition holes. Values are aggregated over 10 realisations.

Borehole	Average inflows to probe holes (ml/min)	Average inflows to overcored KO0017 and KO0018 (ml/min)	Average % increase	Realisation 2 % increase
KO0018	7.1	10.0	41.7 %	15.7 %
KO0017	4.8	5.5	15.3 %	2.3 %
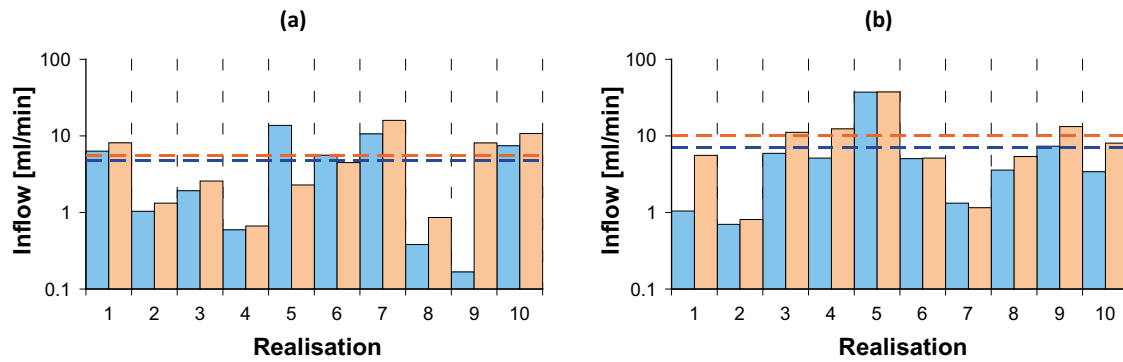
Figure 4-8. *Comparison of total inflows between probe holes (blue) and overcored deposition boreholes (orange) for (a) KO0017G01; and (b) KO0018G01. Results are shown for 10 realisations of the stochastic fracture network, with the average inflow shown by a dashed line.*
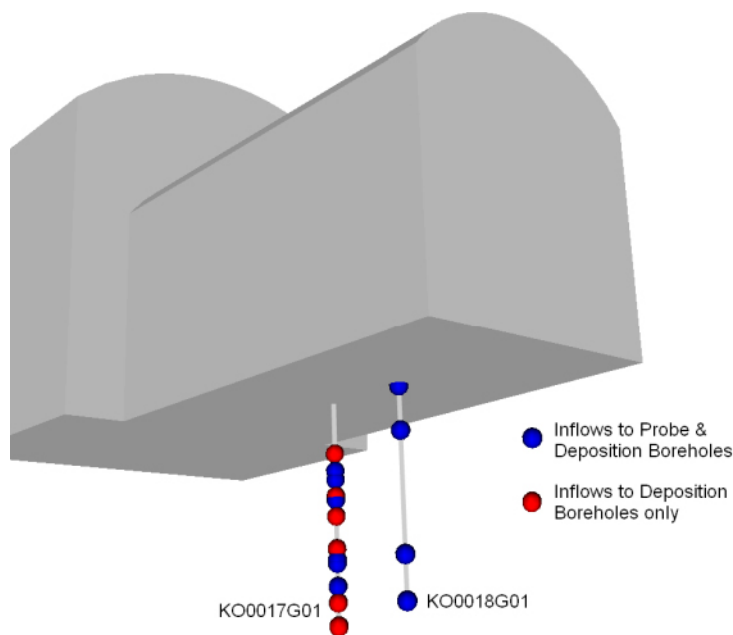
Figure 4-9. *Inflow locations to the overcored boreholes KO0018G01 and KO0017G01 for realisation 2 of the stochastic fracture network. Locations are coloured by whether the inflow existed under probe hole conditions.*

Figure 4-9 illustrates the locations of inflows to overcored boreholes KO0017G01 and KO0018G01, identifying the additional intersections that exist due to overcoring. Although, on overcoring the probe borehole no additional fractures are intersected by KO0018G01, KO0017G01 intersects 7 additional fractures. Figure 4-10 also identifies these additional intersections by illustrating the fracture tessellates local to these two boreholes, coloured by transmissivity.

Inflow locations to the deposition holes are shown in Figure 4-11 for the second realisation of the fracture network, and coloured by inflow rate. In both deposition holes KO0017G01 and KO0018G01 there is a single inflow that dominates for this particular realisation. These inflow locations correspond to the raised inflow rates observed for the probe borehole models, (see Figure 4-2b), although the rates of groundwater ingress have increased.
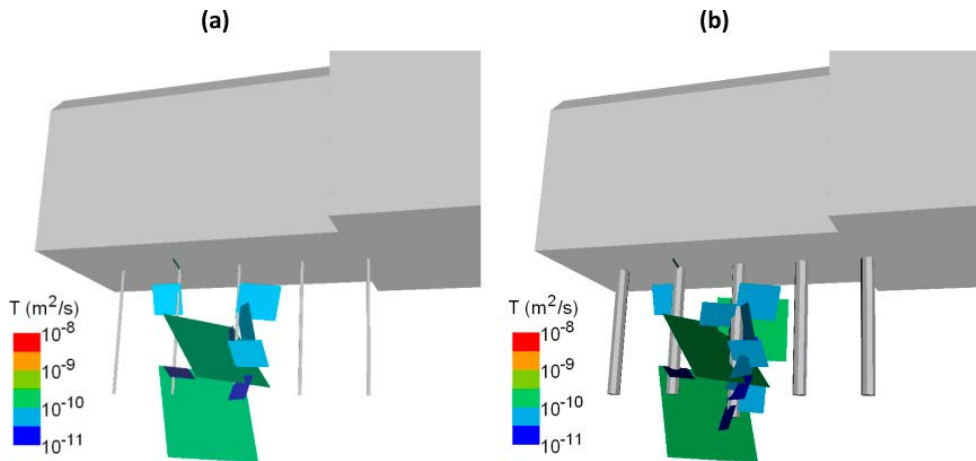
Figure 4-10. *Realisation 2 of the stochastic fracture network illustrating the local fracture tessellates, coloured by transmissivity, that intersect KO0017G01 and KO0018G01 as (a) probe holes and (b) deposition holes.*
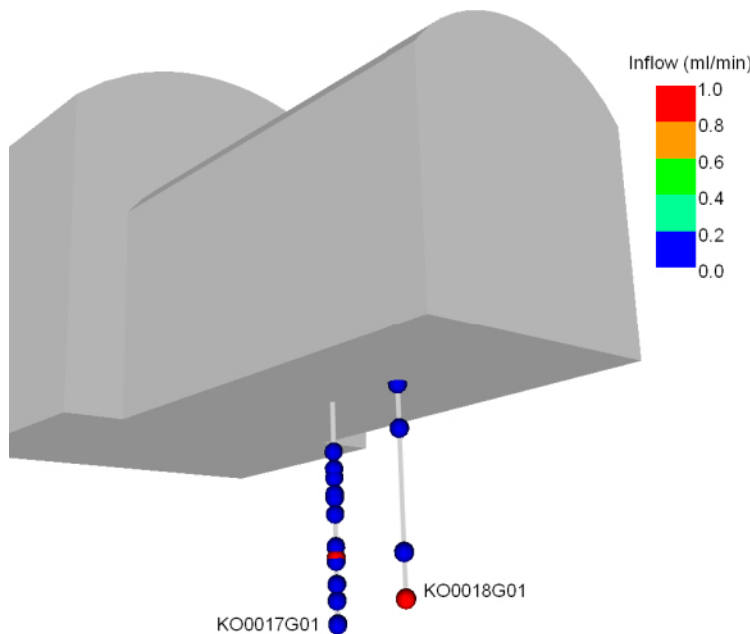
Figure 4-11. *Inflow locations to the overcored boreholes KO0018G01 and KO0017G01, for realisation 2 of the stochastic fracture network. Locations are coloured by inflow rate.*

The second realisation of the stochastic fracture network is shown for two slices local to the deposition holes in Figure 4-12a and Figure 4-12b respectively. Figure 4-12a slices vertically, incorporating all five probing boreholes, and Figure 4-12b takes a horizontal cross-section cutting through at a depth of −418 m. Fracture traces are coloured by transmissivity. Figure 4-12c and Figure 4-12d depict identical slices for the equivalent permeability field, formed from upscaling the fracture network as detailed in Section 3.1.1. Clearly regions of intense fracturing and/or high transmissivity yield correspondingly permeable blocks in the upscaled model. Although the transmissive discrete feature (coloured red in Figure 4-12a and b) appears discontinuous on upscaling (Figure 4-12c and d); this is a consequence of illustrating only a single component of the permeability tensor. This upscaled process will be used to represent the heterogeneity of the bedrock within the TOUGH2 models, and will be applied for simulation of the resaturation of the bentonite in the following section. Equivalent results for realisation 1, and 3 through 10, of the stochastic fracture network are shown in Appendix 1, Figure A1-19 through Figure A1-27 respectively.
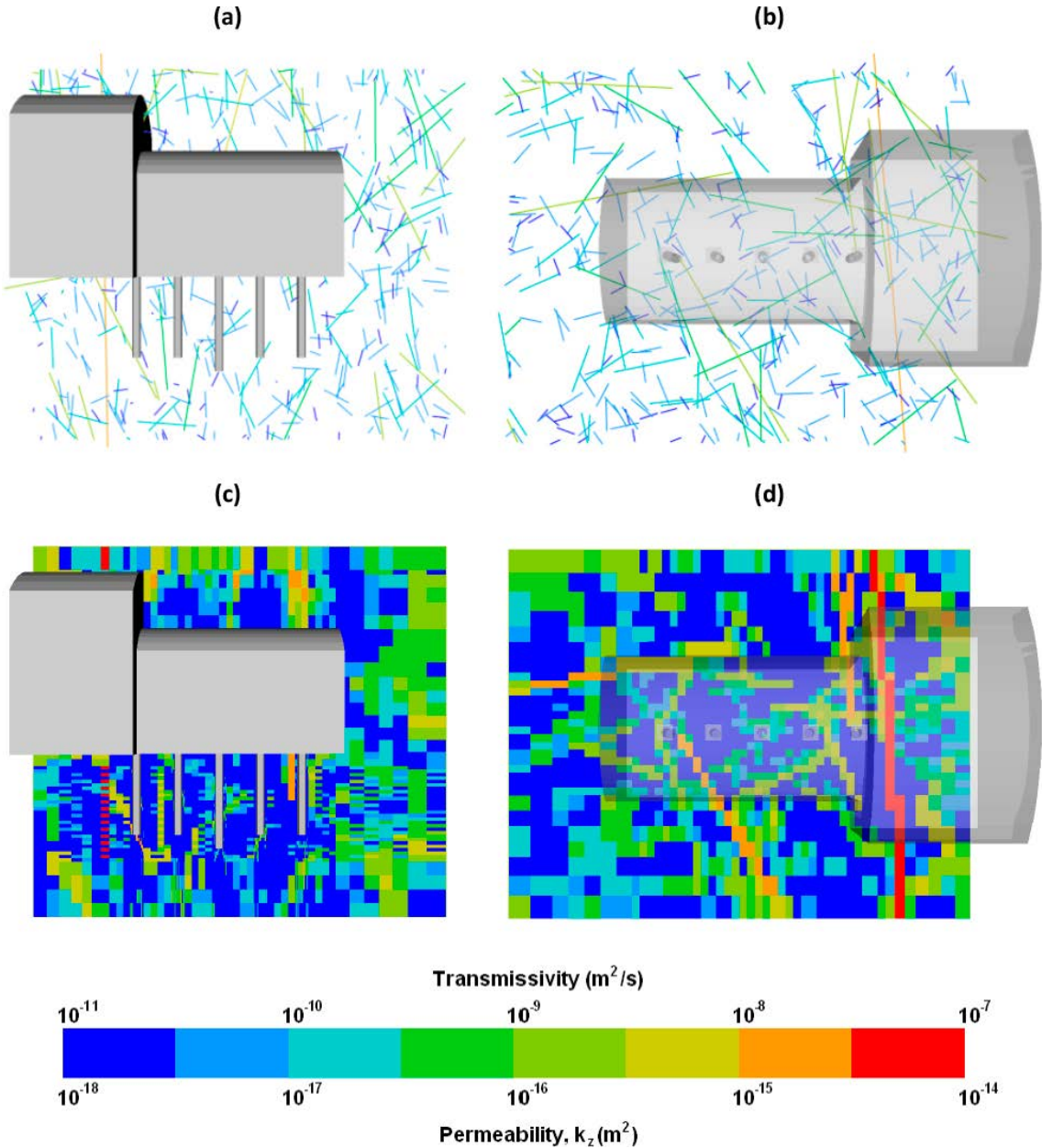
Figure 4-12. *Transmissivity (m^2/s) (a,b) and upscaled permeability (m^2) (c,d) in the deposition hole near-field. For (a,c) a vertical slice through all five probe boreholes is represented; and for (b,d) a horizontal slice is taken at an elevation of −418 m. Results are shown for the second realisation of the stochastic fracture network.*

5 Results for Task 8C2

Task 8C2 considers the resaturation of bentonite emplaced within the deposition holes of the TASO tunnel. Simulations are performed using TOUGH2, considering multiple realisations of the stochastic fracture network, as identified within Chapter 4. One of the main objectives in participating in Task 8C2 modelling is the development of tools and methodologies to understand the interaction between the groundwater flow from a fractured host rock and the resulting resaturation of emplaced bentonite material. Consequently, the models developed in this section include the overcoring of all five probe boreholes (rather than KO0017G01 and KO0018G01 of the BRIE) to provide further insight into this resaturation process. All deposition holes have a radius of 0.15 m, and are represented within the TOUGH2 model as a uniform octagonal prism. The surface area of the deposition hole is maintained, yielding an outer radius of the octagon of 0.1539 m. All deposition holes are 3 m deep with the exception of KO0017G01, which has been excavated to a depth of 3.5 m.

As discussed in Section 3.1.2, TOUGH2 is based on a continuum concept, and in order to simulate the bentonite rock interface, upscaling of the fracture permeability of the rock is required. Upscaling methodologies were detailed in Section 3.1.1, and consist of replacing the fracture network with the equivalent block permeability on the model grid-scale. Results for upscaling ten realisations of the stochastic fracture network are shown in Figure 4-12 and Figure A1-19 through Figure A1-27. In addition, the upscaled permeability blocks for the second realisation of the fracture network are shown in Figure 5-1, illustrating the rock permeability, computed on the TOUGH2 sub-grid, in the vicinity of the BRIE boreholes.

Using the upscaled fracture network, the resaturation of bentonite will be simulated for multiple realisations of the stochastic fracture network. In each case, the TOUGH2 simulations are performed in two phases:

1. Initially, the inflow to all five open deposition holes is calculated, using initial/boundary conditions provided by the task description (Vidstrand et al. 2017).

2. Using the results from the first phase of calculations as initial conditions, the resaturation of emplaced bentonite within each of the five deposition holes is simulated.
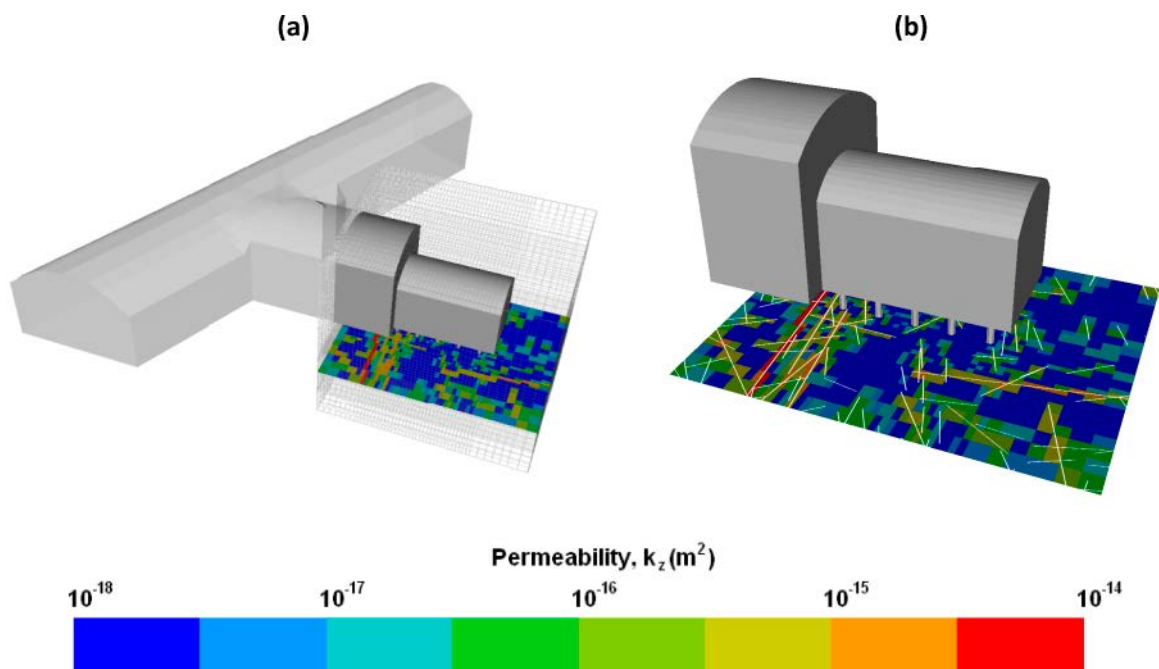
Figure 5-1. *(a) Horizontal slice of the upscaled permeability, computed on a sub-grid, in the vicinity of the probe holes. (b) Upscaled permeability on a ~0.5 m scale, with the traces of the fractures ($T > 10^{-10}$ m^2/s) indicated.*

Analysis of Task 8C1 identified the second realisation of the stochastic fracture network as providing the most consistent results compared to observations. Simulations presented within this Section chapter detail results for this specific realisation of the fracture network, with results for additional realisations shown in Appendix 2.

Two variant scenarios will also be considered:

- A homogeneous case, with rock permeability based on the geometric mean of the upscaled permeabilities (see Section 5.3).

- Sensitivity analysis of the rock matrix permeability, assessing its effects on the resaturation of the emplaced bentonite (see Section 5.4).

5.1   Simulation of open deposition holes

Prior to simulating the resaturation of bentonite emplaced in the deposition holes, inflows to the five open boreholes are calculated. These simulations will provide initial conditions for the resaturation analysis presented in Section 5.2. Boundary conditions within the boreholes are identical to the TASO tunnel, and are held at atmospheric pressure, with 100 % relative humidity. The far-field boundary conditions are as prescribed by the task description (Vidstrand et al. 2017).

Inflows are calculated from the dot product of the inward unit normal to the deposition hole surface, and the liquid flux vector, i,e. $n \cdot v_1$. In this study, the unit normal is approximated as the vector from the surface point of interest to the centre of the deposition hole (rather than perpendicular to the representation of the deposition hole wall). This approximation is not expected to be significant.

A contour plot of the inflows to each of the five deposition holes is shown in Figure 5-2, presented as folded up illustrations of the borehole walls. Results are presented for the second realisation of the fracture network, with contours of inflow corresponding to the first realisation of the fracture network shown in Appendix 2, Figure A2-1. A range of inflows are identified in Figure 5-2; the largest in deposition hole KO0014G01, and up to approximately 18 ml/min at the bottom of the hole. In contrast, only minimal inflows are identified in KO0020G01, c. 0.1 ml/min located at a depth of around −417.9 m.

The locations of the principal inflows to deposition holes KO0017G01 and KO0018G01 can be compared to the CONNETFLOW simulations presented in Figure 4-11. The primary inflow locations to both of these deposition holes are consistent between the numerical methods, occurring at c. −419.3 m in KO0017G01, and at the bottom of KO0018G01.

5.2   Resaturation of deposition holes

Using the inflow simulations calculated as part of Section 5.1 as initial conditions, the resaturation of bentonite emplaced within each of the five deposition holes is considered. Initial liquid saturation on the outer surface of the bentonite is shown in Figure 5-3, along with five subsequent times (0.1 years, 0.5 years, 1 year, 10 years and 100 years). The initial liquid saturation of the bentonite is 36 %, as provided from the task description (Vidstrand et al. 2017) and typical of the water content of bentonite to be used in the BRIE. Realisation two corresponds to the case which was able to model both inflow and pressure build-up. Therefore this realisation was used as a basis for the simulation of resaturation of emplaced bentonite, predicting highly heterogeneous wetting, especially evident at early times. The locations of wetting after a tenth of a year are indentified by liquid saturations above the initial state of 36 %, and are consistent with the inflow locations shown in Figure 5-2 for open borehole conditions.
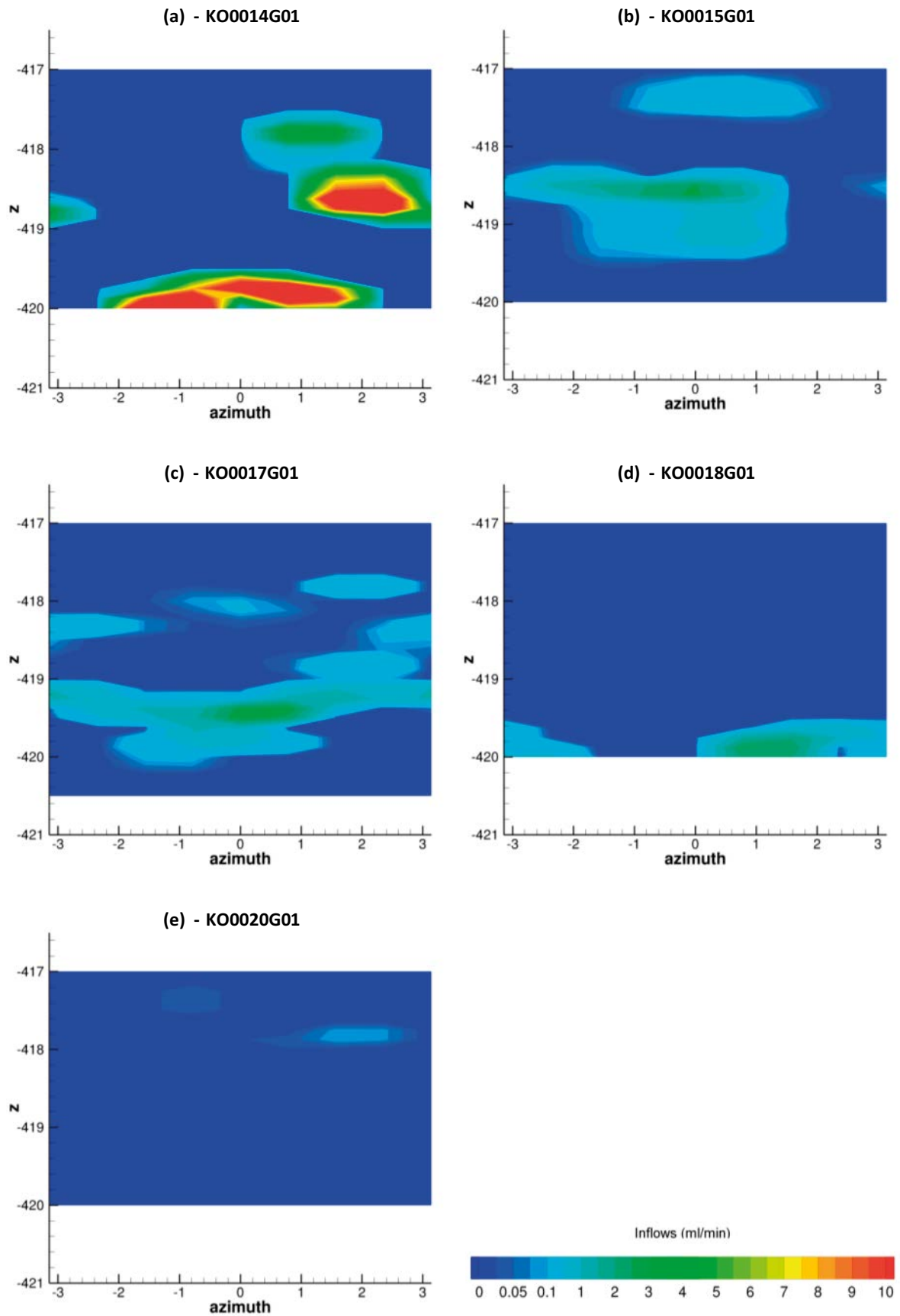
Figure 5-2. *Inflows illustrated against the walls of deposition boreholes (a) KO0014G01; (b) KO0015G01 (c) KO0017G01; (d) KO0018G01; and (e) KO0020G01, for realisation 2 of the upscaled fracture network.*
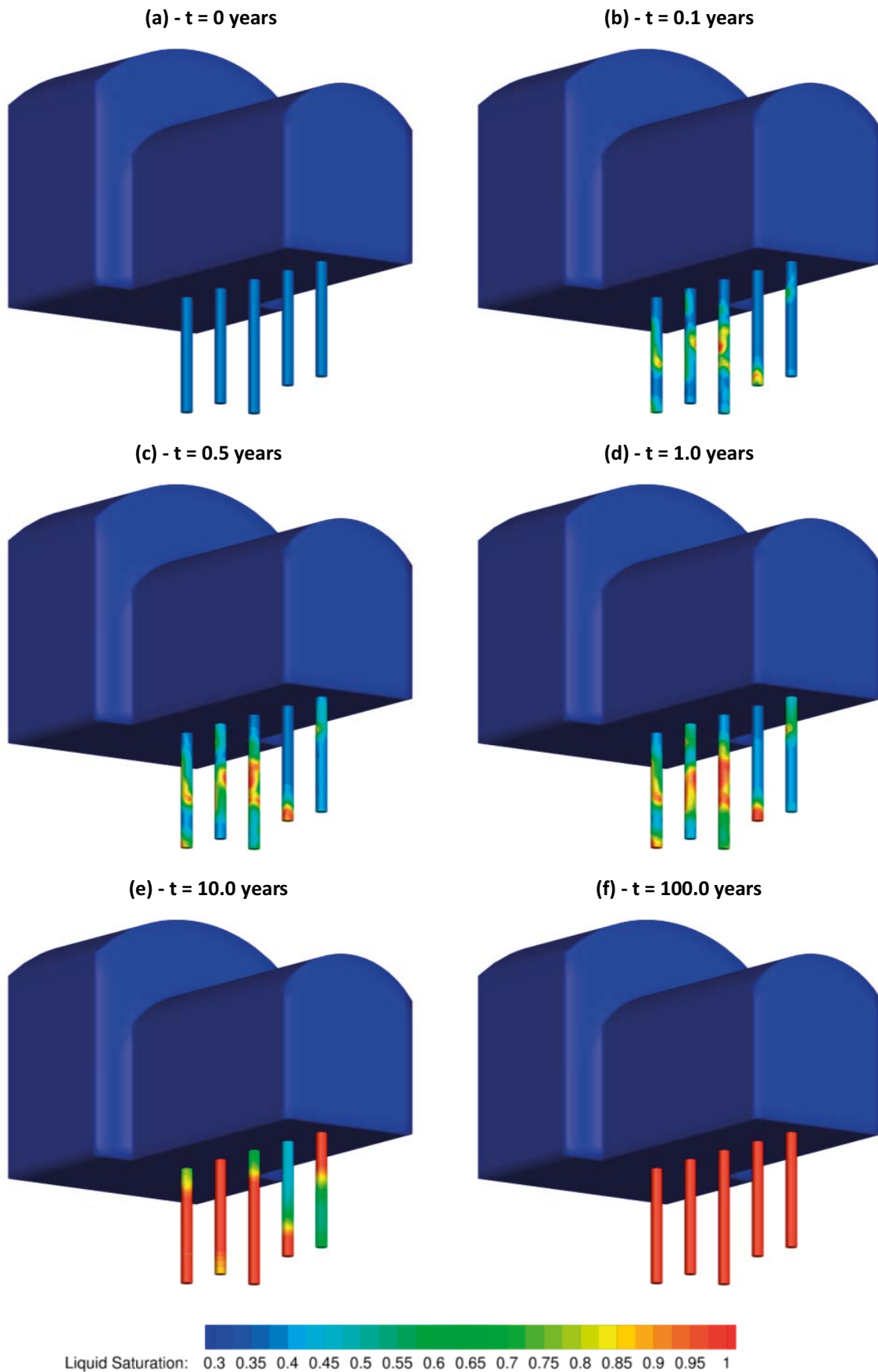
Figure 5-3. *Comparison of bentonite saturation with time through a heterogeneous bedrock description for realisation 2 of the stochastic fracture network at times (a) 0 years, (b) 0.1 years, (c) 0.5 years, (d) 1 year, (e) 10 years, and (f) 100 years.*

The time for each of the five deposition holes to reach 99 % liquid saturation from the initial state (36 %) are detailed in Table 5-1. The first two deposition holes, KO0014G01 and KO0015G01 both resaturate relatively quickly, taking less than 20 years, followed by KO0017G01 at c. 30 years. Each of these boreholes exhibits multiple resaturation points, corresponding to locations of higher permeability grid blocks (i.e. fractures within the DFN representation of the bedrock). In contrast, KO0018G01 contains a single resaturation front, located at the bottom of the deposition hole, with the uptake of groundwater further up the borehole severely limited by the low permeability rock matrix. Consequently, resaturation is slow, taking around 75 years. The inherent heterogeneity of water uptake to the bentonite within a fractured bedrock description is evident, with a factor of 4.5 between the quickest and slowest resaturation times for this single realisation of the fracture network. Resaturation times for each of the deposition holes, located within four additional realisations of the fracture network, are shown in Table A2-1.

Table 5-1. Times for bentonite emplaced within the five deposition holes to achieve 99 % saturation using realisation two of the stochastic fracture network, and the minimum and maximum durations observed over five realisations.

Result	KO0020G01	KO0018G01	KO0017G01	KO0015G01	KO0014G01
Minimum	18.7	10.9	12.0	7.4	9.3
Realisation 2	42.2	75.4	29.2	16.7	18.9
Maximum	42.2	75.4	40.3	25.8	18.9

Contour plots of liquid pressures in the deposition hole near-field are shown in Figure 5-4 and Figure 5-5 for two separate slices through the second realisation of the upscaled fracture network model. As requested in the task description (Vidstrand et al. 2017), the colour scale of the contour plots are: 1.5, 1, 0.5, 0.2, 0.1, 0, −0.1, −0.2, −0.5, −1, −5, −10, −20, and −50 MPa. Pressures on a vertical cross-section incorporating the deposition holes, and parallel with the TASO tunnel central line are shown in Figure 5-4 at 0, 0.1, 0.5, 1, 10, and 100 years. Initially, large suction pressures are observed within the bentonite, drawing groundwater from the surrounding fractured rock and rock matrix. With supply of groundwater to the rock matrix limited by its low permeability negative liquid pressures are readily observed in the surrounding rock matrix to the deposition holes (see, for example, KO0018G01). Over time, and by 100 years, the pressures within the bentonite and rock matrix fully recover to a saturated, undisturbed state. A second, horizontal, cross-section located at an elevation of −418 m, and cutting through all five deposition holes, is shown in Figure 5-5. Corresponding results for the first and tenth realisations of the stochastic fracture network are shown in Figure A2-2 through Figure A2-5.

Contour plots of the liquid saturation in the deposition hole near-field are shown in Figure 5-6 and Figure 5-7 for both a vertical and horizontal slice respectively. Solutions are presented for the second realisation of the stochastic fracture network at times 0, 0.1, 0.5, 1, 10, 100 years. Slices correspond to those shown in Figure 5-4 and Figure 5-5 for liquid pressures, and the desaturation of the rock matrix by the bentonite is evident, especially local to deposition hole KO0018G01. After 100 years, the bentonite has fully resaturated, and the rock matrix returned to its initial, saturated state. Results corresponding to the first and tenth fracture realisations are shown in Figure A2-6 through Figure A2-9.

The evolution of liquid pressure in the bentonite is considered for 24 separate locations within each of the deposition holes using realisation two of the stochastic fracture network. A schematic of these locations, and the nomenclature used, is shown in Figure 5-8. Corresponding figures for the evolution of pressure at each of these locations is presented in Figure 5-9 through Figure 5-13, each considering a separate deposition hole. As expected, pressure increases in the outer skin of the bentonite occur first, with pressures recovering later towards the centre of the bentonite. As discussed previously in this section, pressure recovery in deposition hole KO0018G01 (Figure 5-12) is slow, corresponding to the limited groundwater directly available for resaturation. Equivalent results for the first realisation of the stochastic fracture network are shown in Appendix 2, Figure A2-10 through Figure A2-14, with the tenth realisation shown in Figure A2-15 through Figure A2-19.

(a) - t = 0 years   **(b) - t = 0.1 years**

(c) - t = 0.5 years   **(d) - t = 1.0 years**

(e) - t = 10 years   **(f) - t = 100 years**

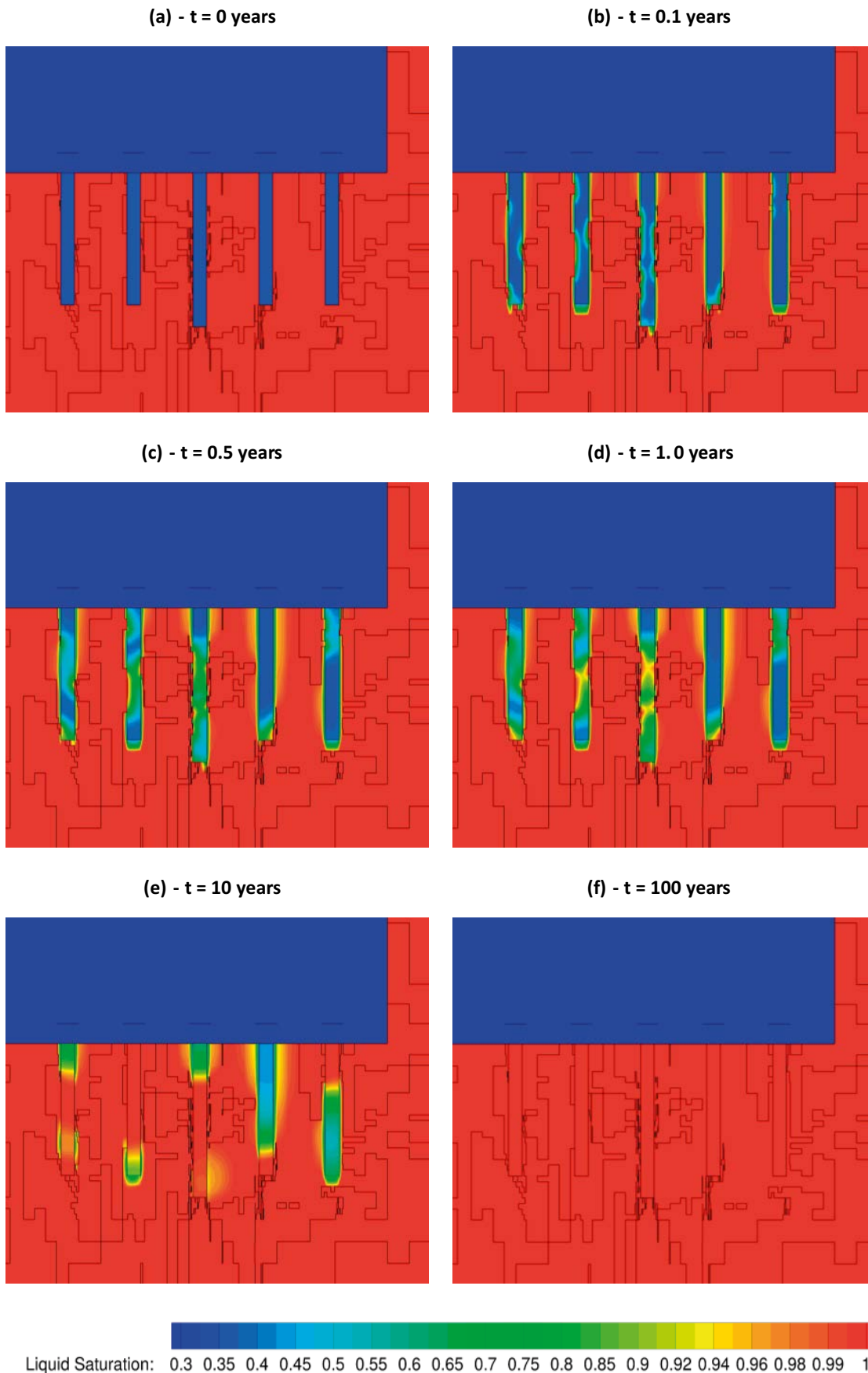Pressure: -50 -20 -10 -5 -1 -0.5 -0.2 -0.1 0 0.1 0.2 0.5 1 1.5
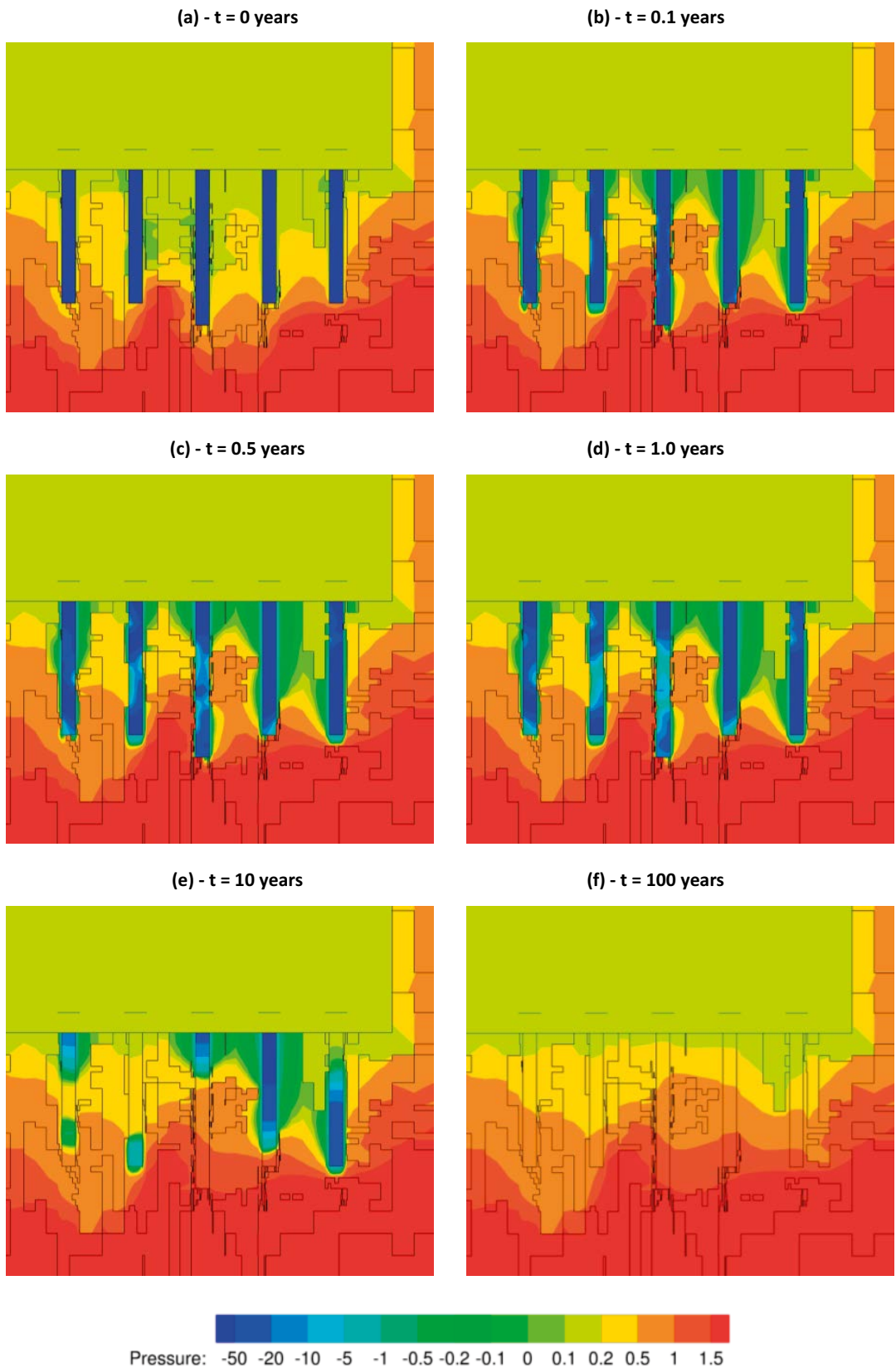
Figure 5-4. *Evolution of pressure (Pa) within the bentonite for a vertical slice including the deposition holes. Results are shown for the second realisation of the stochastic fracture network.*
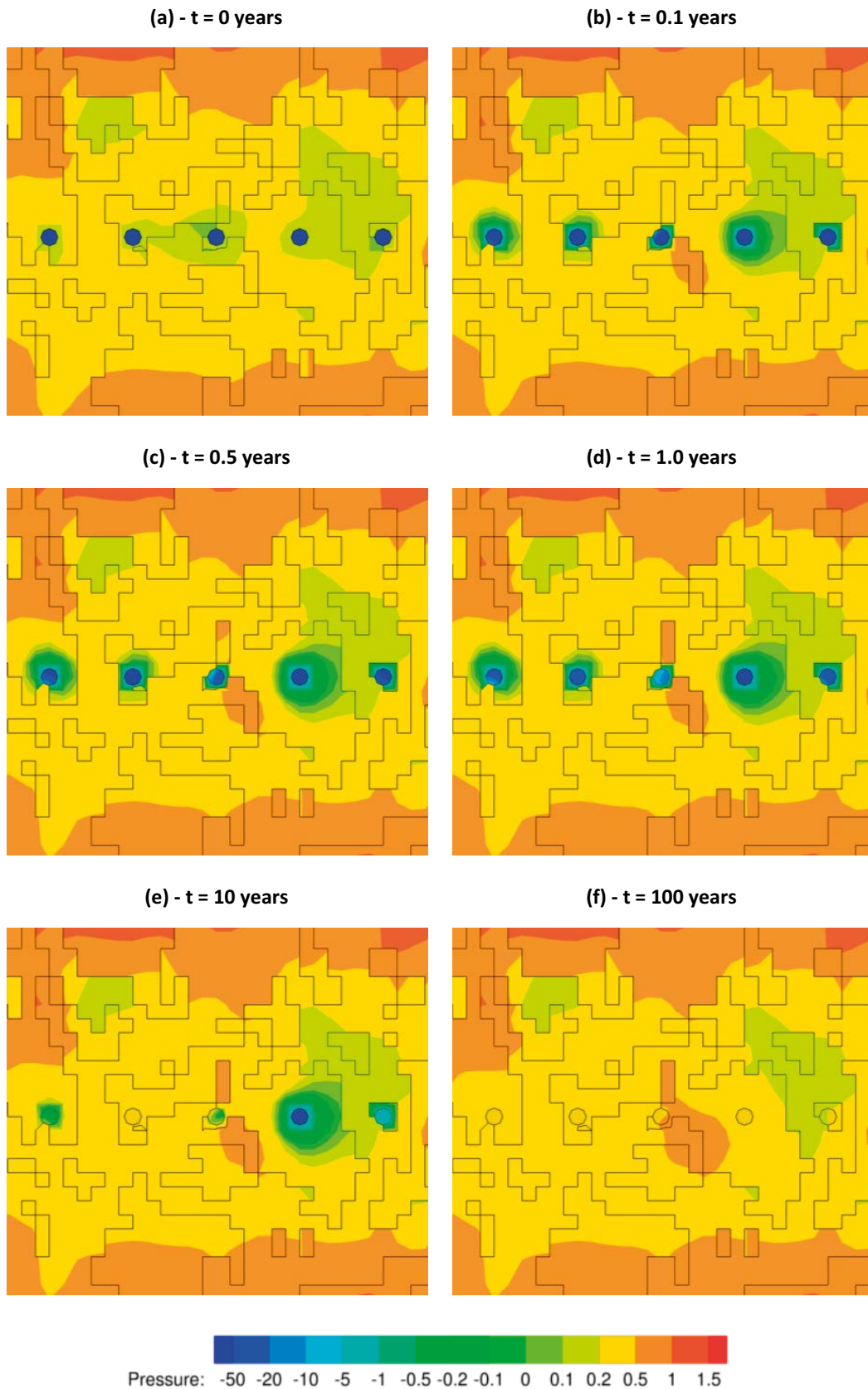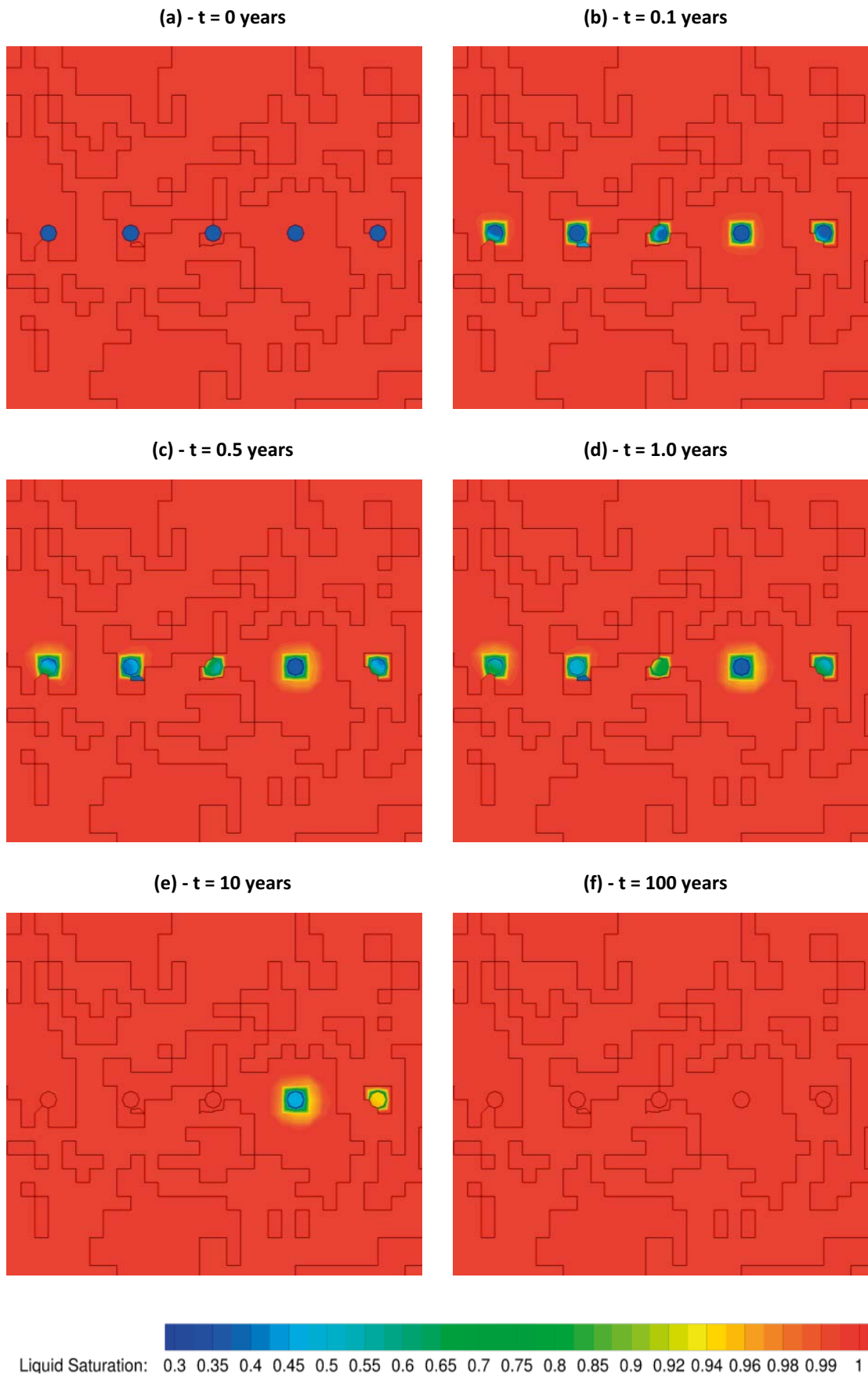
Figure 5-5. *Evolution of pressure (Pa) within the bentonite across a horizontal slice at −418 m elevation. Results are shown for the second realisation of the stochastic fracture network.*

(a) - t = 0 years

(b) - t = 0.1 years

(c) - t = 0.5 years

(d) - t = 1.0 years

(e) - t = 10 years

(f) - t = 100 years

Liquid Saturation: 0.3 0.35 0.4 0.45 0.5 0.55 0.6 0.65 0.7 0.75 0.8 0.85 0.9 0.92 0.94 0.96 0.98 0.99 1

Figure 5-6. *Evolution of saturation within the bentonite for a vertical slice including the deposition holes. Results are shown for the second realisation of the stochastic fracture network.*

(a) - t = 0 years

(b) - t = 0.1 years

(c) - t = 0.5 years

(d) - t = 1.0 years

(e) - t = 10 years

(f) - t = 100 years

Liquid Saturation: 0.3 0.35 0.4 0.45 0.5 0.55 0.6 0.65 0.7 0.75 0.8 0.85 0.9 0.92 0.94 0.96 0.98 0.99 1

Figure 5-7. Evolution of saturation within the bentonite across a horizontal slice at −418 m elevation. Results are shown for the second realisation of the stochastic fracture network.
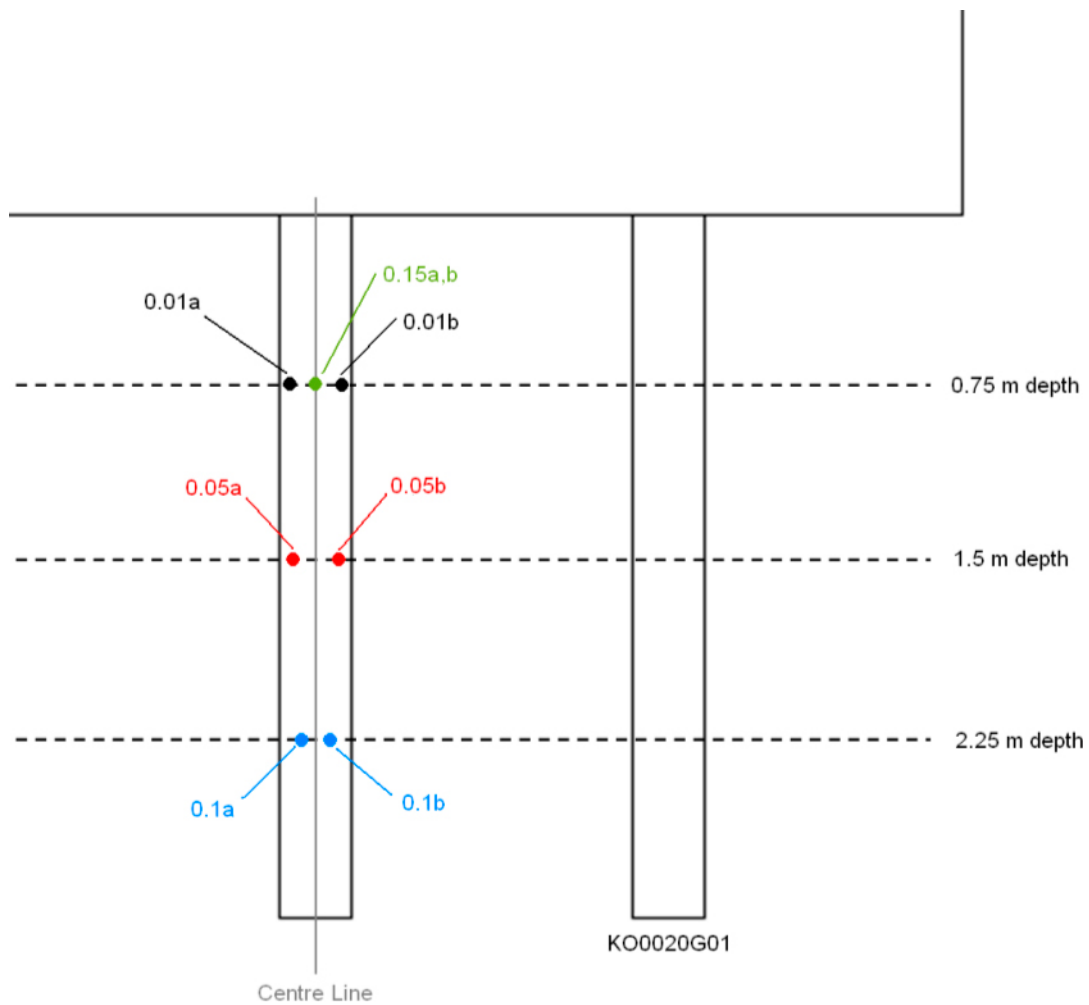
Figure 5-8. *Schematic illustrating monitored points within the bentonite, 0.01 m, 0.05 m, 0.1 m, and 0.15 m from the deposition borehole wall. All points are evaluated at all depths for all five deposition holes considered. Pressure evolutions within the bentonite at these locations are shown in Figure 5-9 through Figure 5-13.*
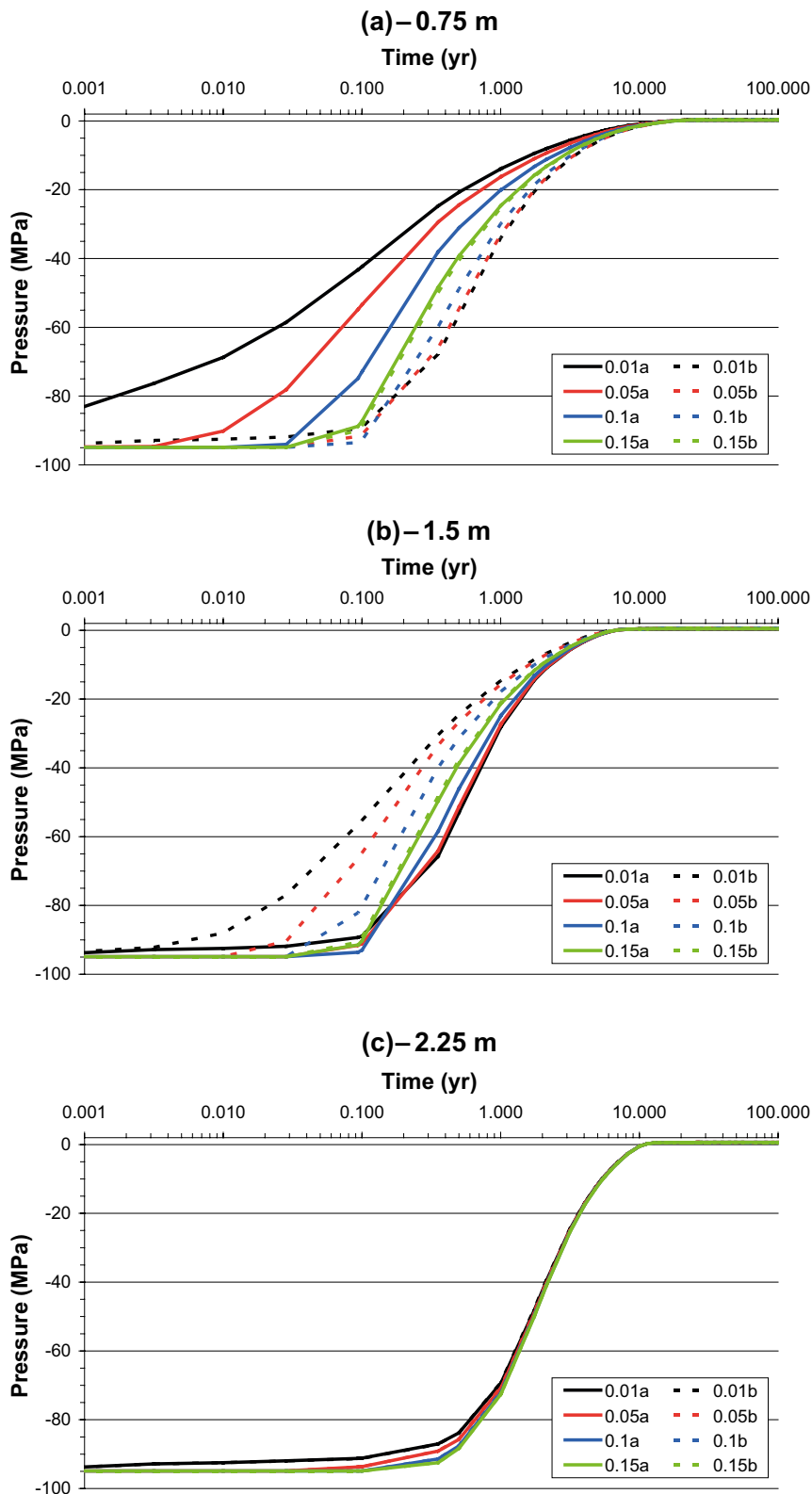
Figure 5-9. *Pressure within the bentonite 0.01 m, 0.05 m, 0.1 m, and 0.15 m from the deposition borehole wall. Results are shown for a slice parallel to the boreholes, with "a" and "b" distances denoting direction from the edge of the deposition hole. The pressure curves shown correspond to the second realisation of the stochastic fracture network. Figures (a, b, c) are for borehole KO0014G01 at depths of 0.75 m, 1.5 m and 2.25 m respectively.*
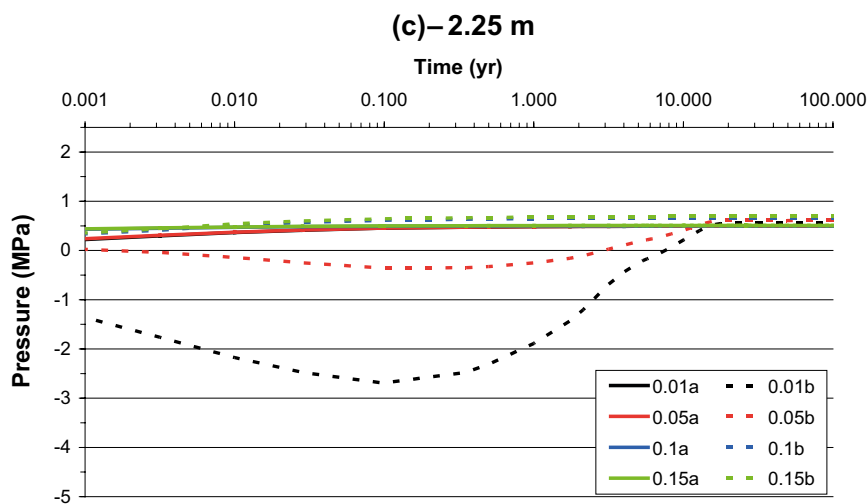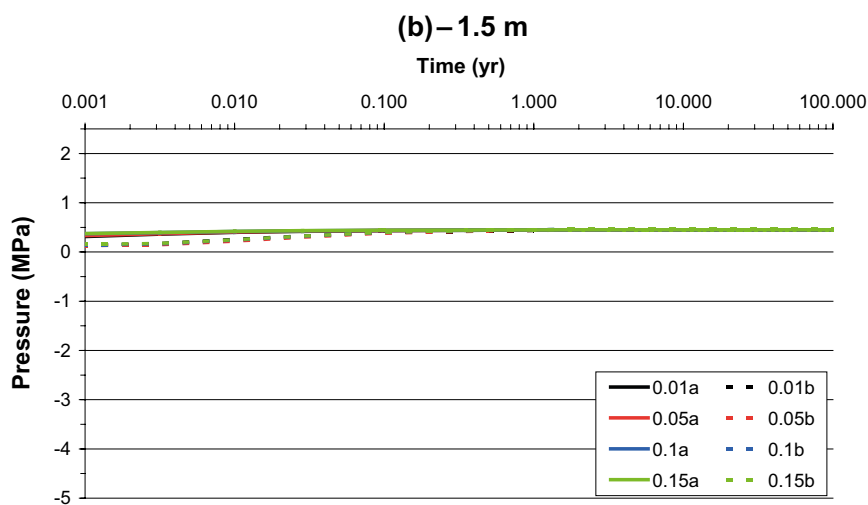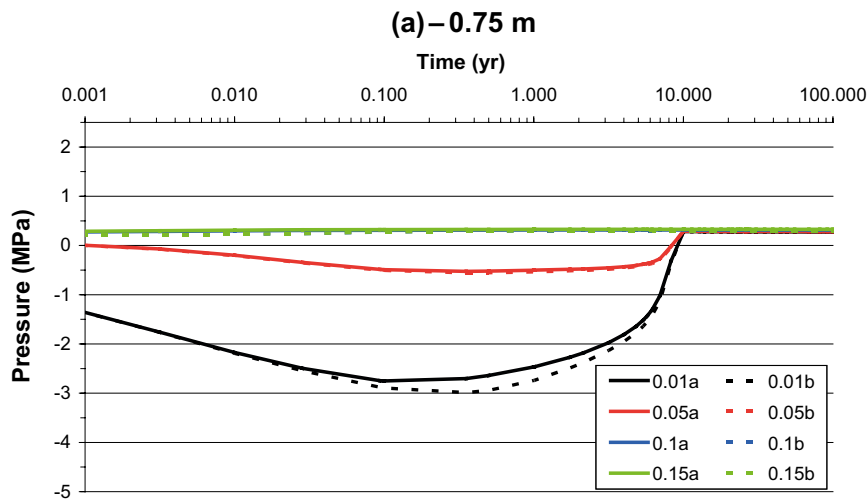
(a) – 0.75 m

(b) – 1.5 m

(c) – 2.25 m
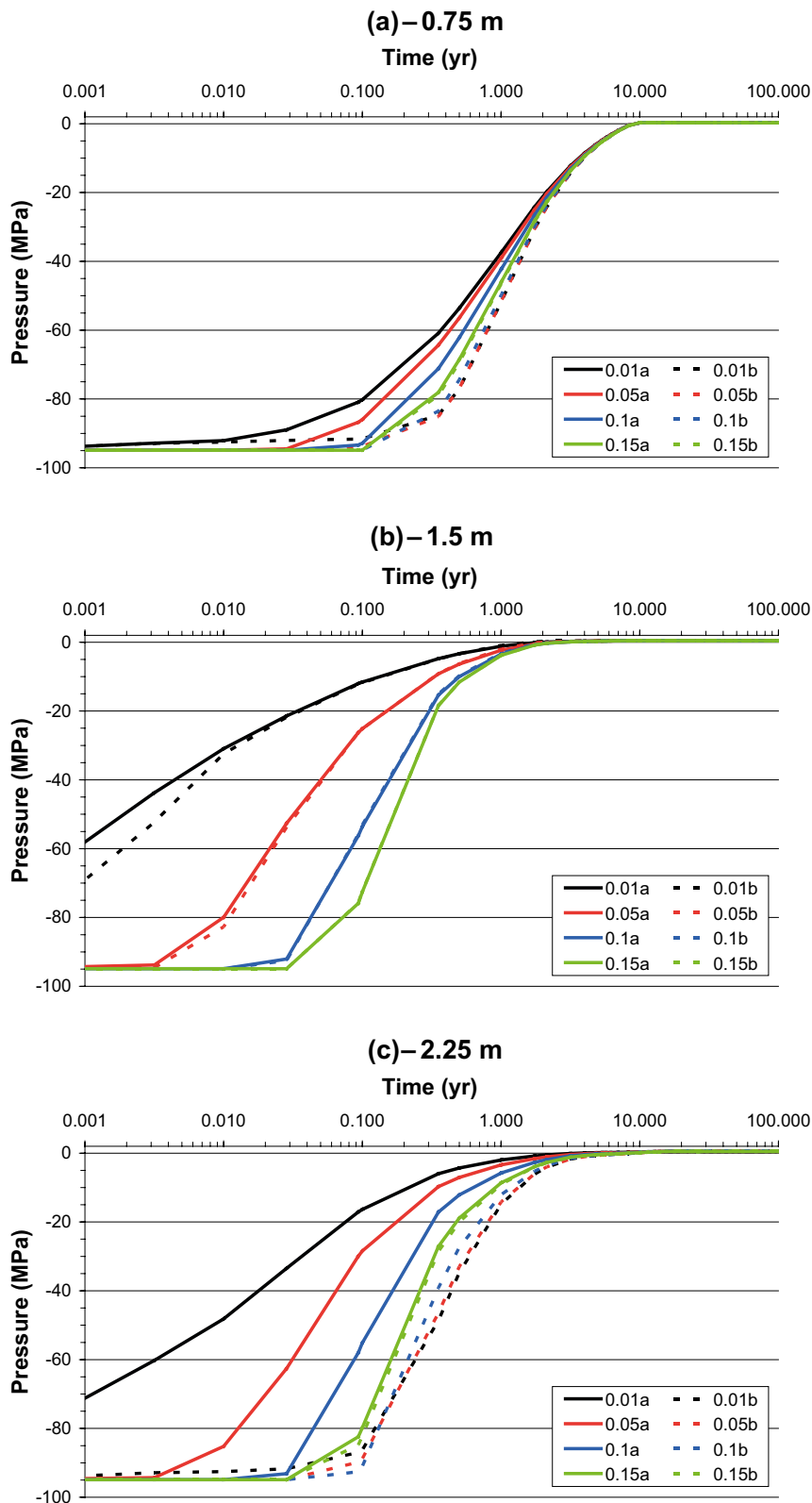
Figure 5-10. *Pressure within the bentonite 0.01 m, 0.05 m, 0.1 m, and 0.15 m from the deposition borehole wall. Results are shown for a slice parallel to the boreholes, with "a" and "b" distances denoting direction from the edge of the deposition hole. The pressure curves shown correspond to the second realisation of the stochastic fracture network. Figures (a, b, c) are for borehole KO0015G01 at depths of 0.75 m, 1.5 m and 2.25 m respectively.*
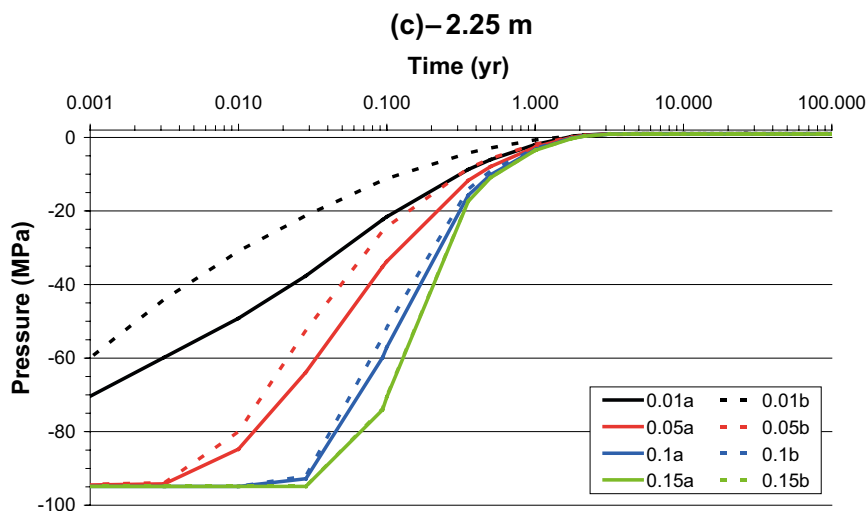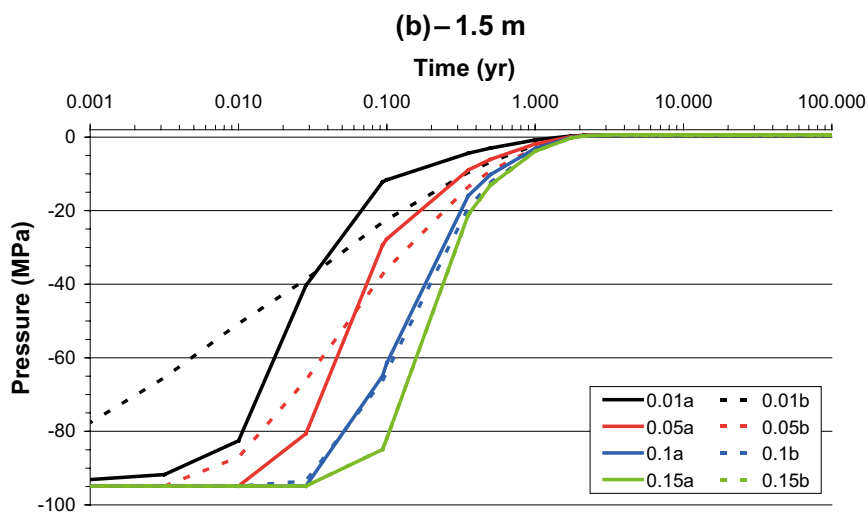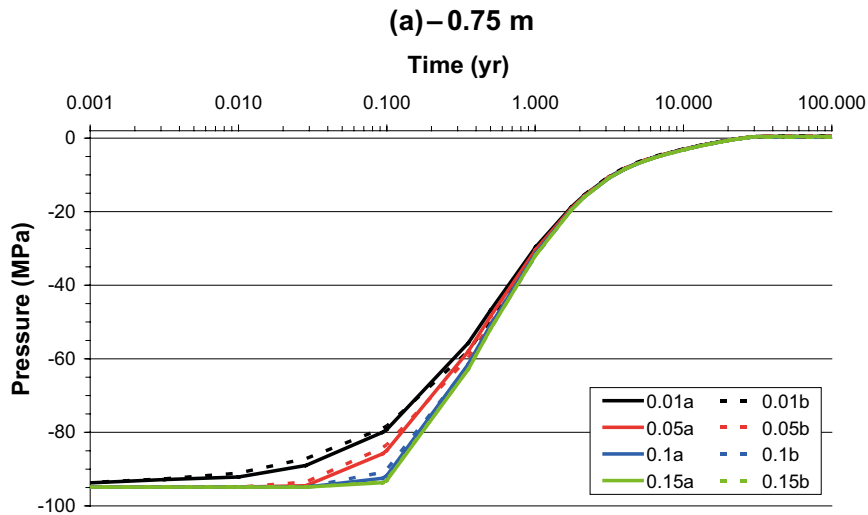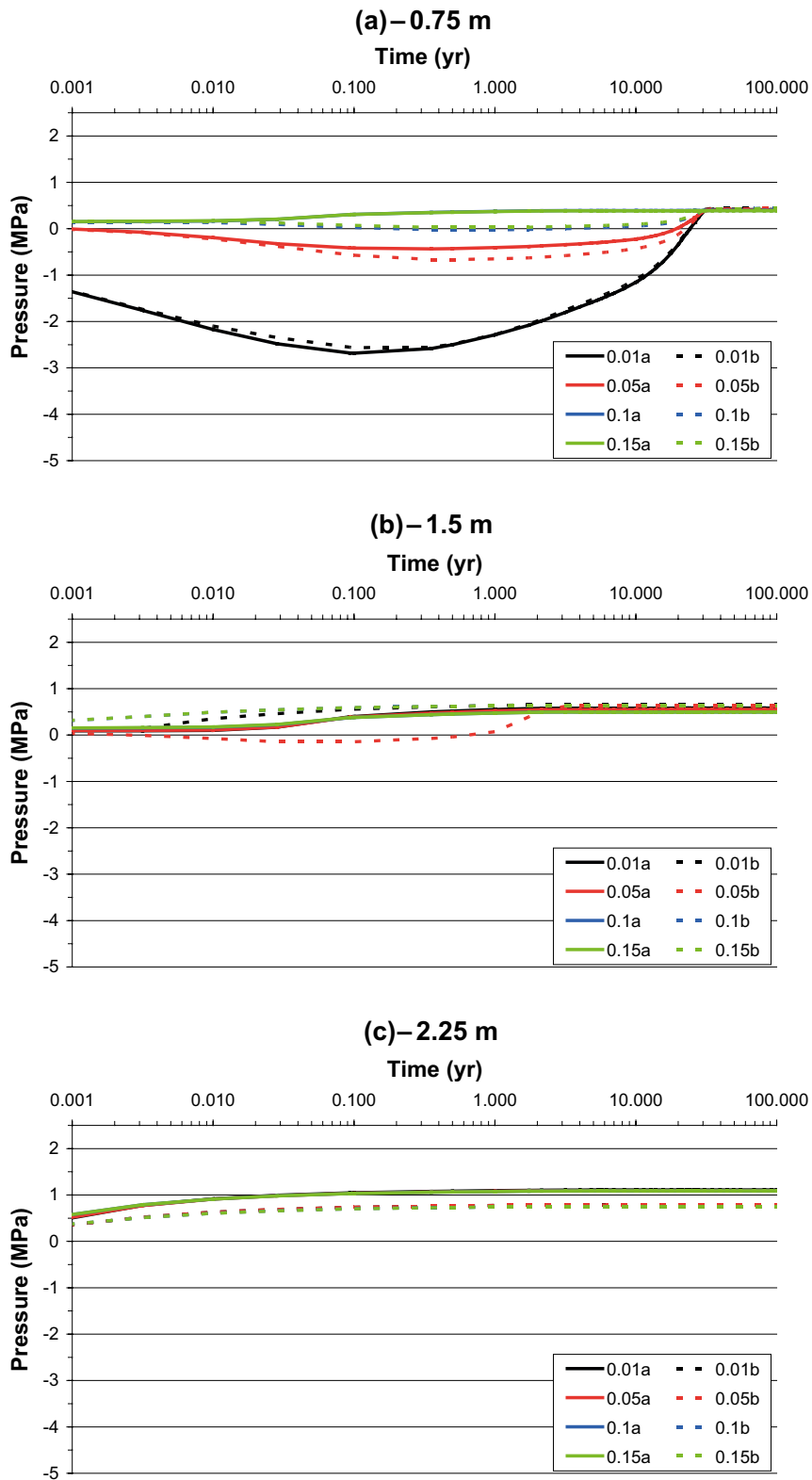
Figure 5-11. *Pressure within the bentonite 0.01 m, 0.05 m, 0.1 m, and 0.15 m from the deposition borehole wall. Results are shown for a slice parallel to the boreholes, with "a" and "b" distances denoting direction from the edge of the deposition hole. The pressure curves shown correspond to the second realisation of the stochastic fracture network. Figures (a, b, c) are for borehole KO0017G01 at depths of 0.75 m, 1.5 m and 2.25 m respectively.*
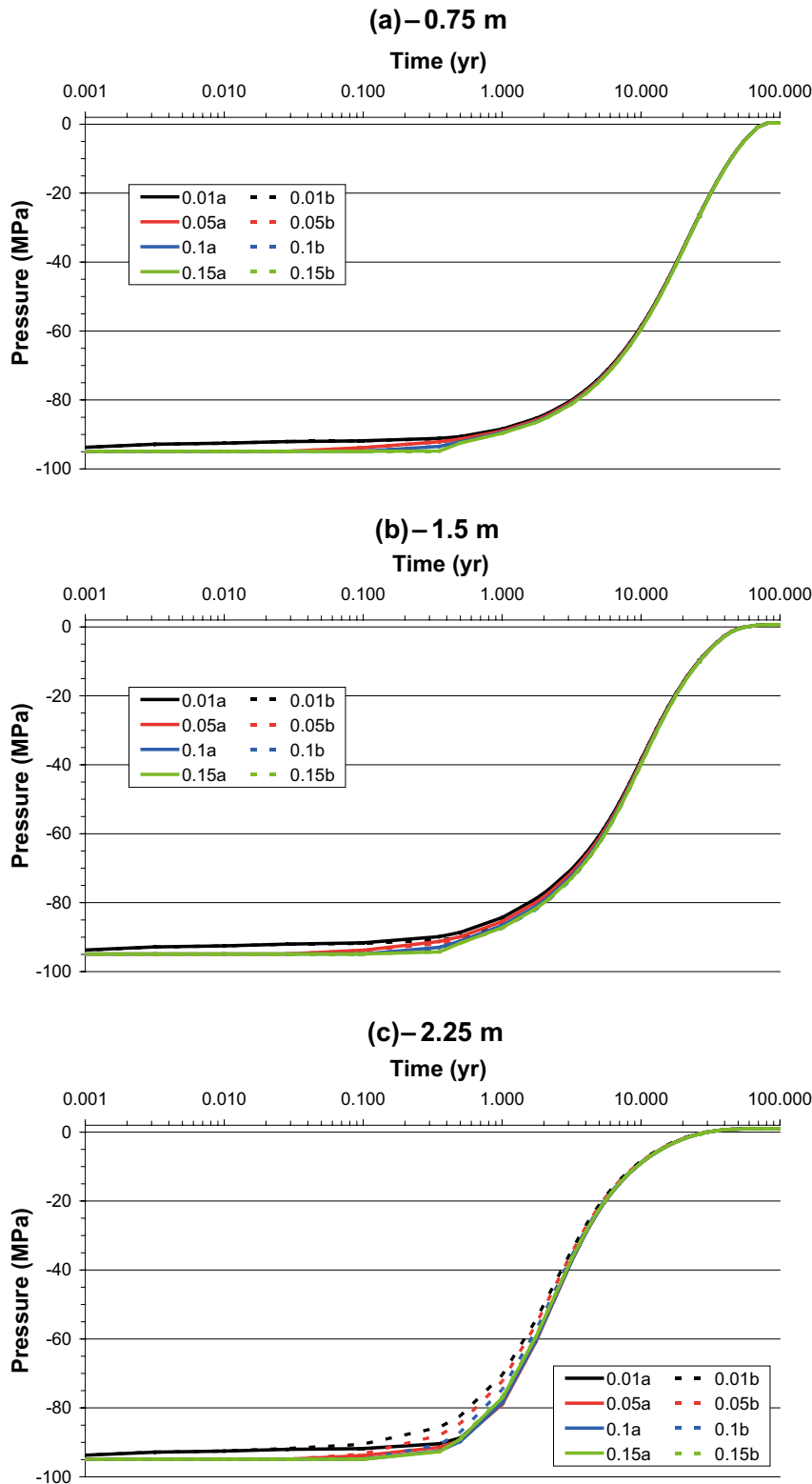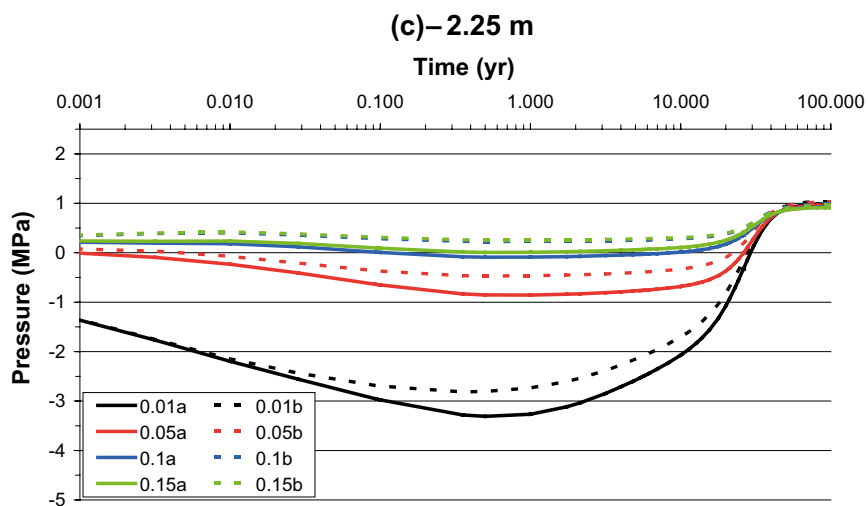
Figure 5-12. *Pressure within the bentonite 0.01 m, 0.05 m, 0.1 m, and 0.15 m from the deposition borehole wall. Results are shown for a slice parallel to the boreholes, with "a" and "b" distances denoting direction from the edge of the deposition hole. The pressure curves shown correspond to the second realisation of the stochastic fracture network. Figures (a, b, c) are for borehole KO0018G01 at depths of 0.75 m, 1.5 m and 2.25 m respectively.*
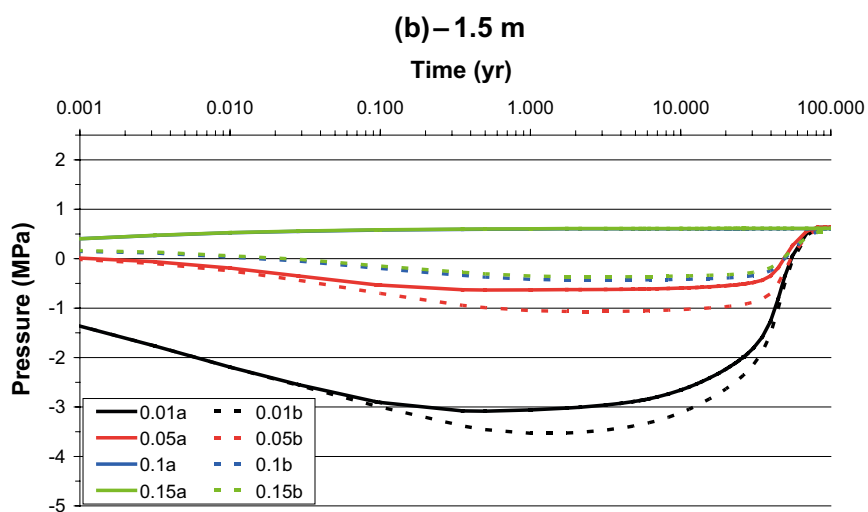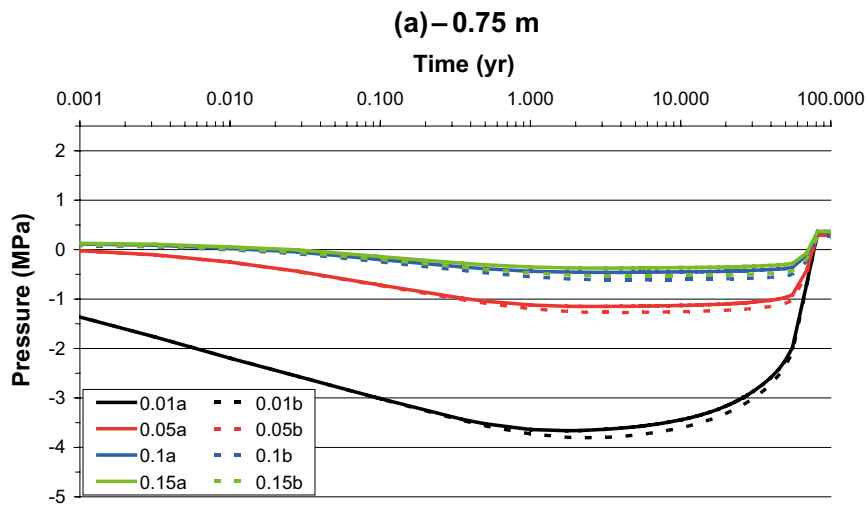
(a) – 0.75 m

(b) – 1.5 m

(c) – 2.25 m
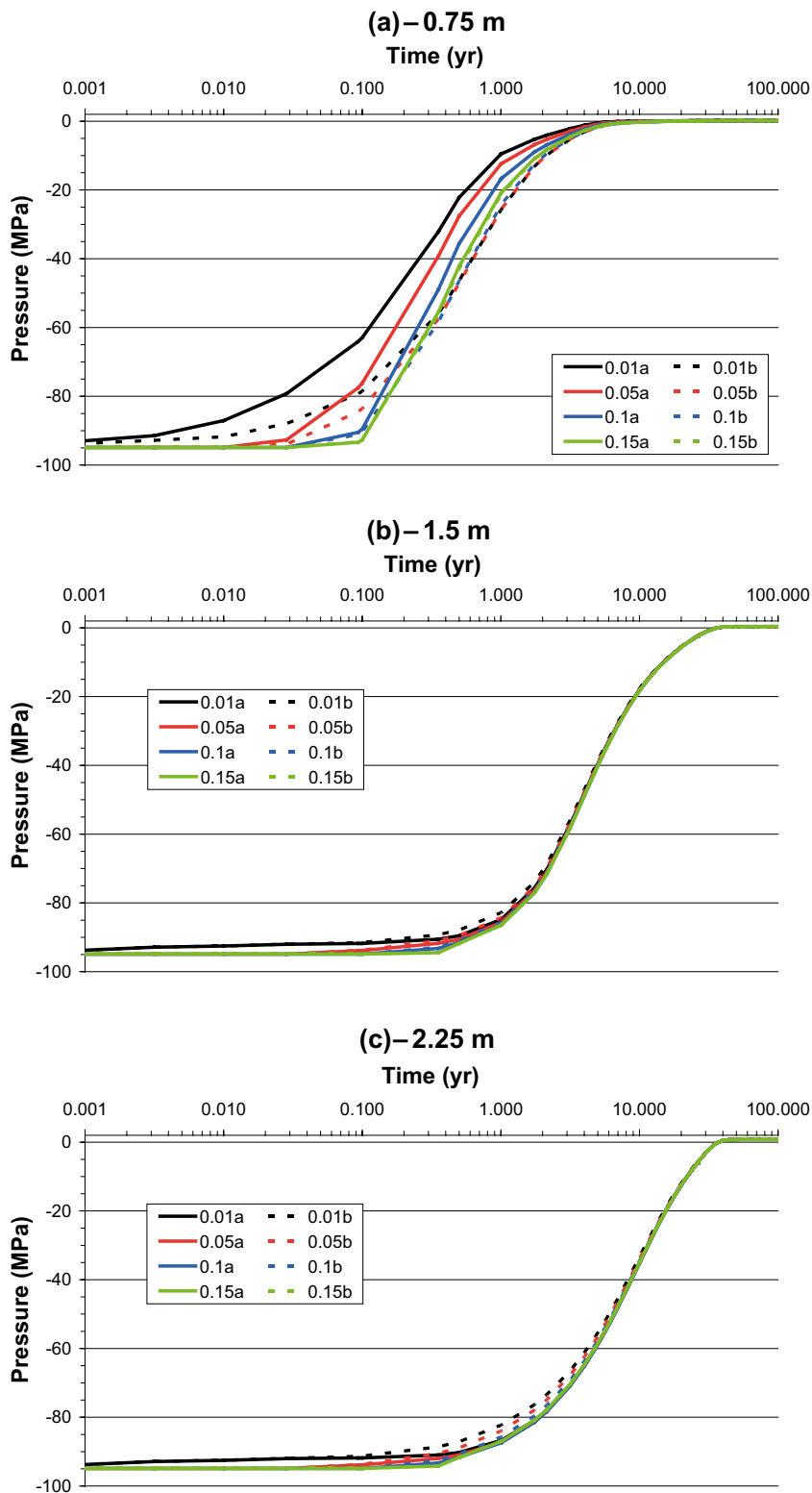
Figure 5-13. *Pressure within the bentonite 0.01 m, 0.05 m, 0.1 m, and 0.15 m from the deposition borehole wall. Results are shown for a slice parallel to the boreholes, with "a" and "b" distances denoting direction from the edge of the deposition hole. The pressure curves shown correspond to the second realisation of the stochastic fracture network. Figures (a, b, c) are for borehole KO0020G01 at depths of 0.75 m, 1.5 m and 2.25 m respectively.*

The evolution of liquid pressure in the bedrock is considered for 24 or 27 separate locations local to each of the deposition holes, using realisation two of the stochastic fracture network. A schematic of these locations, and the nomenclature used, is shown in Figure 5-14. The bedrock local to each deposition hole is analysed at a distance of 0.01 m, 0.05 m, 0.1 m and 0.15 m. In addition, for deposition holes KO0014G01, and KO0020G01, an additional point, 1 m away from the five deposition holes is considered. Results for each of the five deposition holes are shown in Figure 5-15 through Figure 5-19. Generally, pressure changes are greatest local to the deposition holes, with no noticeable change in pressures observed at a distance of 1 m. The liquid saturation is a function of the capillary pressure Function (3-7), and for gas pressures typical of those observed during resaturation of the bentonite a liquid pressure of −3 MPa equates to a liquid saturation c. 40 %; a liquid pressure of −1 MPa equates to a liquid saturation c. 80 %; and liquid pressure of –0.5 MPa equates to a liquid saturation c. 90 % within the rock matrix. From Figure 5-15 through Figure 5-19 the desaturated zone around the deposition holes can be estimated and is consistently simulated up to 5 cm from the deposition hole; persisting for up to a few tens of years. Equivalent results for the first realisation of the stochastic fracture network are shown in Appendix 2, Figure A2-20 through Figure A2-24, with the tenth realisation shown in Figure A2-25 through Figure A2-29.
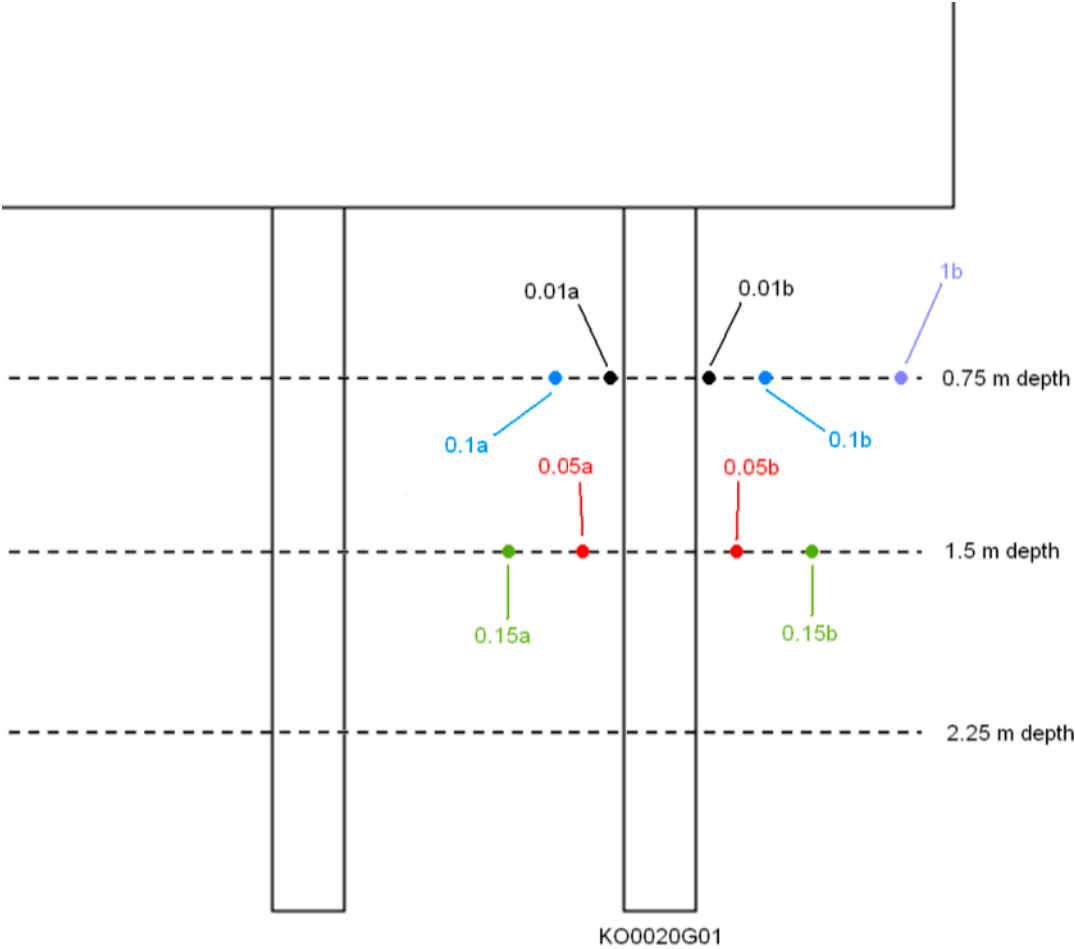
Figure 5-14. *Schematic illustrating monitored points within the bedrock, for pressure evolutions shown in Figure 5-15 through Figure 5-19.*
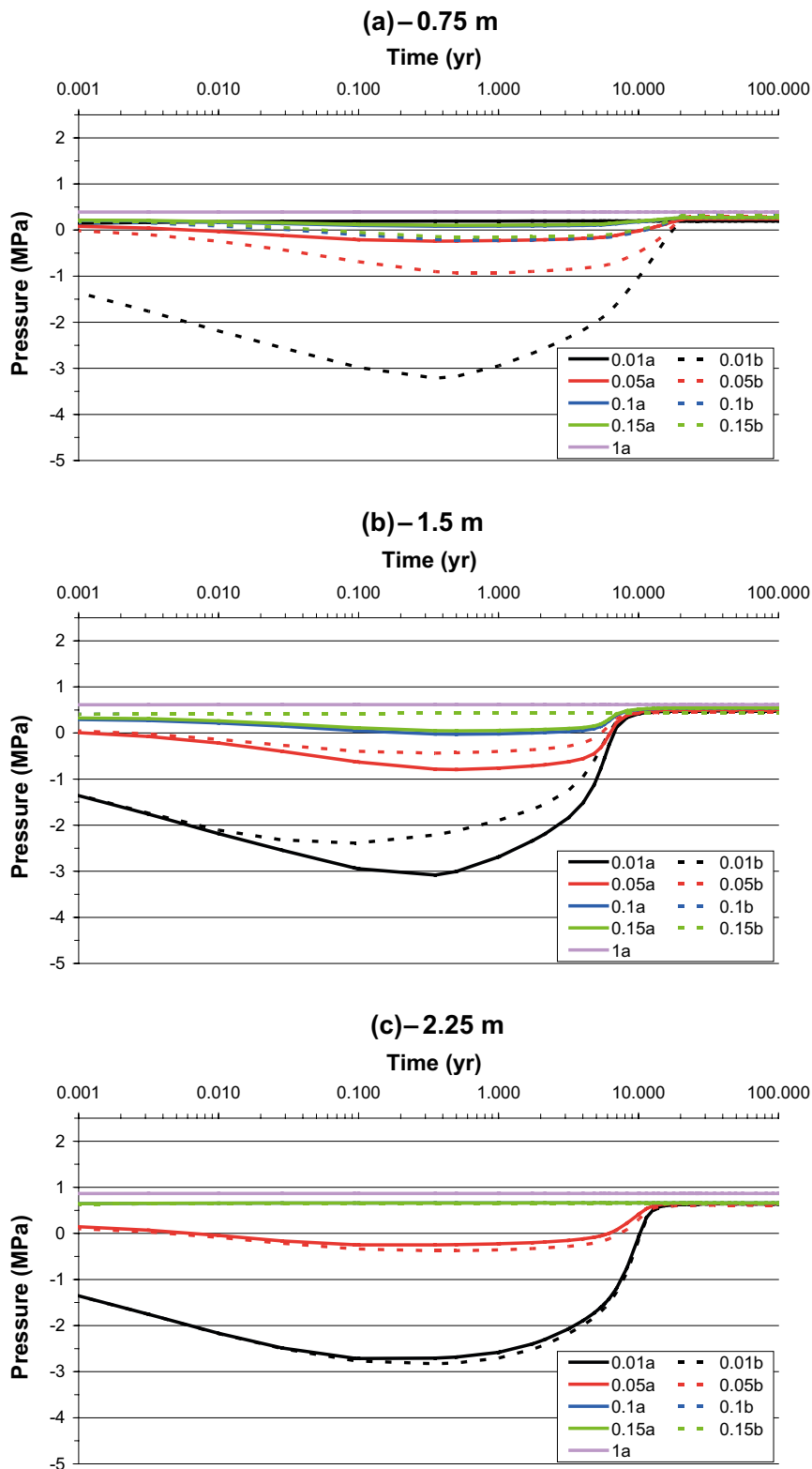
Figure 5-15. *Pressure within the bedrock 0.01 m, 0.05 m, 0.1 m, 0.15 m, 1.0 m and 5.0 m (outward only) from the deposition borehole wall. Results are shown for a slice parallel to the boreholes, with "a" and "b" distances denoting direction from the edge of the deposition hole. The pressure curves shown correspond to the second realisation of the stochastic fracture network. Figures (a, b, c) are for borehole KO0014G01 at depths of 0.75 m, 1.5 m and 2.25 m respectively.*

Figure 5-16. *Pressure within the bedrock 0.01 m, 0.05 m, 0.1 m, 0.15 m, and 1.0 m from the deposition borehole wall. Results are shown for a slice parallel to the boreholes, with "a" and "b" distances denoting direction from the edge of the deposition hole. The pressure curves shown correspond to the second realisation of the stochastic fracture network. Figures (a, b, c) are for borehole KO0015G01 at depths of 0.75 m, 1.5 m and 2.25 m respectively.*

(a) – 0.75 m

(b) – 1.5 m

(c) – 2.25 m

Figure 5-17. *Pressure within the bedrock 0.01 m, 0.05 m, 0.1 m, 0.15 m, and 1.0 m from the deposition borehole wall. Results are shown for a slice parallel to the boreholes, with "a" and "b" distances denoting direction from the edge of the deposition hole. The pressure curves shown correspond to the second realisation of the stochastic fracture network. Figures (a, b, c) are for borehole KO0017G01 at depths of 0.75 m, 1.5 m and 2.25 m respectively.*

Figure 5-18. *Pressure within the bedrock 0.01 m, 0.05 m, 0.1 m, 0.15 m, and 1.0 m from the deposition borehole wall. Results are shown for a slice parallel to the boreholes, with "a" and "b" distances denoting direction from the edge of the deposition hole. The pressure curves shown correspond to the second realisation of the stochastic fracture network. Figures (a, b, c) are for borehole KO0018G01 at depths of 0.75 m, 1.5 m and 2.25 m respectively.*

(a) – 0.75 m

(b) – 1.5 m

(c) – 2.25 m
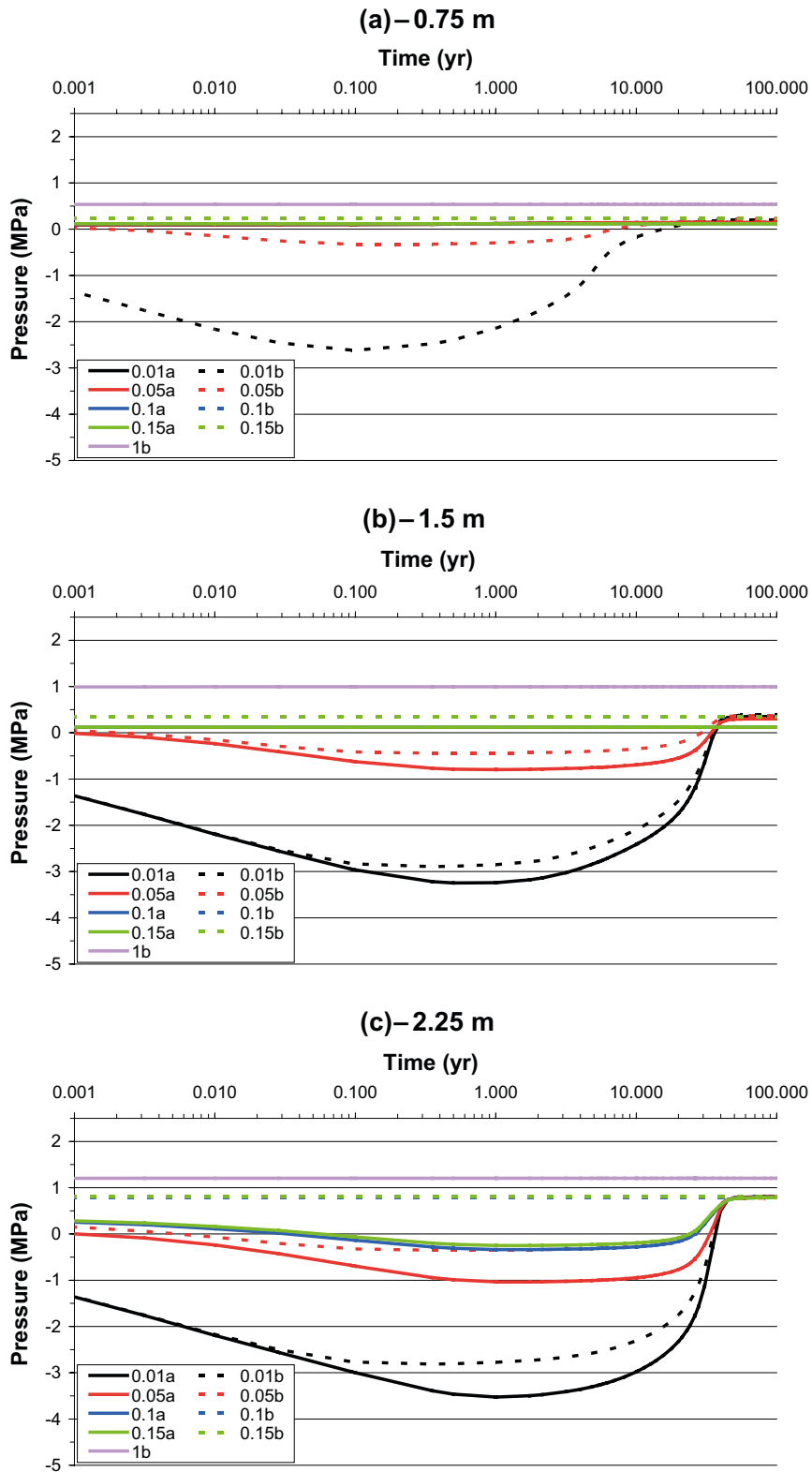
Figure 5-19. *Pressure within the bedrock 0.01 m, 0.05 m, 0.1 m, 0.15 m, 1.0 m and 5.0 m (outward only) from the deposition borehole wall. Results are shown for a slice parallel to the boreholes, with "a" and "b" distances denoting direction from the edge of the deposition hole. The pressure curves shown correspond to the second realisation of the stochastic fracture network. Figures (a, b, c) are for borehole KO0020G01 at depths of 0.75 m, 1.5 m and 2.25 m respectively.*

5.3   Sensitivity case: a homogeneous bedrock description

The upscaling of the discrete fracture network provides an equivalent porous media model of the fractured bedrock description. It is this upscaled representation that has been used to provide results for the heterogeneous resaturation of the bentonite. For realisation 2 of the stochastic fracture network, a variant case is considered, using a homogeneous permeability throughout the bedrock. The permeability and porosity for this homogeneous simulation were taken as the geometric mean values from the upscaling of realisation 2 of the stochastic fracture network; calculated across the individual grid blocks intersected by a fracture. In this instance the geometric mean permeability is 1.99×10^{-17} m^2 and geometric mean porosity is 1.31×10^{-4}. Simulating the resaturation of the bentonite using these mean upscaled properties provides a comparison to the heterogeneous solutions shown in Section 5.2.

The times to 95 % liquid saturation for both the heterogeneous and homogeneous bedrock description are detailed in Table 5-2. The homogeneous case indicates bentonite saturation to reach this level within a period of approximately half a year. For the heterogeneous bedrock description, the bentonite resaturates significantly slower, and only after a period greater than 60 years does the bentonite resaturate in all of the holes. Figure 5-20 illustrates the time evolution of bentonite saturation for both of these TOUGH2 simulations. For a homogeneous bedrock description, resaturation initiates at the bottom of each borehole, with the time-evolution of saturation orientated with the hydraulic gradient (i.e. directed towards the tunnel wall). In the homogeneous case, the outer surface of the bentonite is seen to completely resaturate very quickly, c. 0.1 years. In the heterogeneous case, the saturation is significantly slower.

Although times to 95 % saturation are rapid for the homogeneous model, to reach full saturation can take significantly longer, of order tens of years. This is a consequence of pockets of low gas saturation becoming trapped within the bentonite, as illustrated in Figure 5-21. These localised regions of gas become immobile due to the small relative permeabilities associated with the gas phase at low saturations (see Equation (3-9)). Consequently, it can take significant time for the remaining gas to eventually dissipate from the bentonite. In contrast, the heterogeneous wetting of the bentonite forms pathways within the bentonite for the gas phase to migrate towards the tunnel. In this case, the long times to saturation are a consequence of the restricted groundwater supply through the heterogeneous bedrock description.

Table 5-2. Time to achieve 95 % liquid saturation in each of the five deposition holes. Simulations use the second realisation of the stochastic fracture network, comparing the heterogeneous bedrock with an equivalent homogeneous description.

Bedrock Description	KO0020G01	KO0018G01	KO0017G01	KO0015G01	KO0014G01
Heterogeneous	32.8	62.3	25.2	12.1	16.7
Homogeneous	0.6	0.6	0.6	0.6	0.6

(a) – t = 0 years **(b) – t = 0 years**

(c) – t ~ 1 day **(d) – t ~ 1 day**

(e) – t = 0.1 years **(f) – t = 0.1 years**

Liquid Saturation: 0.3 0.35 0.4 0.45 0.5 0.55 0.6 0.65 0.7 0.75 0.8 0.85 0.9 0.95 1
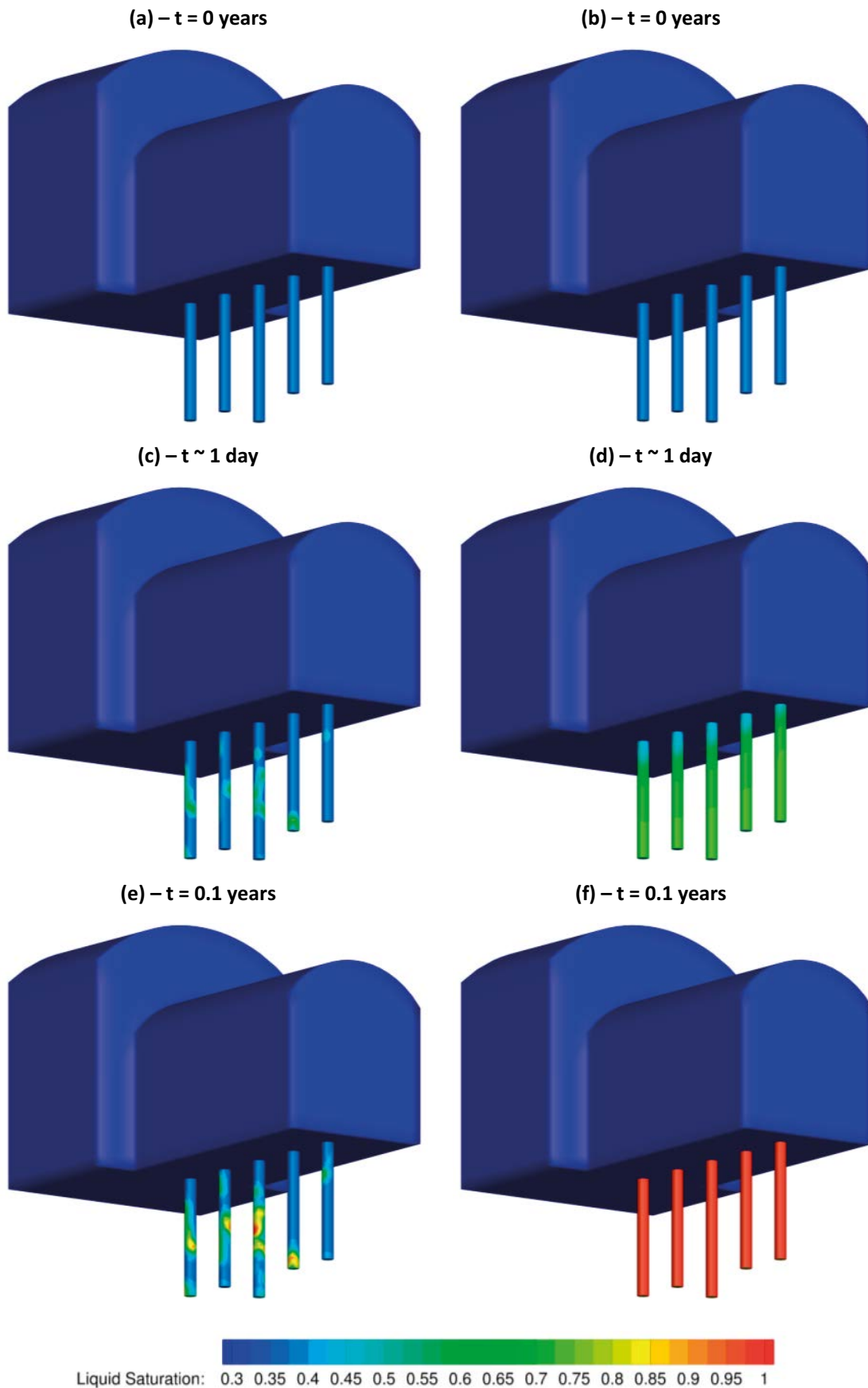
Figure 5-20. *Comparison of bentonite saturation with time through an equivalent homogeneous bedrock (b, d, f) and a heterogeneous bedrock (a, c, e), using the second realisation of the stochastic fracture network.*
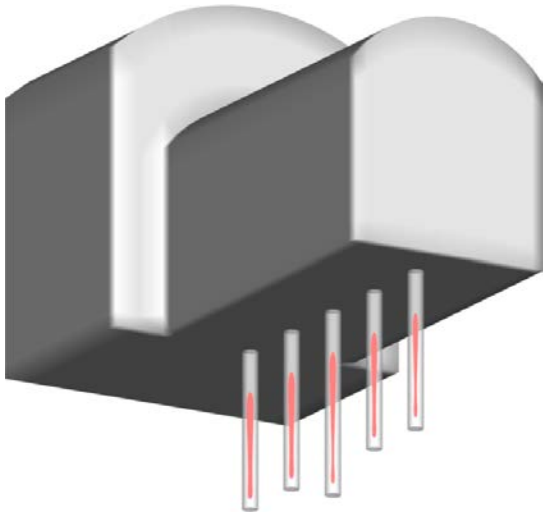
Figure 5-21. Isosurfaces within each of the deposition holes indicating 2 % gas saturation after 1 year. Results are for the equivalent homogeneous bedrock model for realisation 2 of the stochastic fracture network.

5.4 Sensitivity case: rock matrix effects

In the absence of fracture intersections, the low permeability rock matrix significantly constrains the resaturation of the bentonite. Figure 5-22 illustrates a local slice to the deposition holes, parallel to the TASO tunnel, for realisation 2 of the stochastic fracture network after 10 years. Significant regions of desaturation of the rock matrix are observed, especially local to deposition hole KO0018G01. This is a consequence of the large suction pressures within the bentonite, removing groundwater from the surrounding rock matrix which cannot be readily supplied by the fracture network.

The effects of the rock matrix permeability are considered in this section by two variant cases, with simulations performed for a cut down model, containing deposition hole KO0015G01 only:

- The rock matrix permeability is an order of magnitude greater than the base case (10^{-20} m^2)

- The rock matrix permeability is two orders of magnitude greater than the base case (10^{-19} m^2)

The resaturation model is based on realisation 2 of the stochastic fracture network, with rock matrix properties assigned in the upscaled system for grid blocks where the fracture network provides an equivalent permeability below the rock matrix value. Results are presented in Figure 5-23 and Figure 5-24 for times: 0 years, 0.1 years, 1 year and 10 years, with time to 95 % and 99 % saturation detailed in Table 5-3. In the base case, the resaturation of the bentonite is significantly constrained by the rock matrix, with the bentonite still not fully saturated after 10 years. In contrast, when the permeability is increased by an order of magnitude, 99 % saturation of the bentonite is observed by 5 years. The resaturation time to 99 % for the second variant, with a rock matrix permeability of 10^{-19} m^2, is reduced by a further 0.4 years. When considering the times to 95 % liquid saturation, the increase in rock matrix permeability to 10^{-19} m^2 has a greater effect.

Table 5-3. Times for 95 % and 99 % saturation to occur in deposition hole KO0015G01 for the Base case, and two variants in the rock matrix permeability.

Rock matrix variant	Time (years)	
	95 % Saturation	99 % Saturation
Base Case		
Permeability = 10^{-21} m^2	11.7	13.5
Permeability = 10^{-20} m^2	2.2	4.8
Permeability = 10^{-19} m^2	0.6	4.4
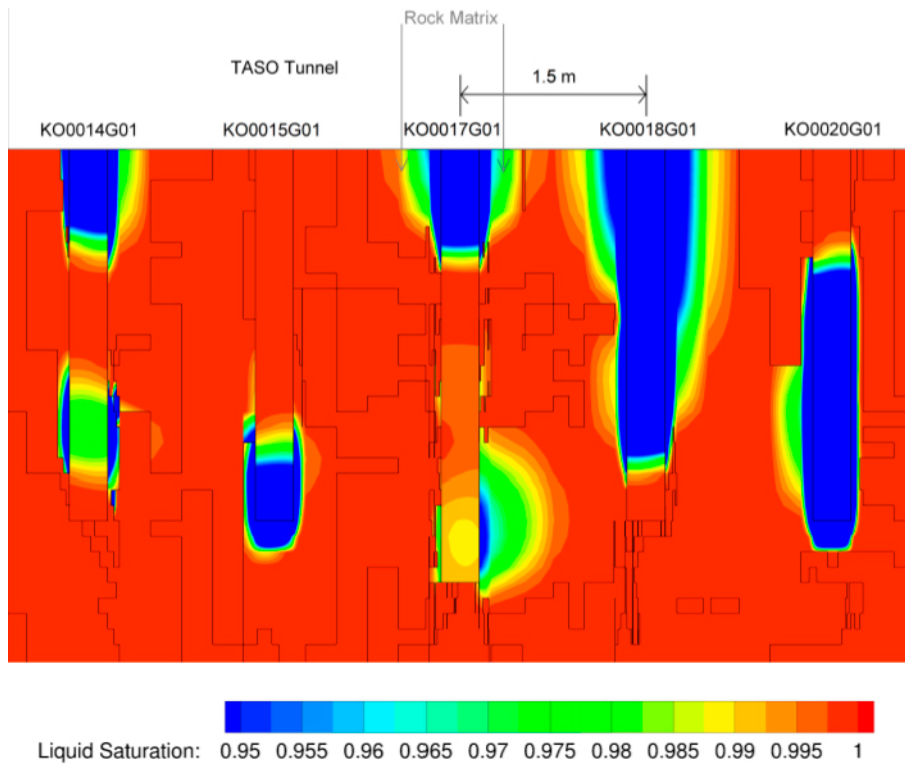
Figure 5-22. *Desaturation of the matrix after 10 years. Contours are shown for a vertical slice through each of the five deposition holes, for the second realisation of the stochastic fracture network.*
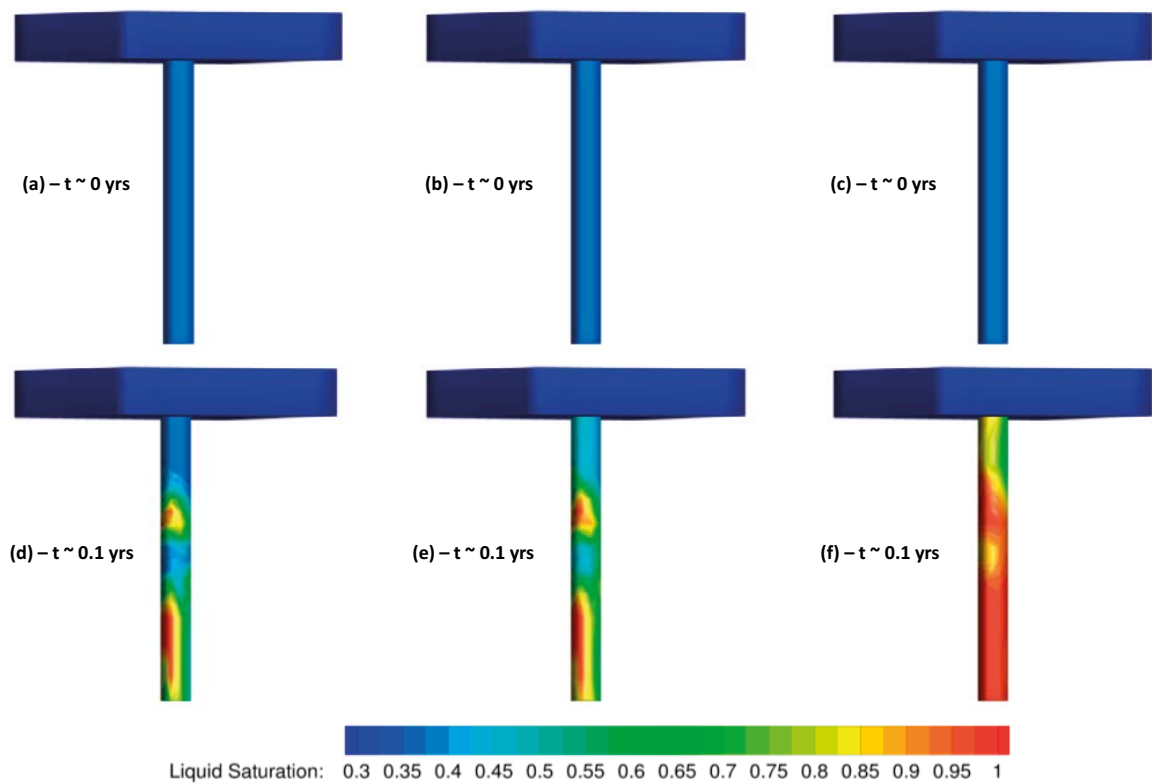
Figure 5-23. *Effects of varying the rock matrix permeability from a base case of 10^{-21} m^2 (a,d) to 10^{-20} m^2 (b,e) and 10^{-19} m^2 (c,f) for a cut down model of borehole KO0015G01 only. Results are shown at initial times (a,b,c) and after 0.1 years (d,e,f).*

(a) – t ~ 1.0 yrs

(b)– t ~ 1.0 yrs

(c) – t ~ 1.0 yrs

(d) – t ~ 10.0 yrs

(e) –t ~ 10.0 yrs

(f) – t ~ 10.0 yrs

Liquid Saturation: 0.3 0.35 0.4 0.45 0.5 0.55 0.6 0.65 0.7 0.75 0.8 0.85 0.9 0.95 1
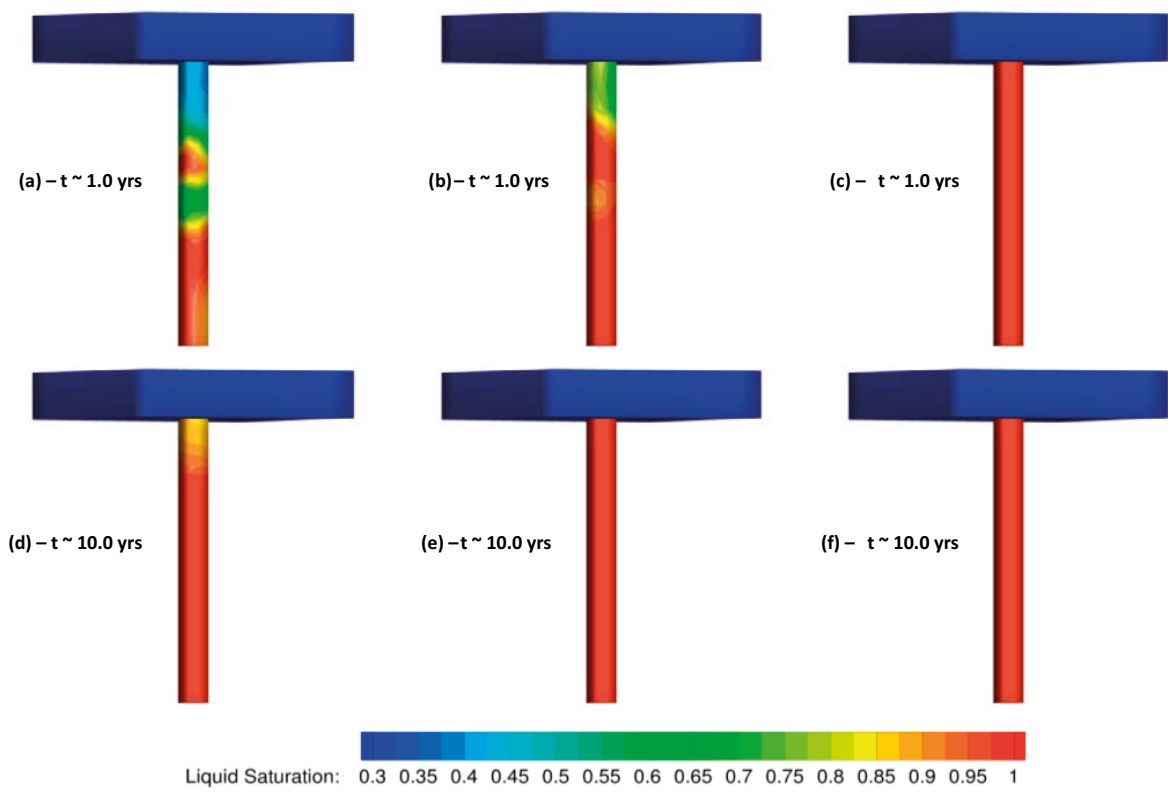
Figure 5-24. *Effects of varying the rock matrix permeability from a base case of 10^{-21} m^2 (a,d) to 10^{-20} m^2 (b,e) and 10^{-19} m^2 (c,f) for a cut down model of borehole KO0015G01 only. Results are shown after 1.0 years (a,b,c) and after 10.0 years (d,e,f).*

6　Discussion and conclusions

The safe disposal of higher-activity radioactive wastes utilise a multiple barrier concept to isolate wastes from the biosphere. Commonly, bentonite is proposed as a buffer material as part of an engineered barrier system (EBS) to surround Spent Fuel/High Level Waste disposal canisters. The Nuclear Decommissioning Authority (NDA) Radioactive Waste Management Directorate (RWMD) are considering using bentonite as part of engineered barrier systems for the disposal of high-level waste and spent fuel within a UK Geological Disposal Facility (GDF).

Through participating in the Äspö Engineered Barrier System Task Force, NDA RWMD intends to further the UK's capabilities by assisting in the development of modelling of coupled Thermal (T), Hydraulic (H), Mechanical (M) and Chemical (C) processes relevant to bentonite. In particular NDA RWMD aim to

- compare and verify techniques and processes developed for modelling the bedrock/bentonite interface with other teams participating in the Task Force,

- identify the important data used to parameterise the rock, to provide a basis for modelling resaturation,

- explore important parameter uncertainty and evaluate the consequences (e.g. rock matrix permeability),

- derive a methodology to integrate the approach taken to both the rock and bentonite,

- build confidence in the ability to model resaturation processes once data become available to compare to predictions, and

- develop methodologies to represent the interaction between the groundwater flow from the rock, and the resaturation of the bentonite material.

Modelling Task 8 and the BRIE at the Äspö HRL has demonstrated the feasibility of using a physically realistic approach to simulate the rock/bentonite interface. This approach explicitly represents the heterogeneity of the fractured bedrock, revealing significant differences to the 'homogeneous' assumptions commonly made to estimate bentonite resaturation. The work has demonstrated that a significantly longer period of time is potentially needed for complete resaturation of the bentonite in fractured rock, than can be estimated using a simplified homogeneous representation. In addition, when modelling the heterogeneity of the fractured bedrock, significant variations in the resaturation time exist

- between stochastic realisations of the fracture network, and

- between deposition holes located within an individual representation of the fracture network.

However, these conclusions depend on assumptions concerning the permeability of the "background rock" or rock matrix.

6.1　Evaluation of conceptual models and modelling approach

Conceptually, a modelling approach was adopted that explicitly represented the heterogeneity of the fractured bedrock, and its hydraulic interaction with the bentonite buffer. As such, two software packages have been used in the modelling of Task 8C:

- Task 8C1 uses the discrete fracture network (DFN) component of the CONNECTFLOW software package to calculate single-phase groundwater flow through the fractured bedrock explicitly. This DFN concept provides a powerful methodology, inherently reflecting the individual flow conduits in the fractured bedrock, and the available field data. Simulations predict the groundwater ingress to each of the five probe boreholes, requiring an accurate characterisation of the fractured host rock. Fracture networks were generated stochastically, with fractures sampled from probability density functions defining four properties: spatial distribution, fracture intensity, fracture orientation and fracture size. Uncertainties in these geometrical properties were analysed by considering ten realisations of the stochastic fracture network. For all realisations, individual fracture transmissivities

were correlated directly to the fracture size. This DFN representation, and subsequent calculation of inflows and pressure build up within the five boreholes of the BRIE, were based on a $(40 \text{ m})^3$ domain, with each simulation taking c. 45 minutes to complete.

- Task 8C2 uses TOUGH2 to simulate two-phase saline groundwater flow through an equivalent representation of the 8C1 bedrock. TOUGH2 was developed by Lawrence Berkeley National Laboratory, and is based on a continuum concept; providing the capability for simulating nonisothermal, multiphase fluid flows. To successfully capture the heterogeneous resaturation of bentonite emplaced within the overcored boreholes, an accurate continuum representation of each of the stochastic realisations of the fracture network was required. The CONNECTFLOW software package was used to calculate equivalent porous medium block properties, providing a permeability tensor and kinematic porosity for each grid block of the TOUGH2 mesh. Grid blocks which contained no connected fractures were treated as rock matrix, with appropriate properties set. The hydration models considered as part of Task 8C2 have significantly greater numerical requirements compared to 8C1, with extensive refinement of the TOUGH2 mesh required to resolve the saturation front. For computations to remain tractable, the model domain is reduced to consider a local region to the five boreholes. Despite this, simulations take a significant time, depending on the realisation considered.

Although the models developed as part of this study are specific to the BRIE at the Äspö HRL, the tools, techniques and methodologies considered are generic, and directly applicable to any future work carried out on UK specific issues for the simulation of hydration of emplaced bentonite by a surrounding fractured rock.

6.2 Lessons learned and implications for Task 8C objectives

6.2.1 Predictability with limited data

Predictions of inflows and resaturation rates within specific deposition holes of the BRIE are difficult due to uncertainties in the wider fracture network of the Äspö HRL. By considering multiple realisations of the fracture network uncertainties in the geometric and hydraulic properties defining the background DFN model can be quantified, with bounding values for inflow rates and resaturation times calculated. In this study, a single realisation was identified as providing the best match to the limited measured data available, and used as a Base Case from there on.

As well as the stochastic analysis of the DFN model parameters, sensitivity analysis of deterministic features should be considered. This study has shown the significant impact of rock matrix permeability on resaturation rates, and the following sensitivity cases (amongst others) are identified:

- Sensitivity to geometric and hydraulic properties of the deterministic features wfracture_01, wfracture_02 and NNW4.

- Large suction pressures within the bentonite form the driving force for bentonite resaturation. The sensitivity to the capillary pressure functions for the rock matrix, fractured rock, and bentonite should be considered.

- The sensitivity of the bentonite resaturation to the mobility of the gas phase is an important consideration. Alternative relative permeability functions for the rock matrix, fractured rock, and bentonite should be considered.

6.2.2 Decision on usage of a deposition hole position

A decision on usage of a deposition hole position can be made during various phases of the excavation process (e.g. after drilling the pilot borehole, or after overcoring to the full deposition hole). A selection criterion determining the suitability of a deposition hole position is difficult to define, but should consider (at least) the following two criteria:

- The total groundwater inflow to the borehole or deposition hole under open (atmospheric) conditions – this criteria will dominate for instances where the inflow is spread over a number of fractures intersecting the deposition hole and/or the rock matrix permeability is relatively high (i.e. of comparable magnitude to the fractures).

- The locations of groundwater ingress to the borehole or deposition hole – this criteria will become increasingly significant as the inflow is concentrated to fewer fractures intersecting the deposition hole and/or the rock matrix permeability is reduced.

6.2.3 Matrix permeability

It was shown in Section 5.4 that the permeability of the rock matrix (even when there are flowing fractures intersecting the deposition hole) has a significant effect on the resaturation of the bentonite. Subsequently, in a sparsely fractured host rock, the effects of the rock matrix permeability on the resaturation processes may potentially be significant. Unfortunately, the characterisation data is insufficient to fully constrain the rock matrix permeability, with the rock matrix a function of geological properties (e.g. lithology, pore/grain size, insitu stress, …) as well as the pervasiveness of microstructures which occur beyond the detection limit of fracture logging tools. Therefore, although modelled as a homogeneous property, the rock matrix will exhibit significant spatial variation, although the magnitudes of rock matrix permeability are likely to be small compared to the effective properties of the fracture network.

6.3 Main conclusions

Through modelling Task 8C, a physically realistic approach to simulating the rock/bentonite interface has been developed, explicitly representing the heterogeneity of the fractured bedrock and revealing significant differences to the homogeneous assumptions commonly made to estimate bentonite resaturation. From the analysis of Task 8C using these new techniques and methodologies, the following conclusions are drawn:

- Accurate representation of the surrounding fractured bedrock is critical to understanding the hydration of emplaced bentonite.
    - The saturation of bentonite is highly heterogeneous; with significant differences in the resaturation time observed between stochastic realisations of the fracture network and between deposition holes located within an individual representation of the fracture network. Differences in resaturation time between the five deposition holes are found to vary from 19.1 years (10.9 years in KO0018G01, 30.0 years in KO0020G01, realisation 1 of the fracture network) up to 58.7 years (16.7 years in KO0015G01, 75.4 years in KO0018G01, realisation 3 of the fracture network) when considering five stochastic representations of the fracture model. In all cases the gas phase is found to diffuse towards the open tunnel, although not necessarily through the bentonite (see Section 5.4). These saturation rates were also found to be dependent on the background permeability of the rock matrix.
    - When an equivalent homogeneous representation of the bedrock is considered, models do not capture the heterogeneous processes that occur during resaturation. Given that the ECPM upscaling approach used to include the heterogeneity of the fracture network within the TOUGH2 continuum model results in some "homogenisation" of the fracture properties, it is necessary to include sufficient refinement within the grid to suitably discretise the fractures intersecting the deposition holes. These refined grids provide additional challenges to maintaining computationally tractable simulations. Alternative conceptual models for the resaturation could include directly linking the DFN to a bentonite continuum model, or perhaps implementing a hybrid DFN-CPM approach.

- When using a heterogeneous description of the bedrock, the locations of groundwater ingress to the deposition hole are as important as total inflows observed under open deposition hole conditions when predicting the saturation times of the bentonite.

- The modelling in Task 8C uses a statistical representation of the fractured bedrock as only limited characterisation of the BRIE, and in particular, the central deposition holes is available. The quantity and type of data available for constraining models is typical of that available during early phases of deposition hole siting. As such, the models developed construct a representation of the fracture system stochastically, with 10 realisations generated to consider uncertainties.
    - On further experimental data becoming available from BRIE it is not expected that any single realisation will fully represent the resaturation profiles observed. Rather, the stochastic realisations generated should provide insight to the heterogeneities in resaturation of emplaced bentonite, and the typical times to reach 99 % liquid saturation.

- Hydraulic properties of the rock matrix are influential to resaturation times of the emplaced bentonite.
  - Reducing the rock matrix permeability by an order of magnitude can reduce resaturation times significantly.
- Although a full safety case for the GDF cannot be produced until both its location and design have been selected, there are a number of safety functions the bentonite buffer can be expected to fulfil. By participating in modelling of Task 8C of the SKB EBS Task Force, NDA RWMD have the opportunity to:
  - Demonstrate sufficient understanding of the saturation process.
  - Ensure the bentonite resaturates on a timescale enabling it to satisfy its important safety functions, such as being
    - sufficiently plastic to mitigate the effects of small rock movements on the container,
    - sufficiently stiff to support the disposal container and maintain its approximate position,
    - able to protect the host rock from detrimental thermal effects,
    - able to limit the transport of dissolved corroding agents to the canister, and
    - being sufficiently dense that microbes are barely active metabolically and so cannot give rise to unfavourable chemical conditions at the surface of the container.
- As a follow up to Task 8C, Task 8D has been launched, with additional hydraulic fracture data provided; typical of the additional data available during repository construction in support of siting decisions for deposition holes. This will allow both the fracture network geometry, and hydraulic properties of the current DFN model to be refined, and their relative importance to the resaturation of bentonite to be assessed.

6.4   Further work

As part of this study on Task 8C, predictions for both inflows and subsequent resaturation profiles of emplaced bentonite are made using statistical representation of the fracture network, with only limited characterisation of the deposition holes available.

A new follow up task has now been defined (Task 8D), providing additional data typical of that generated during repository construction in support of siting decisions for deposition holes. Using this new information, both the fracture network geometry and the hydraulic properties of the Task 8C models can be refined to provide enhanced predictions of inflows and resaturation of emplaced bentonite.

It is recommended that Task 8D is the focus of further study, providing NDA RWMD with the opportunity to

- develop methodologies for calibrating models of the fractured rock using additional site measurements as they become available, and

- consolidate the techniques for modelling the interaction between the groundwater flow from the rock, and the resaturation of the bentonite material developed in this study.

7 Acknowledgements

References

SKB's (Svensk Kärnbränslehantering AB) publications can be found at www.skb.com/publications.

AMEC, 2012a. CONNECTFLOW technical summary, Release 10.4. AMEC/ENV/CONNECTFLOW/15, AMEC, UK.

AMEC, 2012b. NAMMU technical summary, Release 10.4. AMEC/ENV/CONNECTFLOW/8, AMEC, UK.

AMEC, 2012c. NAPSAC technical summary, Release 10.4. AMEC/ENV/CONNECTFLOW/12, AMEC, UK.

Cussler E L, 1984. Diffusion: mass transfer in fluid systems. Cambridge: Cambridge University Press.

NDA, 2010. Geological disposal: generic disposal facility designs. NDA/RWMD/048, Nuclear Decommissioning Authority, UK.

Han P, Bartels D M, 1996. Temperature Dependence of Oxygen Diffusion in H_2O and D_2O. Journal of Physical Chemistry 100, 5597–5602.

Hartley L, Appleyard P, Baxter S, Hoek J, Roberts D, Swan D, 2012. Development of a hydrogeological discrete fracture network model for the Olkiluoto Site Descriptive Model 2011. Posiva Working Report 2012-32, Posiva Oy, Finland.

Hawkins I R, Swift B T, 2009. Simulation HS-PS2: La définition et la comparaison des différentes representations de l'EDZ vis-à-vis du transitoire hydraulique et de la migration des gaz. SERCO/TAS/002738/003, Serco, UK. (In French.)

Hjerne C, Nordqvist R, Harrström J, 2010. Compilation and analyses of results from cross-hole tracer tests with conservative tracers. SKB R-09-28, Svensk Kärnbränslehantering AB.

Hoch A R, James M, 2011. Gas migration and rock-matrix diffusion. SERCO/TAS/000450/001, Serco, UK.

Holton D, Baxter S, Hoch A R, 2012. Modelling coupled processes in bentonite: recent results from the UK's contribution to the Äspö EBS Task Force. Mineralogical Magazine 76, 2865–2871.

Jackson C P, Hoch A R, Todman S, 2000. Self-consistency of a heterogeneous continuum porous medium representation of a fractured medium. Water Resources Research 36, 189–202.

Joyce S, Simpson T, Hartley L, Applegate D, Hoek J, Jackson P, Swan D, Marsic N, Follin S, 2010. Groundwater flow modelling of periods with temperate climate conditions – Forsmark. SKB R-09-20, Svensk Kärnbränslehantering AB.

Marrero T R, Mason E A, 1972. Gaseous diffusion coefficients. Journal of Physical and Chemical Reference Data 1, 3–118.

Oldenburg C M, Pruess K, 1995. EOS7R: Radionuclide Transport for TOUGH2. Report LBL-34868, Lawrence Berkeley National Laboratory, Berkeley, CA.

Pruess K, Oldenburg C, Moridis G, 1999. TOUGH2 User's Guide – Version 2. Report LBNL-43134, Lawrence Berkeley National Laboratory, Berkeley, CA.

Rhén I, Forsmark T, Hartley L, Joyce S, Roberts D, Gylling B, Marsic N, 2009. Bedrock Hydrogeolology. Model testing and synthesis. Site descriptive modelling, SDM-Site Laxemar. SKB R-08-91, Svensk Kärnbärnslehantering AB.

SKB, 2006. Long-term safety for KBS-3 repositories at Forsmark and Laxemar – a first evaluation. Main report of the SR-Can project. SKB TR-06-09, Svensk Kärnbärnslehantering AB.

Vidstrand P, Åkesson M, Fransson Å, Stigsson M, 2017. Task 8 of SKB Task Forces EBS and GWFTS: Modelling the interaction between engineered and natural barriers – An assessment of a fractured bedrock description in the wetting process of bentonite at deposition tunnel scale. A compilation of Task 8 descriptions. SKB P-16-05, Svensk Kärnbärnslehantering AB.

Wilson J, Savage D, Bond A, Watson S, Pusch R, Bennett D, 2010. Bentonite: a review of key properties, processes and issues for consideration in the UK context. QRS-1378ZG-1, Version 1.0, Quintessa Ltd., UK.

Task 8C1: Stochastic Variability of the Fracture Network

Probe Borehole Results

Results corresponding to the fracture transmissivity network, and pressure field local to the five probe boreholes for realisations 1 and 3 through 10 of the stochastic fracture network are shown below. Equivalent illustrations for realisation 2 of the fracture network are shown in Figure 4-5 and Figure 4-6 respectively.

Fracture transmissivities local to the probe boreholes

Figure A1-1 through Figure A1-9 illustrate slices through nine additional realisations of the fracture network in the deposition near-field, with fracture traces coloured by transmissivity. Two slices are shown, one vertical cross-section incorporating all five probing boreholes, and one horizontal cross-section cutting through at the depth of −418 m. Results for realisation 2 of the fracture network are shown in Figure 4-5.
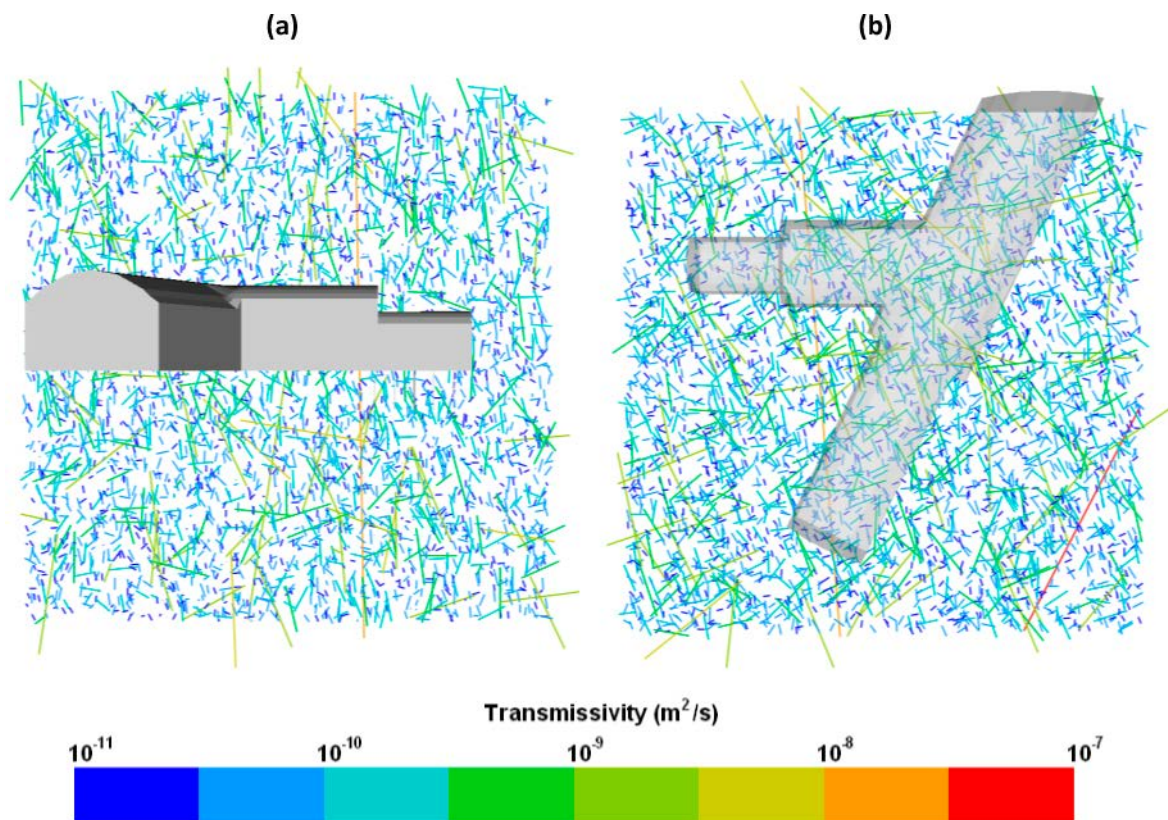
Figure A1-1. *Transmissivity (m²/s) in the borehole near-field for (a) a vertical slice through all five probe boreholes; and (b) a horizontal slice at an elevation of −418 m. Results are shown for the first realisation of the stochastic fracture network.*
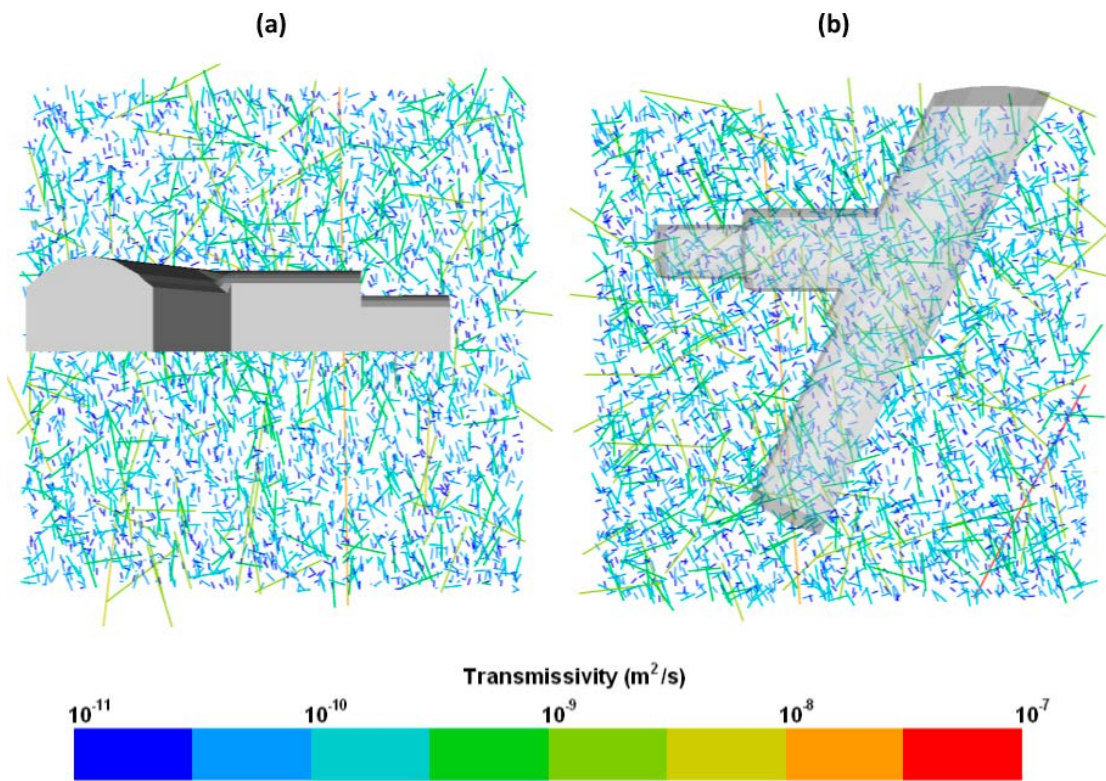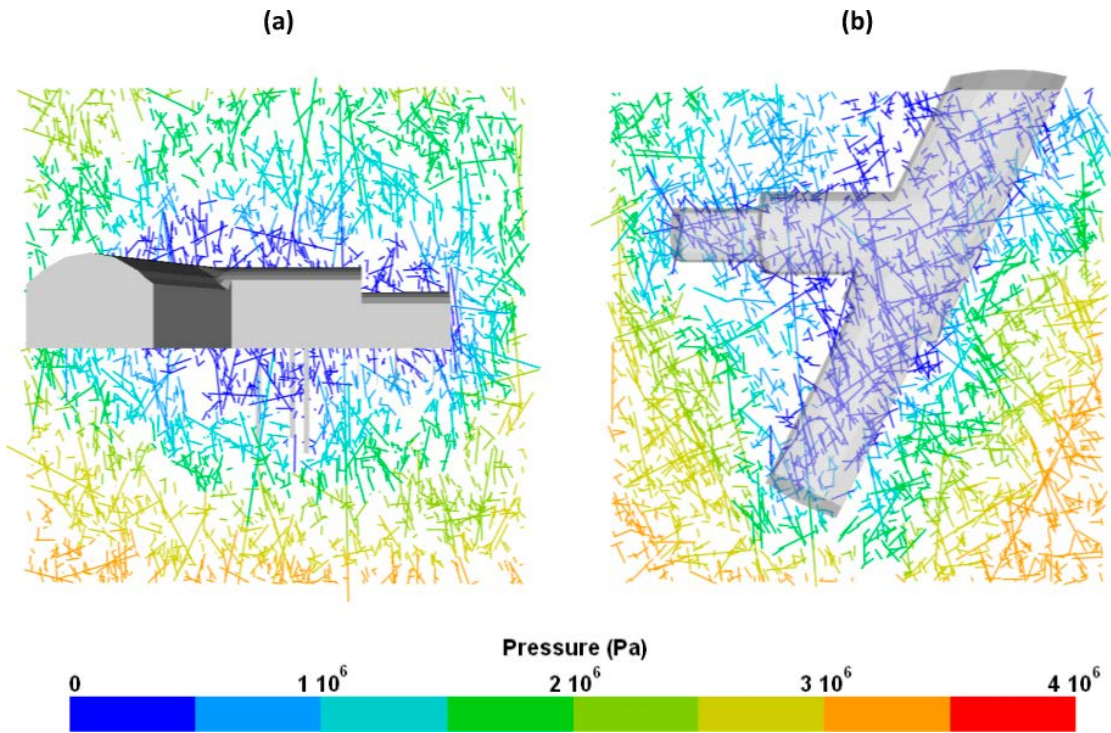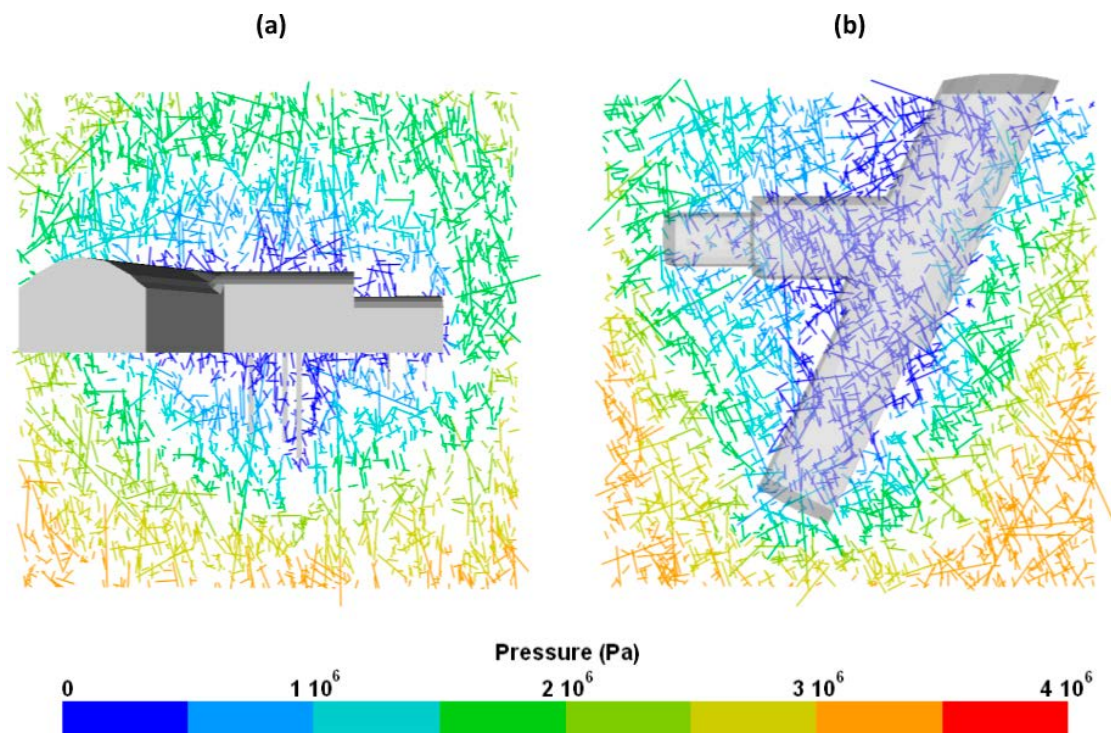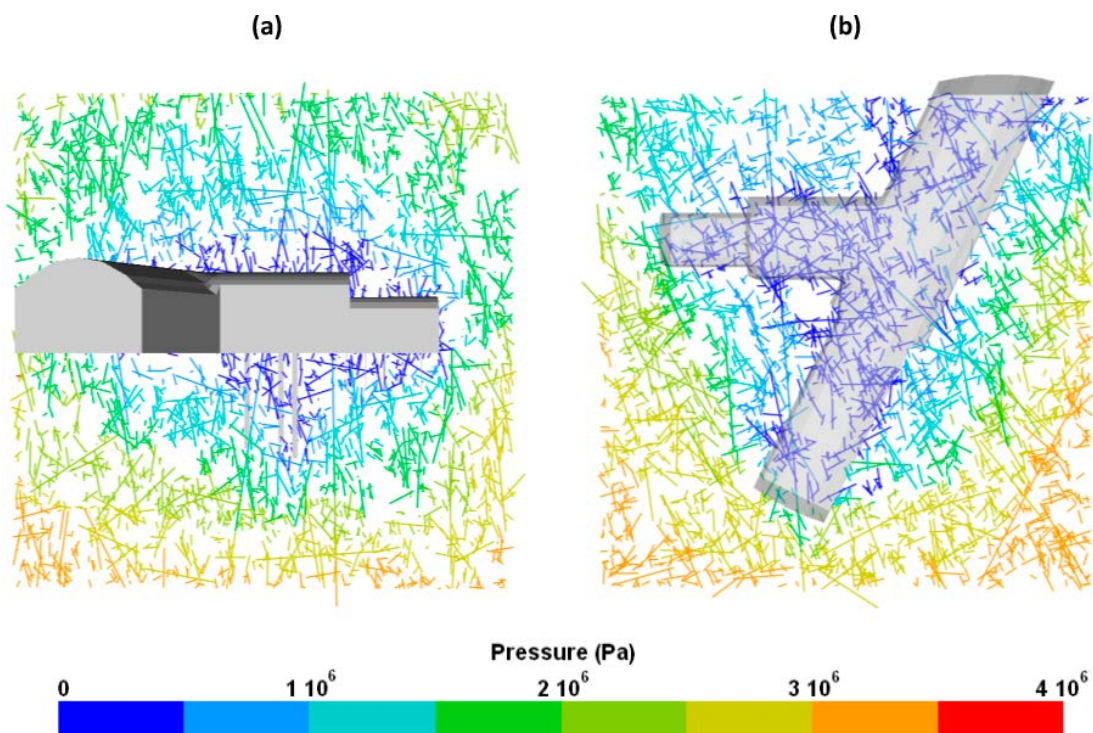
Figure A1-2. *Transmissivity (m²/s) in the borehole near-field for (a) a vertical slice through all five probe boreholes; and (b) a horizontal slice at an elevation of −418 m. Results are shown for the third realisation of the stochastic fracture network.*
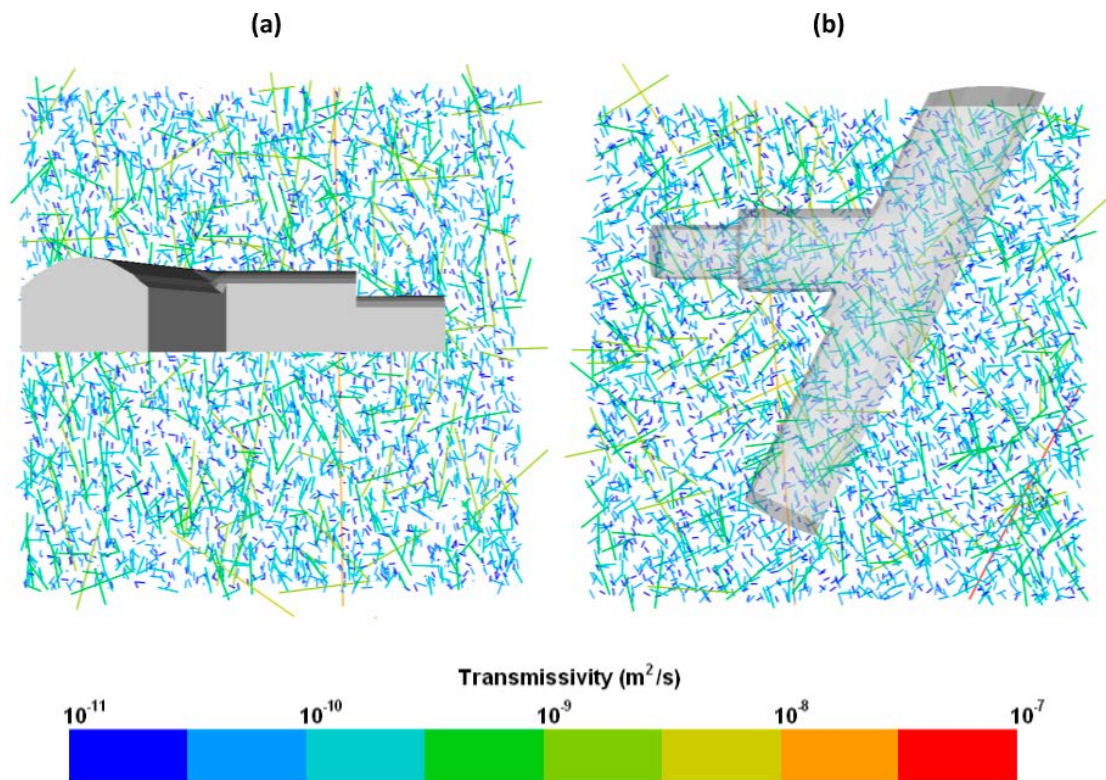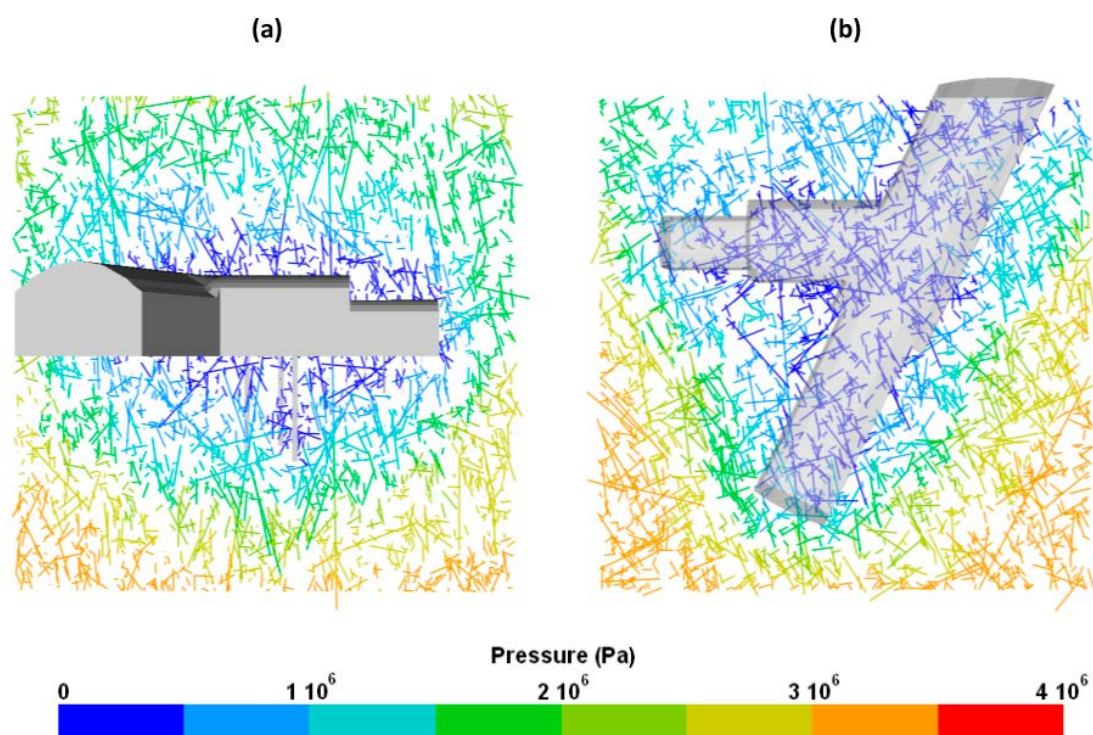

Figure A1-3. *Transmissivity (m²/s) in the borehole near-field for (a) a vertical slice through all five probe boreholes; and (b) a horizontal slice at an elevation of −418 m. Results are shown for the fourth realisation of the stochastic fracture network.*
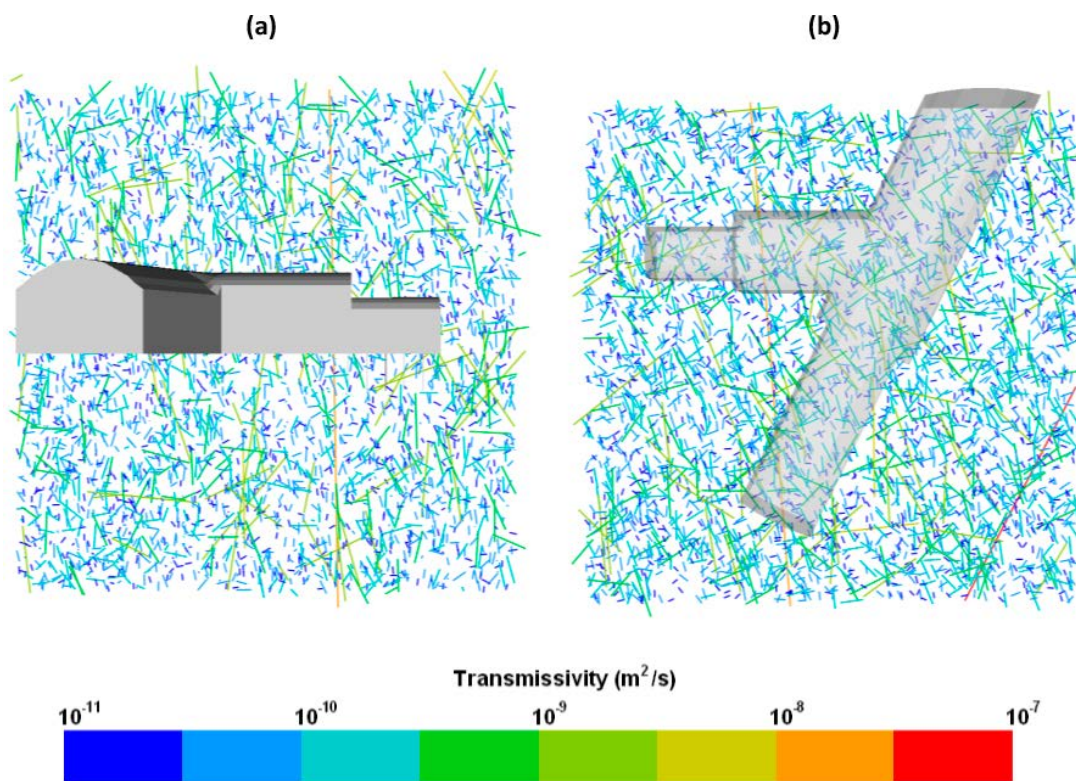
Figure A1-4. *Transmissivity (m²/s) in the borehole near-field for (a) a vertical slice through all five probe boreholes; and (b) a horizontal slice at an elevation of −418 m. Results are shown for the fifth realisation of the stochastic fracture network.*
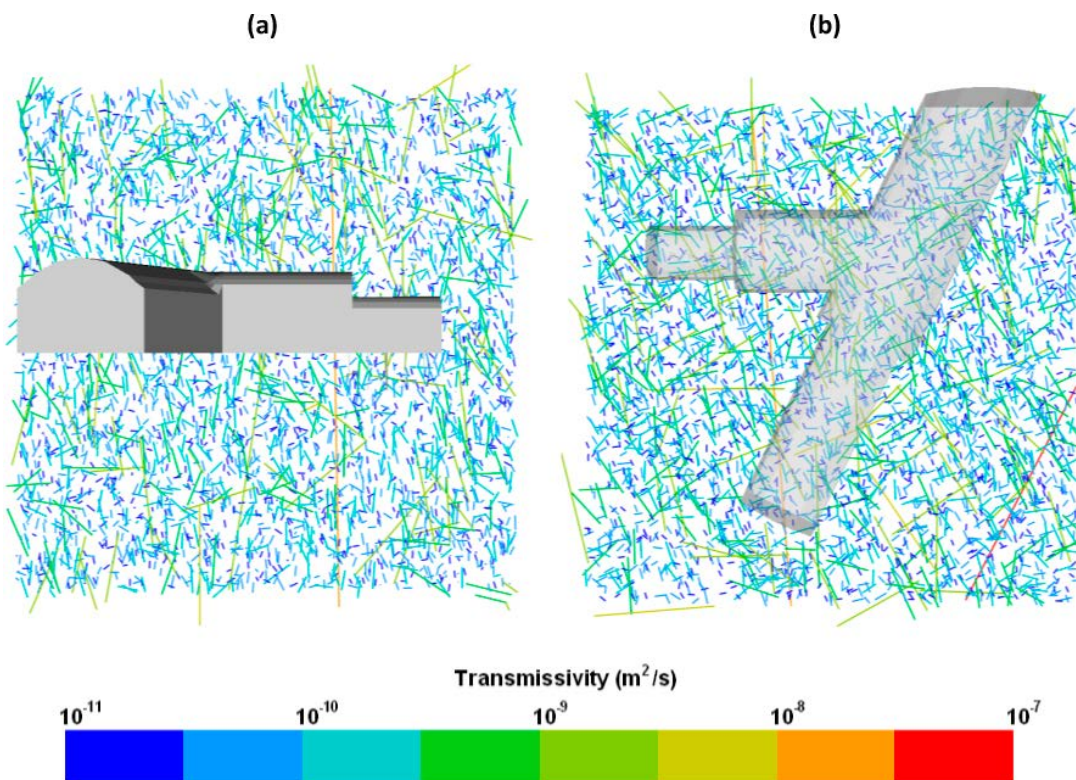
Figure A1-5. *Transmissivity (m²/s) in the borehole near-field for (a) a vertical slice through all five probe boreholes; and (b) a horizontal slice at an elevation of −418 m. Results are shown for the sixth realisation of the stochastic fracture network.*
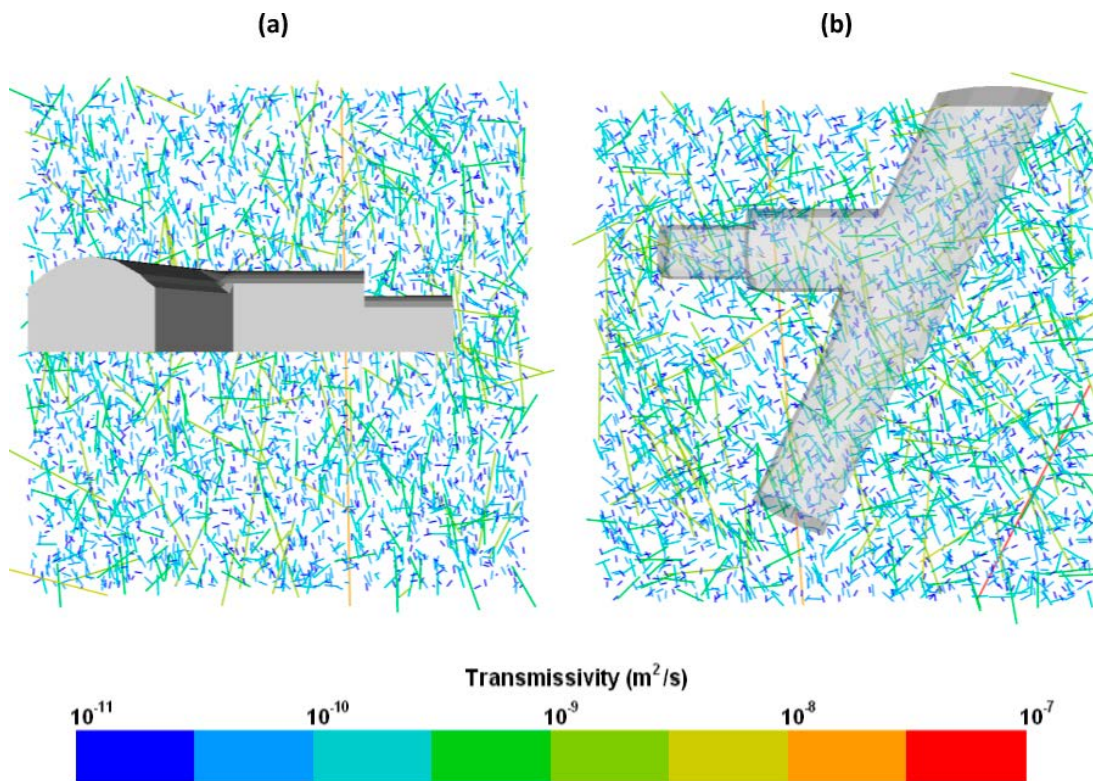
Figure A1-6. *Transmissivity (m²/s) in the borehole near-field for (a) a vertical slice through all five probe boreholes; and (b) a horizontal slice at an elevation of −418 m. Results are shown for the seventh realisation of the stochastic fracture network.*
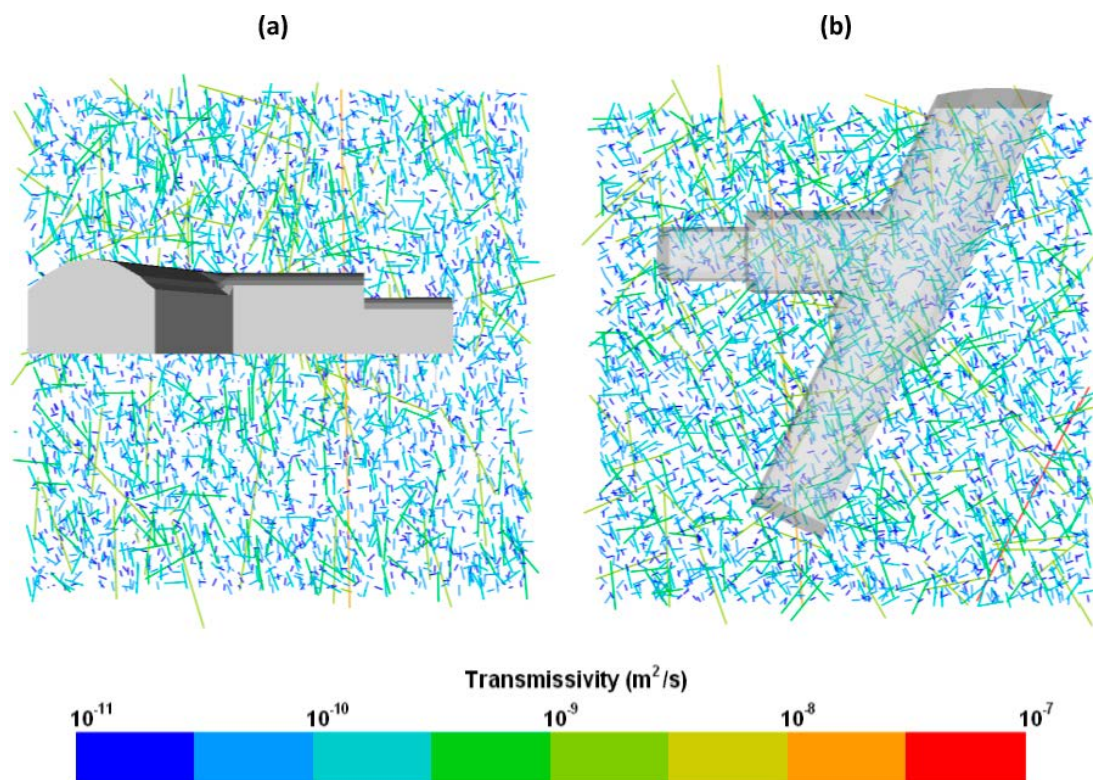
Figure A1-7. *Transmissivity (m²/s) in the borehole near-field for (a) a vertical slice through all five probe boreholes; and (b) a horizontal slice at an elevation of −418 m. Results are shown for the eighth realisation of the stochastic fracture network.*
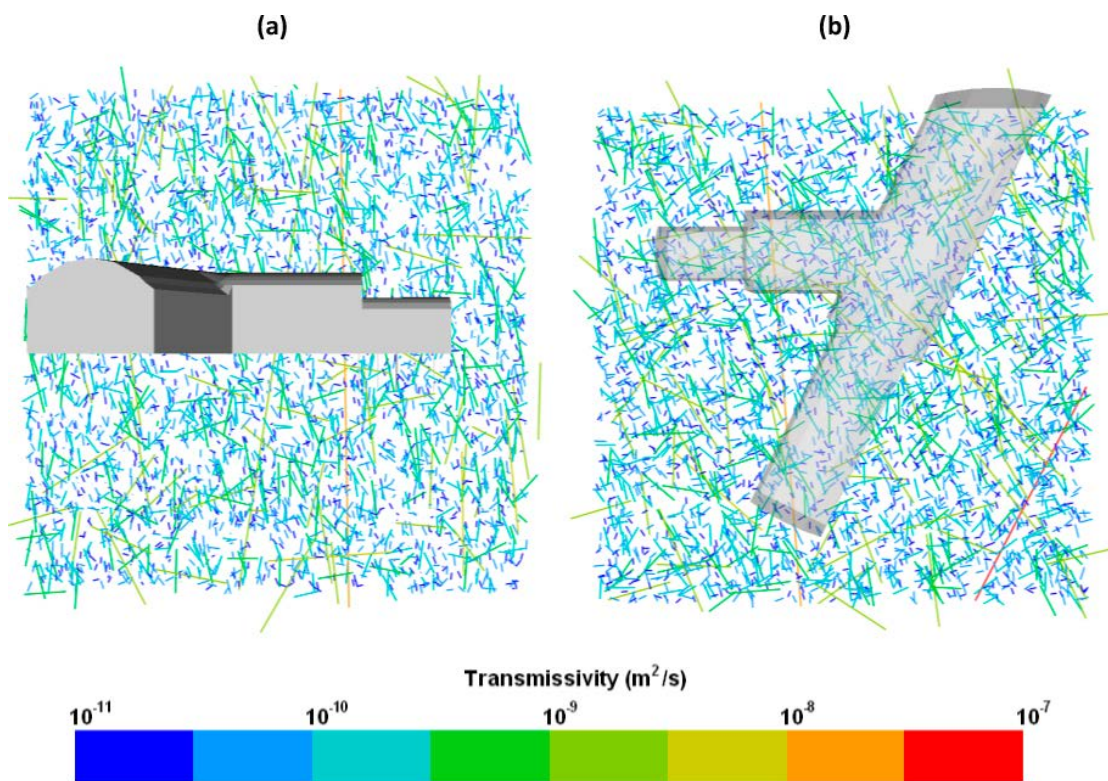
Figure A1-8. *Transmissivity (m^2/s) in the borehole near-field for (a) a vertical slice through all five probe boreholes; and (b) a horizontal slice at an elevation of −418 m. Results are shown for the ninth realisation of the stochastic fracture network.*
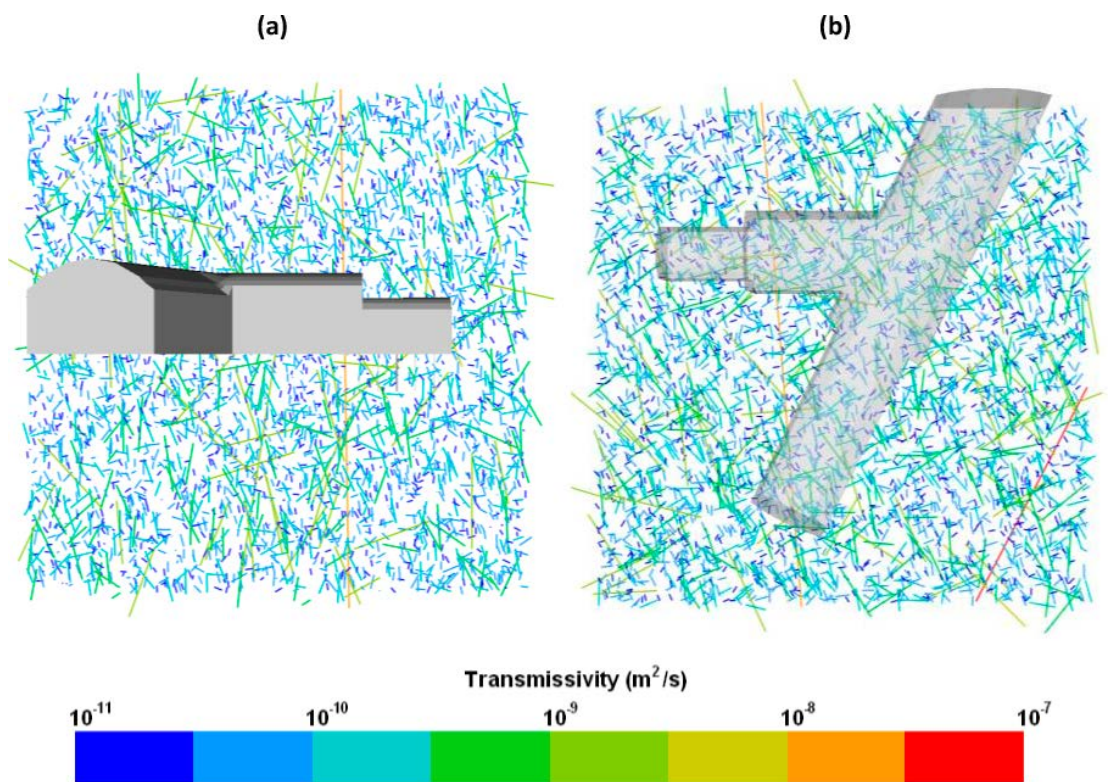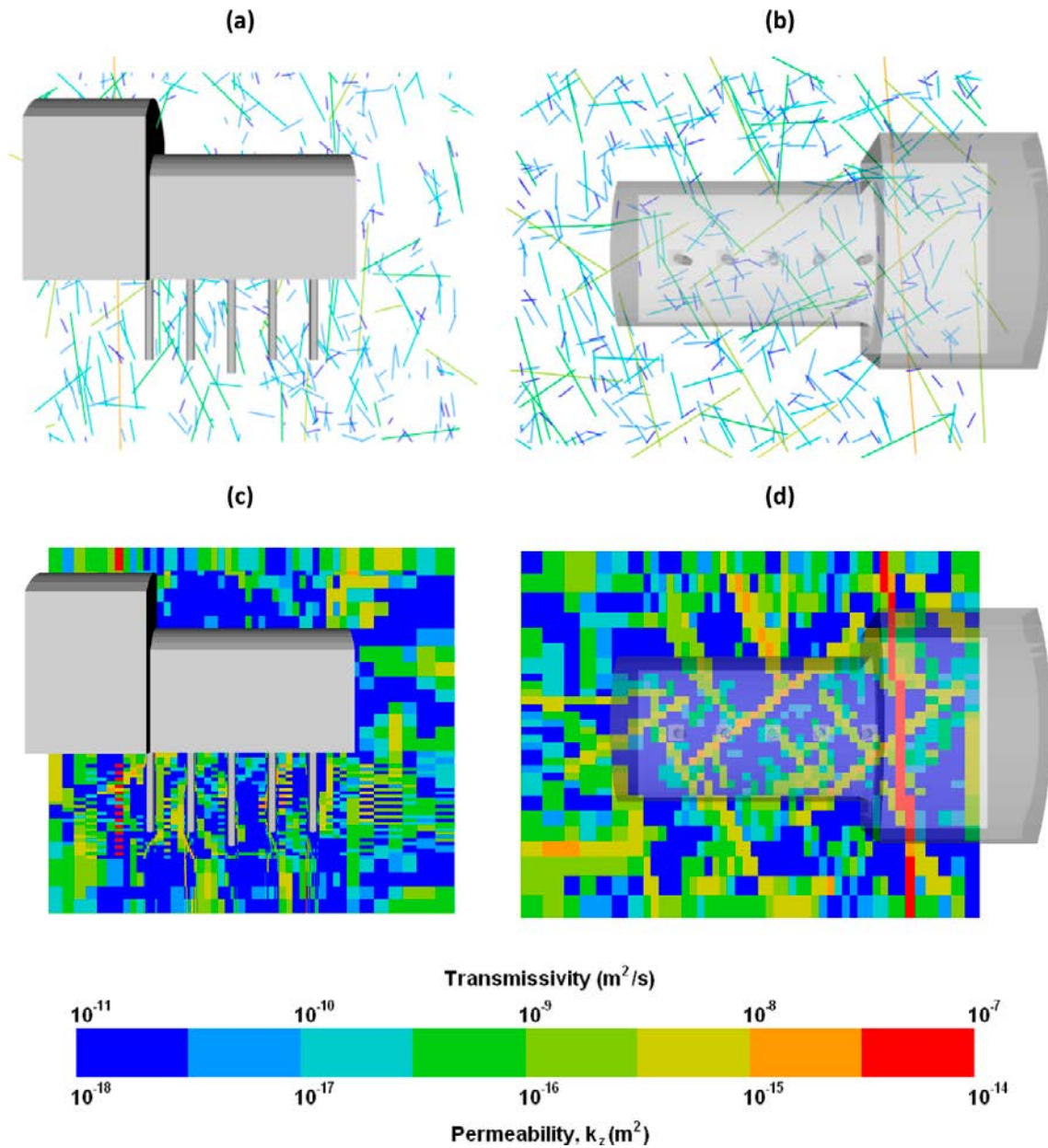

Figure A1-9. *Transmissivity (m^2/s) in the borehole near-field for (a) a vertical slice through all five probe boreholes; and (b) a horizontal slice at an elevation of −418 m. Results are shown for the tenth realisation of the stochastic fracture network.*

Fracture network pressures local to the probe boreholes

Figure A1-10 through Figure A1-18 illustrate slices through nine additional realisations of the fracture network in the deposition near-field, with fracture traces coloured by pressure. Simulations correspond to the scenario of all five boreholes packed-off to 1 m. Two slices are shown, one vertical cross-section incorporating all five probing borehole, and one horizontal cross-section cutting through at the depth of −418 m. Results for realisation 2 of the fracture network are shown in Figure 4-6.
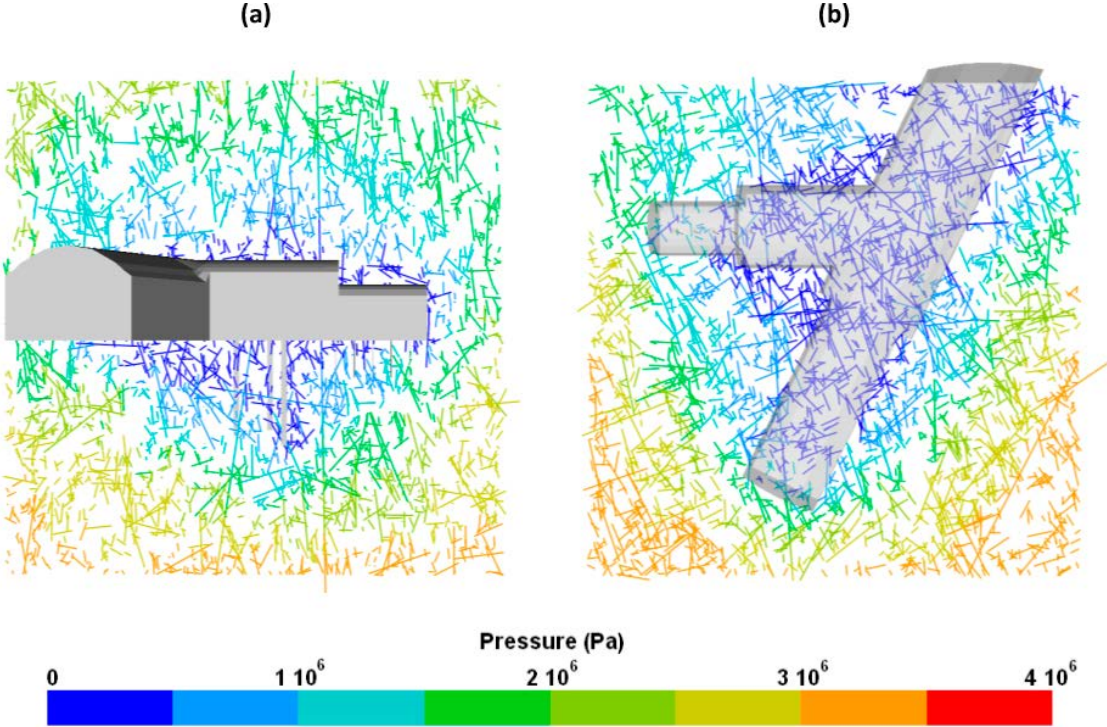
Figure A1-10. Pressure (Pa) in the deposition hole near-field for (a) a vertical slice through all five probe boreholes; and (b) a horizontal slice at an elevation of −418 m. Results are shown for the first realisation of the stochastic fracture network.
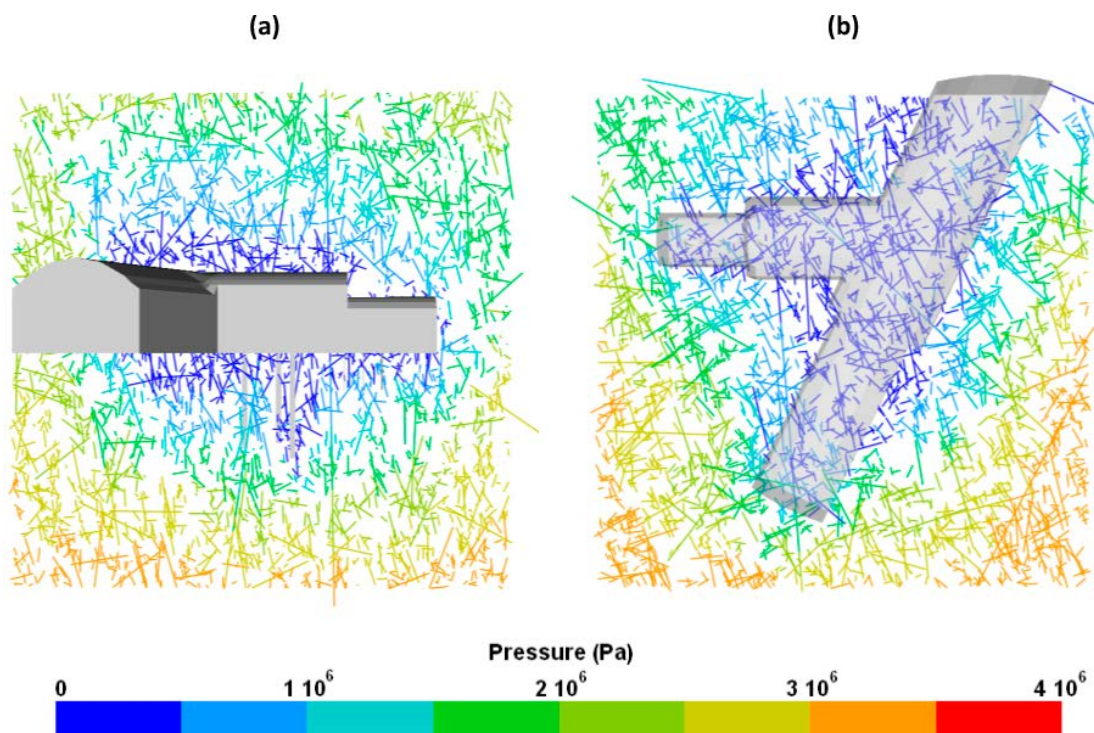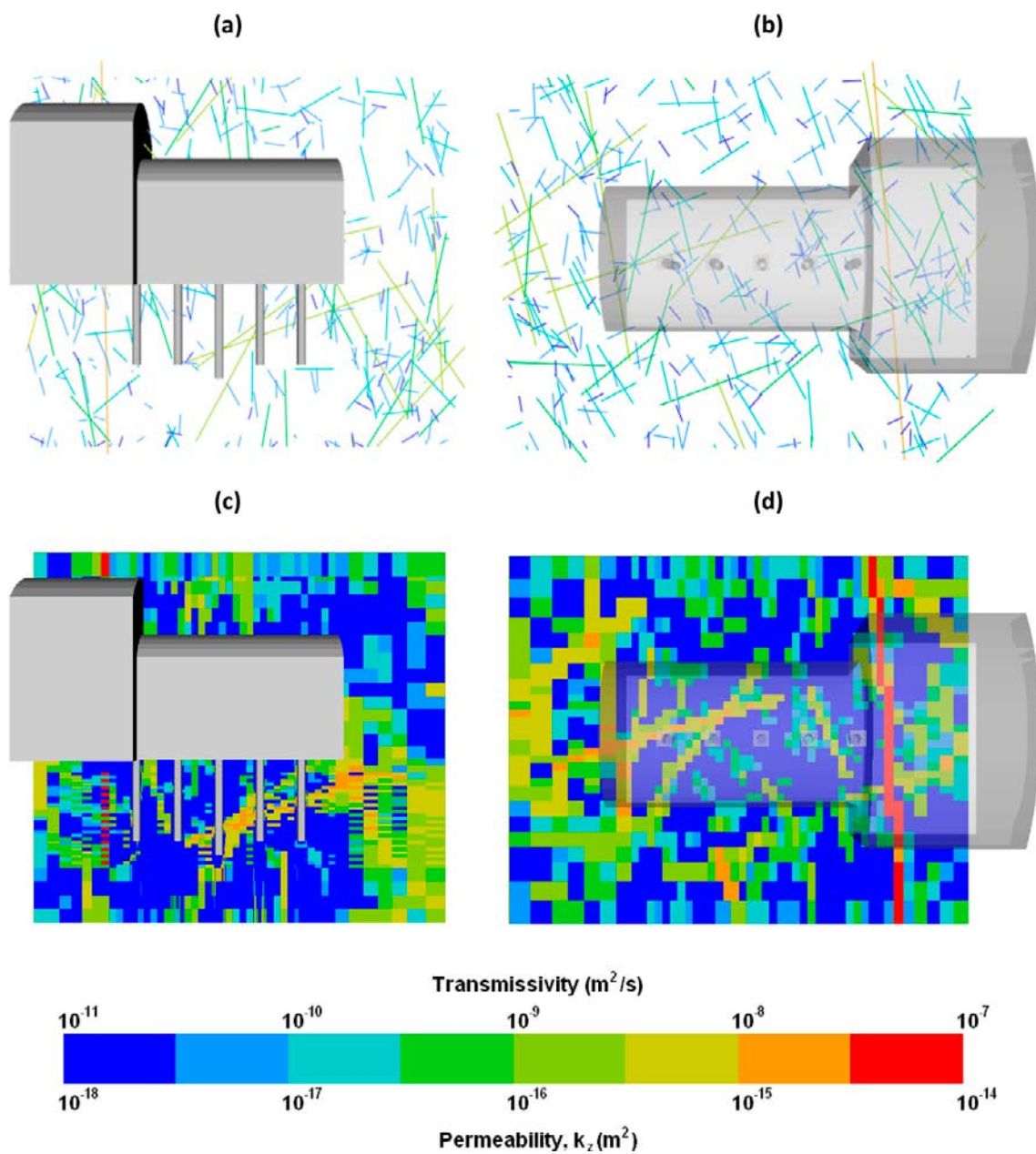
Figure A1-11. *Pressure (Pa) in the deposition hole near-field for (a) a vertical slice through all five probe boreholes; and (b) a horizontal slice at an elevation of −418 m. Results are shown for the third realisation of the stochastic fracture network.*
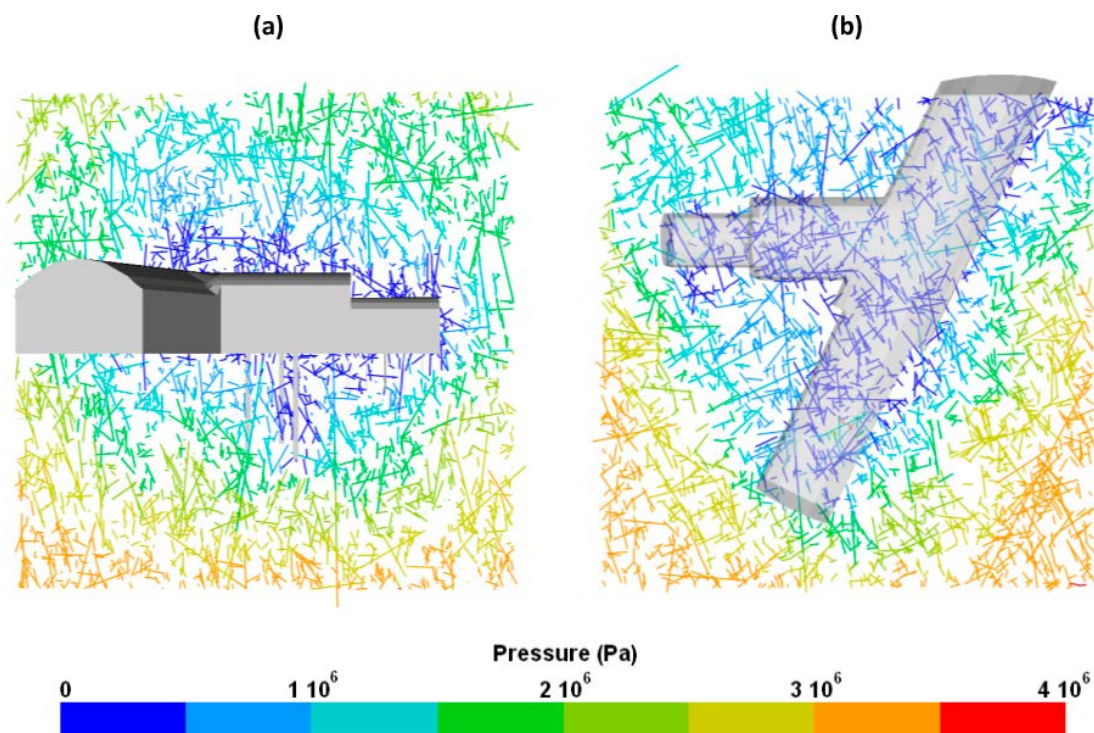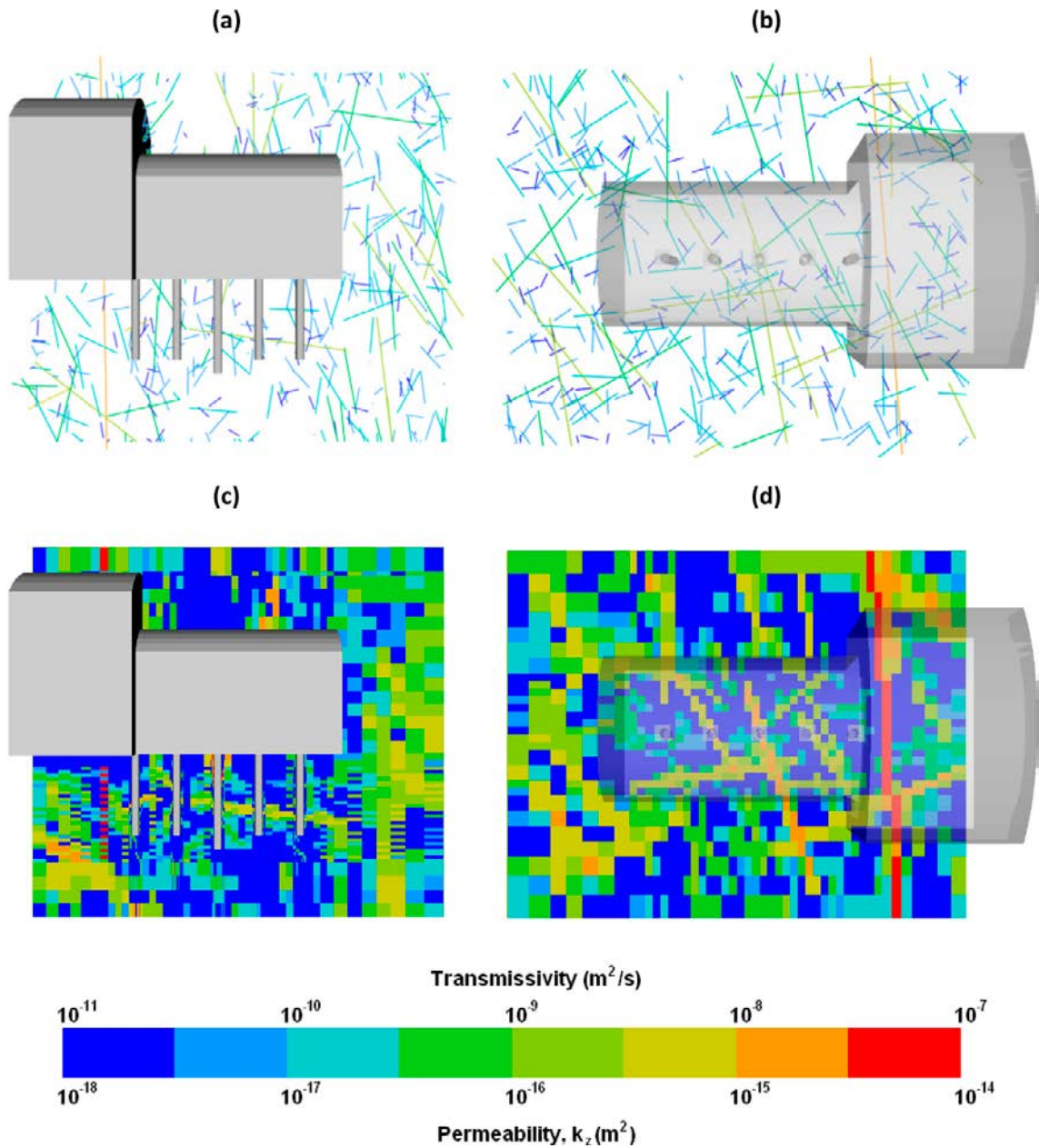

Figure A1-12. *Pressure (Pa) in the deposition hole near-field for (a) a vertical slice through all five probe boreholes; and (b) a horizontal slice at an elevation of −418 m. Results are shown for the fourth realisation of the stochastic fracture network.*
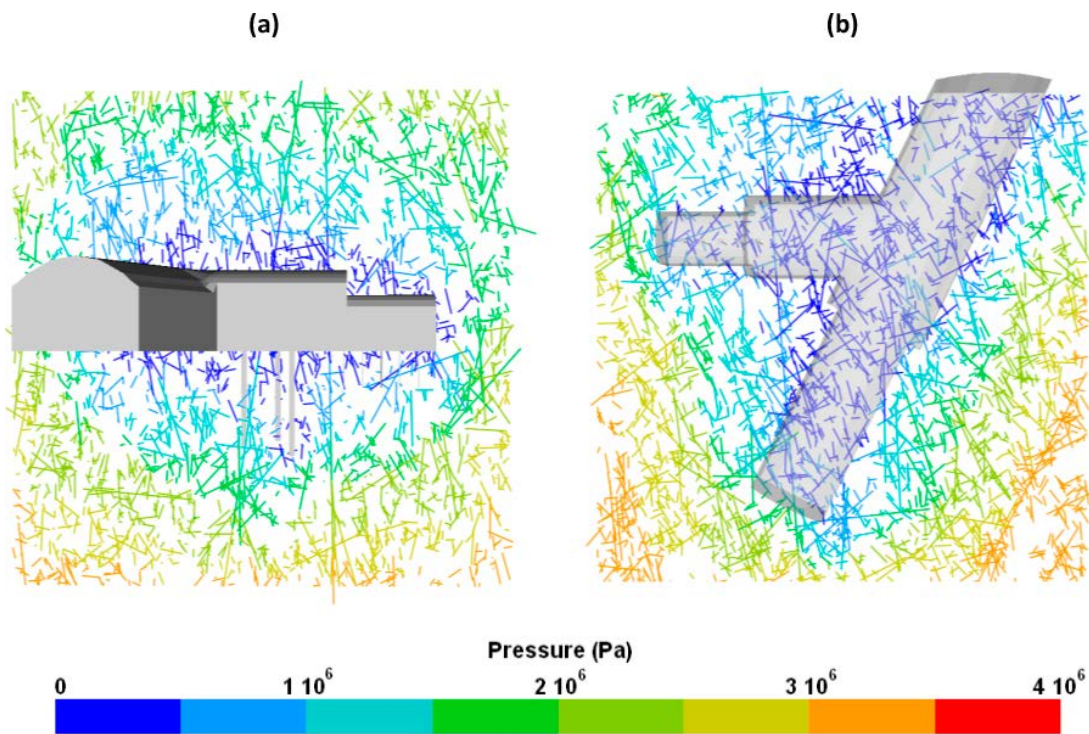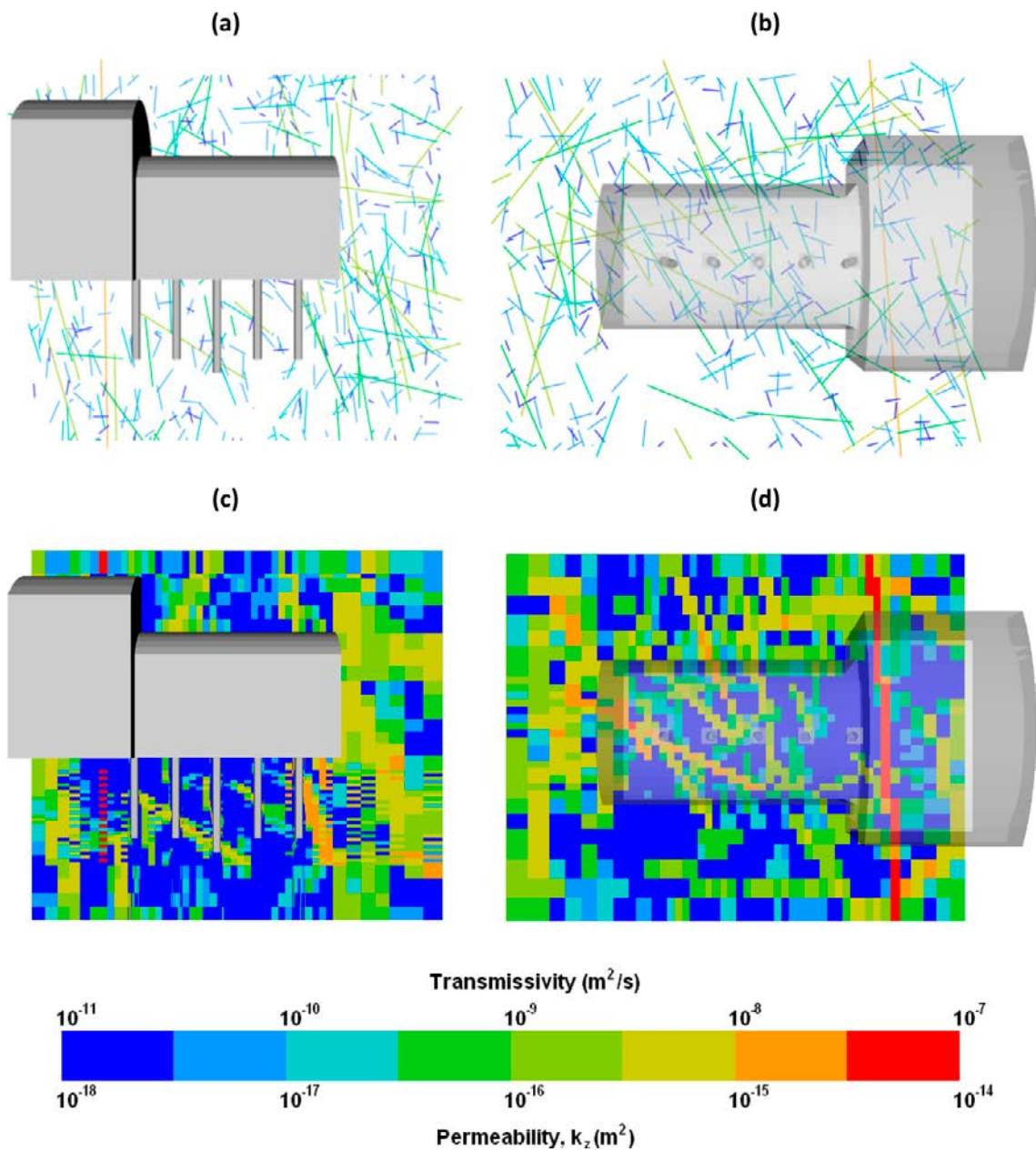
Figure A1-13. *Pressure (Pa) in the deposition hole near-field for (a) a vertical slice through all five probe boreholes; and (b) a horizontal slice at an elevation of −418 m. Results are shown for the fifth realisation of the stochastic fracture network.*
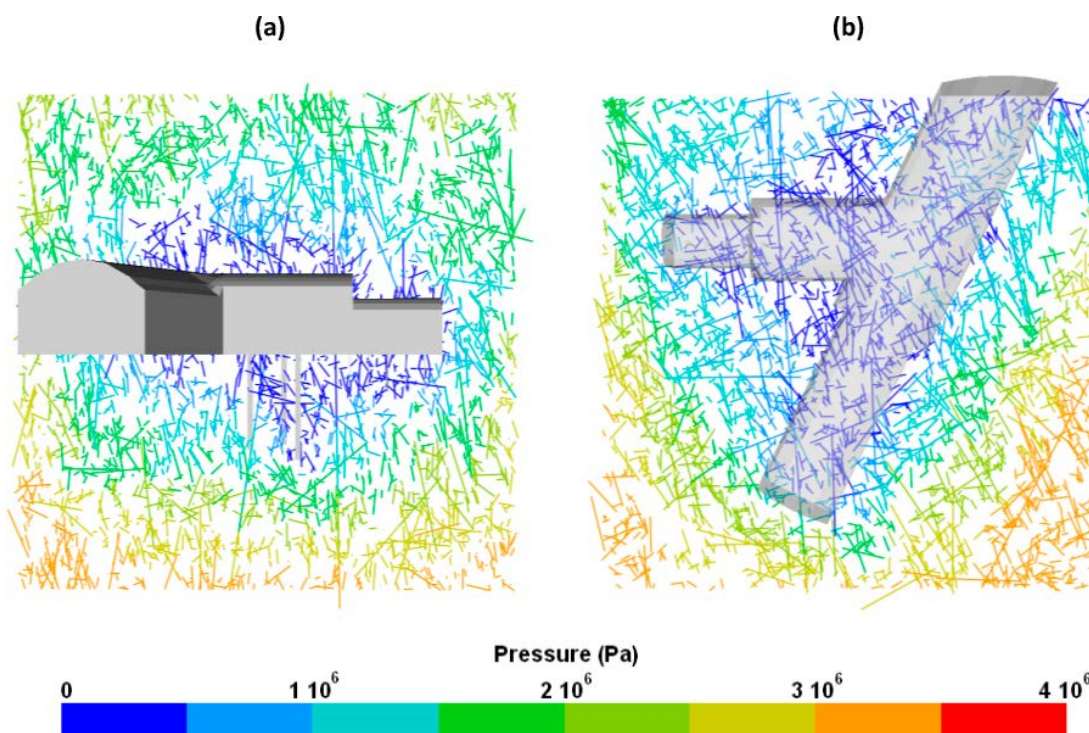
Figure A1-14. *Pressure (Pa) in the deposition hole near-field for (a) a vertical slice through all five probe boreholes; and (b) a horizontal slice at an elevation of −418 m. Results are shown for the sixth realisation of the stochastic fracture network.*

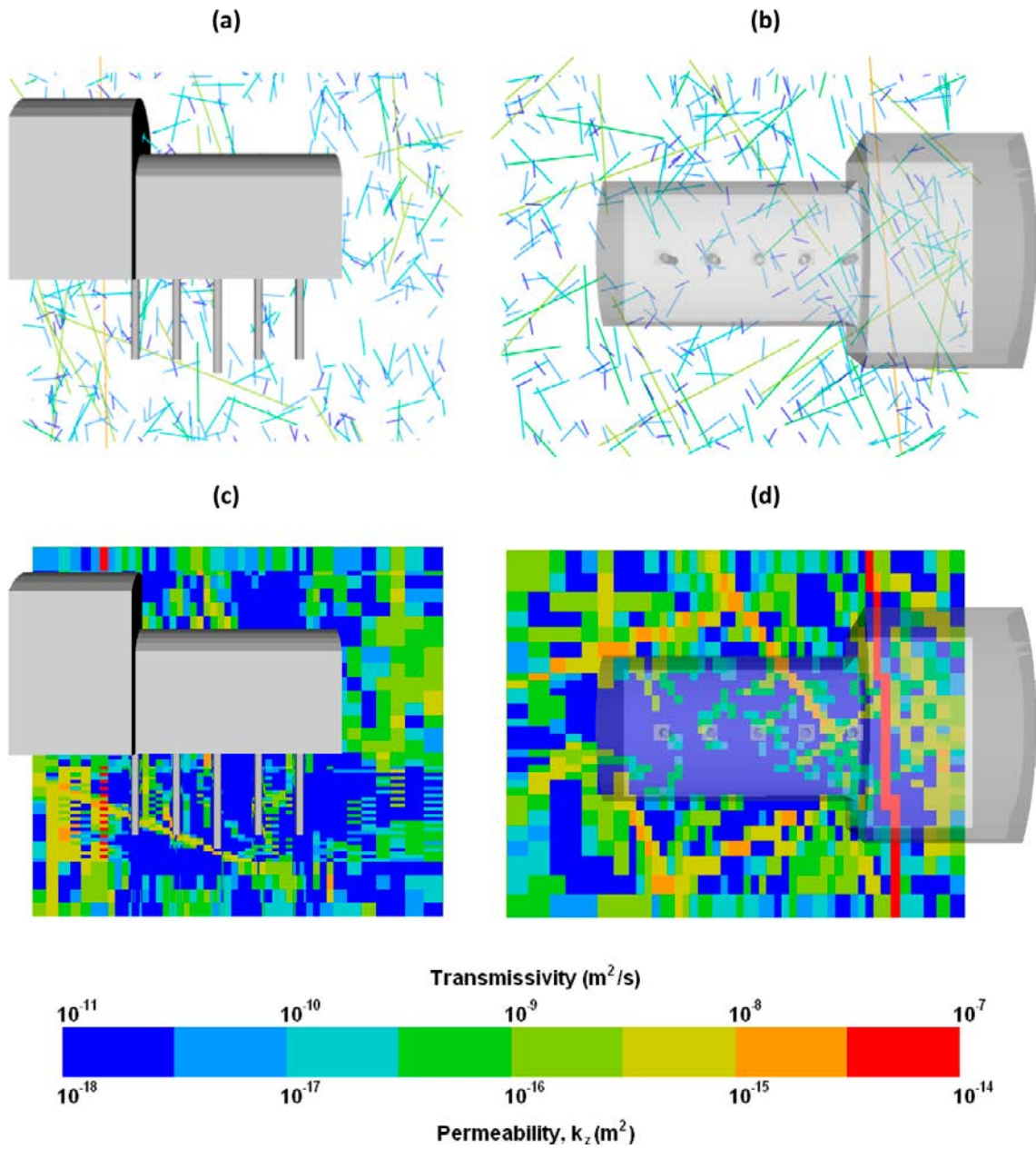**(a)**   **(b)**

Pressure (Pa)

0   1 10^6 2 10^6 3 10^6 4 10^6

Figure A1-15. *Pressure (Pa) in the deposition hole near-field for (a) a vertical slice through all five probe boreholes; and (b) a horizontal slice at an elevation of −418 m. Results are shown for the seventh realisation of the stochastic fracture network.*
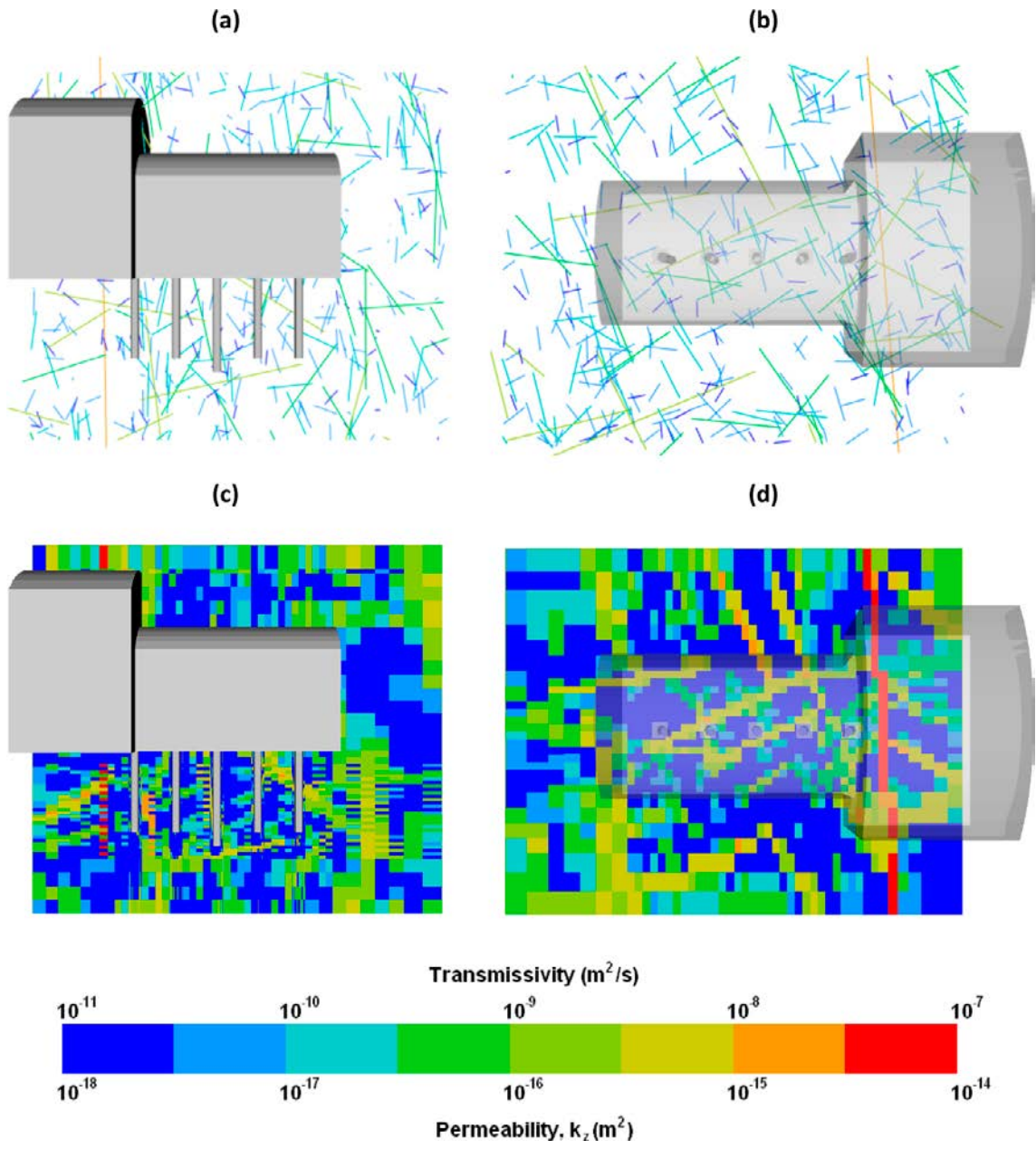

(a)   **(b)**

Pressure (Pa)

0   1 10^6 2 10^6 3 10^6 4 10^6

Figure A1-16. *Pressure (Pa) in the deposition hole near-field for (a) a vertical slice through all five probe boreholes; and (b) a horizontal slice at an elevation of −418 m. Results are shown for the eighth realisation of the stochastic fracture network.*
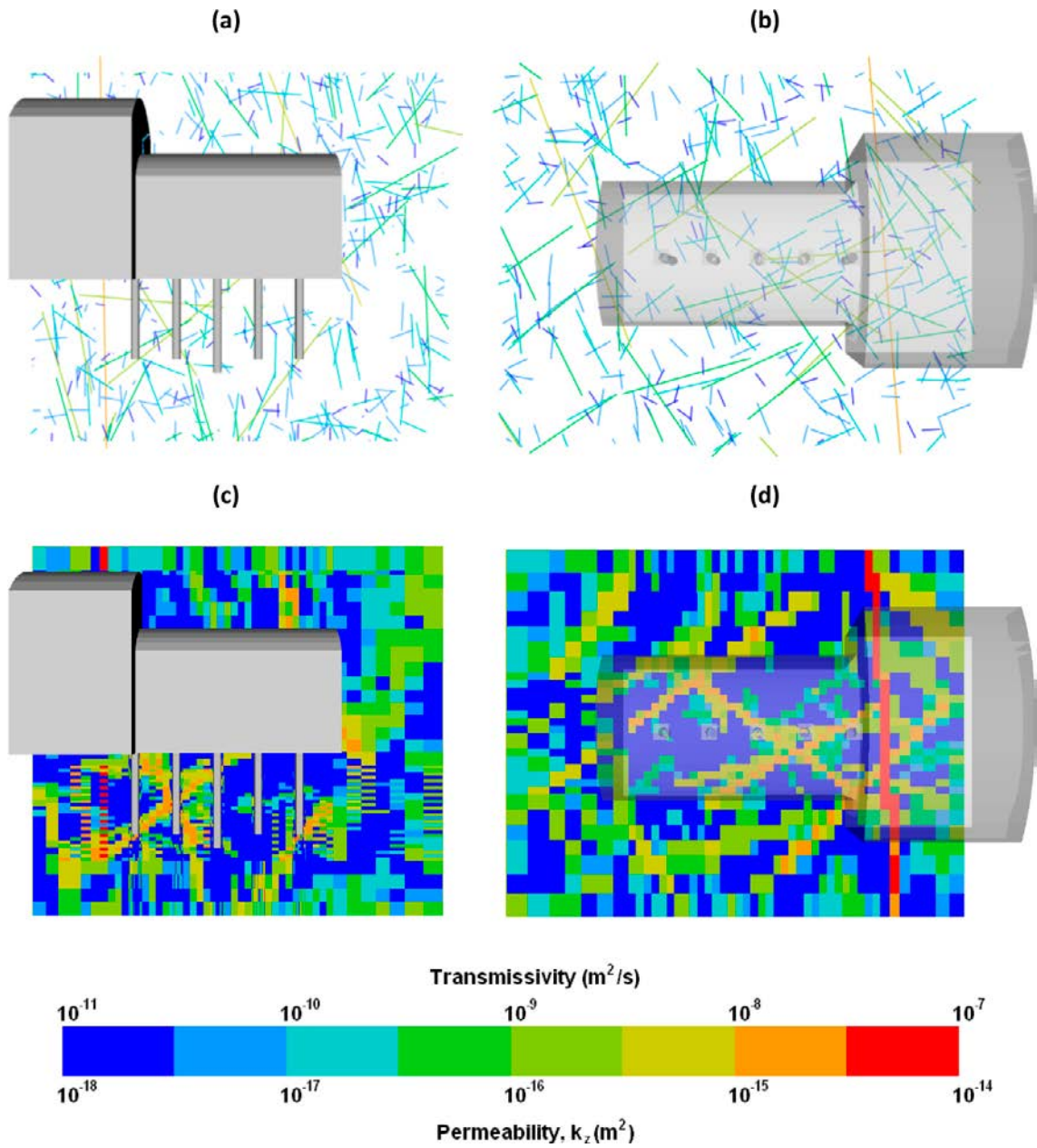
(a)   **(b)**

Pressure (Pa)

0   1 10⁶   2 10⁶   3 10⁶   4 10⁶

Figure A1-17. *Pressure (Pa) in the deposition hole near-field for (a) a vertical slice through all five probe boreholes; and (b) a horizontal slice at an elevation of −418 m. Results are shown for the ninth realisation of the stochastic fracture network.*

(a)   **(b)**

Pressure (Pa)

0   1 10⁶   2 10⁶   3 10⁶   4 10⁶

Figure A1-18. *Pressure (Pa) in the deposition hole near-field for (a) a vertical slice through all five probe boreholes; and (b) a horizontal slice at an elevation of −418 m. Results are shown for the tenth realisation of the stochastic fracture network.*

Deposition Borehole Results

Upscaled permeabilities local to the probe boreholes

Nine realisations of the stochastic fracture network are shown for two slices local to the deposition holes in Figure A1-19 through Figure A1-27. Subfigures (a, c) slice vertically, incorporating all five probing boreholes, where as subfigures (b, d) take a horizontal cross-section cutting through at a depth of −418 m. Fracture traces are coloured by transmissivity, with the equivalent permeability field, formed from upscaling the fracture network, coloured by k_z. For all realisations, regions of intense fracturing and/or high transmissivity yield correspondingly permeable blocks in the upscaled model. Equivalent results for realisation 2, of the stochastic fracture network are shown in Figure 4-12.
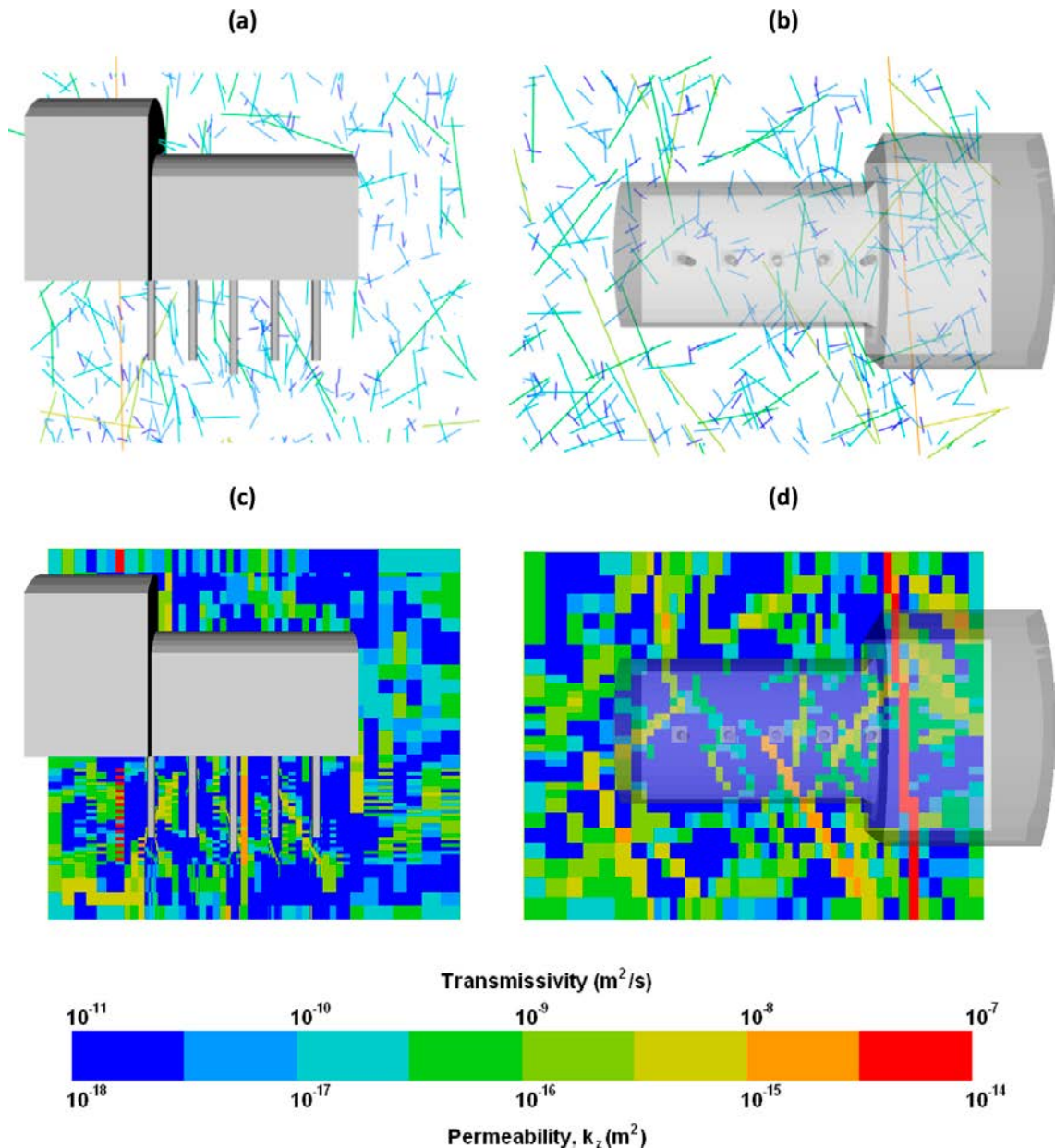
Figure A1-19. *Transmissivity (m²/s) (a,b) and upscaled permeability (m²) (c,d) in the deposition hole near-field for (a,c) a vertical slice through all five probe boreholes; and (b,d) a horizontal slice at an elevation of −418 m. Results are shown for the first realisation of the stochastic fracture network.*

Figure A1-20. *Transmissivity (m^2/s) (a,b) and upscaled permeability (m^2) (c,d) in the deposition hole near-field for (a,c) a vertical slice through all five probe boreholes; and (b,d) a horizontal slice at an elevation of −418 m. Results are shown for the third realisation of the stochastic fracture network.*
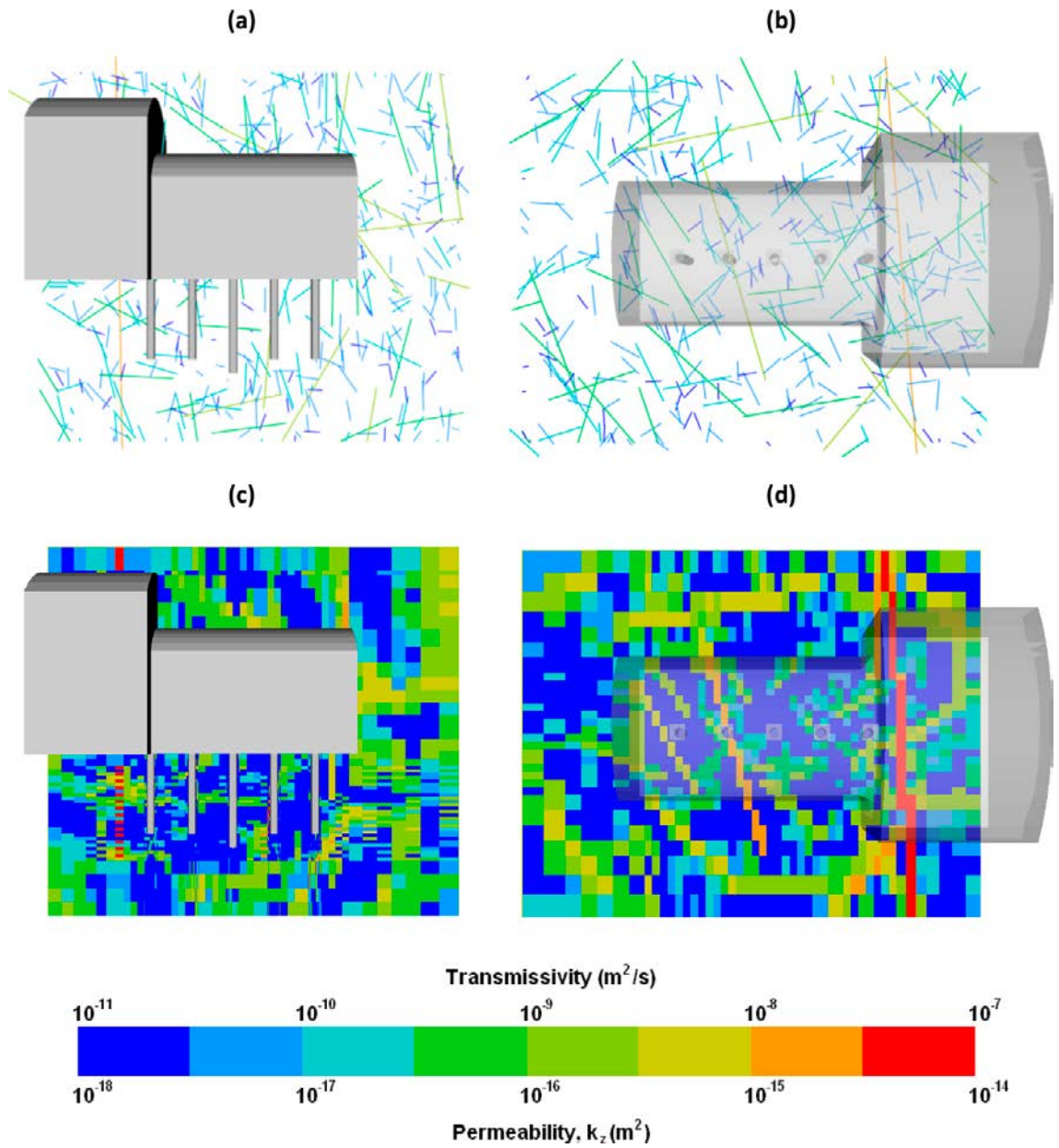
Figure A1-21. *Transmissivity (m²/s) (a,b) and upscaled permeability (m²) (c,d) in the deposition hole near-field for (a,c) a vertical slice through all five probe boreholes; and (b,d) a horizontal slice at an elevation of −418 m. Results are shown for the fourth realisation of the stochastic fracture network.*

Figure A1-22. *Transmissivity (m²/s) (a,b) and upscaled permeability (m²) (c,d) in the deposition hole near-field for (a,c) a vertical slice through all five probe boreholes; and (b,d) a horizontal slice at an elevation of −418 m. Results are shown for the fifth realisation of the stochastic fracture network.*

Figure A1-23. *Transmissivity (m²/s) (a,b) and upscaled permeability (m²) (c,d) in the deposition hole near-field for (a,c) a vertical slice through all five probe boreholes; and (b,d) a horizontal slice at an elevation of −418 m. Results are shown for the sixth realisation of the stochastic fracture network.*

Figure A1-24. *Transmissivity (m²/s) (a,b) and upscaled permeability (m²) (c,d) in the deposition hole near-field for (a,c) a vertical slice through all five probe boreholes; and (b,d) a horizontal slice at an elevation of −418 m. Results are shown for the seventh realisation of the stochastic fracture network.*

Figure A1-25. *Transmissivity (m²/s) (a,b) and upscaled permeability (m²) (c,d) in the deposition hole near-field for (a,c) a vertical slice through all five probe boreholes; and (b,d) a horizontal slice at an elevation of −418 m. Results are shown for the eighth realisation of the stochastic fracture network.*

Figure A1-26. *Transmissivity (m²/s) (a,b) and upscaled permeability (m²) (c,d) in the deposition hole near-field for (a,c) a vertical slice through all five probe boreholes; and (b,d) a horizontal slice at an elevation of −418 m. Results are shown for the ninth realisation of the stochastic fracture network.*

Figure A1-27. *Transmissivity (m²/s) (a,b) and upscaled permeability (m²) (c,d) in the deposition hole near-field for (a,c) a vertical slice through all five probe boreholes; and (b,d) a horizontal slice at an elevation of −418 m. Results are shown for the tenth realisation of the stochastic fracture network.*

Task 8C2: Stochastic Variability of the Fracture Network

Inflow Maps

Contour plots of inflows to each of the five deposition holes is shown in Figure A2-1, presented as folded up illustrations of the borehole walls, for the first realisation of the stochastic fracture network. Contours of inflow corresponding to the second realisation of the fracture network are shown in Figure 5-2.
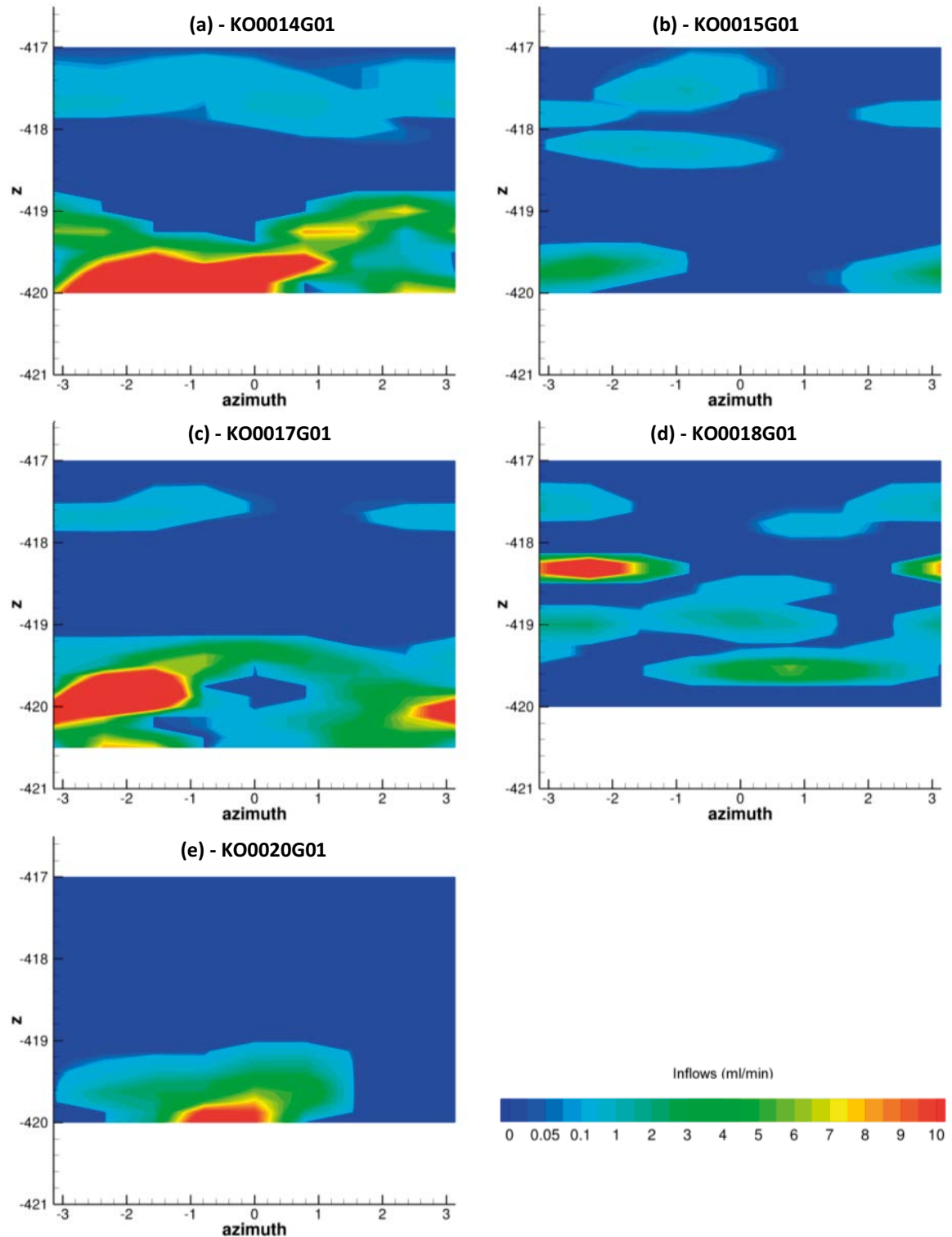
Figure A2-1. *Inflows illustrated against the walls of deposition boreholes (a) KO0014G01; (b) KO0015G01 (c) KO0017G01; (d) KO0018G01; and (e) KO0020G01, for realisation 1 of the upscaled fracture network.*

Bentonite Resaturation Profiles

Resaturation times

The time for each of the five deposition holes to reach 99 % saturation are detailed in Table A2-1 for the first, second, fourth, fifth and tenth realisations of the stochastic fracture network.

Table A2-1. Times (years) to achieve 99 % resaturation for the BRIE boreholes for realisation one, two and ten of the stochastic fracture network.

Realisation	KO0020G01	KO0018G01	KO0017G01	KO0015G01	KO0014G01
1	30.0	10.9	22.6	25.8	17.7
2	42.2	75.4	29.2	16.7	18.9
4	18.7	18.7	40.3	14.5	9.3
5	32.3	21.5	23.7	23.7	11.7
10	30.6	18.4	12.0	7.4	12.0

Pressures in the deposition hole near-field

Contour plots of liquid pressures in the deposition hole near-field are shown in Figure A2-2 and Figure A2-3, for two separate slices through the first realisation of the upscaled fracture network model. As requested in the task description (Vidstrand et al. 2017), the colour scales of the contour plots are: 1.5, 1, 0.5, 0.2, 0.1, 0, −0.1, −0.2, −0.5, −1, −5, −10, −20, and −50 MPa. Corresponding results for the tenth realisation of the fracture network are shown in Figure A2-4 and Figure A2-5 respectively

Saturations in the deposition hole near-field

Contour plots of the liquid saturation in the deposition hole near-field are shown in Figure A2-6 and Figure A2-7 for both a vertical and horizontal slice respectively. Solutions are presented for the first realisation of the stochastic fracture network at times 0, 0.1, 0.5, 1, 10, 100 years, with slices corresponding to those shown in Figure A2-2 and Figure A2-3 for liquid pressures. Equivalent results for the tenth fracture realisation are shown in Figure A2-8 and Figure A2-9.

Pressure evolution within the bentonite

The evolution of liquid pressure of the bentonite is considered for 24 separate locations within each of the deposition holes. A schematic of these locations, and the nomenclature used is shown in Figure 5-8. Results for the first realisation of the stochastic fracture network are shown in Figure A2-10 through Figure A2-14, with the tenth realisation shown in Figure A2-15 through Figure A2-19. Corresponding figures for the second realisation of the fracture network are presented in Figure 5-9 through Figure 5-13.

Pressure evolution within the bedrock

The evolution of liquid pressure in the bedrock is considered for 24 or 27 separate locations local to each of the deposition holes. A schematic of these locations, and the nomenclature used is shown in Figure 5-14. The bedrock local to each deposition hole is analysed at a distance of 0.01 m, 0.05 m, 0.1 m and 0.15 m. In addition, for deposition holes KO0014G01, and KO0020G01, an additional point, 1 m away from the five deposition holes is considered. Results for the first realisation of the stochastic fracture network are shown in Figure A2-20 through Figure A2-24, with the tenth realisation shown in Figure A2-25 through Figure A2-29. Corresponding figures for the second realisation of the fracture network are presented in Figure 5-15 through Figure 5-19.

(a) - t = 0 years

(b) - t = 0.1 years

(c) - t = 0.5 years

(d) - t = 1.0 years

(e) - t = 10 years

(f) - t = 100 years

Pressure: -50 -20 -10 -5   -1 -0.5 -0.2 -0.1 0 0.1 0.2 0.5 1 1.5
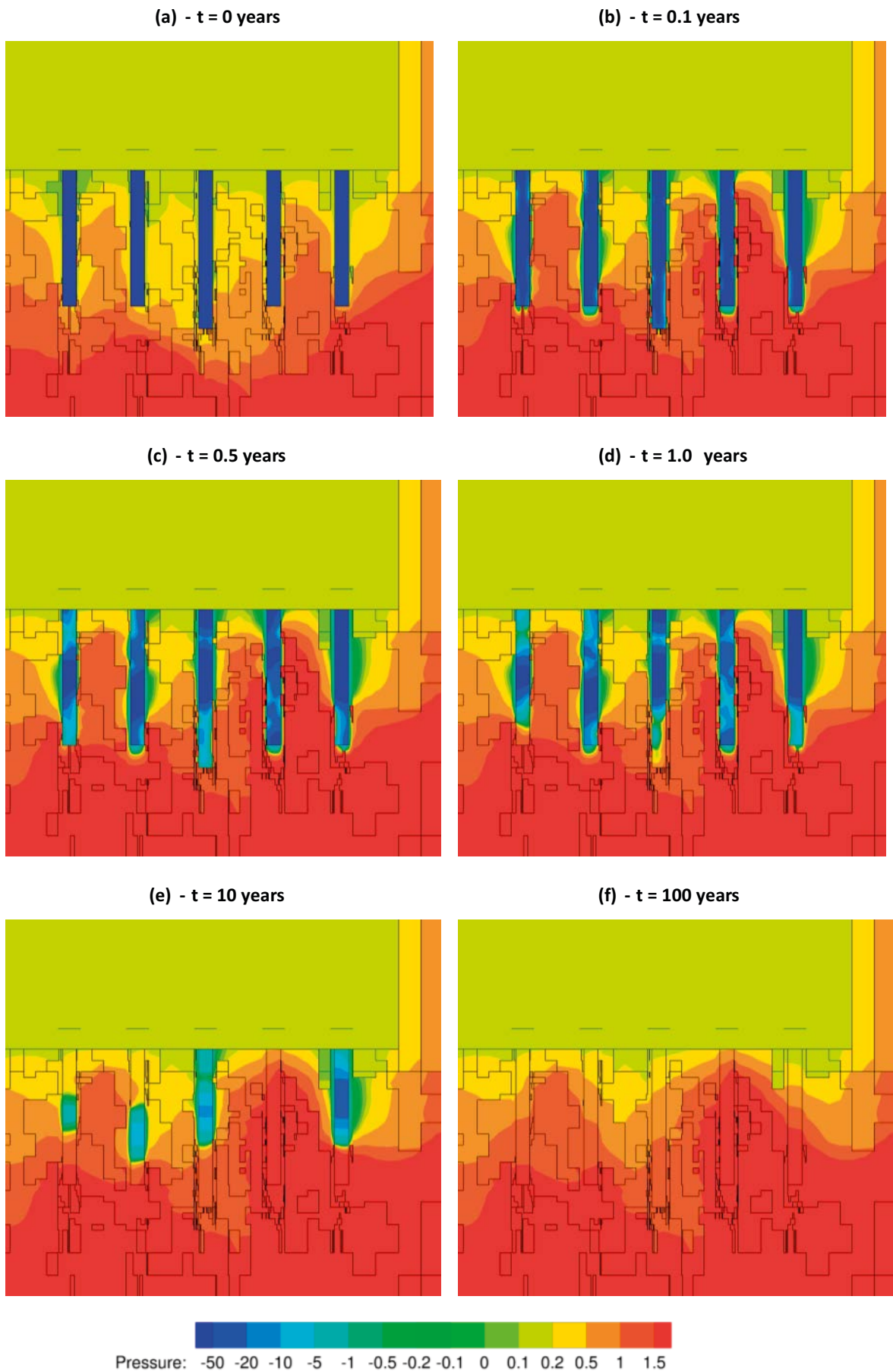
Figure A2-2. *Evolution of pressure (Pa) within the bentonite for a vertical slice including the deposition holes. Results are shown for the first realisation of the stochastic fracture network.*
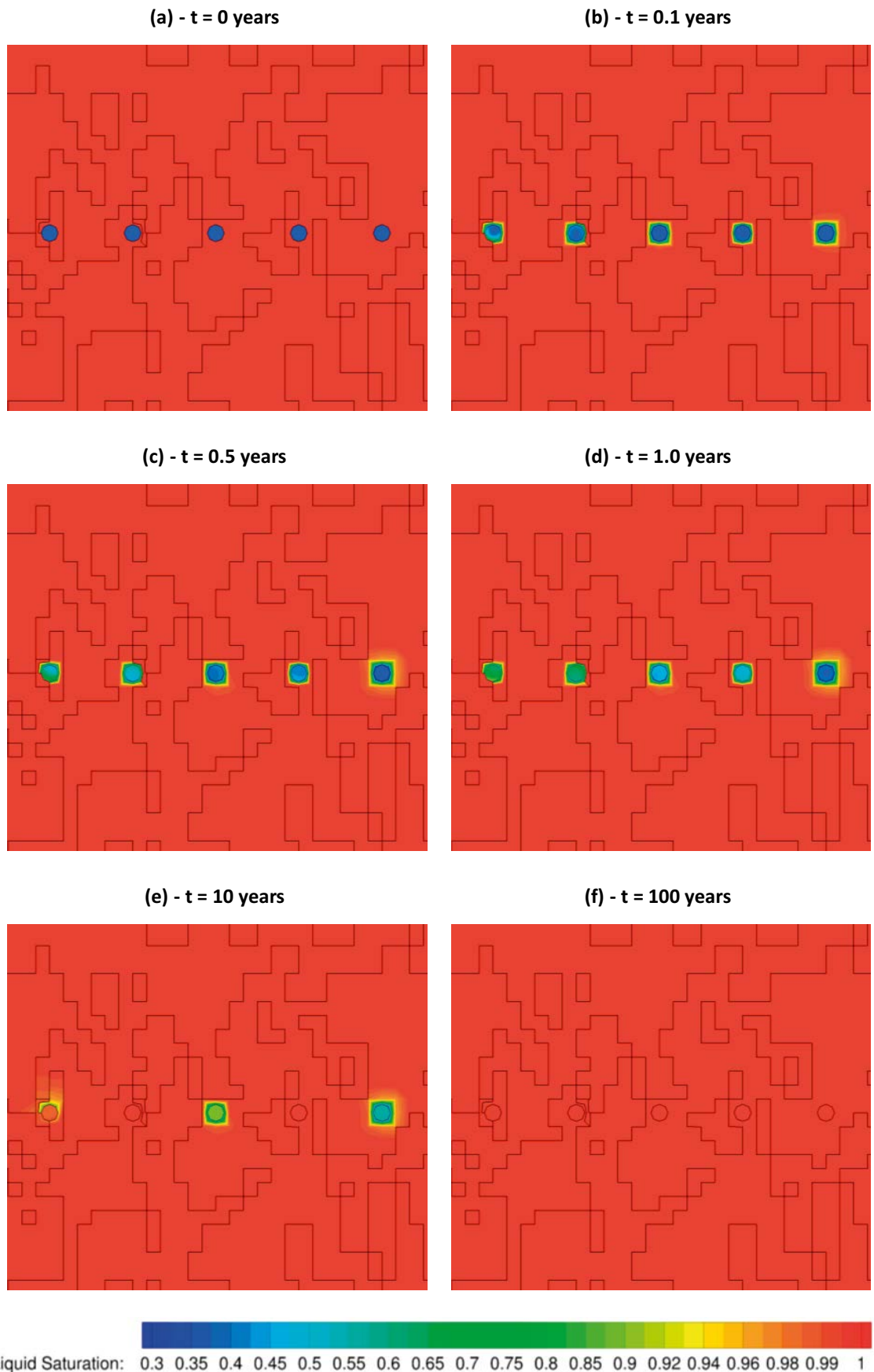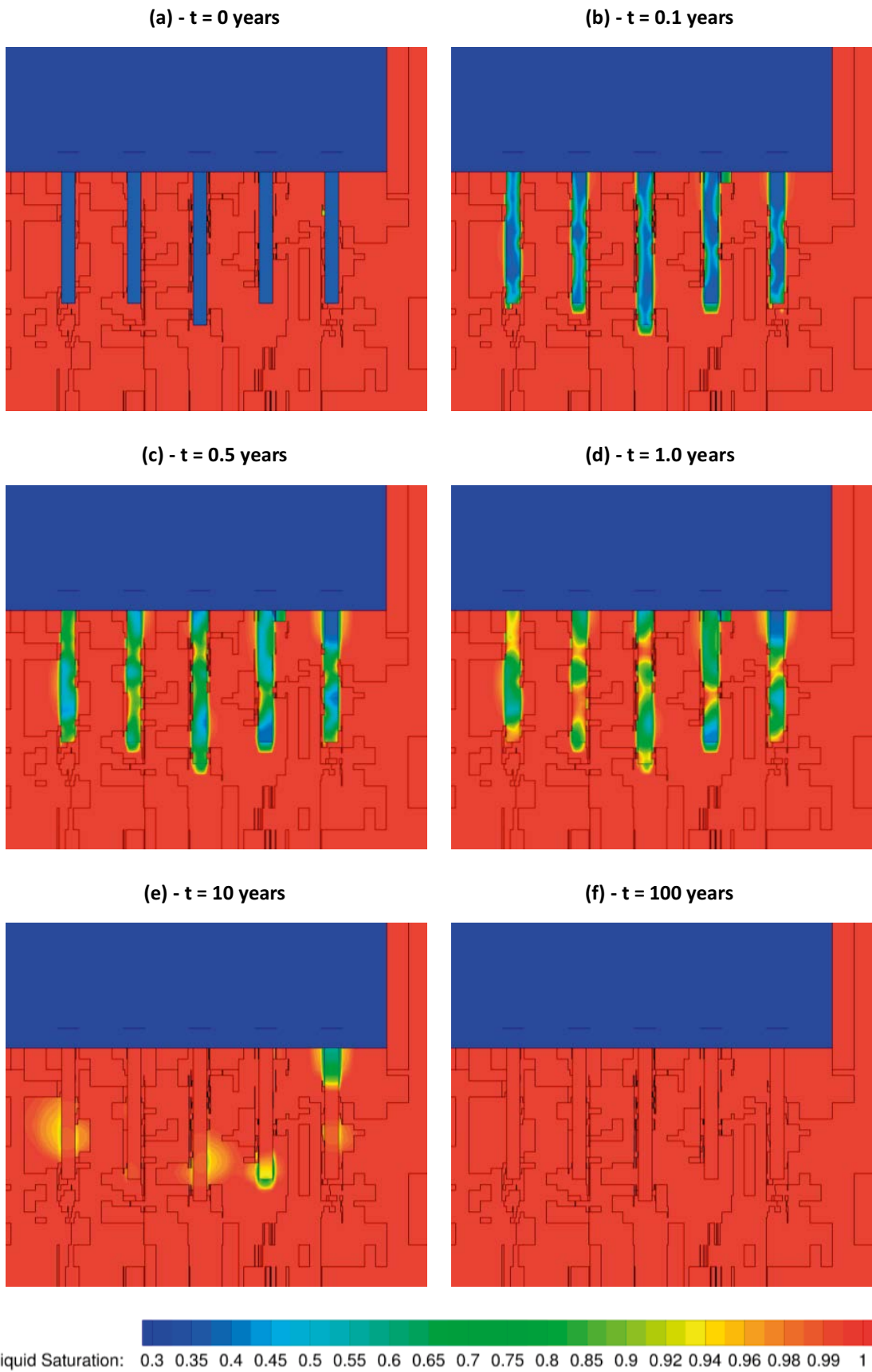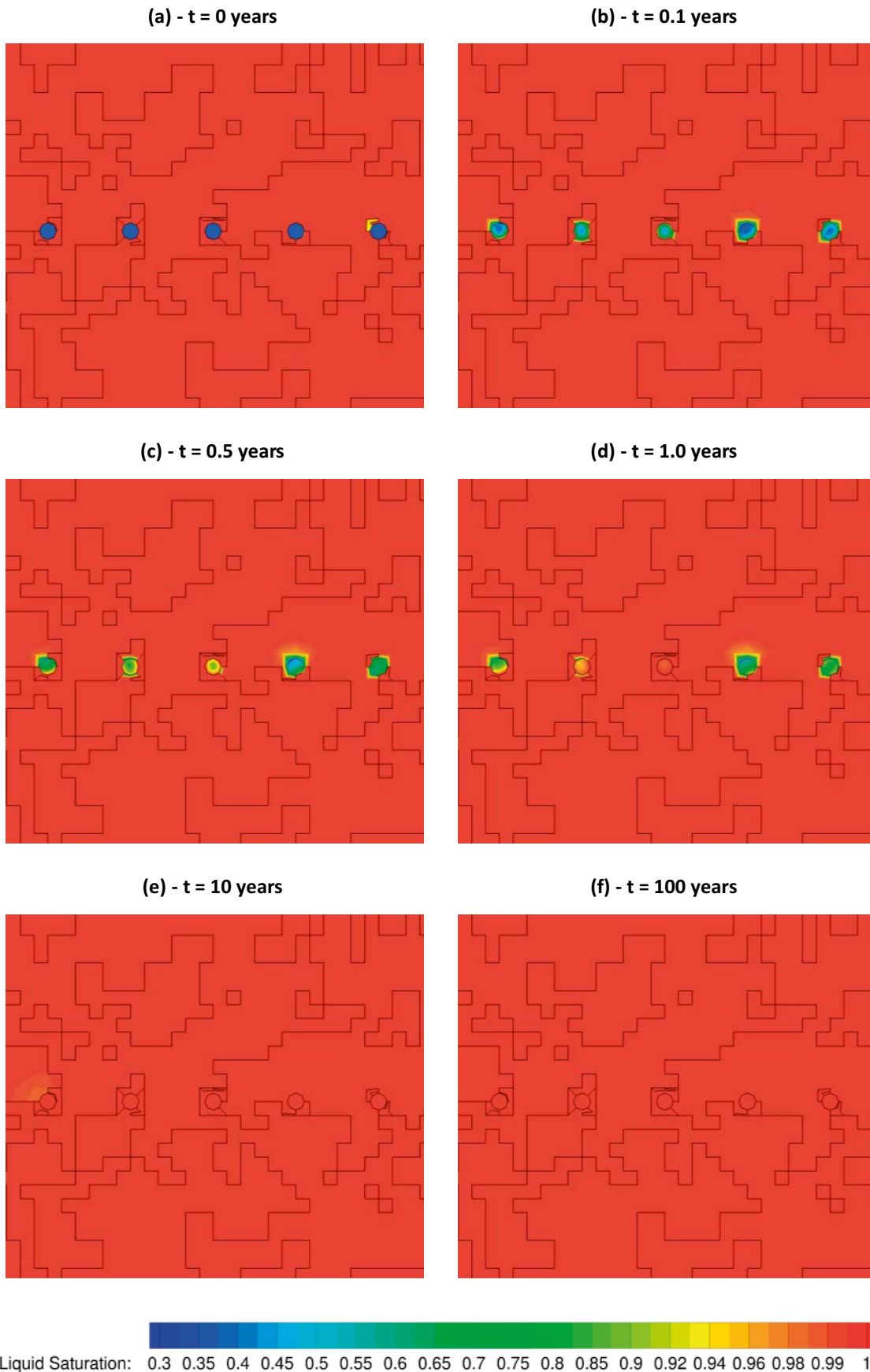
(a) - t = 0 years   **(b) - t = 0.1 years**

(c) - t = 0.5 years   **(d) - t = 1.0 years**

(e) - t = 10 years   **(f) - t = 100 years**

Pressure: -50 -20 -10 -5   -1 -0.5 -0.2 -0.1 0   0.1 0.2 0.5   1   1.5
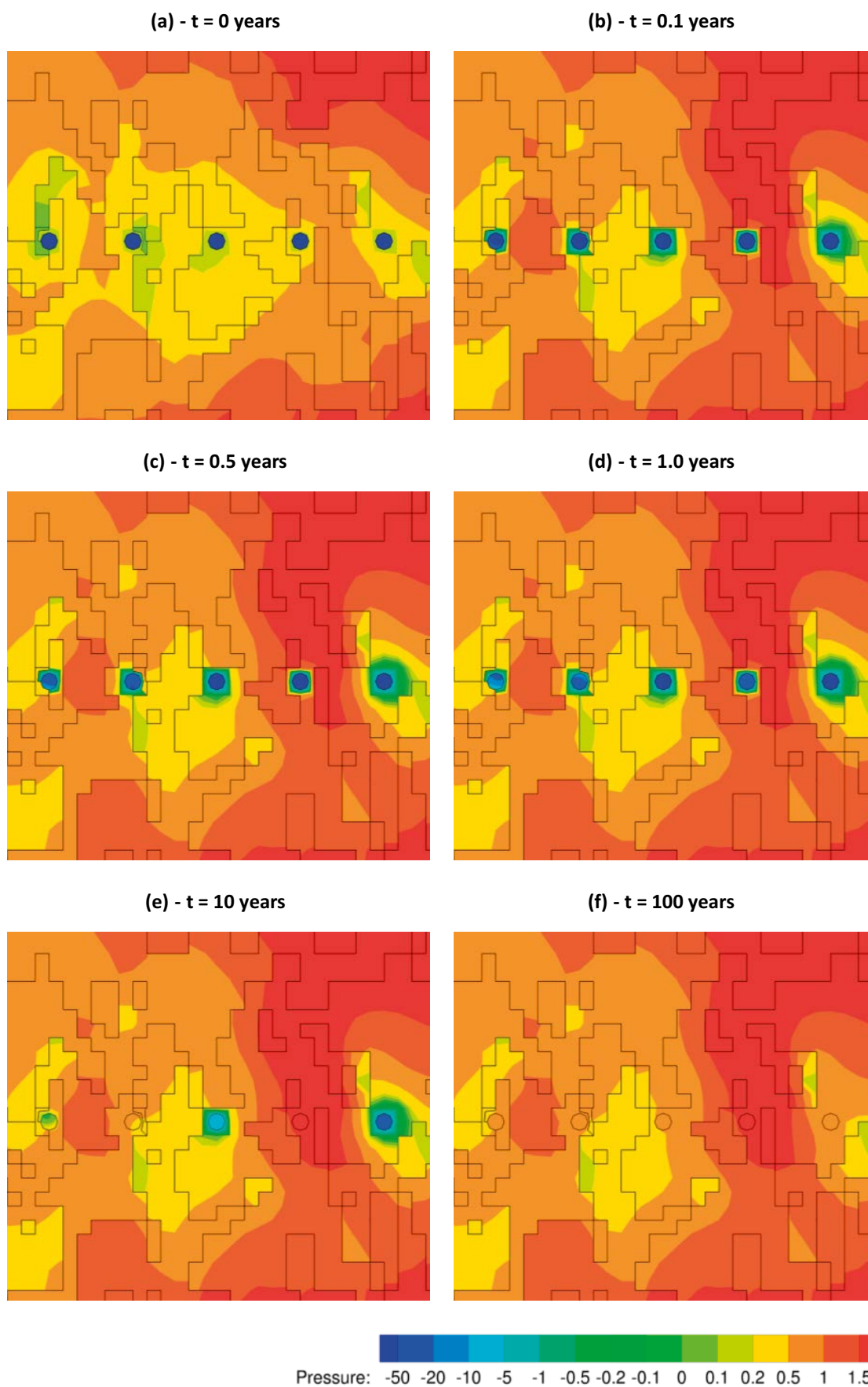
Figure A2-3. *Evolution of pressure (Pa) within the bentonite across a horizontal slice at −418 m elevation. Results are shown for the first realisation of the stochastic fracture network.*

(a) - t = 0 years

(b) - t = 0.1 years

(c) - t = 0.5 years

(d) - t = 1.0 years

(e) - t = 10 years

(f) - t = 100 years

Pressure: -50 -20 -10 -5 -1 -0.5 -0.2 -0.1 0 0.1 0.2 0.5 1 1.5
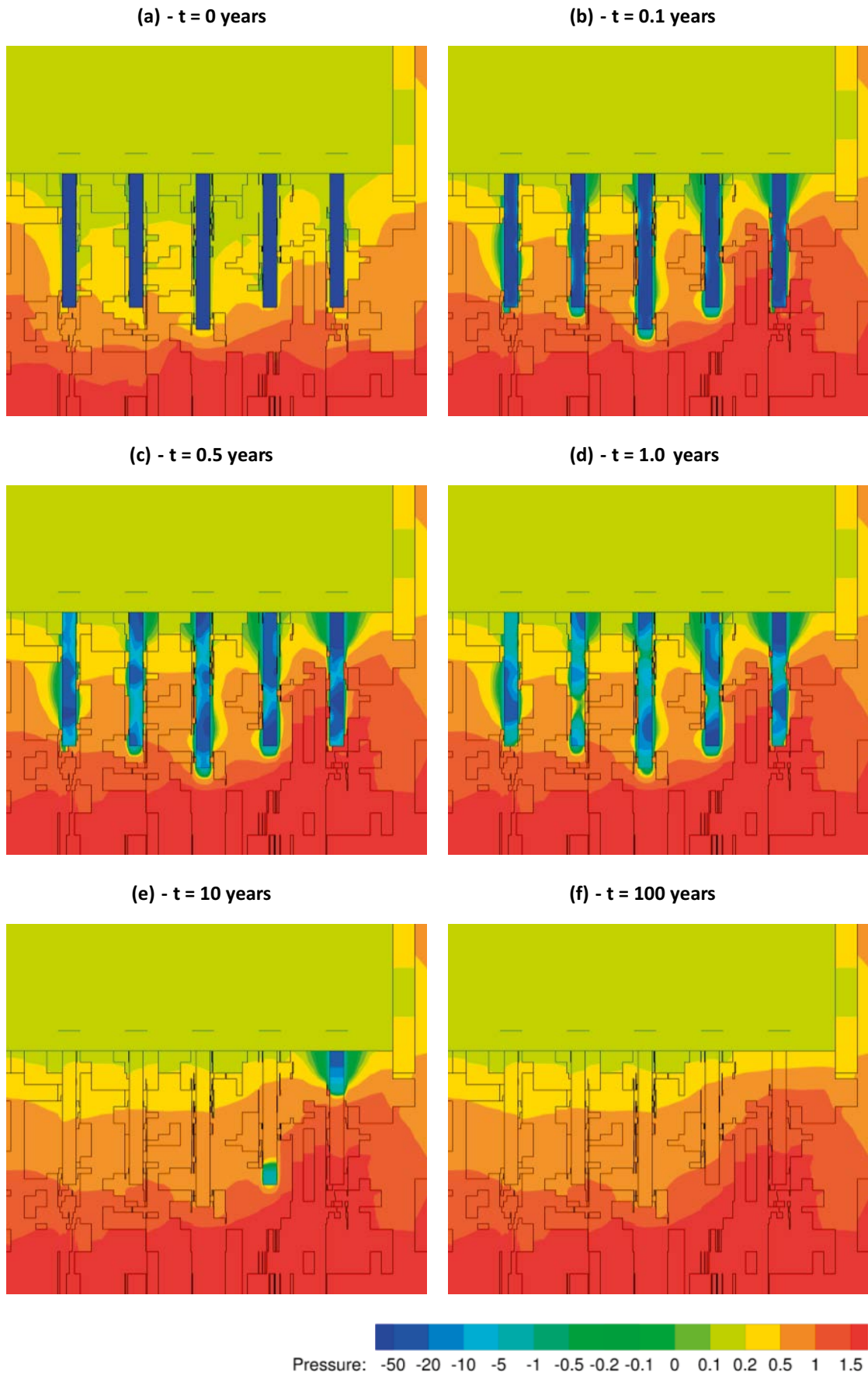
Figure A2-4. *Evolution of pressure (Pa) within the bentonite for a vertical slice including the deposition holes. Results are shown for the tenth realisation of the stochastic fracture network.*

(a) - t = 0 years

(b) - t = 0.1 years

(c) - t = 0.5 years

(d) - t = 1.0 years

(e) - t = 10 years

(f) - t = 100 years

Pressure: -50 -20 -10 -5 -1 -0.5 -0.2 -0.1 0 0.1 0.2 0.5 1 1.5
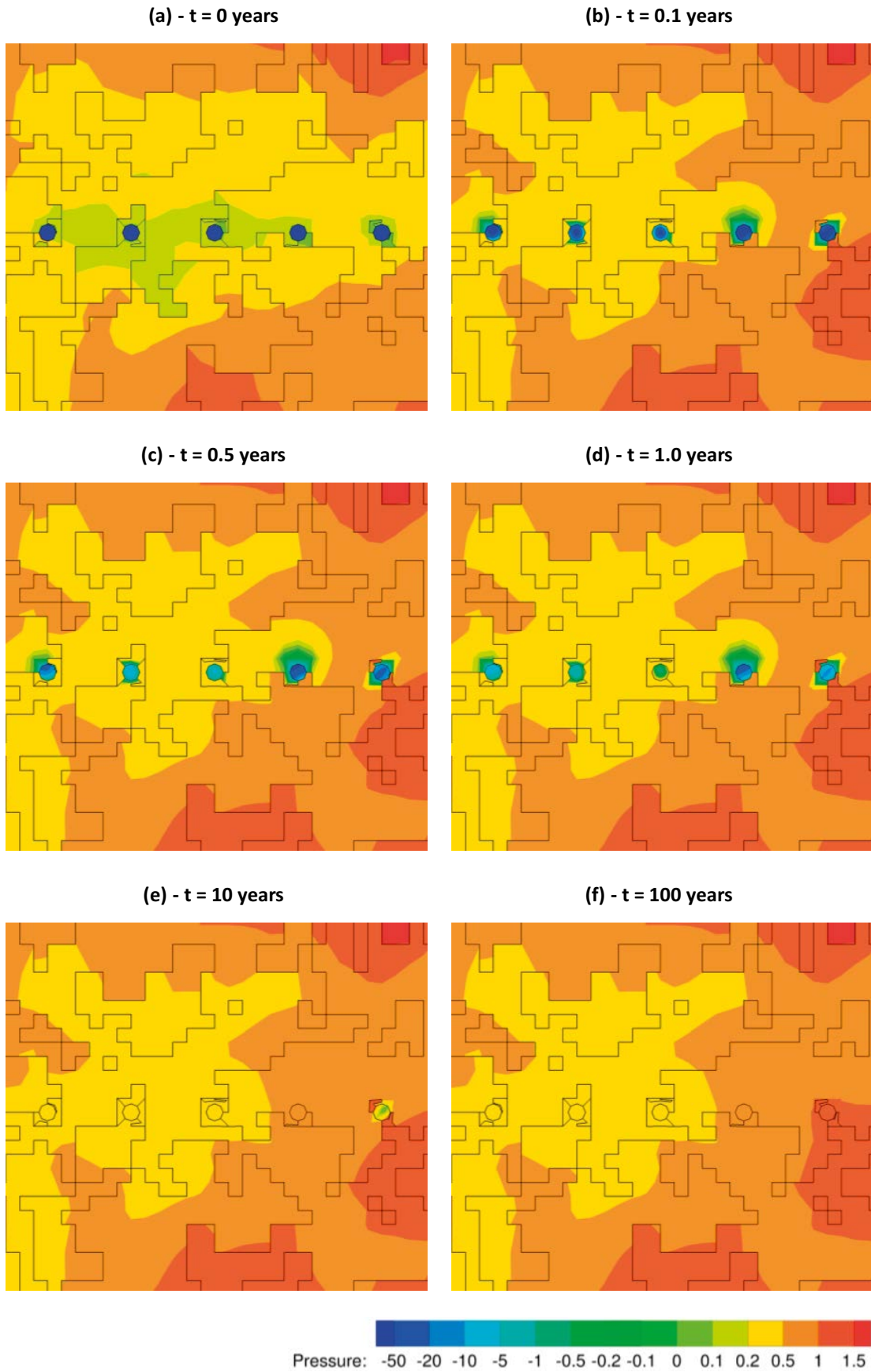
Figure A2-5. *Evolution of pressure (Pa) within the bentonite across a horizontal slice at −418 m elevation. Results are shown for the tenth realisation of the stochastic fracture network.*

(a) - t = 0 years   **(b) - t = 0.1 years**

(c) - t = 0.5 years   **(d) - t = 1.0 years**

(e) - t = 10 years   **(f) - t = 100 years**

Liquid Saturation: 0.3 0.35 0.4 0.45 0.5 0.55 0.6 0.65 0.7 0.75 0.8 0.85 0.9 0.92 0.94 0.96 0.98 0.99 1
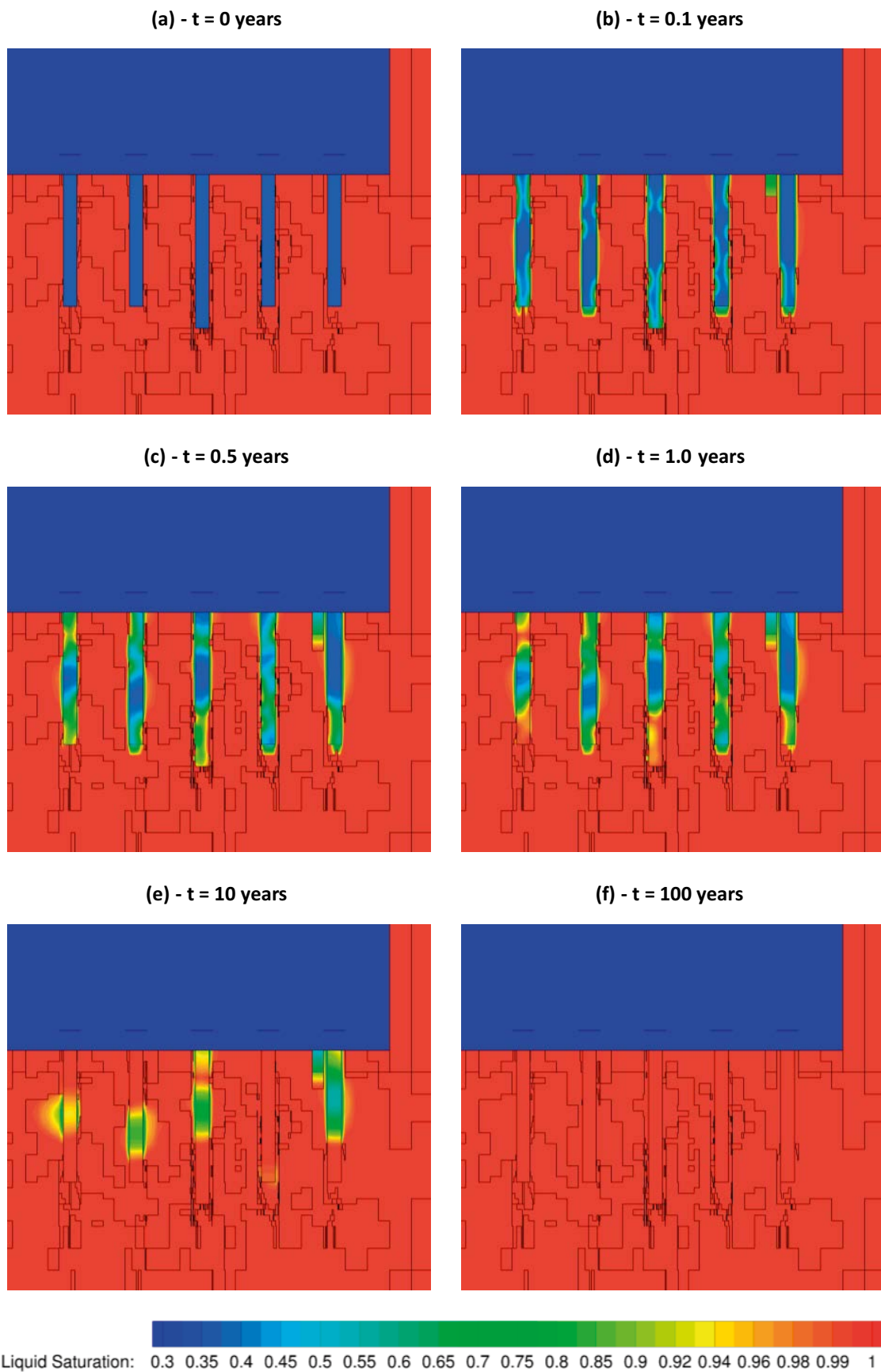
Figure A2-6. Evolution of saturation within the bentonite for a vertical slice including the deposition holes. Results are shown for the first realisation of the stochastic fracture network.

(a) - t = 0 years

(b) - t = 0.1 years

(c) - t = 0.5 years

(d) - t = 1.0 years

(e) - t = 10 years

(f) - t = 100 years

Liquid Saturation: 0.3 0.35 0.4 0.45 0.5 0.55 0.6 0.65 0.7 0.75 0.8 0.85 0.9 0.92 0.94 0.96 0.98 0.99 1

Figure A2-7. *Evolution of saturation within the bentonite across a horizontal slice at −418 m elevation. Results are shown for the first realisation of the stochastic fracture network.*

(a) - t = 0 years **(b) - t = 0.1 years**

(c) - t = 0.5 years **(d) - t = 1.0 years**

(e) - t = 10 years **(f) - t = 100 years**

Liquid Saturation: 0.3 0.35 0.4 0.45 0.5 0.55 0.6 0.65 0.7 0.75 0.8 0.85 0.9 0.92 0.94 0.96 0.98 0.99 1

Figure A2-8. *Evolution of saturation within the bentonite for a vertical slice including the deposition holes. Results are shown for the tenth realisation of the stochastic fracture network.*

(a) - t = 0 years

(b) - t = 0.1 years

(c) - t = 0.5 years

(d) - t = 1.0 years

(e) - t = 10 years

(f) - t = 100 years

Liquid Saturation: 0.3 0.35 0.4 0.45 0.5 0.55 0.6 0.65 0.7 0.75 0.8 0.85 0.9 0.92 0.94 0.96 0.98 0.99 1

Figure A2-9. *Evolution of saturation within the bentonite across a horizontal slice at −418 m elevation. Results are shown for the tenth realisation of the stochastic fracture network.*

(a) – 0.75 m

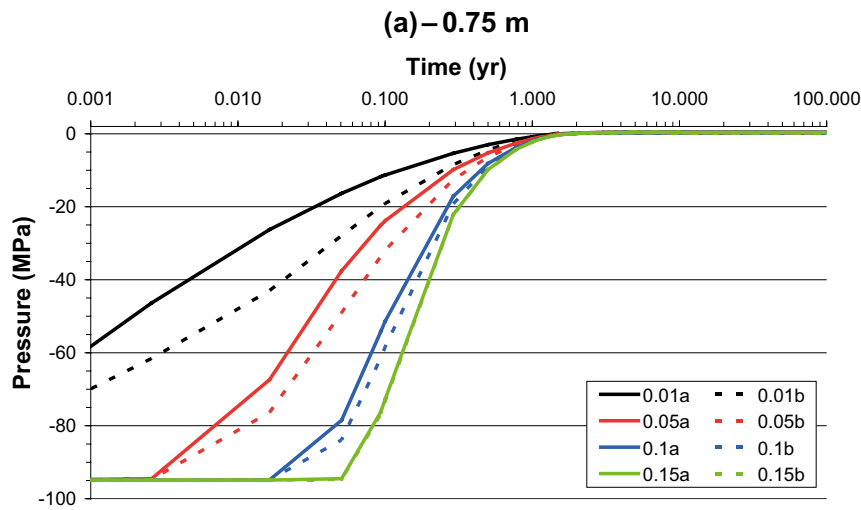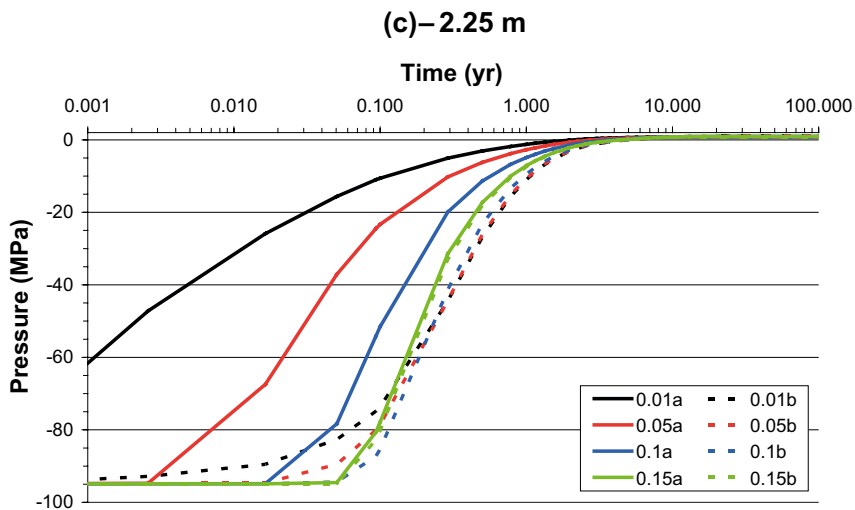**(b) – 1.5 m**

(c) – 2.25 m
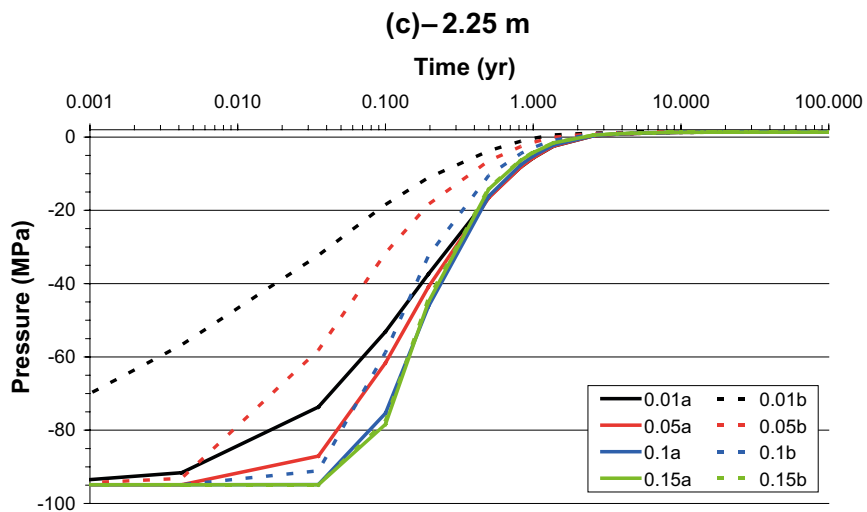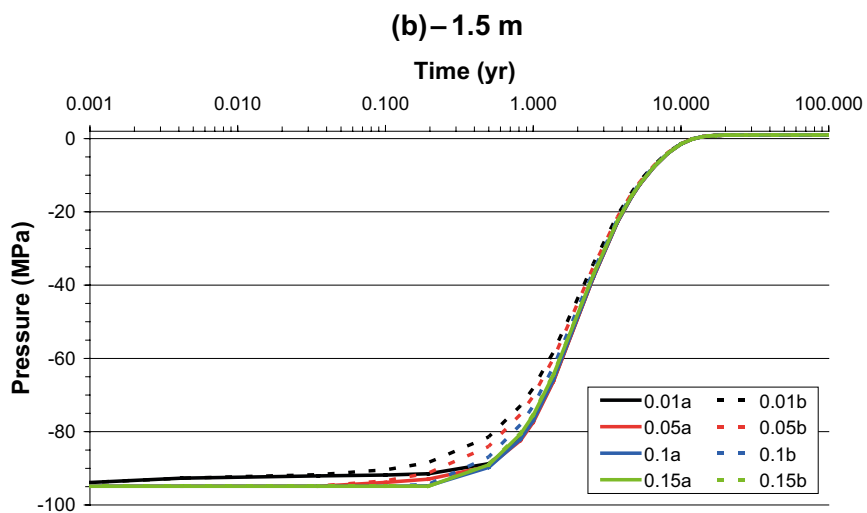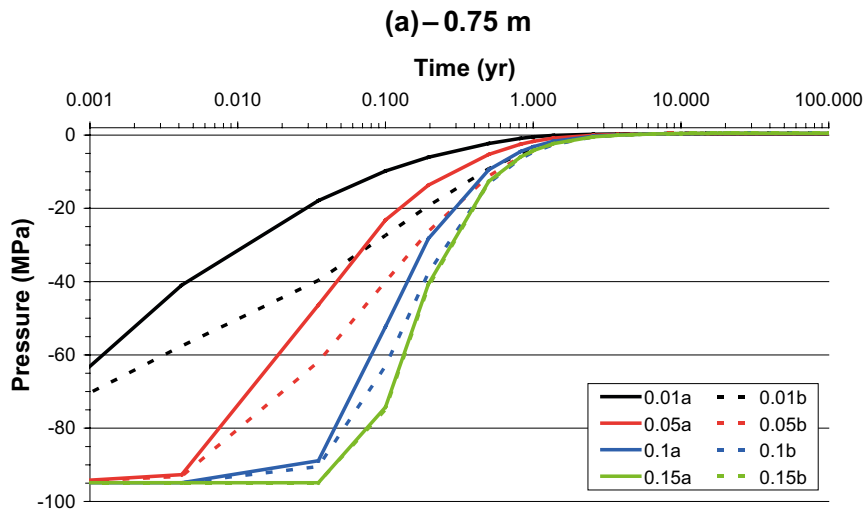
***Figure A2-10.** Pressure within the bentonite 0.01 m, 0.05 m, 0.1 m, and 0.15 m from the deposition borehole wall. Results are shown for a slice parallel to the boreholes, with "a" and "b" distances denoting direction from the edge of the deposition hole. The pressure curves shown correspond to the first realisation of the stochastic fracture network. Figures (a, b, c) are for borehole KO0014G01 at depths of 0.75 m, 1.5 m and 2.25 m respectively.*
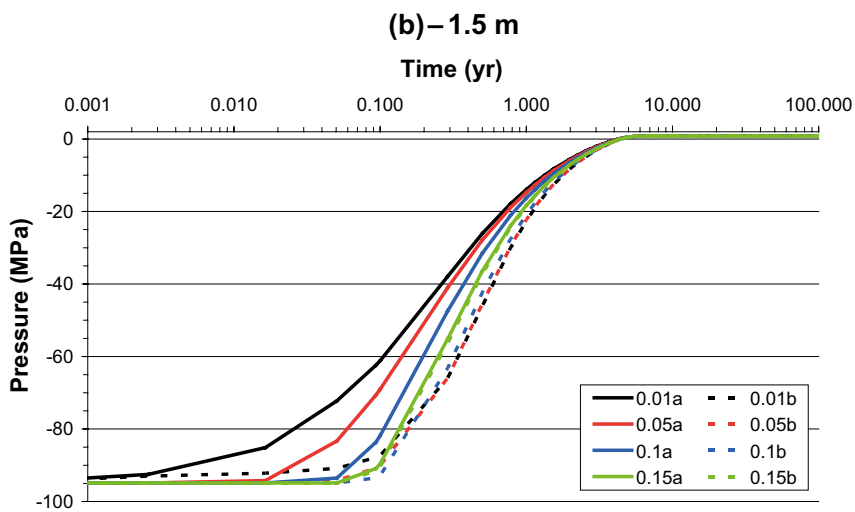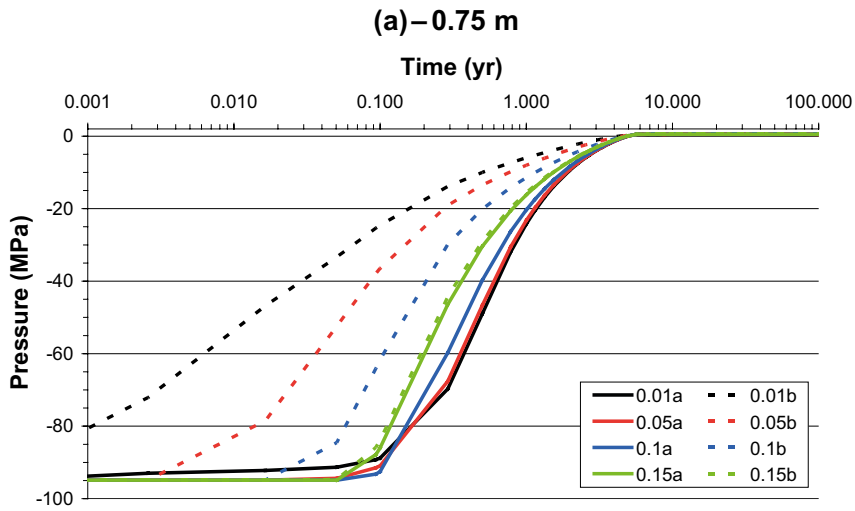
(a) – 0.75 m

(b) – 1.5 m

(c) – 2.25m
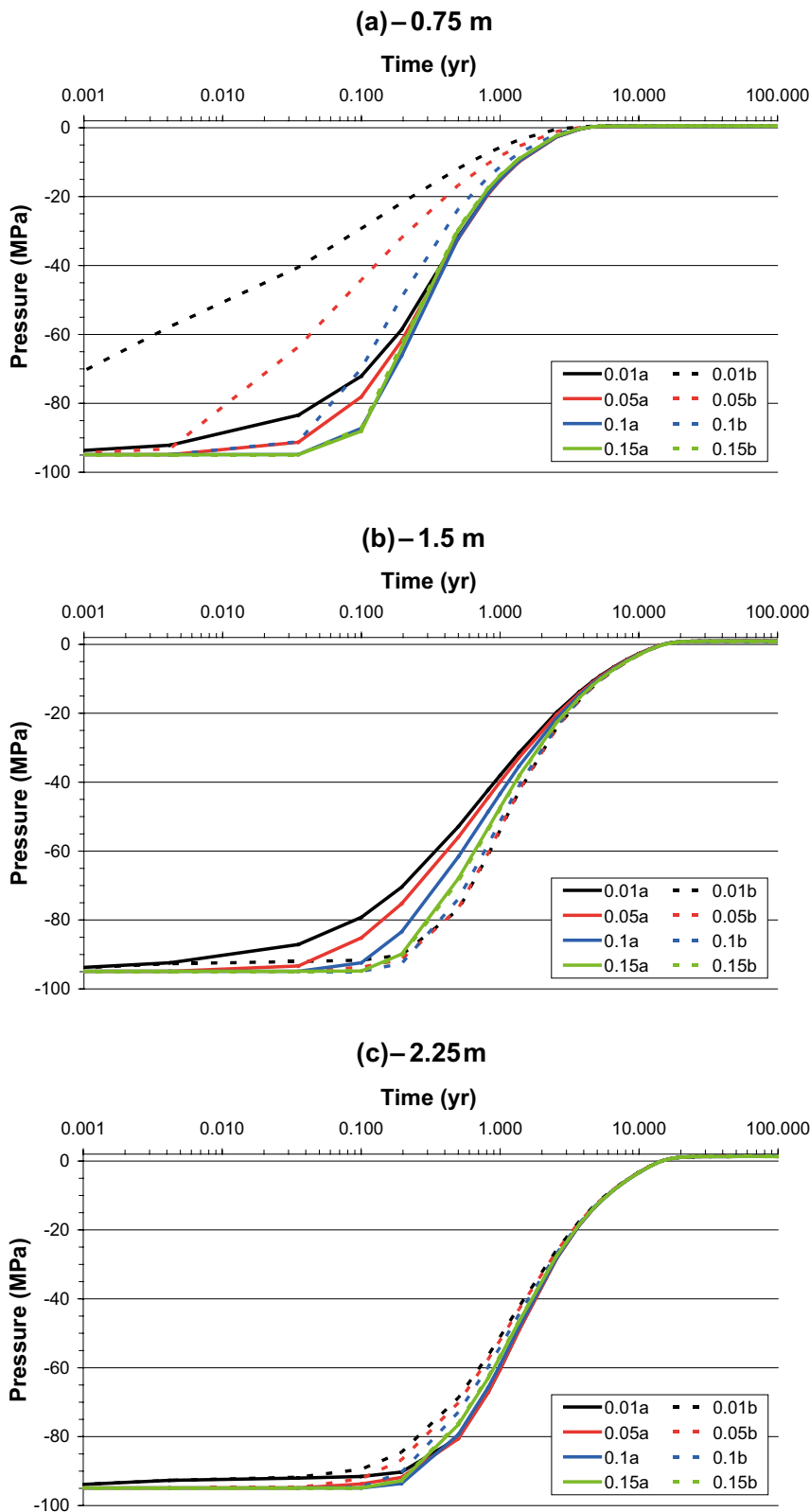
Figure A2-11. *Pressure within the bentonite 0.01 m, 0.05 m, 0.1 m, and 0.15 m from the deposition borehole wall. Results are shown for a slice parallel to the boreholes, with "a" and "b" distances denoting direction from the edge of the deposition hole. The pressure curves shown correspond to the first realisation of the stochastic fracture network. Figures (a, b, c) are for borehole KO0015G01 at depths of 0.75 m, 1.5 m and 2.25 m respectively.*
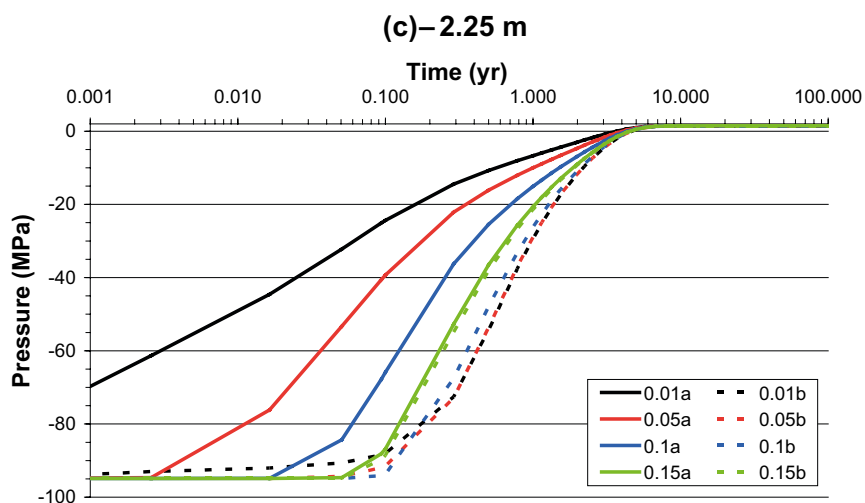
(a) – 0.75 m

(b) – 1.5 m

(c) – 2.25 m
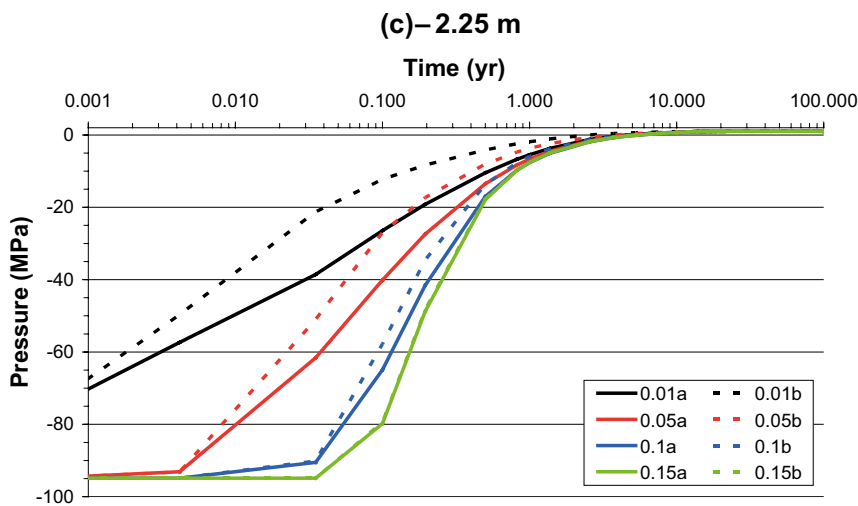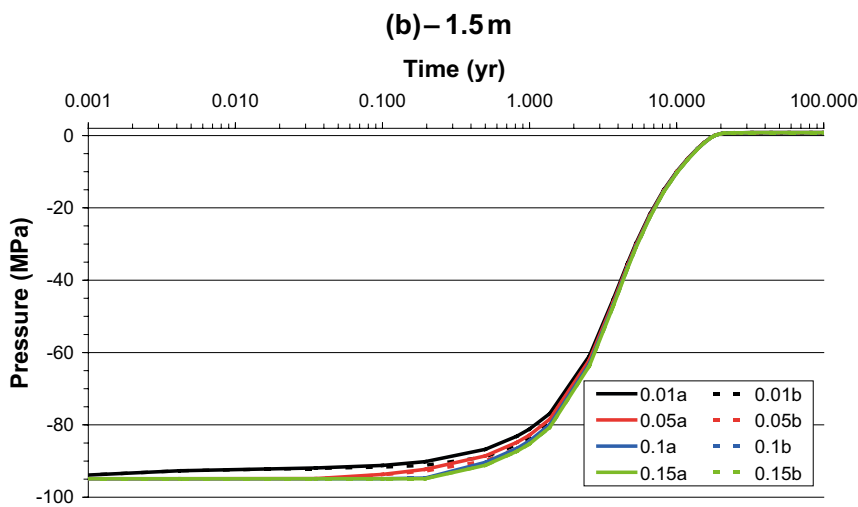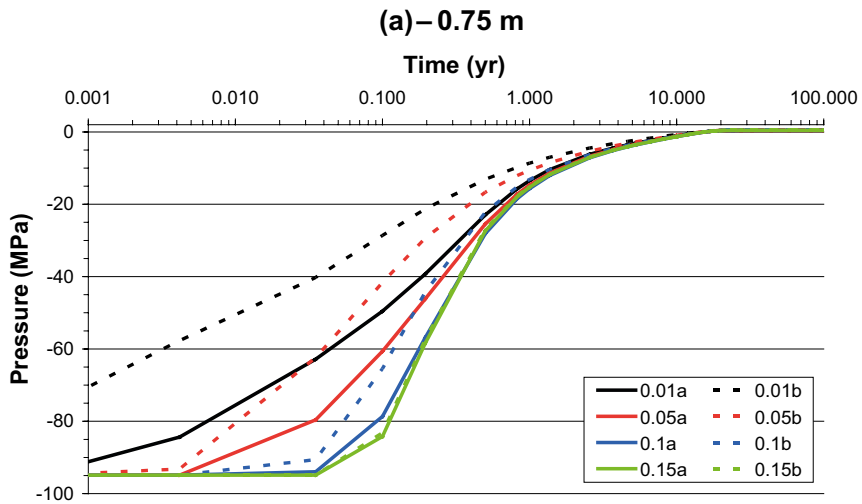
Figure A2-12. *Pressure within the bentonite 0.01 m, 0.05 m, 0.1 m, and 0.15 m from the deposition borehole wall. Results are shown for a slice parallel to the boreholes, with "a" and "b" distances denoting direction from the edge of the deposition hole. The pressure curves shown correspond to the first realisation of the stochastic fracture network. Figures (a, b, c) are for borehole KO0017G01 at depths of 0.75 m, 1.5 m and 2.25 m respectively.*
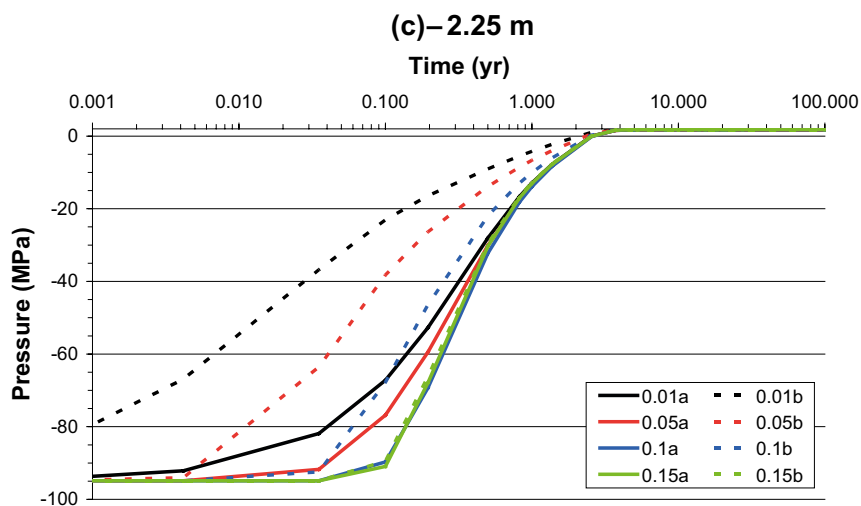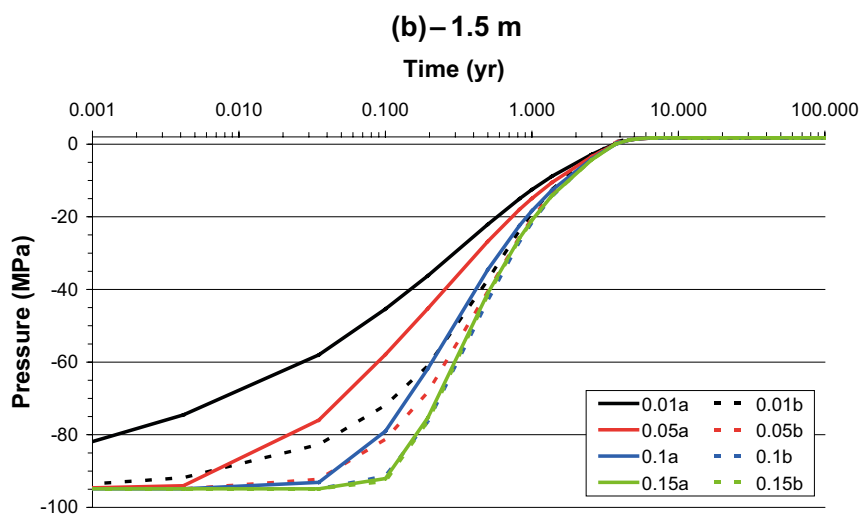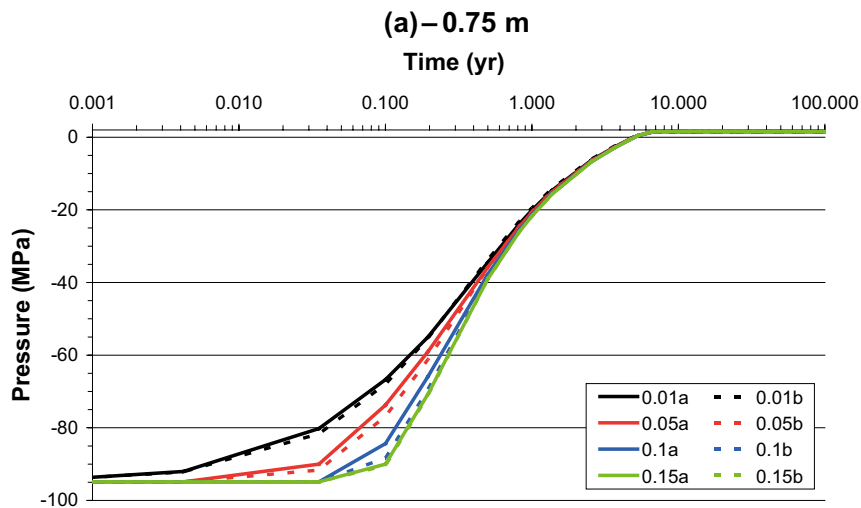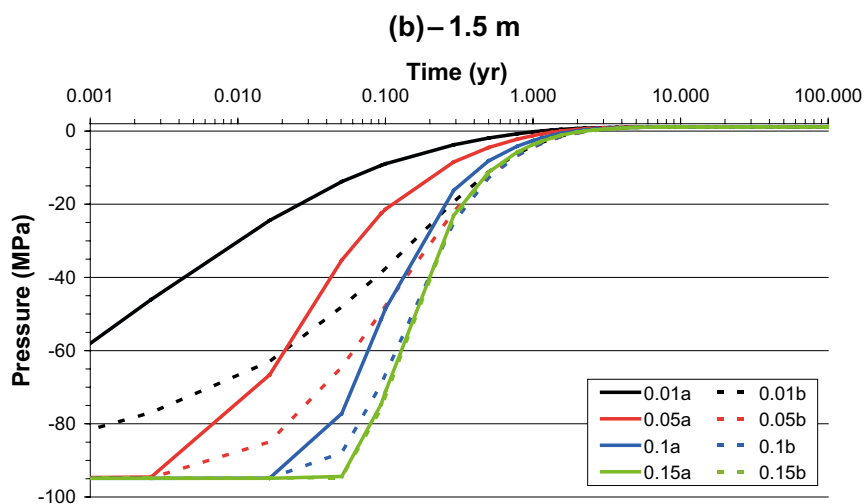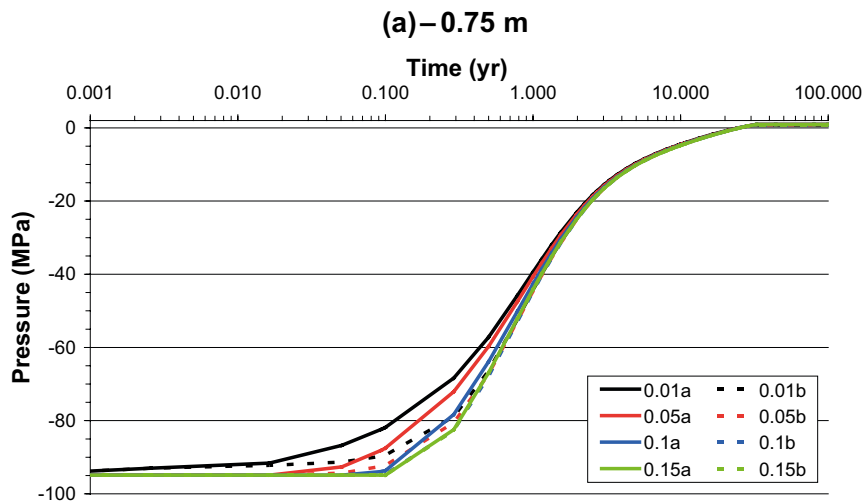
Figure A2-13. *Pressure within the bentonite 0.01 m, 0.05 m, 0.1 m, and 0.15 m from the deposition borehole wall. Results are shown for a slice parallel to the boreholes, with "a" and "b" distances denoting direction from the edge of the deposition hole. The pressure curves shown correspond to the first realisation of the stochastic fracture network. Figures (a, b, c) are for borehole KO0018G01 at depths of 0.75 m, 1.5 m and 2.25 m respectively.*
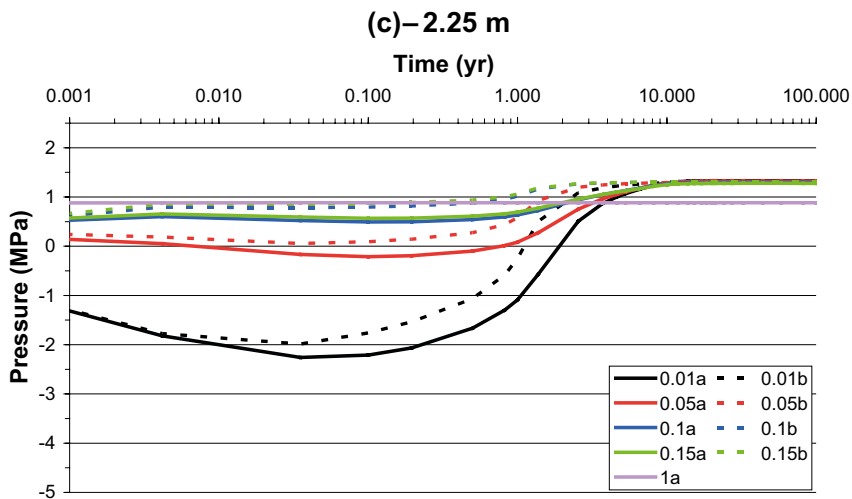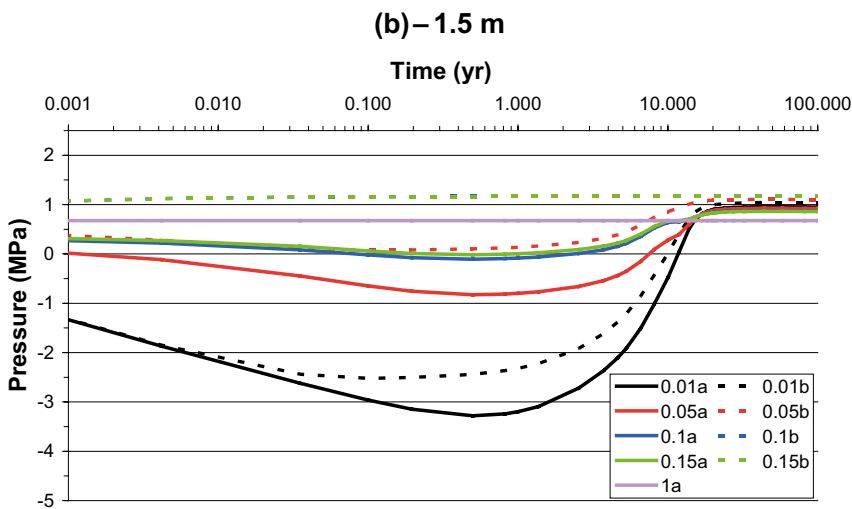
(a) – 0.75 m

(b) – 1.5 m

(c) – 2.25 m
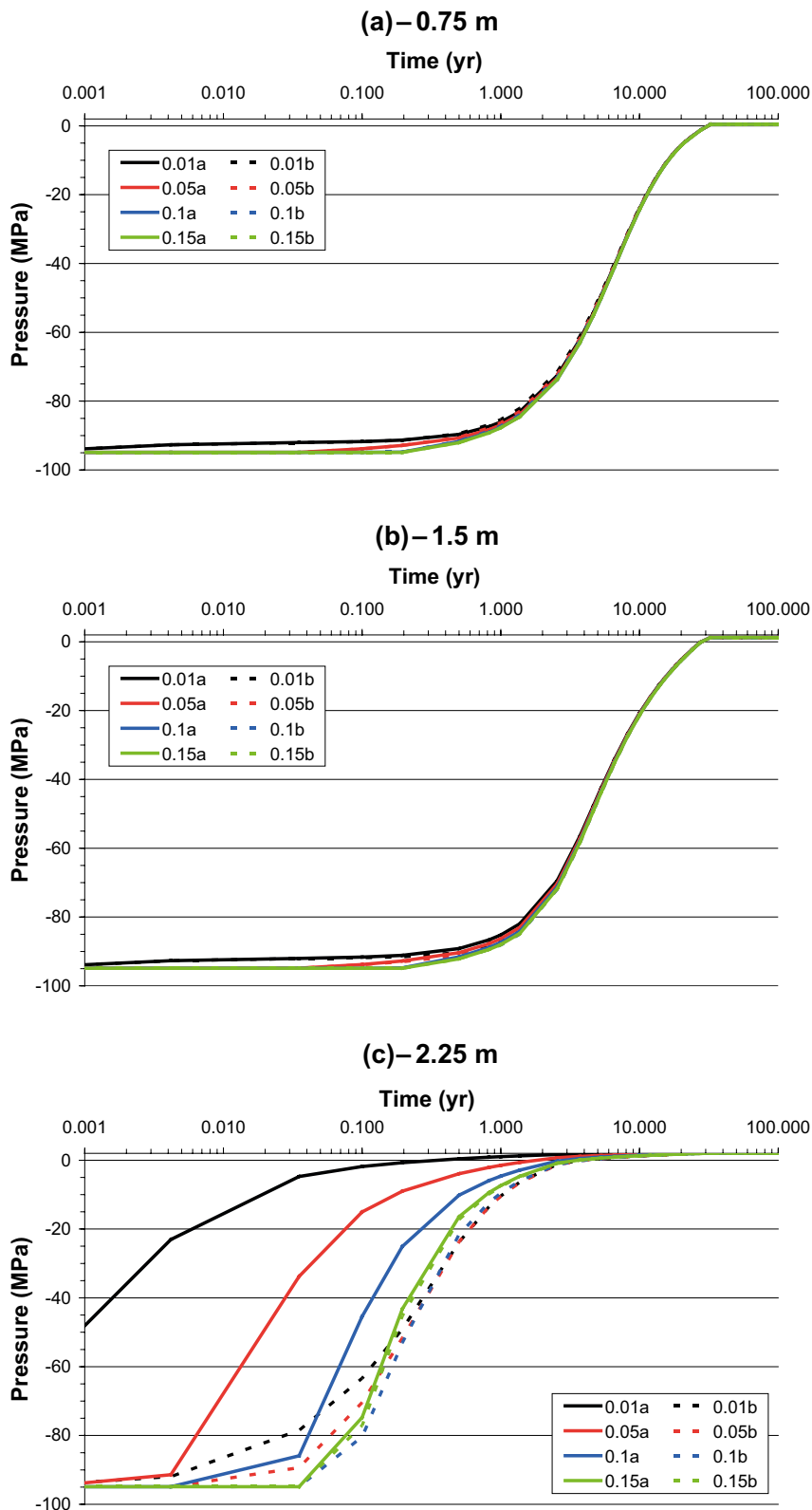
Figure A2-14. *Pressure within the bentonite 0.01 m, 0.05 m, 0.1 m, and 0.15 m from the deposition borehole wall. Results are shown for a slice parallel to the boreholes, with "a" and "b" distances denoting direction from the edge of the deposition hole. The pressure curves shown correspond to the first realisation of the stochastic fracture network. Figures (a, b, c) are for borehole KO0020G01 at depths of 0.75 m, 1.5 m and 2.25 m respectively.*
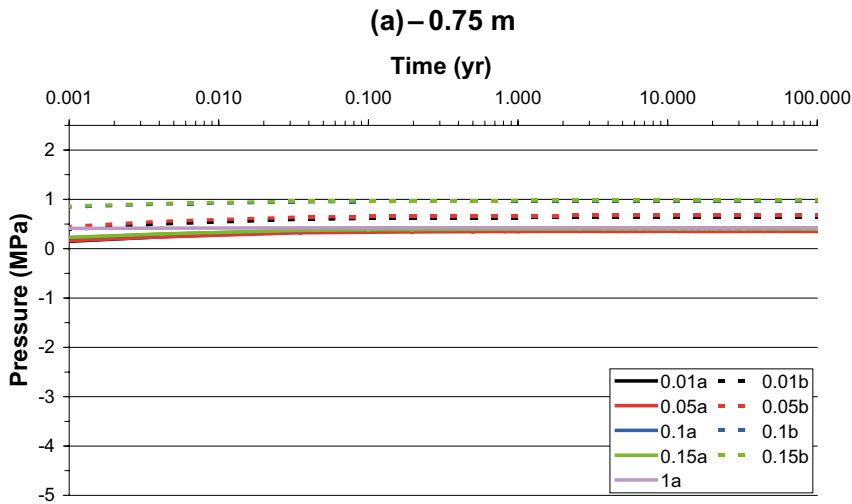
(a) – 0.75 m

(b) – 1.5 m

(c) – 2.25 m
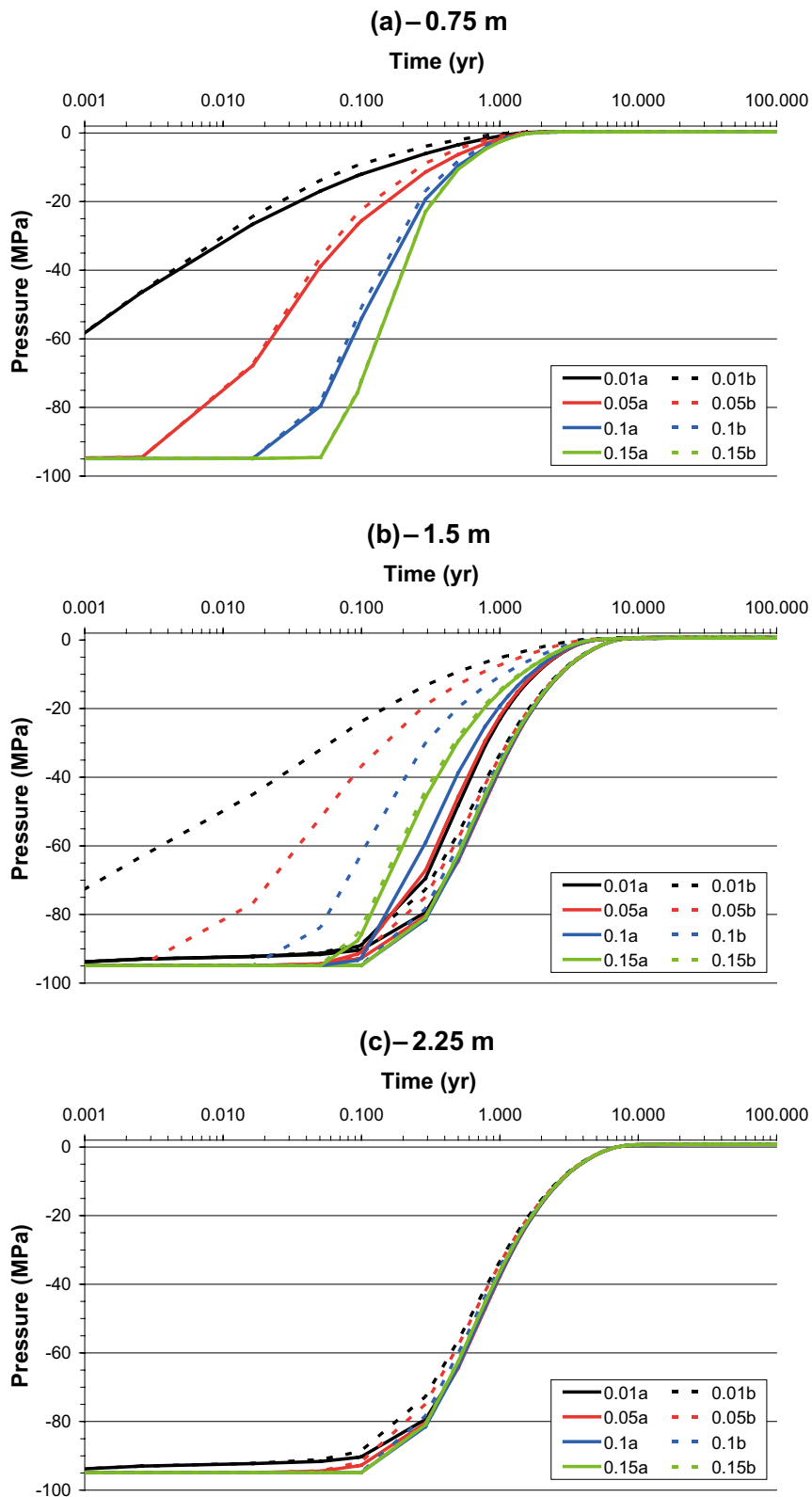
Figure A2-15. *Pressure within the bentonite 0.01 m, 0.05 m, 0.1 m, and 0.15 m from the deposition borehole wall. Results are shown for a slice parallel to the boreholes, with "a" and "b" distances denoting direction from the edge of the deposition hole. The pressure curves shown correspond to the tenth realisation of the stochastic fracture network. Figures (a, b, c) are for borehole KO0014G01 at depths of 0.75 m, 1.5 m and 2.25 m respectively.*
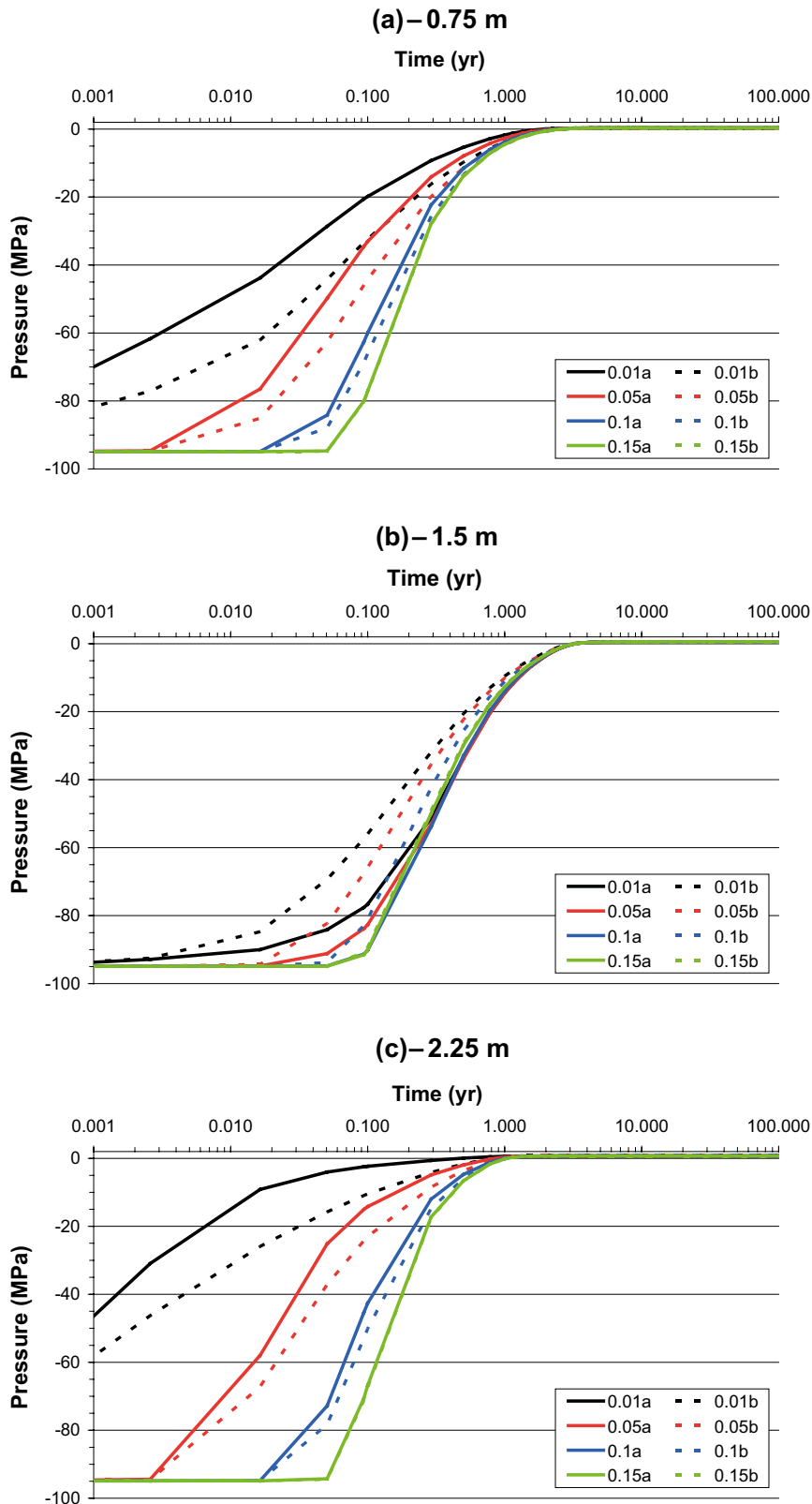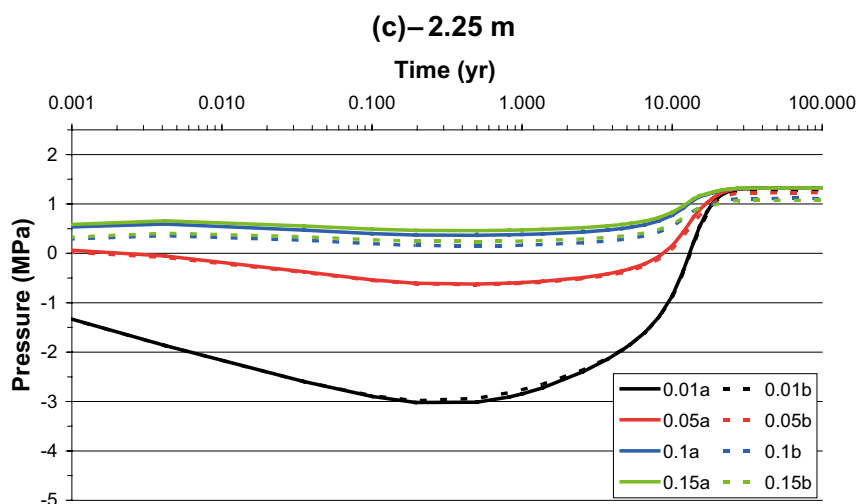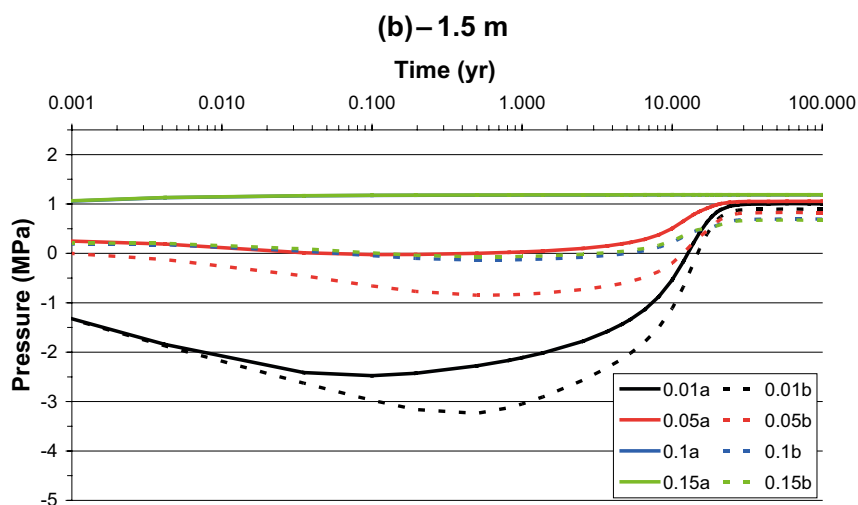
Figure A2-16. *Pressure within the bentonite 0.01 m, 0.05 m, 0.1 m, and 0.15 m from the deposition borehole wall. Results are shown for a slice parallel to the boreholes, with "a" and "b" distances denoting direction from the edge of the deposition hole. The pressure curves shown correspond to the tenth realisation of the stochastic fracture network. Figures (a, b, c) are for borehole KO0015G01 at depths of 0.75 m, 1.5 m and 2.25 m respectively.*

(a) – 0.75 m

Time (yr)

(b) – 1.5 m

Time (yr)

(c) – 2.25 m

Time (yr)
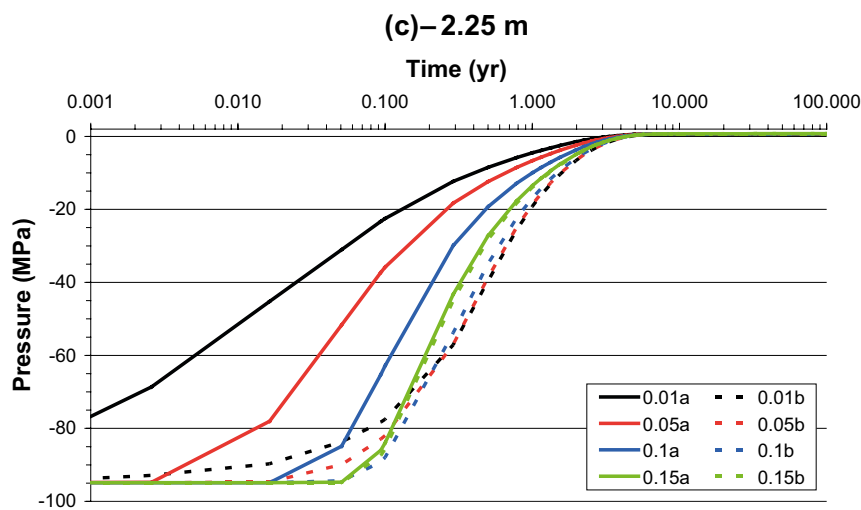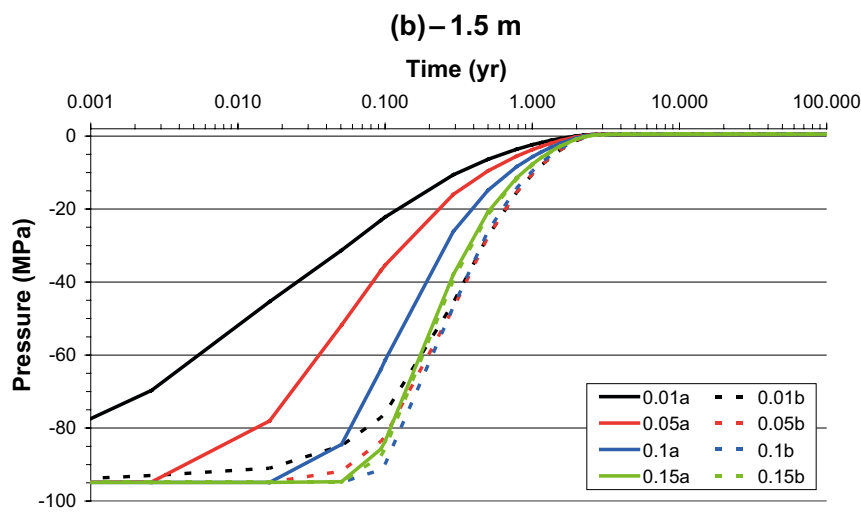
Figure A2-17. *Pressure within the bentonite 0.01 m, 0.05 m, 0.1 m, and 0.15 m from the deposition borehole wall. Results are shown for a slice parallel to the boreholes, with "a" and "b" distances denoting direction from the edge of the deposition hole. The pressure curves shown correspond to the tenth realisation of the stochastic fracture network. Figures (a, b, c) are for borehole KO0017G01 at depths of 0.75 m, 1.5 m and 2.25 m respectively.*

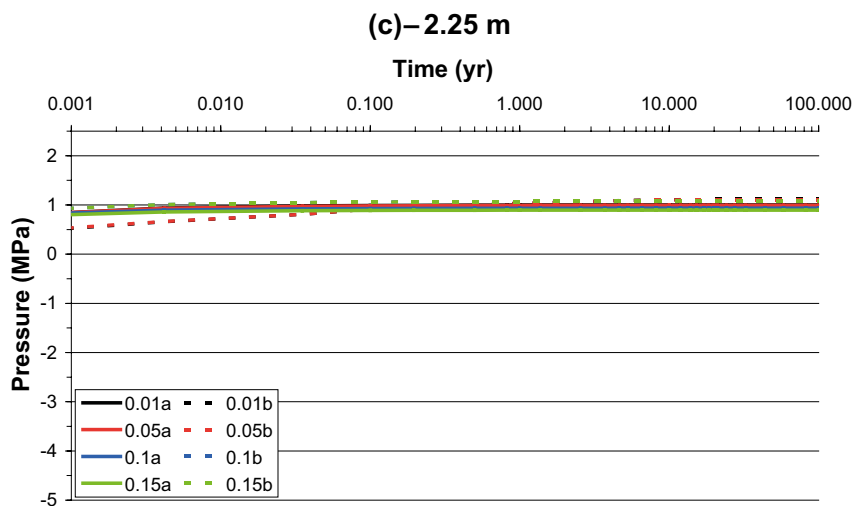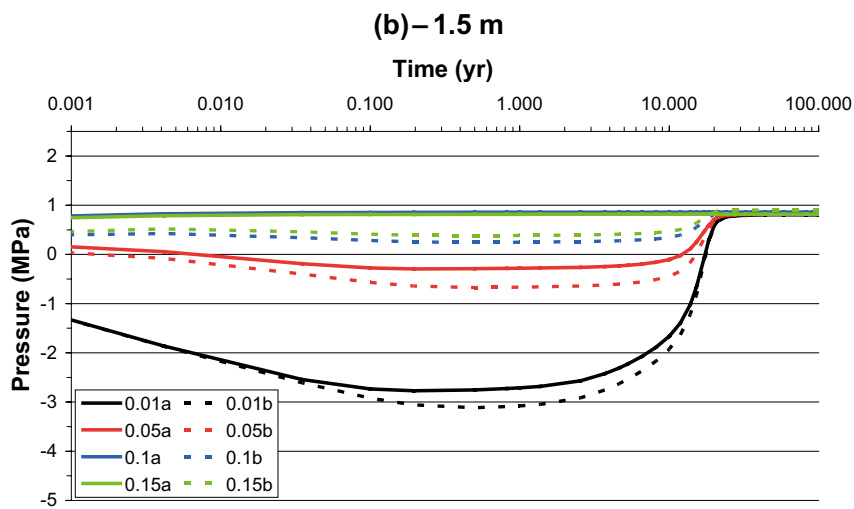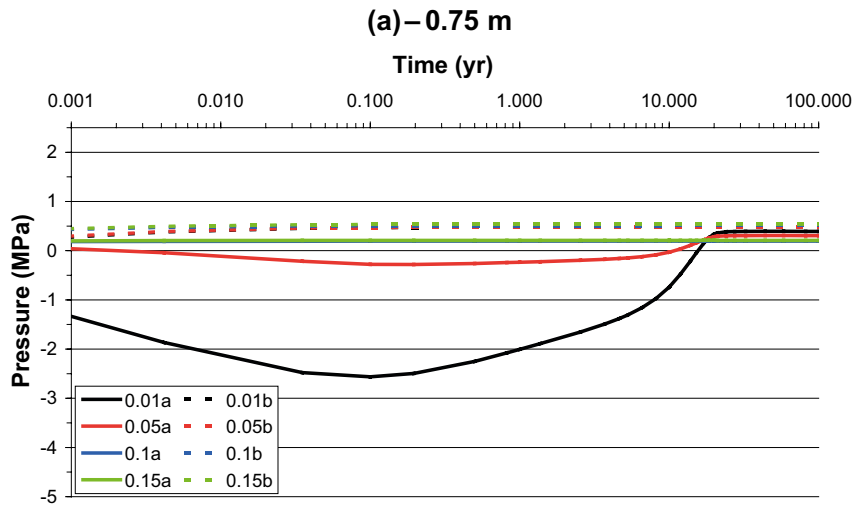**Figure A2-18.** *Pressure within the bentonite 0.01 m, 0.05 m, 0.1 m, and 0.15 m from the deposition borehole wall. Results are shown for a slice parallel to the boreholes, with "a" and "b" distances denoting direction from the edge of the deposition hole. The pressure curves shown correspond to the tenth realisation of the stochastic fracture network. Figures (a, b, c) are for borehole KO0018G01 at depths of 0.75 m, 1.5 m and 2.25 m respectively.*
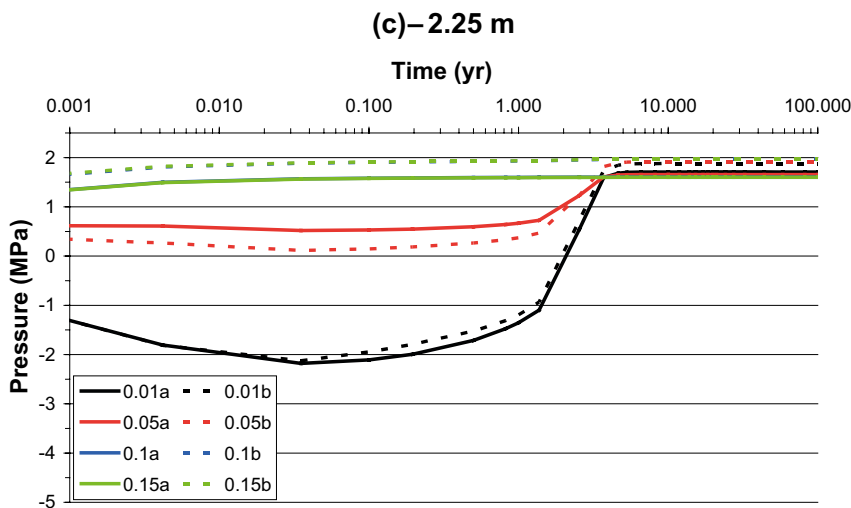
(a) – 0.75 m

(b) – 1.5 m

(c) – 2.25 m

Figure A2-19. *Pressure within the bentonite 0.01 m, 0.05 m, 0.1 m, and 0.15 m from the deposition borehole wall. Results are shown for a slice parallel to the boreholes, with "a" and "b" distances denoting direction from the edge of the deposition hole. The pressure curves shown correspond to the tenth realisation of the stochastic fracture network. Figures (a, b, c) are for borehole KO0020G01 at depths of 0.75 m, 1.5 m and 2.25 m respectively.*
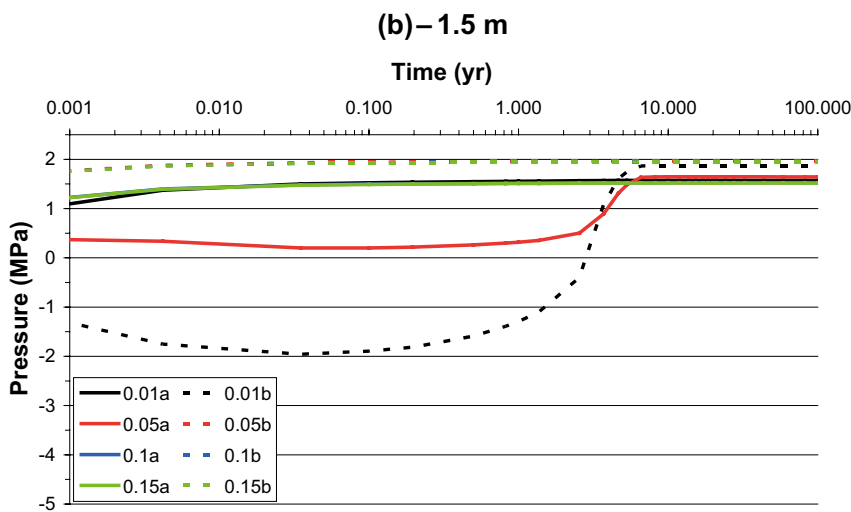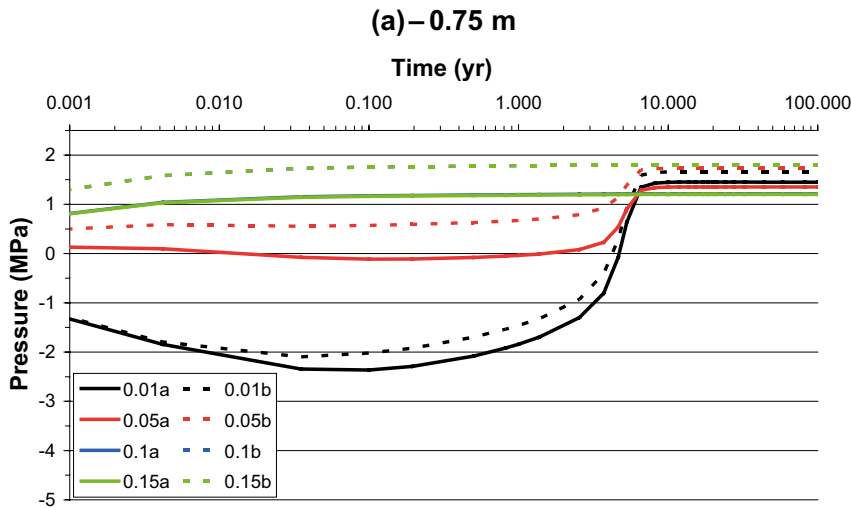
(a) – 0.75 m

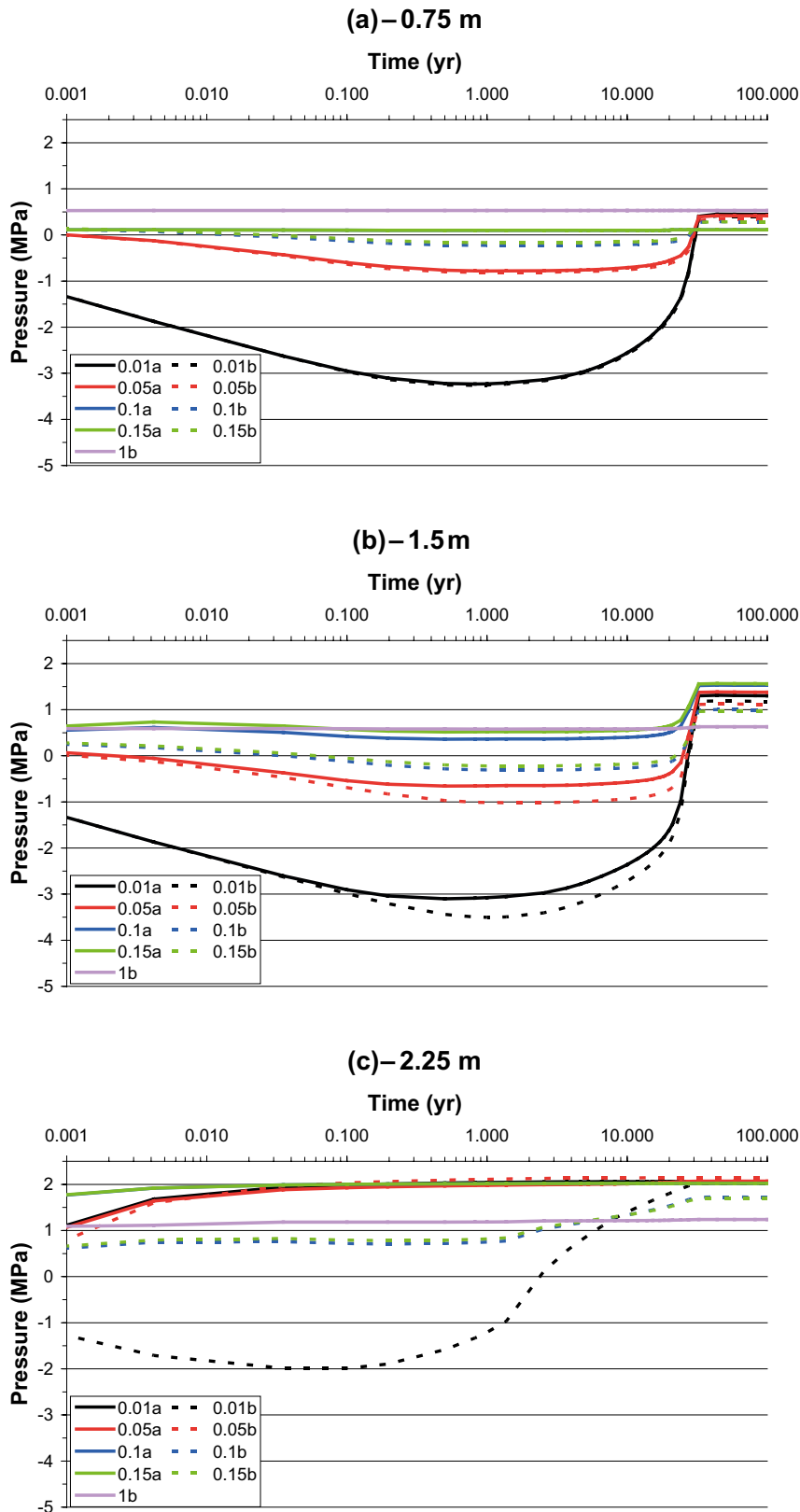**(b) – 1.5 m**

(c) – 2.25 m

Figure A2-20. Pressure within the bedrock 0.01 m, 0.05 m, 0.1 m, 0.15 m, 1.0 m and 5.0 m (outward only) from the deposition borehole wall. Results are shown for a slice parallel to the boreholes, with "a" and "b" distances denoting direction from the edge of the deposition hole. The pressure curves shown correspond to the first realisation of the stochastic fracture network. Figures (a, b, c) are for borehole KO0014G01 at depths of 0.75 m, 1.5 m and 2.25 m respectively.

(a) – 0.75 m

(b) – 1.5 m

(c) – 2.25 m
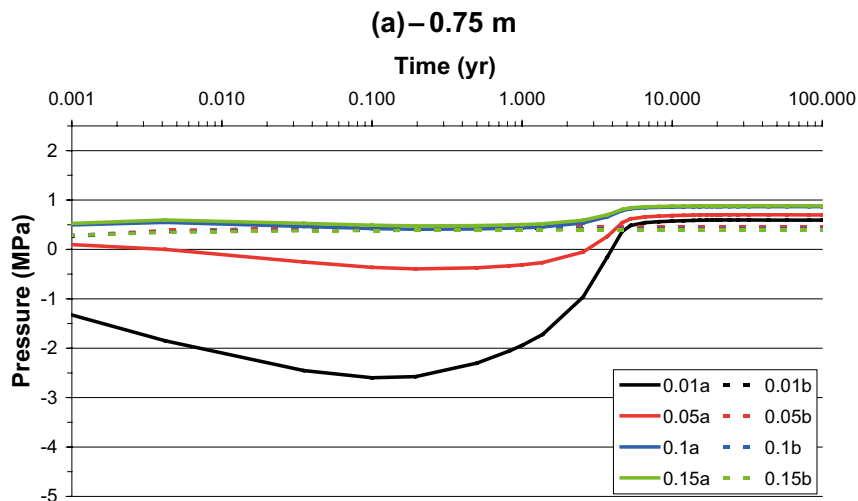
Figure A2-21. *Pressure within the bedrock 0.01 m, 0.05 m, 0.1 m, 0.15 m, and 1.0 m from the deposition borehole wall. Results are shown for a slice parallel to the boreholes, with "a" and "b" distances denoting direction from the edge of the deposition hole. The pressure curves shown correspond to the first realisation of the stochastic fracture network. Figures (a, b, c) are for borehole KO0015G01 at depths of 0.75 m, 1.5 m and 2.25 m respectively.*
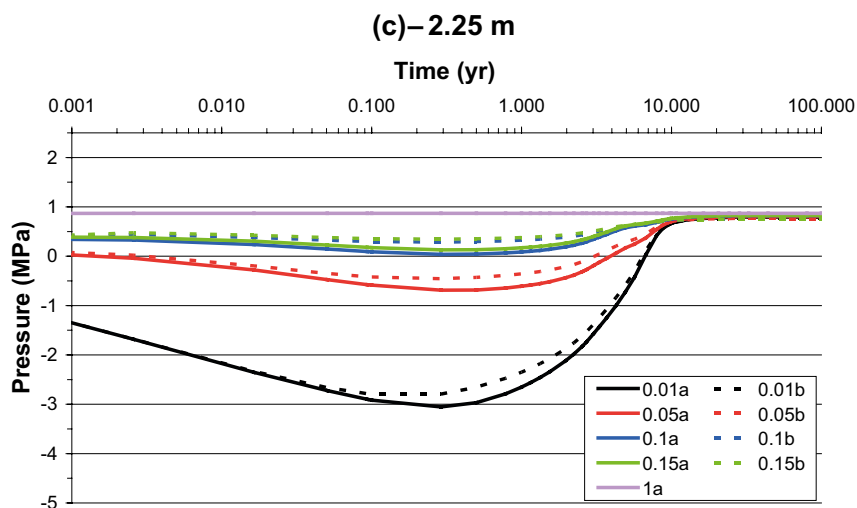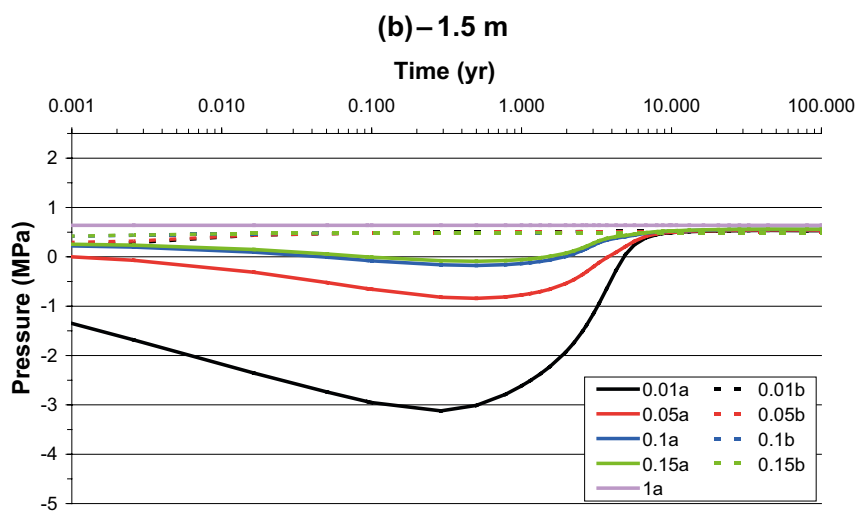
(a) – 0.75 m

Time (yr)

(b) – 1.5 m

Time (yr)

(c) – 2.25 m

Time (yr)

Figure A2-22. Pressure within the bedrock 0.01 m, 0.05 m, 0.1 m, 0.15 m, and 1.0 m from the deposition borehole wall. Results are shown for a slice parallel to the boreholes, with "a" and "b" distances denoting direction from the edge of the deposition hole. The pressure curves shown correspond to the first realisation of the stochastic fracture network. Figures (a, b, c) are for borehole KO0017G01 at depths of 0.75 m, 1.5 m and 2.25 m respectively.
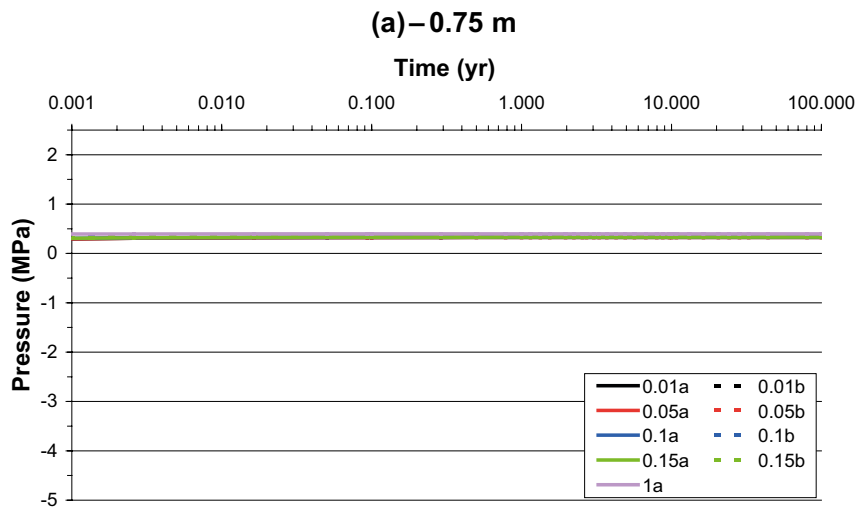
(a) – 0.75 m

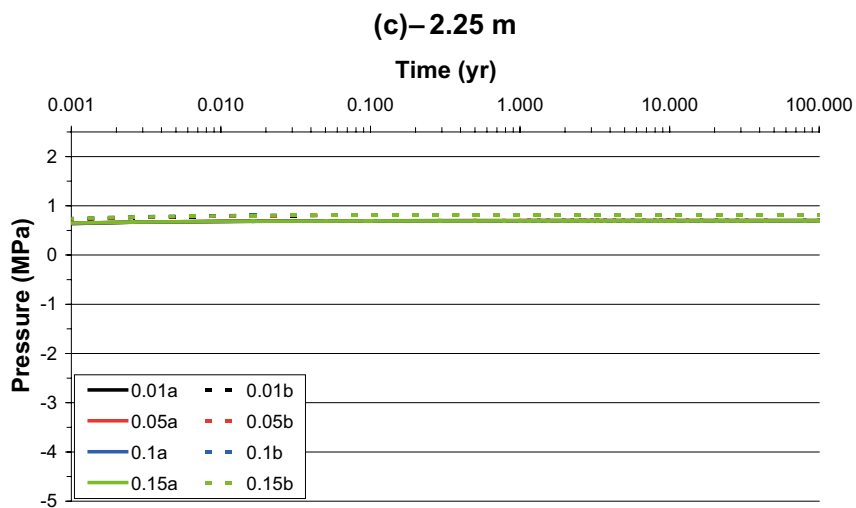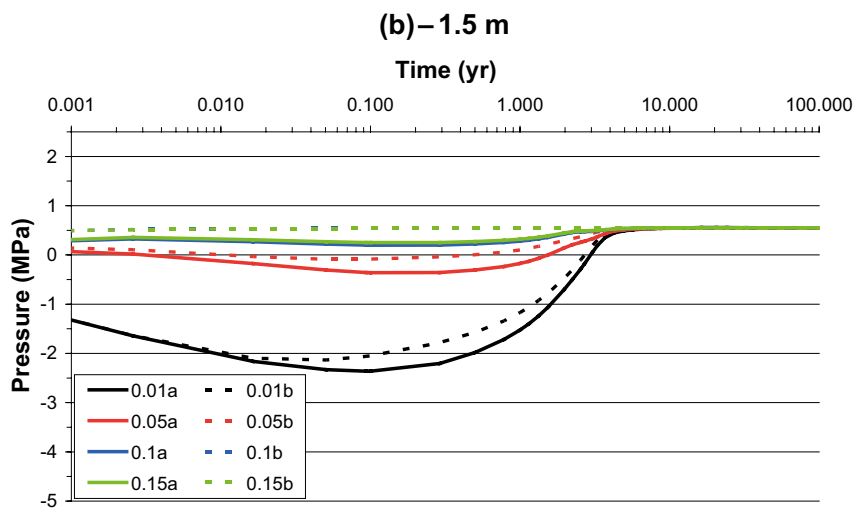**(b) – 1.5 m**

(c) – 2.25 m

Figure A2-23. Pressure within the bedrock 0.01 m, 0.05 m, 0.1 m, 0.15 m, and 1.0 m from the deposition borehole wall. Results are shown for a slice parallel to the boreholes, with "a" and "b" distances denoting direction from the edge of the deposition hole. The pressure curves shown correspond to the first realisation of the stochastic fracture network. Figures (a, b, c) are for borehole KO0018G01 at depths of 0.75 m, 1.5 m and 2.25 m respectively.
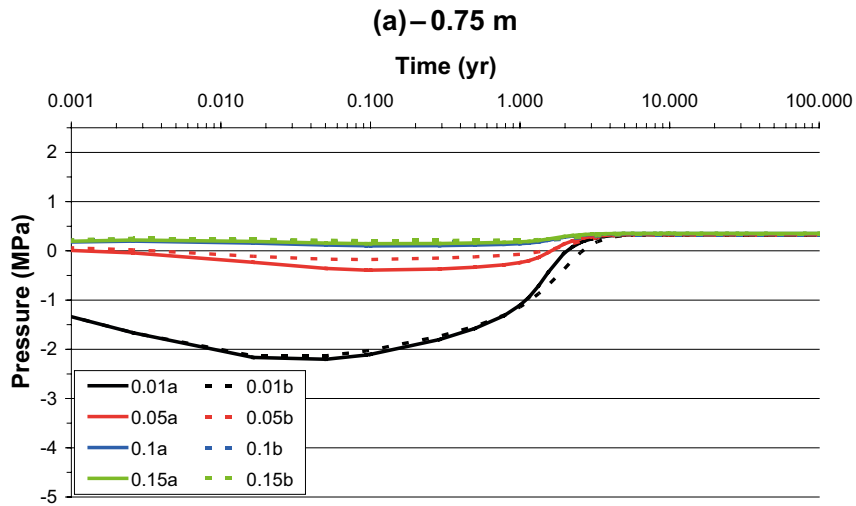
(a) – 0.75 m

(b) – 1.5 m

(c) – 2.25 m

Figure A2-24. Pressure within the bedrock 0.01 m, 0.05 m, 0.1 m, 0.15 m, 1.0 m and 5.0 m (outward only) from the deposition borehole wall. Results are shown for a slice parallel to the boreholes, with "a" and "b" distances denoting direction from the edge of the deposition hole. The pressure curves shown correspond to the first realisation of the stochastic fracture network. Figures (a, b, c) are for borehole KO0020G01 at depths of 0.75 m, 1.5 m and 2.25 m respectively.
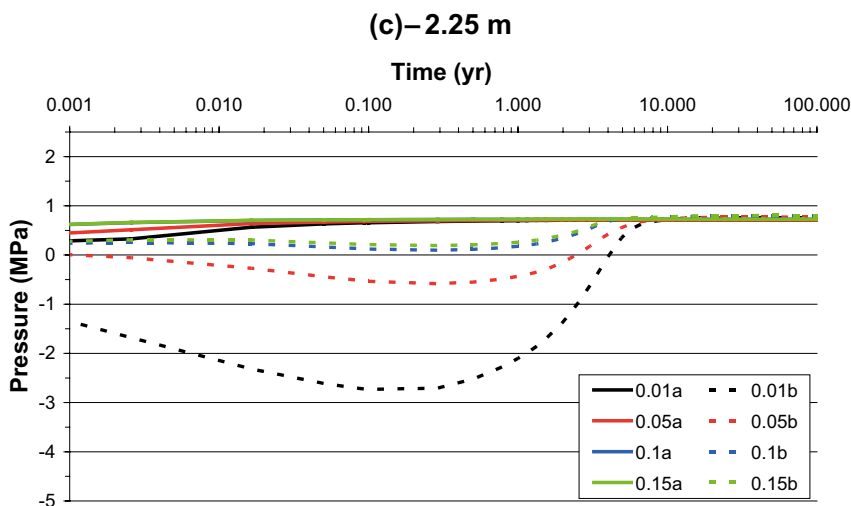
(a) – 0.75 m

(b) – 1.5 m

(c) – 2.25 m

Figure A2-25. *Pressure within the bedrock 0.01 m, 0.05 m, 0.1 m, 0.15 m, 1.0 m and 5.0 m (outward only) from the deposition borehole wall. Results are shown for a slice parallel to the boreholes, with "a" and "b" distances denoting direction from the edge of the deposition hole. The pressure curves shown correspond to the tenth realisation of the stochastic fracture network. Figures (a, b, c) are for borehole KO0014G01 at depths of 0.75 m, 1.5 m and 2.25 m respectively.*
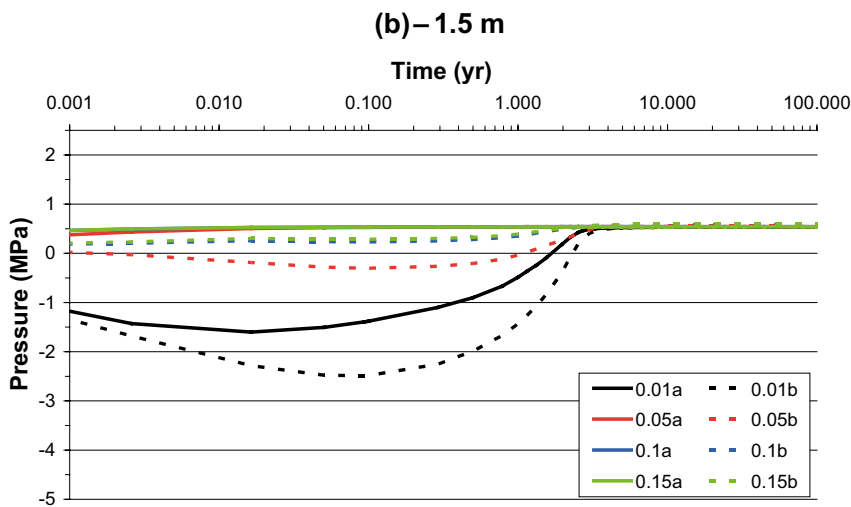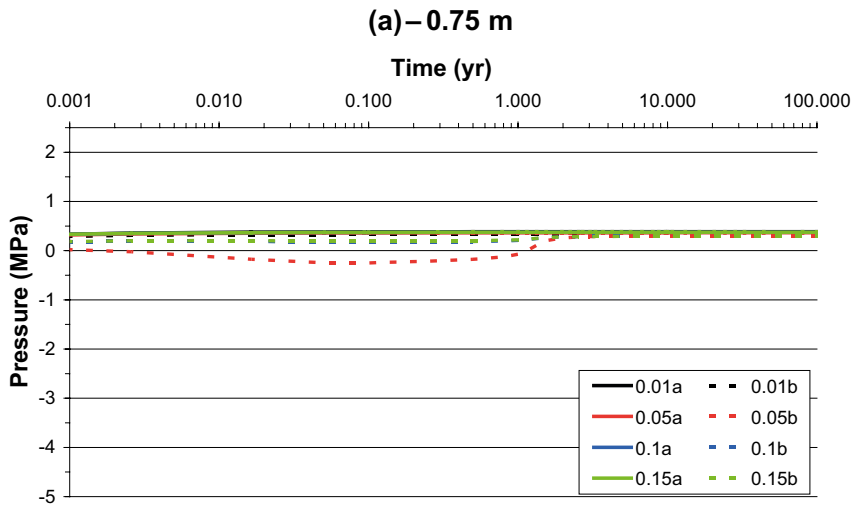
Figure A2-26. *Pressure within the bedrock 0.01 m, 0.05 m, 0.1 m, 0.15 m, and 1.0 m from the deposition borehole wall. Results are shown for a slice parallel to the boreholes, with "a" and "b" distances denoting direction from the edge of the deposition hole. The pressure curves shown correspond to the tenth realisation of the stochastic fracture network. Figures (a, b, c) are for borehole KO0015G01 at depths of 0.75 m, 1.5 m and 2.25 m respectively.*
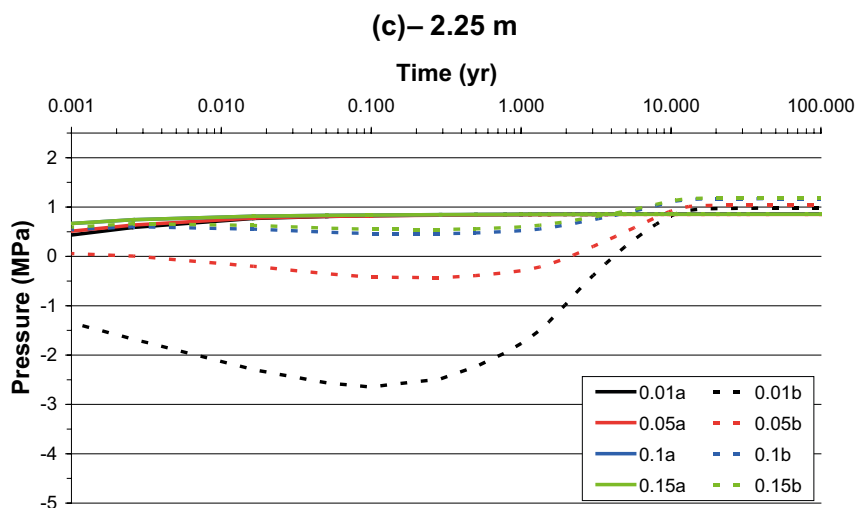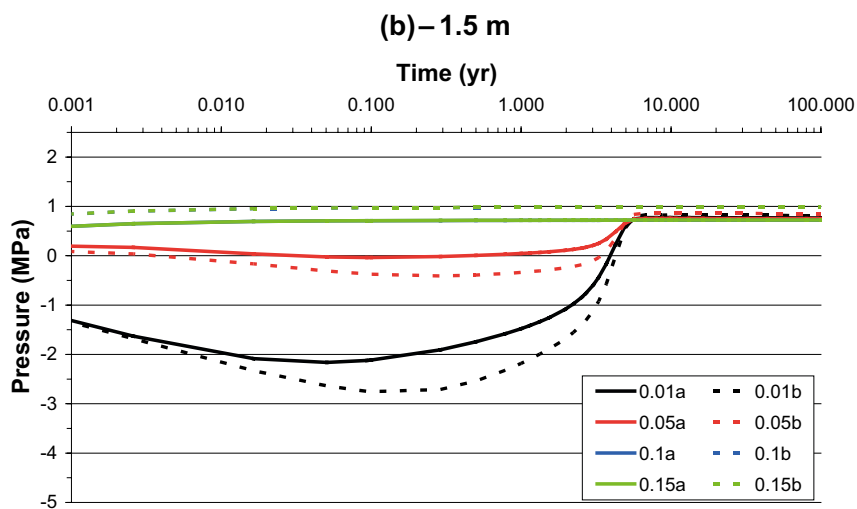
(a) – 0.75 m

Time (yr)

(b) – 1.5 m

Time (yr)

(c) – 2.25 m

Time (yr)

Figure A2-27. *Pressure within the bedrock 0.01 m, 0.05 m, 0.1 m, 0.15 m, and 1.0 m from the deposition borehole wall. Results are shown for a slice parallel to the boreholes, with "a" and "b" distances denoting direction from the edge of the deposition hole. The pressure curves shown correspond to the tenth realisation of the stochastic fracture network. Figures (a, b, c) are for borehole KO0017G01 at depths of 0.75 m, 1.5 m and 2.25 m respectively.*
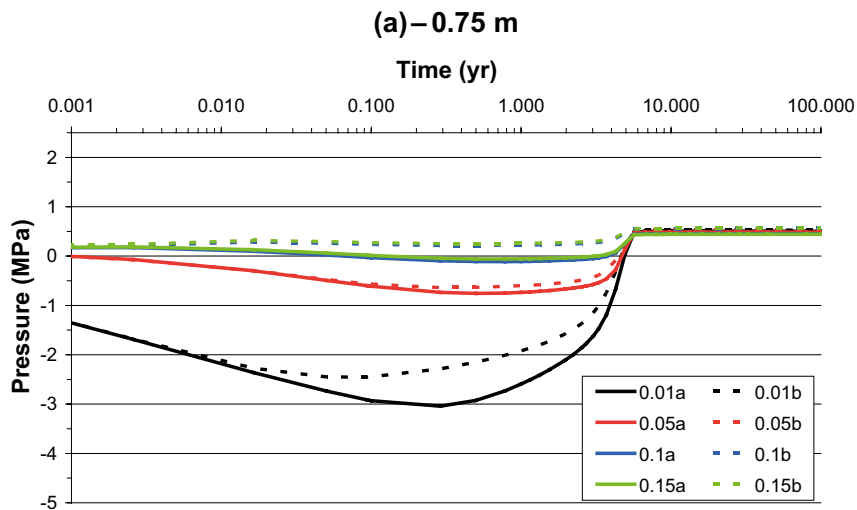
(a) – 0.75 m

Time (yr)

(b) – 1.5 m

Time (yr)

(c) – 2.25 m

Time (yr)

Figure A2-28. Pressure within the bedrock 0.01 m, 0.05 m, 0.1 m, 0.15 m, and 1.0 m from the deposition borehole wall. Results are shown for a slice parallel to the boreholes, with "a" and "b" distances denoting direction from the edge of the deposition hole. The pressure curves shown correspond to the tenth realisation of the stochastic fracture network. Figures (a, b, c) are for borehole KO0018G01 at depths of 0.75 m, 1.5 m and 2.25 m respectively.
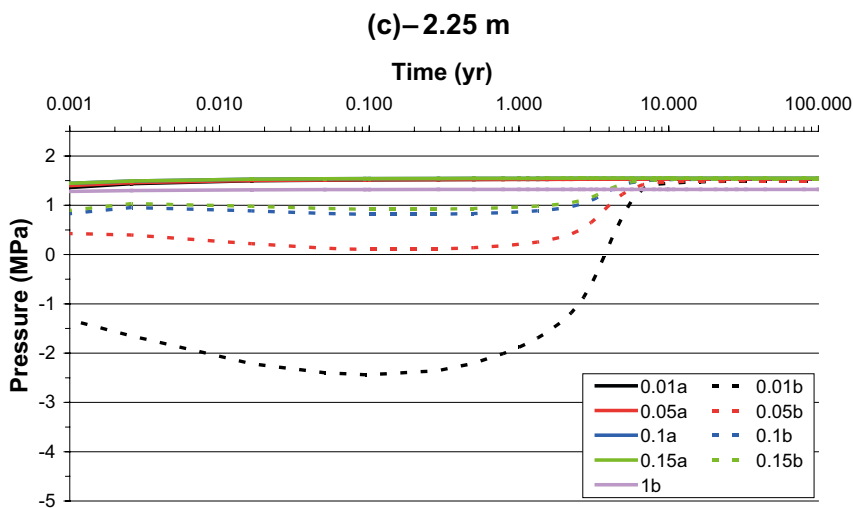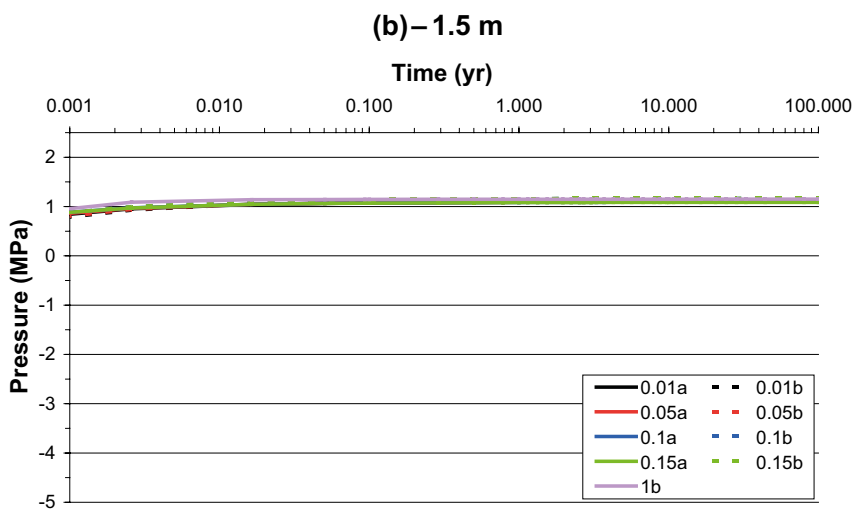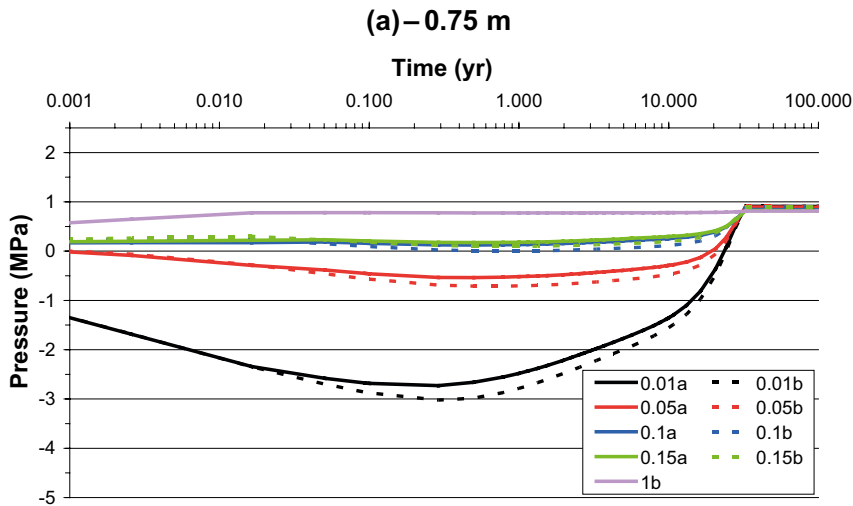
(a) – 0.75 m

(b) – 1.5 m

(c) – 2.25 m

Figure A2-29. *Pressure within the bedrock 0.01 m, 0.05 m, 0.1 m, 0.15 m, 1.0 m and 5.0 m (outward only) from the deposition borehole wall. Results are shown for a slice parallel to the boreholes, with "a" and "b" distances denoting direction from the edge of the deposition hole. The pressure curves shown correspond to the tenth realisation of the stochastic fracture network. Figures (a, b, c) are for borehole KO0020G01 at depths of 0.75 m, 1.5 m and 2.25 m respectively.*

SKB is responsible for managing spent nuclear fuel and radioactive waste produced by the Swedish nuclear power plants such that man and the environment are protected in the near and distant future.

skb.se